Mapping the Cellular and Spatial Landscape of Metastatic Melanoma

Ruth Allen

A thesis submitted in fulfilment of the requirements for the degree of Doctor of Philosophy

Faculty of Medicine and Health

The University of Sydney

June 2024

1 INTRODUCTION 19

1.1 METASTATIC MELANOMA 19

1.1.1 Pathogenesis 19

1.1.2 Incidence 20

1.1.3 Current therapies/treatment strategies 21

1.2 TUMOUR MICROENVIRONMENT OF METASTATIC MELANOMA 21

1.2.1 Lymphocytes 22

1.2.2 Innate cells 23

1.2.3 Structural Cells and the Extracellular Matrix 26

1.2.4 Tumour cells 27

1.3 MELANOMA AND IMMUNOTHERAPY 28

1.3.1 Mechanisms of Response and Resistance 28

1.3.2 Immune related adverse events 29

1.3.3 VISTA: a new immunotherapy target 29

1.3.3.1 Clinical Trials targeting VISTA 30

1.3.3.2 VISTA in tissue 30

1.3.3.3 VISTA and hypoxia 32

1.3.3.4 VISTA in inflammatory disease 32

1.4 ADJUVANT RADIOTHERAPY TO TREAT METASTATIC MELANOMA 32

1.4.1 Current clinical guidelines for radiotherapy use 33

1.4.2 Radiotherapy mechanisms in the TME 33

1.4.3 Abscopal Effect 34

1.4.4 Radiotherapy & Immunotherapy 35

1.4.5 Emerging radiotherapy technologies 36

1.5 EXPERIMENTAL APPROACHES TO SINGLE CELL OMICS 36

1.5.1 From immunofluorescence to whole-genome mapping 37

1.5.2 Current approaches to spatial omics 37

1.5.3 Analysing single cell omics 39

1.6 THE PRESENT STUDY 41

2 MATERIALS AND METHODS 42

2.1 FRESH TUMOUR DISSOCIATION 42

2.2 FLOW CYTOMETRY 42

2.2.1 Sample preparation and staining 42

2.2.2 Sample Acquisition 42

2.2.3 Flow Cytometry Data Analysis 43

2.3 MULTIPLEX IMMUNOHISTOCHEMISTRY (MIHC) STAINING 44

2.3.1 Tissue preparation 44

2.3.2 OPAL™ IHC Staining *44*
2.3.3 Imaging *45*
2.4 IMAGING MASS CYTOMETRY 47
2.4.1 Tissue Staining *47*
2.4.2 Tissue Ablation *48*
2.4.3 Preliminary Analysis *48*
2.4.4 Cell segmentation (Cell Profiler) and targeted cell phenotyping *48*
2.4.5 Cell segmentation, supervised clustering and spatial analysis *49*
2.5 RNASCOPE *IN SITU* HYBRIDISATION 51
2.5.1 Tissue Preparation *51*
2.5.2 In situ hybridisation *51*
2.5.3 Controls *52*
2.5.4 Imaging *52*
2.5.5 Data analysis *52*
2.6 XENIUM *IN SITU* HYBRIDISATION 53
2.6.1 Tissue Preparation *53*
2.6.2 Tissue deparaffinization *54*
2.6.3 Tissue decrosslinking *54*
2.6.4 Hybridisation *55*
2.6.5 Post-hybridisation wash and ligation *55*
2.6.6 Tissue amplification *55*
2.6.7 Autofluorescence Quenching *55*
2.6.8 Nuclear Staining *56*
2.6.9 Imaging *56*
2.6.10 Data analysis *56*
2.7 PHENOCYCLER FUSION (PCF) 61
2.7.1 Tissue Preparation *61*
2.7.2 Tissue Staining *61*
2.7.3 PCF Imaging *61*
2.8 HEMATOXYLIN AND EOSIN-STAINING 62
2.8.1 H&E Staining *62*
2.8.2 H&E Imaging *63*
3 DETAILED PHENOTYPING OF MYELOID POPULATIONS WITHIN METASTATIC MELANOMA REVEALS PD-L2+ MYELOID CELLS ARE ASSOCIATED WITH RESPONSE TO ANTI-PD-1 THERAPY (MANUSCRIPT IN PREPARATION FOR SUBMISSION) 64
3.1 INTRODUCTION 66
3.2 MATERIALS AND METHODS 67

3.3 RESULTS 70
3.4 DISCUSSION 81
4 MAPPING THE CELLULAR LANDSCAPE OF METASTATIC MELANOMA TUMOURS 89
4.1 INTRODUCTION 89
4.2 MATERIALS AND METHODS 90
4.2.1 Imaging Mass Cytometry 90
4.3 RESULTS 90
4.3.1 Clinical Cohort 90
4.3.2 Established alternate methods for the analysis of high-parameter imaging mass cytometry data 91
4.3.2.1 Method 1: Mapping the cellular landscape of tumours using supervised cell segmentation and manual phenotyping 91
4.3.2.2 Method 2: Using an assisted AI-platform to map the cellular landscape of tumours 101
4.3.2.3 Method III: Unsupervised Clustering 103
4.3.3 Spatial analysis reveals how immune and tumour cells interact in metastatic melanoma high-tumour regions 106
4.3.4 Applying a different approach to understand the role of the TME and its impact on clinical outcomes 109
4.3.5 Tumour composition did not differ between treatment allocations 109
4.3.6 Higher immune and non-lymphoid cells in high-tumour regions of treatment naïve metastatic melanoma tumours are associated with survival 109
4.3.6.1 Validation of the impact of the TME on clinical outcome used unbiased approach (Method III) 122
4.3.7 Low presence of immune and non-lymphocytic cells in high-tumour regions of treatment naïve metastatic melanoma tumours are associated with relapse 122
4.3.7.1 Manual Gating 122
4.3.7.2 Unbiased clustering 125
4.3.8 Impact of radiotherapy on (local) relapse 125
4.3.8.1 Spatial analysis reveals innate and non-immune cell interactions distinguish patients who survived longer 133
4.3.8.2 Spatial analysis reveals immune, tumour and structural cells associated with relapse 141
4.4 DISCUSSION 142
5 COMBINING SPATIAL TRANSCRIPTOMICS AND SPATIAL PROTEOMICS TO MAP THE IMMUNE LANDSCAPE OF TUMOURS 150
5.1 INTRODUCTION 150
5.2 MATERIALS AND METHODS 151
5.2.1 Experimental Design of Xenium in situ hybridisation study 151
5.3 RESULTS 151

5.3.1 In situ analysis of treatment naïve metastatic melanoma using RNAscope 151
5.3.1.1 Establishing protocols for the detection of multiple cytokines within the TME. 151
5.3.2 Establishing analysis pipeline for spatial transcriptomics 152
5.3.2.1 Supervised clustering of single cell data 156
5.3.2.2 Cluster annotation 165
5.3.3 Application of spatial transcriptomics data 167
5.3.3.1 Tumour cells make up the majority of high-tumour regions 167
5.3.3.2 Tumour cells, endothelial cells and fibroblasts are associated with survival in melanoma patients with high risk of relapse 168
5.3.3.3 Tumour cells, T cells and fibroblasts are associated with lack of relapse in melanoma patients with high risk of relapse 169
5.3.4 Establishing protocols for combined spatial transcriptomics and spatial proteomics 169
5.3.4.1 Post-in situ hybridisation proteomics reveals validity of non-ablative transcriptomic imaging 169
5.3.4.2 Imaging Mass Cytometry (IMC) 170
5.3.4.3 PCF 174
5.3.4.4 Haematoxylin and Eosin staining 174
5.4 Discussion 174
6 DISCUSSION 185
6.1 Introduction 185
6.2 Experimental tools in the field of cancer immunology 185
6.2.1 Flow Cytometry & CyTOF 185
6.2.2 Imaging Mass Cytometry 186
6.2.3 In situ Hybridisation 187
6.3 Combining multiple experimental methods 189
6.3.1 Practical realities of multi-omic datasets 190
6.3.2 Projects with many methods require many experts 190
6.3.3 Analysing data efficiently and judiciously 191
6.4 Linking tumour composition with patient outcomes in metastatic melanoma 192
6.4.1 Investigating the myeloid compartment 192
6.4.2 CD4 T cells as important drivers of anti-tumour response 193
6.4.3 Approaching tumour heterogeneity 193
6.5 Comparing cohorts and methods 195
6.6 Future directions 195
6.7 Conclusion 196
7 REFERENCES 199

Statement of Originality

I certify that to the best of my knowledge the content of this thesis is my own work. This thesis has not been submitted for any other degree or purposes.

I certify that the intellectual content of this thesis is the product of my own work and that all the assistance received in preparing this thesis has been appropriately credited and acknowledged as below.

Chapter 3 (manuscript in preparation to be submitted)
AT – performed CyTOF experiment, data analysis performed by Ruth Allen.
MT – performed some flow cytometry experiments, data analysis performed by Ruth Allen
SS – performed some flow cytometry experiments, data analysis performed by Ruth Allen
Chapter 4
FA & EP – assisted with and developed some of analysis pipeline used (IMC)
Chapter 5
RI – performed sectioning of TMA
TA – assisted Xenium staining and acquisition (as part of Sydney Cytometry core facility)
XB – performed PCF staining and imaging (Melanoma Institute Australia)
FA – assisted with analysis (Xenium)

_____

Ruth Allen

28th June 2024

As supervisor for the candidature upon which this thesis is based, I can confirm that the authorship attribution statements above are correct.

_____

Associate Professor Umaimainthan Palendira

28th June 2024

Acknowledgements

I am so lucky to have to many people to thank. I have had amazing support across the four years it took to produce this thesis. My time as a PhD candidate has been a privilege and a pleasure due to all those mentioned here.

I want to first thank my unbelievably amazing supervisors. Mainthan and Angela, you have stayed with me from the beginning of my research journey over six years ago. Your support over both the difficult and exciting times of this PhD is the reason I am at the finish line. Mainthan, your ever-present optimism and genuine wonder of immunology is infectious. Your open invitation to me and anyone else in the department for a chat in your office has never been taken for granted. Angela, the past 6 years with me have proven that you are quite possibly one of the most patient people in the world. You are always seven steps ahead in everything, making sure your students are supported and prepared. I love when we are on the same wavelength and don't need to speak in full sentences (although sometimes I should indeed finish the sentence). Scott, I am so happy you came onto the supervisory dream team - your eye for detail and thoughtful feedback have been so useful. More than that, teaching with you has taught me so much, but most of all is the most fun with you!

I would also like to thank Professor Angela Hong for trust, support and encouragement you gave to me in this project. Thank you to A/Prof Ellis Patrick for the ongoing collaboration and support of this project. A HUGE thankyou is required for Farhan Ameen for the patience, time and interest you have given to this project. Thank you also to the Melanoma Institute of Australia for their ongoing support in a multitude of ways across my candidature.

I want to thank all my friends at CPC for the endless (stairwell) chats, coffees, data discussions, and strolls when everything felt too hard. I would not have completed this thesis without you. I also want to thank past members of the Palendira lab who I learnt so much from.

Finally, I would like to thank the patients involved in the studies presented in this thesis. I am privileged to be able to perform research using these samples.

Abstract

Novel treatment strategies for metastatic melanoma have significantly improved patient outcomes in the last decade. To increase the number of patients that respond to available therapies and do not develop resistance, researchers must uncover the biological mechanisms involved in response. This study aimed to address this by profiling the cellular composition of metastatic melanoma and identifying novel features involved in tumour progression and response to therapy. First, we examine the immune infiltrate of metastatic melanoma tumours using high-parameter cytometry and employ particular attention to the phenotypic diversity of the myeloid compartment. In this study we identify two novel myeloid populations that are enriched in tumours of patients that responded to PD-1 immunotherapy when compared to non-responders. This study also profiled checkpoint regulator VISTA was expressed on multiple immune infiltrates, particularly macrophages and other myeloid populations. Secondly, we employ high-parameter imaging techniques (Imaging Mass Cytometry and Xenium *in situ* hybridisation) to examine the spatial landscape of metastatic melanoma in treatment naïve lymph-node associated samples from 100 patients with metastatic melanoma that were enrolled in clinical trial ANZMTG 01.02/TROG 02.01. As this trial was conducted before the availability of systemic therapies, our study had the unique opportunity to perform a detailed analysis of the TME of treatment naïve metastatic melanoma. Using both manual and supervised clustering approaches, we identify many different cell types in high-tumour regions of metastatic melanoma, including immune, stromal and tumour cells. Interestingly, we see multiple distinct tumour cell phenotypes across samples. Thirdly, we then match this detailed analysis of the TME with patient clinical details including relapse location, relapse time, nodal spread status and survival time to understand what was common between patients who had better outcomes. We find that patients with more activated, proliferating and functional immune cells within tumour regions were more likely not to relapse and to survive longer. Interestingly, supervised clustering of these data identified a tumour cell population that was associated with better outcomes. Throughout these studies, we compare the accuracy, efficiency and value of the various computational methods employed to analyse high-parameter proteomic and transcriptomic data. We also establish a true multi-omics experiment by successfully performing sequential *in situ* hybridisation (transcriptomics), high-dimensional protein staining (proteomics) and histochemical staining. This thesis presents a comprehensive overview of the TME in metastatic melanoma, identifies novel cell populations involved in both response to immunotherapy and tumour progression, and evaluates methods used to

analyse multi-omics datasets. This work contributes to a better understanding of how cells co-operate within tumours, highlights possible avenues for clinical treatment strategies and progresses the implementation of spatial omics in tumour immunology.

Publications produced during candidature not included in this thesis

Lee H, Ferguson AL, Quek C, Vergara IA, Pires daSilva I, **Allen R**, Gide TN, Conway JW, Koufariotis LT, Hayward NK, Waddell N, Carlino MS, Menzies AM, Saw RPM, Shklovskaya E, Rizos H, Lo S, Scolyer RA, Long GV, Palendira U, Wilmott JS. **Intratumoral CD16+ Macrophages Are Associated with Clinical Outcomes of Patients with Metastatic Melanoma Treated with Combination Anti-PD-1 and Anti-CTLA-4 Therapy**. Clin Cancer Res. 2023 Jul 5;29(13):2513-2524. doi: 10.1158/1078-0432.CCR-22-2657. PMID: 36790412.

Nahar KJ, Marsh-Wakefield F, Rawson RV, Gide TN, Ferguson AL, **Allen R**, Quek C, da Silva IP, Tattersal S, Kiely CJ, Sandanayake N, Carlino MS, McCaughan G, Wilmott JS, Scolyer RA, Long GV, Menzies AM, Palendira U. **Distinct pretreatment innate immune landscape and posttreatment T cell responses underlie immunotherapy-induced colitis**. JCI Insight. 2022 Nov 8;7(21):e157839. doi: 10.1172/jci.insight.157839. PMID: 36173679; PMCID: PMC9675442.

Ferguson AL, Sharman AR, **Allen RO**, Ye T, Lee JH, Low TH, Ch'ng S, Palme CE, Ashford B, Ranson M, Clark JR, Patrick E, Gupta R, Palendira U. **High-Dimensional and Spatial Analysis Reveals Immune Landscape-Dependent Progression in Cutaneous Squamous Cell Carcinoma**. Clin Cancer Res. 2022 Nov 1;28(21):4677-4688. doi: 10.1158/1078-0432.CCR-22-1332. PMID: 36044477.

Abbreviations

APC	**Antigen presenting cell**
AR	Antigen Retrieval
Bcl	B-cell lymphoma
CAR-	Chimeric Antigen Receptor
CBA	Cytokine Bead Array
CBL	Checkpoint blockade therapy
CCL	Chemokine ligand
CCR	Chemokine Receptor
CD	Cluster of Differentiation
cDC	Conventional dendritic cell
CTL	Cytotoxic T lymphocyte
CTLA-4	Cytotoxic T lymphocyte associated protein 4
CXCL	Chemokine (C-X-C motif) ligand
CyTOF	Mass Cytometry Time of flight
DC	Dendritic cell
DMSO	Dimethyl Sulfoxide
DNA-Ir	DNA-Intercalator
ECM	Extracellular Matrix
EDTA	Ethylenediaminetetraacetic Acid
EGF	Epidermal growth factor
FCS	Foetal Calf Serum
FFPE	Formalin-fixed paraffin embedded
Fit-SNE	Fast Interpolation-based t-SNE
FSC-A	Forward scatter area
FSC-H	Forward scatter height
HCC	Hepatocellular carcinoma
HIF	Hypoxia inducible factor
HRP	Horse radish peroxidase
iDC	Inflammatory DC
IDO	Indoleamine 2,3-dioxygenase
IFN	Interferon
Ig	Immunoglobulin
IHC	Immunohistochemistry
IL	Interleukin
IMC	Imaging Mass Cytometry
irAE	immune-related adverse events
LAG-3	Lymphocyte activation gene 3
LN	lymph node
LPS	lipopolysaccharide
Mϕ	Macrophage
M1	Classically activated macrophage
M2	Alternatively activated macrophage

mAb	Monoclonal antibody
MCP	Monocyte chemoattractant protein
MFI	Mean Fluorescence Intensity
MHC	Major Histocompatibility Complex
MIP	Macrophage inflammatory protein
NGFR	Nerve Growth Factor Receptor
NK	Natural Killer
PBS	Phosphate Buffered Serum
PCF	PhenoCycler Fusion
PD-1	Programmed Death 1
PD-L1	Programmed Death Ligand 1
PFA	Paraformaldehyde
PKM2	Pyruvate kinase muscle isozyme M2
RORγt	RAR-related orphan receptor gamma
rcf	relative centrifugal force
RPMI	Roswell Park Memorial Institute
SC	Subcutaneous
SRT	Sterotactic Radiotherapy
TAM	Tumour-Associated Macrophage
Tbet	T-box transcription factor
TCR	T cell receptor
TGF-β	Transforming growth factor
TIL	Tumour infiltrating lymphocyte
TIM	Tumour inducible myeloid cell
TIM-3	T cell immunoglobulin and mucin-domain containing-3
TLR	Toll-like receptor
TMA	Tissue microarray
TME	Tumour microenvironment
TNF	Tumour Necrosis Factor
Tr8	Tumour-resident CD8+ T cell
Treg	Regulatory T cell
Trm	Tissue Resident Memory T Cell
t-SNE	t-distributed Stochastic Neighbourhood Embedding
VEGF	Vascular endothelial growth factor
VISTA	V-domain Ig Suppressor of T cell activation

List of Tables

Table No.	Figure Title	Page No.
Table 2.1	Flow Cytometry Reagents	43
Table 2.2	Flow Cytometry Antibodies	43
Table 2.3	Tissue Staining Reagents	45
Table 2.4	OPAL IHC Reagents	46
Table 2.5	OPAL IHC Antibodies	46
Table 2.6	IMC Reagents	49
Table 2.7	IMC Antibodies	49
Table 2.8	RNAScope Reagents	53
Table 2.9	Xenium in situ Hybridisation Reagents	57
Table 2.10	Xenium in situ Gene Panel	57
Table 2.11	Phenocycler Fusion Antibodies	62
Table 2.12	Hematoxylin and Eosin (H&E) Staining Reagents	63
Table 4.1	Clinical trial ANZMTG 01.02/TROG 02.01/NCT00287196 patient details	92
Table 4.2	Markers employed to define cell phenotypes in manual gating	99
Table 4.3	Proportions of cell clusters identified in Figure 4.6 compared between patients alive or dead at clinical trial end point.	122
Table 4.4	Proportions of cell clusters identified in Figure 4.6 compared between patients that relapsed and those that did not by clinical trial end point.	131
Table 4.5	Pairwise analysis of average distance between cell clusters reveals cellular relationship that differ between patients grouped by survival and extranodal spread status.	140
Table 5.1	Top-expressed transcripts across clusters	157

List of Figures

Figure No.	Figure Title	Page No.
Figure 2.1	Imaging Mass Cytometry Experimental Workflow	47
Figure 2.2	Imaging Mass Cytometry analysis workflow	49
Figure 2.3	Xenium in situ Experimental Workflow	53
Figure 3.1	B and T cell populations and subsets in metastatic melanoma tumour tissue	71
Figure 3.2	Metastatic melanoma tissue contained phenotypically diverse and distinct myeloid cell subsets with varying expression of immune checkpoint and modulatory markers	73
Figure 3.3	Myeloid populations in melanoma identified using CyTOF	75
Figure 3.4	PD-L2+ myeloid cells are high in tumours of PD-1-responders	78
Figure 3.5	Mapping the VISTA expression of immune infiltrates in treatment-naïve metastatic melanoma tumours	79
Supplementary Figure 3.1	Proportions of immune cells do not differ between male and female patients or between tumour location	86
Supplementary Figure 3.2	Metastatic melanoma tissue contained phenotypically diverse and distinct myeloid cell subsets with varying expression of immune checkpoint and modulatory markers	87
Supplementary Figure 3.3	VISTA in tumour tissue is primarily expressed on immune cells.	88
Figure 4.1	Patient cohort flowchart from randomisation to primary outcomes	93
Figure 4.2	Imaging Mass Cytometry staining of metastatic melanoma tissues	94
Figure 4.3	Gating strategy for identifying cells in the TME of metastatic melanoma	97
Figure 4.4	Cellular composition of metastatic melanoma tumours	98
Figure 4.5	Tumour and immune cells in metastatic melanoma identified using assisted cell analysis software.	101

Figure 4.6	Supervised clustering performed on metastatic melanoma biopsies reveals 14 distinct cell populations.	103
Figure 4.7	Spatial interactions within high-tumour regions of treatment naïve metastatic melanoma.	106
Figure 4.8	No differences in tumour composition between patients treated with adjuvant radiotherapy and no radiotherapy.	109
Figure 4.9	Higher quantities of CD8 T cells in tumour regions are associated with survival in metastatic melanoma	110
Figure 4.10	Higher quantities of CD4 T cells in tumour regions are associated with survival in metastatic melanoma patients	112
Figure 4.11	Higher quantities of B cells in tumour regions are associated with survival in metastatic melanoma patients	113
Figure 4.12	Quantities of innate immune cells in tumour regions are not associated with survival in metastatic melanoma patients	114
Figure 4.13	Higher quantities of non-leukocytes in tumour regions are associated with survival in metastatic melanoma patients	115
Figure 4.14	Tumour cells in tumour regions are not associated with survival in metastatic melanoma patients	116
Figure 4.15	Cell populations associated with longer survival in metastatic melanoma patients	119
Figure 4.16	Immune and tumour cell densities of patients separated by extranodal spread and survival.	120
Figure 4.17	Higher quantities of CD8 T cells in tumour regions are associated with no relapse in metastatic melanoma	123
Figure 4.18	Higher quantities of CD4 T cells in tumour regions are associated with no relapse in metastatic melanoma	124
Figure 4.19	B cell quantities in tumour regions are not associated with relapse in metastatic melanoma	126
Figure 4.20	Quantities of innate immune cells in tumour regions are not associated with relapse in nodal melanoma	127
Figure 4.21	Quantities of non-leukocytes in tumour regions are associated with relapse in metastatic melanoma patients	128

Figure 4.22	Tumour cell quantities in tumour regions are not associated with relapse in nodal melanoma patients	129
Figure 4.23	Tumour quantities of lymphocytes are not significantly different between treatment allocations and relapse conditions	133
Figure 4.24	Tumour quantities of innate immune cells are not significantly different between treatment allocations and relapse conditions	134
Figure 4.25	Tumour quantities of tumour cells are not significantly different between treatment allocation and relapse conditions.	135
Figure 4.26	Immune and tumour cell density does not differ between relapse location or treatment allocations.	136
Figure 4.27	Spatial interactions associated with survival within high-tumour areas of treatment naïve metastatic melanoma	137
Figure 4.28	Spatial interactions associated with relapse within high-tumour areas of treatment naïve metastatic melanoma	138
Figure 5.1	Cellular location of IFNγ in metastatic melanoma	153
Figure 5.2	IL-10 transcripts do not differ between cutaneous SCC patients with and without disease progression	154
Figure 5.3	Representative staining of RNAscope negative control probe in metastatic melanoma samples	155
Figure 5.4	Xenium slide 1 pre-acquisition	158
Figure 5.5	Xenium slide 2 pre-acquisition	159
Figure 5.6	Representative Xenium *in situ* mRNA staining in metastatic melanoma tissue.	160
Figure 5.7	Heatmap of transcript expression across 20 clusters identified using supervised clustering	161
Figure 5.8	Cell clusters identified using supervised clustering	162
Figure 5.9	Cell clusters associated with survival in metastatic melanoma	163
Figure 5.10	Cell clusters associated with relapse in metastatic melanoma	164

Figure 5.11	Imaging mass cytometry performed on tumour tissue following transcriptomic staining	171
Figure 5.12	CD4 T cells are associated with survival in metastatic melanoma patients	173
Figure 5.13	No difference in innate immune cell proportions between metastatic melanoma patients alive or dead at clinical follow-up.	175
Figure 5.14	No significant differences in proportion of non-immune cells in metastatic melanoma patients alive or dead at follow-up.	176
Figure 5.15	Phenocycler Fusion fluorescent image of metastatic melanoma cores after staining and acquisition with Xenium platform.	177
Figure 5.16	Representative images of PCF cores successfully stained after Xenium *in situ* analysis	178
Figure 5.17	H&E staining of samples after mRNA and protein staining.	179
Figure 5.18	IMC, Xenium in situ hybridisation, PCF and H&E staining on one tumour sample.	180
Figure 6.1	Graphical summary of the findings of this study investigating the cellular composition of metastatic melanoma	197

1 INTRODUCTION

1.1 Metastatic Melanoma

Metastatic melanoma is the most aggressive form of skin cancer. It is estimated that the rate of melanoma diagnosed worldwide will increase by more than 50% by 2040 (Arnold et al., 2022). There has been no improvement in mortality rates in minority and lower socioeconomic populations, and low-income countries have disproportionately higher melanoma-related deaths to melanoma incidence (Chen et al., 2022a, Arnold et al., 2022). Ipilimumab (anti-CTLA-4) was the first monoclonal antibody (mAb) approved for use in melanoma in 2011, followed by nivolumab (anti-PD1) in 2014 (Koenig, 2011, Hazarika et al., 2017). Immunotherapies have resulted in a significant decrease in lifetime mortality risk for melanoma of the skin since 2013, particularly in males (Health and Welfare, 2023, Switzer et al., 2022). Despite the success of immunotherapies such as these there were an estimated 325 000 people diagnosed with melanoma and 57 000 deaths attributed to melanoma worldwide in 2020 (Arnold et al., 2022).

1.1.1 Pathogenesis

Cutaneous melanoma is caused by unrepaired genetic damage, driven by ultraviolet radiation and genetic causes (Long et al., 2023b). Both UVA and UVB can cause melanoma by inducing DNA damage that leads to melanoma progression (de Gruijl, 2002). Indoor tanning beds, which produce both UVA and UVB, have been clearly linked to increased melanoma risk (Lazovich et al., 2010), with the WHO classifying indoor tanning as a group 1 carcinogen in 2009 (Mogensen and Jemec, 2010, 2012). Data suggests a reduction in the use of tanning beds since 2010, particularly in young populations, however much of North America, Europe, Australia and New Zealand do not have clear laws in respect of tanning beds (Mathes et al., 2023, Rodriguez-Acevedo et al., 2020). Phenotypic factors such as skin, eye and hair colour and response to sunburn are used to determine skin-type and associated risks of skin cancer, often through simple categorisations such as the Fitzpatrick skin phototype scale, which can be completed without specialist equipment. However, these approaches are highly subjective and have been shown to be employed inappropriately in clinical settings (Ware et al., 2020, Pimentel, 2020). Other geographical factors such as altitude and latitude are linked to melanoma incidence due to their relationship with UV-levels (Chang et al., 2009, Crombie, 1979).

UV-independent mutations also play an important role in incidence of melanoma. $BRAF^{V600e}$, a protein involved in the MAPK signalling pathway, is mutated in approximately half of patients with metastatic melanoma (Edlundh-Rose et al., 2006, Ullrich and Byrne, 2012), Network (2015). The development of BRAF-inhibitors shortly followed, and early clinical trials reporting significant improvement in progression free survival led to BRAF-inhibitors becoming standard care for patients with metastatic melanoma (Hauschild et al., 2012, Chapman et al., 2011, McArthur et al., 2014). Alongside BRAF-inhibitors, Mitogen-Activated Protein Kinase (MEK) inhibitors were also being developed to improve efficacy of and resistance to BRAF-inhibition as they also target the MAPK signalling pathway. Clinical trials testing MEK inhibitors in BRAF-mutated melanoma were successful and led to BRAF/MEK inhibitor combination treatment strategies(Flaherty et al., 2012, King and Nathan, 2014). The three different combinations of BRAF and MEK inhibitors currently approved for use in metastatic melanoma are very similar in terms of efficacy and toxicity risk (Garutti et al., 2022).

It is known that approximately 10-15% of melanoma patients have family history of melanoma, often associated with a melanoma-associated germline mutation such as CDKN2A (Toussi et al., 2020, Saginala et al., 2021). Emerging evidence also shows an important role of the gut microbiome in melanoma development and progression, with one group finding specific bacterial and fungal communities were associated with melanoma invasiveness as well as regression (Vitali et al., 2022).

1.1.2 Incidence

Global incidence of melanoma in 2020 was estimated at 325,000 people with the highest incidence recorded in Australia, New Zealand, North America as well as Western and Northern Europe (Arnold et al., 2022, Labani et al., 2021). Importantly, data suggests that the burden of metastatic melanoma disease will increase with the aging population(Yuan et al., 2024). It is important to note however that global statistics are highly variable and are difficult to collate accurately due to differences in health access, screening and treatment for melanoma worldwide (Yuan et al., 2024).

In 2023, melanoma of the skin was the third most commonly diagnosed cancer in Australia after prostate and breast cancer (Health and Welfare, 2023). Melanoma incidence rates in Australia have been steadily decreasing for people under the age of 40 since the late 1990s,

likely linked to public health campaigns such as ‘slip slop slap’ and related advertisements of the 1980s (Health and Welfare, 2023, Cramb et al., 2020, Iannacone et al., 2015).

1.1.3 Current therapies/treatment strategies

Current treatment options for metastatic melanoma include surgery, immunotherapy, targeted therapies, chemotherapy and radiation therapy. Before 2010, these options were limited to surgery, chemotherapy, interleukin-2 (IL-2) and interferon-alpha (IFN-α) targeted therapies, and radiotherapy, resulting in metastatic melanoma patients having extremely poor outcomes. However, along with BRAF-targeted therapies, immunotherapy has become standard of care in stage III and stage IV melanoma in recent years, and has resulted in significant improvement in patient outcomes (Wolchok et al., 2017, Wolchok et al., 2022, Knight et al., 2023, Patel et al., 2023, Blank et al., 2024). Following the success of anti-PD-1/PDL-1, there was a significant influx of other possible targets into clinical trials to find effective therapies for patients who do not respond or develop resistance to available therapies. These include other drugs targeting other gene mutations within the MAPK pathway, various checkpoint receptor inhibitors (LAG-3, TIGIT, ICOS, OX40), however very few of these have progressed beyond phase II trials due to their efficacy compared to currently used therapies, with notable exceptions such as anti-LAG-3-therapy administered in conjunction with anti-PD-1 (Maher et al., 2024, Gide et al., 2023). More recently, there is increasing evidence to support immunotherapy being administered pre-surgery (neoadjuvant) rather than after surgical resection (adjuvant) therapy (Reijers et al., 2022, Amaria et al., 2022). Cell-based therapies such as tumour infiltrating lymphocyte (TIL) therapy and Chimeric Antigen Receptor T (CAR-T) cell therapy are gaining momentum in the melanoma space, but are not widely accessible at this time (Betof Warner et al., 2023, Gajra et al., 2022, Ghilardi et al., 2024, Razavi et al., 2021). Gaining insight from the successes and failures of the last ten years by detailing the immunological modulations caused by these therapies will allow us to understand how best to combine available therapies to improve patient response, resistance and survival.

1.2 Tumour Microenvironment of Metastatic Melanoma

The tumour microenvironment of metastatic melanoma consists of tumour cells, immune cells (including lymphocytes, dendritic cells, myeloid-derived suppressor cells and macrophages), as well as structural components such as blood vessels, fibroblasts and enzymes such as

collagenases. These cells are dynamically interacting which creates a plastic environment that directs tumour growth or suppression.

1.2.1 Lymphocytes

T cells comprise most of the immune infiltrate in metastatic melanoma (Erdag et al., 2012). Chronic stimulation of T cells commonly reported in viral infections and tumours results in an exhausted T cell state (Miller et al., 2019). Higher numbers of exhausted tumour-infiltrating lymphocytes are associated with progressive disease, incomplete response to immunotherapy and chronic tumour stimulation (Oliveira et al., 2021). CD8 T cells are well established in their association with better outcomes in melanoma patients (Azimi et al., 2012, Veatch et al., 2022, Erdag et al., 2012). Previous work from our research group established the association of $CD103^+$ Tumour resident ($CD69^+$) CD8 T cells with improved survival as well as response to immunotherapy (Edwards et al., 2018). Tissue-resident memory CD8 T cells play an important role in preventing tumour escape in melanoma, and have been shown to comprise a large proportion of the tumour-antigen-specific population in melanoma (Park et al., 2019, Duhen et al., 2018). We also know that exhausted or 'dysfunctional' CD8 T cell phenotypes in melanoma do not exist as one discrete population but can employ many different phenotypes, and have been shown to be able to proliferate and differentiate (Li et al., 2019).

CD4 T cells have been shown to directly kill melanoma cells through multiple mechanisms, including by the TNF family ligand TRAIL expressed on the cell surface of CD4 T cells (Nguyen et al., 2000). Tumour-antigen recognising CXCL13+ CD4 T cells have been shown in melanoma to correlate with patient survival as well as CD8 T cell and macrophage activation (Veatch et al., 2022). CD4 T cell subsets have been implicated in both pro- and anti-tumour responses. Notably, regulatory T cells (Tregs) have been linked to both good and bad outcomes in melanoma (Jacquelot et al., 2016, Ma et al., 2012). T_H2 cells have been shown to be enriched more than T_H1 cells in melanoma tumour tissue, contributing to a tumorigenic environment (Halim et al., 2017, Grotz et al., 2015). Conversely, adoptive T cell therapy in melanoma mouse models showed a potent anti-tumour effect of T_H2 cells (Mattes et al., 2003). T_H17 cells have been shown to have both pro and anti-tumour effects, driven by mediators produced by other cells in the TME including T cells, melanoma cells, cancer associated fibroblasts and myeloid cells (Chen and Gao, 2019, Martin-Orozco et al., 2009). Interestingly, glycolysis and hypoxia favour the development of T_H17 cells over Tregs in melanoma (Shi et al., 2011).

γδ T cells have been shown to be important tumour mediators in melanoma (Toia et al., 2019). γδ T cells are not MHC restricted and have been shown to produce anti-tumour cytokines TNF-α and IFN-γ as well as kill melanoma cells *in vitro* (Cordova et al., 2012). Proportions of peripheral γδT cells were associated with survival in immunotherapy-treated melanoma patients (Wistuba-Hamprecht et al., 2016), however, suppression of IL-17 on γδ T cells was shown to supress melanoma development in mouse models, pointing to the complicated role of γδ T cells in melanoma progression (Li et al., 2014). Recent work investigating the role of γδ T cells in the context of anti-PD-1 therapy in melanoma found that PD-1+Vδ1+ T cells retained functional effector capacities that were inhibited by anti-PD-1 therapy. These studies show that γδ T cells have an important role in both tumour progression and response to therapy.

B cells have been associated with both anti-tumour responses and pro-tumour responses in melanoma, highlighting a need to better understand the plasticity of B cells in the TME (Rodgers et al., 2022, Griss et al., 2019). We know that high expression of B cell signatures and B cell receptor diversity is associated with improved survival in melanoma patients (Iglesia et al., 2016). One study found a tumour-induced plasmablast-like-enriched B cell population with a CD27/CD38/PAX5 gene signature correlated with survival, in addition to CD8 T cell and macrophage numbers in melanoma (Griss et al., 2019). Interestingly, this same study found that loss of tumour-associated B cell signatures due to anti-CD20 therapy resulted in loss of CD8 and CD4 T cells and loss of tertiary lymphoid structures, all of which was resolved after termination of therapy (Griss et al., 2019). Furthermore, IgA antibodies produced by plasma B cells have been linked to worse outcomes in melanoma patients (Bosisio et al., 2016, Germain et al., 2015). B cells within melanoma tumours have been shown to upregulate genes involved in activation, inflammation, immune checkpoint, exhaustion and immunosuppression (Griss et al., 2019). Organised aggregates of T and B cells, dendritic cells and high endothelial venules (HEVs) that form within tumours, known as tertiary lymphoid structures, have an important anti-tumour role in melanoma (Cabrita et al., 2020, Attrill et al., 2022a, Cipponi et al., 2012)

1.2.2 Innate cells

Myeloid-derived suppressor cells (MDSCs) are a major contributor to tumour development (Cole et al., 2021). It is therefore imperative that MDSCs are further defined to allow us to best target them due to the heterogeneity between tumour type and patient (De Cicco et al., 2020).

MDSC with a suppressive phenotype promote a pro-tumour milieu in the TME and contribute to lack of response and resistance to immunotherapy (Weber et al., 2018). We must better understand the phenotypic and functional diversity of myeloid cells in the TME (Mantovani et al., 2021).

Macrophages are a 'double-edged sword' in tumours due to their plasticity and ability to interact with many immune and tumour subsets in the TME (Biswas and Mantovani, 2010, Zhou et al., 2022b, Mantovani and Marchesi, 2022). Categorisations of tumour-associated macrophages must continue to move away from M1/M2 oversimplifications if we are to advance our understanding of tumour immunology and avoid misinterpretation. Human macrophages are known to express a variety of markers, including but not limited to; CD14, CD16, CD68, CD13, CD11c, HLA-DR/MHC-II, mannose receptor CD206/MCR1, PD-1, PD-L1, arginase-1 and CD86 and have been seen to produce TNF-α and VEGF (Roussel et al., 2017, Liu et al., 2022a, Gordon et al., 2017, Wang et al., 2024, Villaseñor-Cardoso et al., 2013).

Many studies have highlighted the link between macrophages and tumour progression. Recent work found that immunotherapy-treated melanoma patients with higher CD16+ macrophages densities had longer progression-free survival (Lee et al., 2023). Another group found that tumour-infiltrating T cells were more closely associated with CD14-expressing cells than tumour cells in metastatic melanoma tumours (Martinek et al., 2022). Further, one recent study found that melanoma patients with tumour-infiltrating CD8 T cells located within high proximity to CD163+ macrophages had worse survival rates (De Logu et al., 2023). Another group showed that particular pattern recognition receptor genes highly expressed in one macrophage population were highly correlated with prognosis in cutaneous melanoma (Zhao et al., 2021). Macrophages are also important mediators of response to both immunotherapy and systemic therapies (Lee et al., 2023, Massi et al., 2019, Yan et al., 2021, Wu et al., 2022). Tumour-associated macrophage marker CD163 expression is associated with PD-1 and LAG-3 expression, and was found to associate with worse survival in cutaneous melanoma (Kim et al., 2020). Experimental approaches such as single-cell transcriptomics have added to our understanding of tumour-associated macrophages as a highly diverse and plastic group of cells(Cheng et al., 2021, Mulder et al., 2021).

Dendritic cells (DCs) modulate the TME by activating T cells with tumour antigens, phagocytosing tumour antigens and processing and presenting these antigens to T cells to

activate them, produce cytokines and communicate with other innate immune cells. Gene therapies targeting the activation of DCs in melanoma models that have shown these activated DCs stimulate increased production of antigen-specific T cell and natural killer cells (Wenthe et al., 2023). Additionally, one group has successfully reprogrammed tumour cells to exhibit cDC1 phenotype and function in melanoma mouse models (Zimmermannova et al., 2023), with these anti-tumour properties currently utilized in the development of DC vaccines in many cancers, including melanoma (Li et al., 2023a, Yazdani et al., 2020, Javed et al., 2016, Adamik et al., 2023). Broadly, markers of dendritic cells in melanoma include CD11c, HLA-DR, CD13, and CD1c and CD141 to delineate conventional dendritic cells 1 (cDC1) and 2 (cDC2) (Roussel et al., 2017, Schwarze et al., 2022, Hornsteiner et al., 2024, Villaseñor-Cardoso et al., 2013).

Natural killer (NK) cells are important anti-tumour mediators in melanoma (Zhao et al., 2023). NK cells within melanoma tumours exhibit gene expression programs associated with cytotoxicity, chemokine synthesis and DC recruitment (de Andrade et al., 2019). In melanoma patients treated with an *in-situ* tumour vaccination, NK cells promoted Treg apoptosis and were associated with better patient response (Jin et al., 2023). NK cells from melanoma can exhibit an exhausted phenotype similar to T cell populations, and this exhaustion has been shown to be reversable with anti-TIM-3 therapy (da Silva et al., 2014). NK cells have also been associated with worse patient outcomes in melanoma (de Jonge et al., 2019). We know that melanoma cells can evade recognition by NK cells through multiple mechanisms, including upregulation of nerve growth factor receptor (NGFR) (Lehmann et al., 2023). Interestingly, NK cell interaction with melanoma cells has been shown to increase NK cell recruitment (Parodi et al., 2015), however increased NK cell infiltration has been shown to cause melanoma cells to become resistant to NK-cell-mediated death (Balsamo et al., 2012).

Neutrophils can kill cancer cells directly through antibody-dependent cellular toxicity (ADCC) (Matlung et al., 2018). However, elevated neutrophil-to-lymphocyte ratios have been associated with poor prognosis in melanoma (Mallardo et al., 2023, Zhan et al., 2018). Neutrophil extracellular traps have also been correlated with necrosis and larger tumours in melanoma (Weide et al., 2023), with mouse models identifying that neutrophil-secreted Annexin A1 favoured melanoma metastasis (Sandri et al., 2023). Interestingly, extracellular vesicles derived from melanoma cell lines have been shown to polarise neutrophils towards a pro-tumour (ARG1/CXCR4/VEGF-expressing) phenotype (Guimarães-Bastos et al., 2022). It

has also been shown that neutrophils play an important role in immunotherapy-mediated anti-tumour response in melanoma, and they have been identified as a possible biomarker of response (Hirschhorn et al., 2023, Benguigui et al., 2024, Cristinziano et al., 2022).

1.2.3 Structural Cells and the Extracellular Matrix

The tumour extracellular matrix (ECM) is made up of a variety of proteins, including matrix metalloproteinases, collagens, fibronectin and proteoglycans that together construct the physical scaffold of the tumour (Popovic and Tartare-Deckert, 2022). ECM stiffness is closely linked to melanoma cell survival, migration, and epithelial-mesenchymal transition (Ahmadzadeh et al., 2017), with fibroblasts and endothelial cells being the predominant cell populations involved in tumour architecture.

Fibroblasts regulate the contents of the ECM by producing the majority of extracellular matrix proteins, including collagens, fibronectin, matrix metalloproteinase and enzymes required for ECM remodelling, and promote melanoma progression by producing mediators that promote melanoma cell survival and motility (Liu et al., 2019c, Romano et al., 2021). Fibroblasts activated by melanoma cells showed enhanced secretion of lactate, cytokines and proteins related to angiogenesis such as vascular endothelial growth factor A (VEGF-A) (Mazurkiewicz et al., 2022). Cancer-associated fibroblasts' (CAFs) role in melanoma is partially regulated by B-catenin, as dampening B-catenin expression in CAFs resulted in the reduced expression of CAF-associated markers, inability to respond to melanoma cells and reduced motility (Liu et al., 2019c). Additionally, CAFs have been shown to downregulate NK cell cytotoxicity and cytokine production in melanoma co-culture models (Balsamo et al., 2009). Fibroblasts have also been associated with BRAF/MEK inhibitor resistance in melanoma (Fedorenko et al., 2015, Hirata et al., 2015, Diazzi et al., 2022, Kim et al., 2016, Berestjuk et al., 2022).

Endothelial cells within the tumour actively supress inflammatory responses through autophagy (Verhoeven et al., 2023). High-endothelial venules form within tumour tissue from post-capillary venules and are important routes for lymphatic entry into the tumour (Asrir et al., 2022). A recent study found that genetic deletion of VEGF-R2 in endothelial cells led to enhanced hypoxia, reduced infiltration of T cells and profound reduction in blood flow to the tumour (Kido et al., 2022). The tumour endothelium is also the starting point for complement

cascade in the tumour, promoting neutrophil-mediated permeability of blood vessels that increased melanoma cell dissemination (Liu et al., 2022b).

1.2.4 Tumour cells

Tumour phenotypes in melanoma, as in most cancers, are highly heterogeneous. One study approached this by classifying melanocytes into four developmental states: melanocytic stem cell, foetal, neonate and adult, with genes associated with immune response and pigmentation increasing with each consecutive stage (Belote et al., 2021). The study observed that melanoma tumours are comprised of cells from many developmental programs, with large heterogeneity across patients (Belote et al., 2021). More recently, a study defined melanoma cell states by transcriptional clusters and found that none of the cell states were associated with genetic profiles of BRAF and NRAS mutational status, suggesting individual melanoma phenotypes are driven by non-genetic causes (Pozniak et al., 2024). The same study also observed HLA-DR+ melanoma cells were enriched in areas with immune cells, in particular CD8 T cell-dense areas, while HLA-DR- melanoma cells and CD8 T cells did not colocalise (Pozniak et al., 2024).

Melanoma cells can downregulate expression of melanoma antigens and appear as normal mesenchymal cells of CAFs (Pozniak et al., 2024). Melanoma tumour cell recognition by melanoma antigen-specific T cells was reduced after exposure to inflammatory cytokine TNF-α (Landsberg et al., 2012). Genes such as *AXL* and *HMGA2* are indicative of a dedifferentiated cell state and are markers of progression and prognosis (Belote et al., 2021, Raskin et al., 2013). TCF4 expression in melanoma cells in a mesenchymal-like state was inversely correlated with sensitivity to both BRAF and MEK inhibitors, identifying a possible clinical target to address response and resistance in melanoma (Pozniak et al., 2024). One study found podoplanin expression was associated with dedifferentiated melanoma populations and function as a possible biomarker for invasive dedifferentiated melanoma (de Winde et al., 2021).

Tumour cells can also develop vascular-like structures without involvement of endothelial cells through a process known as vascular mimicry. One study found vascular mimicry was medicated by PARP1 expression in melanoma, and targeting this may reduce spread of metastasis (Fernández-Cortés et al., 2023). Another study observed vascular mimicry in a human melanoma cell line was important for monocyte recruitment through adhesion

molecules and chemokine production (Tan et al., 2022). Melanoma cells can also transdifferentiate into an endothelial cell-like phenotype, acquiring CD31 and VE-cadherin expression (Li et al., 2020).

1.3 Melanoma and Immunotherapy

As melanoma is a highly immunogenic tumour, it is an excellent target for immunotherapy. Immunotherapies anti-CTLA-4 and anti-PD1/PD-L1 have had significant success in metastatic melanoma. Recently, PD-1/Lag3 combination immunotherapy was first shown in melanoma brain metastasis to have progression-free and overall survival rates to support use (Tawbi et al., 2021). Despite the success of immunotherapy in melanoma, there remains a significant proportion of people who do not respond or develop resistance to immunotherapy (Long et al., 2023a). The key to uncovering mechanisms of response and resistance is a detailed understanding of the complex and plastic relationship between immune cells, tumour cells and their local environment.

1.3.1 Mechanisms of Response and Resistance

Due to the complex and active nature of the TME, there have been many investigations into mechanisms of response and resistance to immunotherapy in melanoma. Higher tumour mutational burden is associated with response to PD-1 immunotherapy, while tumour purity and heterogeneity is associated with lack of response to PD-1 (Liu et al., 2019b). Tumour-resident memory CD8 T cells have been shown to predict response to immunotherapy (Damei et al., 2023). We also know that CD39+ tumour-resident CD8 T cells predict recurrence-free survival in patients treated with immunotherapy (Attrill et al., 2022b). The proximity of CD8 T cells that were both antigen-experienced and proliferating to tumour cells in pre-treatment samples has also been associated with response to immune-checkpoint inhibitors (ICIs) (Moldoveanu et al., 2022). ECM molecule EMILIN-2 modulates PD-L1 expression in melanoma cells, and its expression has been associated with higher PD-L1 expression in melanoma patients as well as response to anti-PD1 therapies (Fejza et al., 2021). Tumour-associated HEVs in metastatic melanoma are predictive of better response and survival with immunotherapy (Asrir et al., 2022). Analyses of cutaneous melanoma skin samples using a TCGA dataset found melanoma cells with a dedifferentiated gene signature were associated with partial or no response to ICI therapy (Belote et al., 2021).

1.3.2 Immune related adverse events

Immune activation in normal tissue after immunotherapy treatment can lead to immune-related adverse events (iRAEs), also known as ‘toxicities. The most common iRAEs in melanoma are those involving the gastrointestinal tract, including colitis and diarrhea (Patrinely et al., 2021, Schonfeld et al., 2022). Rarer iRAEs include nephritis, myocarditis, type 1 diabetes and, in very rare cases, death (Park et al., 2023). Greater incidence of iRAEs in melanoma patients has been associated with lower frequencies of Tregs, upregulation of CD69 expression on CD8 T cells and increased proportion of MDSCs (Lepper et al., 2023). We also know that the development of colitis in immunotherapy-treated melanoma patients is associated with higher circulating monocytes at baseline (Nahar et al., 2022). Development of autoantibodies is also a likely driver of immunotherapy-induced iRAEs, and B cells have recently been identified as possible biomarkers of iRAEs and predictors of ICI response (Taylor et al., 2022, Willsmore et al., 2020).

1.3.3 VISTA: a new immunotherapy target

Inhibitory signalling is a vital mechanism of self-tolerance. V-domain Immunoglobulin Suppressor of T Cell Activation, or VISTA, is an established inhibitory receptor and ligand expressed on a variety of immune and tumour cells, in particular myeloid cells and monocytes (Li et al., 2021). VISTA is an unfavourable prognostic factor in cutaneous melanoma (Choi et al., 2020). VISTA emerged as one of many possible targets for immune checkpoint blockade therapy initially due to its homology to PD-L1. It has since been shown to be upregulated in response to PD-1 therapy as a possible mechanism of resistance, but its expression is regulated by a pathway distinct from PD-1/PD-L1 regulation (Blando et al., 2019, Rosenbaum et al., 2020, Gao et al., 2017a, Kakavand et al., 2017, Li et al., 2023c). This positions VISTA as a uniquely suitable candidate for combination therapy. VISTA can behave as both a receptor and a ligand (Yuan et al., 2021), is expressed widely across both healthy and diseased tissues, and plays an important homeostatic role within the human body (Thakkar et al., 2022). It was also shown in primary melanoma that VISTA expression is highly expressed on CD11b myeloid cells, and this correlated with higher recurrence and mortality in these patients (Vesely et al., 2024).

1.3.3.1 Clinical Trials targeting VISTA

In response to initial articles reporting the likely success of targeting VISTA in solid tumours, there have been multiple clinical trials targeting VISTA in patients with solid tumours. Currently there are three anti-VISTA antibodies and one oral VISTA antagonist being assessed in Phase I clinical trials, as well as an upcoming anti-VISTA mAb clinical trial yet to start recruiting (Martin et al., 2023).

CA-170 is a small molecule drug target developed by Curis that binds and blocks PD-L1, PD-L2 and VISTA in advanced solid tumours of lymphomas (Curis, 2016). It has been demonstrated that CA-170 only binds minimally to VISTA and has a limited capacity to disrupt VISTA receptor-ligand interactions (Gabr and Gambhir, 2020). Curis also sponsors another Phase I anti-VISTA mAb clinical trial using a molecule initially developed by Janssen for advanced cancers (2020b). Janssen cancelled this clinical trial in 2019 citing 'a business decision' but later the cancellation was reported as being due to dose limiting toxicity related to cytokine release syndrome (Ascierto et al., 2022, Janssen Research and Development, 2016). There is also a Phase I/II mAb that is targeting VISTA under the name HMBD-002 with Hummingbird Biosciences, which is being trialled both alone and in combination with anti-PD-1 in patients with advanced solid malignancies (Bioscience, 2021). Additionally, an anti-VISTA mAb is being evaluated alone and with anti-PD1 (Melero et al., 2020, 2020c). The IgG isotype of anti-VISTA mAbs has a profound impact on the functional profile and clinical effect of the antibody. IgG4 may not activate immune cells like IgG1 mAbs do and therefore may be an option to address the safety concerns surrounding early VISTA clinical trials (Mostböck et al., 2022).

1.3.3.2 VISTA in tissue

It is important to understand that VISTA is widely expressed across immune infiltrates and has an important regulatory role in homeostasis. VISTA is reported to be highly expressed on myeloid cells, in particular macrophages (Yoon et al., 2015). VISTA expression is positively correlated with CD33 expression in cutaneous melanoma, and it has been found that VISTA is expressed largely by CD33+ myeloid cells within the tissue (Choi et al., 2020). VISTA expression is also upregulated on macrophages and neutrophils in response to LPS *in vitro* (Ma et al., 2022). It is well established that macrophages play an important role in polarising the T cell response to the tumour. One investigation demonstrated that VISTA agonist activated

human PBMC monocytes (shown by HLA-DR, PD-L1, CD80 and CD40 upregulation) and was able to activate CD4 T cells, demonstrating a functional role for VISTA on monocytes (Rogers et al., 2019).

Unravelling the various roles of VISTA cannot be done without identifying the ligands that it interacts with. Reported ligands include PSGL-1, VSIG-3, and VSIG-8. PSGL-1 is an adhesion molecule that mediates leukocyte trafficking by binding to selectins (Norman et al., 1995, Sperandio et al., 2003). It has been shown to be a negative regulator of T cell function, and this property may be exploited in viral or tumour contexts to promote exhaustion (Tinoco et al., 2016). It has been highlighted as an important ligand in the context of immunotherapy due to its role in recruitment to peripheral tumour sites. VSIG-3 functions as a cell adhesion molecule, and is highly expressed in the brain and testes (Xie et al., 2021). VSIG-3 is also highly expressed in advanced human glioma and is associated with poor prognosis (Ghouzlani et al., 2021). The ligand VSIG-8 has possible clinical significance. One study demonstrated that VSIG-8 interacts with VISTA to inhibit T cell function, and subsequently described a novel anti-VSIG-8 molecule that has the potential to enhance VISTA blockade when used in conjunction with an anti-VISTA mAb (Chen et al., 2022b).

Clinical data surrounding expression patterns of VISTA varies between cancers. VISTA has been reported as being associated with both positive and negative clinical outcomes. It has been reported as a predictor of improved survival in endometrial cancer (Zong et al., 2022), a predictor of positive outcomes in colorectal cancer and hepatocellular carcinoma (HCC) (Wu et al., 2021) and a good prognostic factor in triple negative breast cancer (Zong et al., 2020). Conversely, VISTA expression has also been reported as being associated with a higher mortality rate and lower survival in non-small cell lung cancer (NSCLC) (Long et al., 2022) and correlated with shorter overall survival and tumour necrosis in clear cell renal carcinoma patients with venous tumour thrombi (Zapała et al., 2022). In NSCLC, high expression of VISTA on CD4 T cells was associated with poor prognosis and a dampened cytokine response (Ma et al., 2022). These studies demonstrate that VISTA may be an important checkpoint blockade for multiple cancers, however mechanisms of VISTA in regulating the immune response are varied in different immunological contexts and cannot be understood as a ‘one size fits all’ clinical approach.

1.3.3.3 VISTA and hypoxia

Hypoxia, or reduced cellular oxygen availability, is a known condition of TMEs as tumour cells consume oxygen at an increased rate that deprives resident immune cells of necessary oxygen, thereby altering their function and contributing to exhaustion (Hu et al., 2022). VISTA expression and hypoxia are tightly linked, with HIF1α binding to the VISTA promotor directly, upregulating VISTA expression on myeloid cells in murine models (Deng et al., 2019). We also know that VISTA engages with PSGL-1, one of the known ligands of VISTA, at an acidic pH due to the high histidine content. This means that VISTA is much more biologically active in acidic conditions such as hypoxia, often found in the TME (Johnston et al., 2019). Further, one group developed an anti-VISTA mAb that targeted the histidine-rich epitope of VISTA, and this was able to successfully restore T cell responsiveness (Johnston et al., 2019). It is also clear that hypoxia drives resistance to immunotherapy by its connection to alternate metabolic programs in tumour cells (Kopecka et al., 2021).

1.3.3.4 VISTA in inflammatory disease

VISTA also has significant therapeutic potential for treating inflammatory diseases. VISTA is well known to suppress inflammatory responses and as such is linked to decreased production of IFNγ and TNFα in prostate cancer patients (Gao et al., 2017b). Treating monocytes from the same patients with anti-VISTA mAb resulted in significant reversal of monocyte-mediated suppression of T cell IFNγ production (Gao et al., 2017a). Similarly, silencing VISTA in human endometrial and ovarian cancer cell lines restored T cell proliferation and IFNγ and TNFα secretion (Mulati et al., 2019). In viral infections, VISTA is important in COVID-mediated cytokine storm and severe disease (Shahbaz et al., 2021) and is likely to be a direct ligand in phagocytosis of HIV-infected apoptotic T cells (Shahbaz et al., 2020, Xu et al., 2021). VISTA RNA expression (*vsir*) is also downregulated on monocytes and DCs in PBMCs of multiple sclerosis patients compared to healthy controls, suggesting the potential for VISTA therapy in other neurodegenerative diseases (Derakhshani et al., 2022).

1.4 Adjuvant radiotherapy to treat metastatic melanoma

Radiotherapy was first used to treat melanoma in the 1970s (Creagan et al., 1978). Stereotactic radiotherapy (SRT) was introduced to the clinic in the 1990s, which allowed a high radiotherapy dose per fraction to be delivered to tumour site in a shorter time frame. Since 2015, there has been a move away from radiotherapy towards systemic therapies (ICI,

BRAF/MEK inhibitors) in patients who fit criteria for radiotherapy treatment (Kibel et al., 2023).

1.4.1 Current clinical guidelines for radiotherapy use

Today, radiotherapy is employed in melanoma under specific conditions. Adjuvant radiotherapy after lymph node dissection is often performed if patients do not respond to neoadjuvant therapy or are ineligible for systemic therapies and have extranodal spread, large involved nodes, positive margins or recurrent disease (Hong, 2024). It is also employed to assist symptom management in palliated metastatic melanoma patients with cerebral metastases, bone pain, spinal cord compression and soft tissue metastases causing pain (Hong, 2024). Patients with brain metastases often undergo multiple treatment modalities, including SRT, to treat site of disease (Hong, 2024, Feng et al., 2017). Although systemic therapies are favoured over radiotherapy in metastatic melanoma, a small retrospective study found that lymph-node basin relapse recurrence was similar in patients treated with systemic therapies compared to radiotherapy, however systemic therapies were associated with reduced incidence of overall recurrence or progression (Kibel et al., 2023).

1.4.2 Radiotherapy mechanisms in the TME

Radiotherapy causes tumour cell death by inducing DNA damage that leads to interruption of cell cycle and death of tumour cells via apoptosis and necroptosis pathways. In turn this process releases tumour-associated antigens, inflammatory mediators and cell adhesion molecules which altogether aim to reinvigorate the local immune environment (Chicas-Sett et al., 2020, Rogers et al., 2019). This is sometimes termed an ‘in-situ vaccination’, as the activation of antigen-presenting cells and availability of antigens mimics the response intended by vaccination.

Radiotherapy has been shown to induce both immunosuppressive and immunostimulatory effects in melanoma (Wennerberg et al., 2017). Melanoma is often categorised as a radioresistant tumour, possibly due to the overexpression of repair genes in melanoma cells (Kauffmann et al., 2008). Other groups have shown that radiation increases the immunogenicity of melanoma by releasing neoantigens in radiation-induced cell death, thereby reinvigorating the immune system (Werthmöller et al., 2016)

It is established that radiotherapy promotes presentation of tumour-associated antigens by APCs, and additionally that radiation can increase T cell exposure to tumour antigen *in vivo* by cross presentation (Sharabi et al., 2015). One group suggests that stereotactic ablative radiotherapy may be causing a systemic activation of CD8 T cells (Ratnayake et al., 2022). Radiotherapy-induced T cell activation has also been reported in stage I NSCLC and a Phase I study including multiple solid tumours (Tang et al., 2017, Zhang et al., 2017). One specific subset of B cells, B-1 cells, were shown *in vitro* to interact with murine melanoma cell line B-16 cells and facilitate a pro-tumour environment with the increased production of IL10 and subsequent radio-resistance of the B-1 cells (Laurindo et al., 2013). Radiotherapy has also been shown to modulate expression of immune checkpoints in non-melanoma skin cancer (Wang et al., 2023c).

There is a need for biomarkers to be able to determine the extent to which and at what stage radiotherapy may be clinically effective for the patient. Stage III melanoma patients with BRAF mutation treated with adjuvant radiotherapy had more than 4 times the increased risk of local or region lymph node recurrence (Wolfe et al., 2021). Ratnayake et al found a higher baseline signature of lower naïve CD8 T cells along with TIM3+ expression on multiple T cell populations, in particular CD4 T cells was most predictive of a poor response to radiotherapy (Ratnayake et al., 2022).

1.4.3 Abscopal Effect

There is evidence to suggest that radiotherapy may have impacts beyond the irradiated site, however this is extremely controversial. This is known as the 'abscopal effect', a term coined by R.H. Mole from ab- ("away from") and scopus ("target") (Yilmaz et al., 2019, Mole, 1953). It is difficult to analyse evidence of the abscopal effect as it is a rare occurrence. A retrospective analysis of metastatic melanoma patients treated with palliative radiotherapy between 1998 and 2020 found that 15 out of 118 patients (12.7%) developed an abscopal response (Ollivier et al., 2022). Abscopal response was classified according to iRECIST (Response Evaluation Criteria in Solid Tumours) criteria, which defined it as either complete or partial response in at least one metastasis that was not treated with radiotherapy (Seymour et al., 2017). Another retrospective study of melanoma patients treated with anti-PD-1 and radiotherapy observed an abscopal response in 31.5% (17/61) of patients (Saiag et al., 2022). The mechanisms behind the abscopal effect are unclear, and evidence to date is usually conducted in mouse models. An

in vivo study in mouse mammary carcinoma cells found radiation led to improved control of distant untreated lesions through type I IFN signalling (Yamazaki et al., 2020). Additionally, immune checkpoints were found to be upregulated in a distant, non-irradiated site of a radiation-induced oral mucosal injury rat model, denoting a "bystander effect" of radiotherapy (Wang et al., 2023c).

1.4.4 Radiotherapy & Immunotherapy

There is a general need for a greater understanding of what conditions will elicit a strong response to radiotherapy, and how radiotherapy can best be implemented for melanoma patients. Clinically, radiotherapy is often used in conjunction with immunotherapy, particularly in melanoma, however there is conflicting evidence on the combinatorial effect of radiotherapy and immunotherapy (Hong, 2024). Initial excitement surrounded reports of the abscopal effect of radiotherapy combined with immunotherapy (Postow et al., 2012, Golden et al., 2015, Bernstein et al., 2016) However, a small Phase-II trial of immunotherapy and radiotherapy in melanoma patients showed no significant difference with the addition of radiotherapy but did report a subset of patients that responded to therapy only after radiotherapy addition (Sundahl et al., 2019, Spaas et al., 2023)

As previously outlined, radiotherapy had been shown to upregulate immune checkpoints that are current targets of immunotherapy (Ratnayake et al., 2022, Wang et al., 2023c). It follows that radiotherapy may be an important treatment to be used in conjunction with immunotherapy to increase availability of immune checkpoint proteins and immunogenicity of the tumour at the irradiated site (Wennerberg et al., 2017, Rogers et al., 2019, Liu et al., 2022c). Radiotherapy and PD-1 blockade together have been shown to increase endogenous T cell infiltration of established B16 tumours in a mouse model (Sharabi et al., 2015). One metastatic melanoma patient who had unexpected acceleration of tumour growth on immunotherapy was treated with hypofractionated radiotherapy and had a complete response with no further immunotherapy treatment (Alhumaid et al., 2023). Another metastatic melanoma patient exhibited evidence of radioimmunotherapy 'synergy' and abscopal effect in their complete response (Rahnea-Nita et al., 2024).

One limitation of radiotherapy in conjunction with immunotherapy is that there is likely to be persistence of radiation-induced immunosuppression which is the opposite outcome expected

and desired for immunotherapy treatments (Grassberger et al., 2018). Thus, the order of the treatments can be important, and it has been shown that radiation administered before immunotherapy, particularly ipilimumab, resulted in better overall survival than radiation after ipilimumab (Schoenfeld et al., 2015). Additionally, some argue that immunotherapy combined with stereotactic radiotherapy that excludes lymph nodes is a radio/immunotherapy combination that allows for a better anti-tumour response (Galluzzi et al., 2023). These studies support the idea that there are some patients for whom radiotherapy alone or in combination with immunotherapy results in a more robust anti-tumour response.

Toxicity concerns remain an important part of the conversation, however there is no clear evidence that suggests toxicity rates are higher in radiotherapy- and immunotherapy-treated patients compared to immunotherapy alone (Verma et al., 2018, Guan et al., 2023, Leaman-Alcibar et al., 2022, Li et al., 2022). There is evidently an important place for radiotherapy in tumour treatment, however there need to be better predictors of patient response and understanding of the interplay with other therapies, in particular specific immunotherapies.

1.4.5 Emerging radiotherapy technologies

There has been significant development of cutting-edge therapies that employ radiation to treat tumours with better precision and cause fewer side effects. Neutron Capture Enhanced Particle Therapy (NCEPT) delivers extremely targeted radiotherapy doses to tumours via neutron capture agents or ‘NCA’s (Howell et al., 2024). Recently, NCEPT was successfully performed using a simulation model in China (Kielly et al., 2024). Proton radiation therapy has gained significant funding into its development, however there is not yet clear evidence of its advantage over traditional photon radiation therapy (Chen et al., 2023b).

1.5 Experimental approaches to single cell omics

We are now in the era of spatial proteomics and transcriptomics, often simplified as ‘omics’. *Nature* announcing ‘single cell multimodal omics’ and ‘spatially resolved transcriptomics’ as methods of the year for 2019 and 2020 respectively signified this new focus on spatial biology (2020a, Marx, 2021). Much of the widespread use of spatial omics can be attributed to commercialisation of these technologies by companies such as 10X Genomics and Nanostring (Chen et al., 2023a). Commercialisation standardises reagents and theoretically increases access to these technologies, but at the cost of significantly impeding non-commercial

contribution and development in this rapidly evolving field (Alexandrov et al., 2023). For the field of spatial omics to remain accessible, useful and reproducible to the scientific field, this area of science should prioritise transparency and access to protocols, software and technologies.

1.5.1 From immunofluorescence to whole-genome mapping

Immunohistochemistry (IHC), immunofluorescence (IF) and *in situ* hybridisation (ISH) are techniques used in research and the clinic for decades and remain widely used today (Falcon et al., 2013, Li and Yang, 2020, Viratham Pulsawatdi et al., 2020). These techniques are particularly employed across cancer research, so much so that the Society for the Immunotherapy of Cancer released a statement outlining best practices for IHC and IF staining and validation (Taube et al., 2020).

However, limitations of traditional IHC led to the development of multiplex IHC (mIHC), a technique that employs the cyclic addition and removal of primary antibodies and fluorescent tags to allow for multiple markers to be detected in one sample (Granier et al., 2017). mIHC became accessible to most researchers in the last decade, costing approximately $40 USD per experiment (Tan et al., 2020, Stack et al., 2014). Although these technologies can employ multiple markers successfully, fluorescent overlap and other chemical principles limits the expansion of these techniques to include more than 7-8 markers at a time (Lazarus et al., 2019). Tissue targets not available in FFPE, such as protein molecules, were able to be targeted by *in situ* hybridisation in recent years through commercially available technologies such as RNAScope (Wang et al., 2012).

Despite recent advancements in single cell sequencing and multiplex flow cytometry that increased greatly the quantifiable targets within a sample, these techniques could not fulfill the need for high parameter approaches that preserved spatial information (Moldoveanu et al., 2022). To meet these needs, experimental approaches to assess high numbers of genes, transcripts and proteins within tissue developed, often termed the field of spatial omics.

1.5.2 Current approaches to spatial omics

Spatial omics can reveal detailed cell states and phenotypes, define how cells behave differently between regions or ‘neighbourhoods’, and provide a comprehensive view of the

entire environment of tissue assessed (Williams et al., 2022). There are many different technologies available to assess genes, transcripts and proteins within tissue, however this thesis focusses on those pertaining to this study.

Antibody-dependent methods to assess protein localisation in FFPE tissues includes cyclic immunofluorescence (e.g. PhenoCycler-Fusion/CODEX), multiplexed ion bean imaging (MIBI), and Imaging Mass Cytometry (IMC) (Bressan et al., 2023, Williams et al., 2022). IMC employs cytometry by time of flight (CyTOF) technology in antibody staining to resolutions of 1µm and can profile up to 40 markers (Ferguson et al., 2022, Veenstra et al., 2021, Bressan et al., 2023). These technologies require significant investment in instruments and reagents, and resolution for IMC is relatively coarse (Bressan et al., 2023).

Current spatial transcriptomic approaches can be categorised into either imaging methods or sequencing methods. Imaging methods include ISH approaches as well as *in situ* sequencing (ISS). These methods employ probes that are labelled complementary to the mRNA target of interest. ISH was first employed in 1989 in *drosophila* and became publicly available in the early 2000s (Tautz and Pfeifle, 1989, Femino et al., 1998, Levsky et al., 2002). ISH works by hybridising gene-specific probes to mRNA within FFPE tissue, while ISS employs rolling circle amplification of target transcripts before addition of one- or two-base specific probes linked to an individual fluorophore (Williams et al., 2022). Because of this, ISH methods are more efficient at mRNA detection, but ISS approaches can assess larger sample areas within a comparable timeframe (Williams et al., 2022, Moses and Pachter, 2022). Sequencing methods capture spatial information using arrays or microdissection before performing next-generation sequencing (NGS) on samples (Williams et al., 2022). All spatial transcriptomic technologies require good tissue quality with intact mRNA and prevention of RNA contamination. Further to this, some cell types such as lymphocytes have much lower RNA content compared to other cells which may lead to less accurate profiling of these populations; however, methods have increasingly been able to accurately profile cells with low RNA quantity and quality (Andreeff et al., 1978, Wang et al., 2019).

In the relatively small amount of time that these new technologies have been available, some groups have embarked on the difficult task of comparing these methods. One study used breast cancer FFPE tissue to compare Chromium X, Visium Cyt-assist and Xenium systems, focussing on how the newer Xenium system compared to the older systems. They found that

Xenium *in situ* analysis reliably detected transcripts and had a greater or comparable specificity and sensitivity to the Chromium and Visium systems (Janesick et al., 2023). They also found a high degree of concordance between probe detection of HER2 (tumour marker) and CD20 (B cell marker) transcripts and protein expression in the Xenium dataset (Janesick et al., 2023).

Employing single-cell approaches is extremely expensive which limits the accessibility of these technologies for most laboratories (Marx, 2022). Many researchers have combined different single-cell approaches alongside more accessible methods such as basic IHC, however this approach is made difficult with the 'closed box systems' commercial developers employ (Millar, 2020, Alexandrov et al., 2023). Additionally, many of these approaches rely on pre-designed panels developed by commercial teams, and this may impact the scope of discovery research using these methods. It is expected that these technologies will progress toward multi-omics within one experimental approach, 3D profiling of tissues and live imaging (Bressan et al., 2023).

1.5.3 Analysing single cell omics

It is an ongoing challenge to be able to accurately perform dimensionality reduction of single cell datasets and to integrate data between platforms (Marx, 2021). Although some attempts have been made to collaborate and share 'best practices' of analyses of this kind of data, there remains a need to develop standardised approaches to genomic and transcriptomic analysis (Liu et al., 2019b, Heumos et al., 2023, Cuevas-Diaz Duran et al., 2024).

Before downstream analysis, single cell omics data needs to undergo pre-processing, cell segmentation and normalisation. Following this, data can undergo dimensionality reduction and unbiased clustering to produce cell 'clusters' or phenotypes, mapping and visualisation as well as integration with other data (Williams et al., 2022, Bressan et al., 2023). The influx of these technologies has required researchers, many without extensive computational experience, to perform data analyses in R and Python. Packages such as Seurat have been developed with this in mind, aiming to assist researchers not based in mathematical modelling and include read-in tools for specific transcriptomic platforms like Xenium (Marx, 2022, Hao et al., 2024). There has also been significant development in artificial intelligence-based algorithms within this field, employing machine learning as well as deep learning to address some of the issues

in single cell analysis (Heumos et al., 2023, Erfanian et al., 2023, Ma and Xu, 2022, Alexandrov et al., 2023).

Having the ability to perform spatial transcriptomics does not always mean they are the most appropriate experimental approach for any given study (Bressan et al., 2023). Some researchers prefer flow cytometry and *in situ* immunofluorescence over spatial transcriptomics to track antibodies within the nucleus as they are less expensive and offer "visual proof" (Marx, 2022). Many researchers in the field also urge the focus on accessibility of transcriptomic data, emphasising ethical sharing of transcriptomic primary and metadata in order to adhere to scientific values of transparency and reproducibility (Jackson and Pachter, 2023). This would also increase access to transcriptomic datasets, allowing scientists to use high-parameter data without having the upfront cost and expertise otherwise required. There needs to be significant improvement in scalability, reproducibility and cost in order for these technologies to be adopted in the clinic, despite recent studies in cancer tissues that show promising results (Comiter et al., 2023, Irmisch et al., 2021, Mulholland and Leedham, 2024).

1.6 The present study

Over the last 10 years, there have been significant successes in novel treatment strategies for melanoma. However, inducing an effective, robust response in all melanoma patients remains challenging. This is largely due to our lack of understanding of the mechanisms of response and resistance of metastatic melanoma. The studies presented in this thesis addressed this by conducting a detailed investigation of the TME of metastatic melanoma and identifying features that are associated with patient response to therapy, lack of relapse and improved survival.

In the first results chapter of this thesis, we aimed to:

1. **a)** quantify the immune milieu of metastatic melanoma using cytometry techniques on tumour dissociates from metastatic melanoma patients, focussing particularly on the diverse phenotypes of the myeloid compartment; and

b) compare these cell populations in patients treated with anti-PD-1 monotherapy to identify signatures associated with immunotherapy response.

We wanted to complement this initial study with a detailed examination of the TME using methods that preserved spatial context. To do this we used a high-parameter imaging approach to produce detailed data on the TME of metastatic melanoma. Our aims in this work were to:

2. **a)** profile both quantities of and relationships between immune and tumour cell types and subtypes in metastatic melanoma and compare these between patient outcomes; and

b) establish an analysis pipeline to produce accurate and practical results from spatially resolved imaging mass cytometry data.

After establishing a robust protocol for proteomic staining in the second study presented here, we wanted to mirror our approach and apply it to a novel *in situ* hybridisation technique, allowing transcriptomic data to be produced on the same cohort. As such, the aims of the third study of this thesis were to:

3. **a)** perform transcriptomic profiling on metastatic melanoma tumour tissue using novel techniques to compare populations identified between patient outcomes; and

b) establish a viable multi-omics protocol to perform IMC, PCF and H&E after *in situ* hybridisation.

2 Materials and Methods

2.1 Fresh Tumour Dissociation

Tumour samples were excised during surgery from surgeons at the Melanoma Institute of Australia. Tumour dissociation for samples used in this project was performed by Melanoma Institute Biobank using the Miltenyi Biotec Tumour Dissociation Kit (cat #130-095-929) that employs enzymatic and mechanical digestion with the Miltenyi Biotec gentleMACS© tissue dissociator. Single cell tumour suspensions were then resuspended in freeze media (Table 2.1) at ~$10x10^6$ cells/mL and aliquoted into 1.5mL cryovials (Corning) and placed in Nalgene Cryo-1°C/min Freezing Container in a -80°C freezer, followed by long term storage in liquid nitrogen tanks until experimental use.

2.2 Flow Cytometry

2.2.1 Sample preparation and staining

Cryopreserved single cell tumour dissociates were thawed in a 37°C water bath. Cells were treated in ACK lysis buffer (Gibco) for 1 minute at RT to lyse red blood cells. Cells were then stained with fluorochrome-conjugated antibodies for 30 minutes at 4°C (Table 2.2). If intracellular staining was performed, cells were resuspended in Fix/Perm buffer (BD Pharmingen) and incubated for 40 minutes at 4°C in the absence of light to permeabilise the cells. Cells were then washed in Perm/Wash buffer (BD Pharmingen) and intracellular antibodies were applied to cells and samples incubated for 40 minutes at 4°C in the absence of light. Following staining, cells were fixed for 30 minutes on ice in 4% PFA in FACS buffer (Table 2.2). Cells were centrifuged at 1455 rcf for 4 minutes at 4°C, the supernatant was discarded, and the cells resuspended in FACS buffer. All samples were stored at 4°C while awaiting analysis.

2.2.2 Sample Acquisition

Stained samples and controls were analysed on a BD five laser LSR Fortessa (Sydney Cytometry, the University of Sydney). Unstained cells and single colour controls were run with each experiment, as well as fluorescence Minus One (FMO) controls for all intracellular markers (Table 2.2) to determine changes in background fluorescence when permeabilising the cells. Live/dead stain, Zombie Aqua™ Fixable Viability Kit (Table 2.1) was applied to separate

unstained cells to use as a cell viability control as intracellular staining protocol impacts the reliability of this staining.

2.2.3 Flow Cytometry Data Analysis

Data collected was analysed using FlowJo v10. Data analysis was performed in GraphPad Prism was used to analyse quantitative data from FlowJo analysis and generate graphical data. Box and whisker plots were used to visualise data. Box lines correspond to 25th percentile, median, and 75th percentile, and whiskers extend to minimum and maximum points. All data points are shown.

Table 2.1 Flow Cytometry Reagents

Reagent	Source	Details
Fluorescence Activated Cell Sorting (FACS) buffer	*Lab Prepared*	Phosphate buffered saline (PBS) (Lonza Group Ltd) solution containing 1% heat-inactivated Fetal Calf Serum (FCS) (AusGeneX) and 0.05% Ethylenediamine tetraacetate (EDTA) (Thermo Fisher Scientific)
RP10 Media	*Lab Prepared*	Roswell Park Memorial Institute (RPMI) media 1640 (contains L-glutamine and HEPES) supplemented with 10% FCS (AusGeneX) and 0.02% Penicillin-Streptomycin (Thermo Fisher)
Fix/Perm Buffer	BD Pharmingen	5% Formaldehyde, 1.76% Methanol 4X Fix/Perm Buffer diluted 1:4 (v/v) with BD Pharmingen Transcription Factor Diluent Buffer.
Perm/Wash Buffer	BD Pharmingen	Perm/Wash Buffer diluted 1:5 (v/v) with BD Pharmingen Transcription Factor Diluent Buffer.
Zombie Aqua Fixable Viability Kit	BioLegend	Diluted 1:100 in PBS
Freeze Media	*Lab Prepared*	10% DMSO in heat-inactivated FCS

Table 2.2 Flow Cytometry Antibodies

Marker	**Clone**	**Manufacturer**
CD3	OKT3	Biolegend
CD4	RPA-T4	BD Biosciences
CD8a	HIT8a	Biolegend
CD19	HIB19	Biolegend
CD69	FN50	BD Biosciences

Marker	Clone	Manufacturer
CD103	Ber-ACT8	BD Biosciences
CD36	5-271	Biolegend
CD98 (LAT-1)	MEM-108	Biolegend
PKM2	D78A4	CST
HIF1a	546-16	Biolegend
CD45	2D1	Biolegend
CD1c	L161	Biolegend
CD11c	B-ly6	BD Biosciences
CD13	L138	BD Biosciences
CD14	M5E2	BD Biosciences
CD141	M80	Biolegend
CD206	15-2	Biolegend
HLA-DR	G46-6	BD Biosciences
Clec9A	3A4	BD Biosciences
VISTA	730804	R&D systems
PD-1	EH12.1	BD Biosciences
PD-L1	29E.2A3	Biolegend

2.3 Multiplex Immunohistochemistry (mIHC) staining

2.3.1 Tissue preparation

Formalin-Fixed Paraffin Embedded (FFPE) tissue sections were baked at 60°C for 60 minutes. Slides were placed in xylene for 10 minutes (Table 2.3) and then rehydrated using an ethanol gradient (100%, 95%, 70%, 50%) for 5 minutes each. Antigen retrieval (AR) to expose epitopes masked during fixation was performed in either TRIS-EDTA buffer (pH9) or sodium citrate buffer (pH6) (Table 2.3) depending on the antibody intended for staining.

2.3.2 OPAL™ IHC Staining

All staining was performed on 4μm thick FFPE tissues. Samples were covered with 3% Hydrogen Peroxide (Table 2.3) to block endogenous peroxidases. Tissues were then blocked with OPAL™ blocking buffer (Akoya) and incubated in a humidified chamber at RT for 10 minutes. The primary antibodies listed in Table 2.3 were used with OPAL™ Horse Radish Peroxidase (Akoya) as the secondary antibody. OPAL™ Tyramide Signal Amplification (TSA) buffer plus the appropriate fluorophore (Table 2.3) was then applied to each slide for 10 minutes at RT in a humidified chamber to amplify the signal. Slides were then counterstained

with DAPI (Table 2.3) and mounted with Prolong Diamond (Life Technologies) and stored at 4°C in the dark until imaged.

2.3.3 Imaging

Single colour positive controls were made for all stains plus an unstained control as a tissue auto-fluorescence control. Images were taken on Mantra fluorescent microscope (Akoya Biosciences/PerkinElmer) at the Australian Centre Microscopy & Microanalysis (ACMM) Facility at the University of Sydney using Mantra imaging software.

Table 2.3 Tissue Staining Reagents

Reagent	Source	Details
Phosphate-Buffered Saline (PBS)	Gibco	Potassium phosphate monobasic (1.06mM), Sodium Chloride (155.17mM) and Sodium phosphate dibasic (2.97mM) at pH 7.4. Stored at room temperature.
Dulbecco's Phosphae-Buffered Saline (DPBS)	Gibco	Potassium chloride (2.67mM), Potassium phosphate monobasic (1.47mM), sodium chloride (137.93mM) and sodium phosphate dibasic (8.06mM). Stored at room temperature.
Antigen Retrival (AR) 6 Buffer	*Lab Prepared*	10mM Sodium Citrate (Sigma Aldrich), 0.05% $Tween_{20}$ (Sigma Aldrich), adjusted to pH6 in triple distilled water (TDW).
Antigen Retrieval (AR) 9 Buffer	*Lab Prepared*	10mM TRIS 1mM EDTA (Thermo Fisher Scientific), $Tween_{20}$, adjusted to pH9.
TRIS-buffered Saline with $Tween_{20}$ (TBS-T)	*Lab Prepared*	0.1M TRIS-HCl (Sigma Aldrich), 0.15M NaCl (Sigma Aldrich), 0.05% $Tween_{20}$ made up in TDW and adjusted to pH 7.5.
Casein Block (Blocking Buffer)	Perkin Elmer	Included in OPAL IHC Kit (Table 2.4). Used at concentration provided.
Xylenes	Sigma Aldrich	Histological grade mixture of xylenes.
3% hydrogen peroxide (H_2O_2)	Sigma Aldrich	30% H_2O_2 diluted in PBS.
DAPI (4′,6-diamidino-2-phenylindole)	Cell Signalling	Used at 1μg/mL diluted in TBS-T

Table 2.4 OPAL IHC Reagents

Reagent	Source	Details
OPAL™ 7-Colour Manual IHC Kit	PerkinElmer	Containing: - Opal TSA Fluorophores - DMSO - 1X Plus Amplification Diluent - Spectral DAPI solution - OPAL polymer horse-radish peroxidase (HRP) - Blocking Buffer/Antibody Diluent

Table 2.5 IHC Antibodies

Marker	Source	Clone	Manufacturer
CD3	Rabbit	MRQ-39	Cell Marque
CD4	Rabbit	104R-15	Cell Marque
CD8	Rabbit	Ab4055	Abcam
CD103	Rabbit	EPR4166(2)	Abcam
SOX10	Mouse	BC34	Biocare Medical
CD68	Mouse	Kp-1	Cell Marque
CD11c	Rabbit	Ab52632	Abcam
CD14	Rabbit	Polyclonal	Sigma Aldrich
VISTA	Mouse	730804	R&D Systems
FXIIIA	Sheep	SAF13A-AP	Affinity Biologicals
Anti-mouse conjugated to Alexa Fluor® 647	Rabbit	Polyclonal	Jackson Immuno Research

2.4 Imaging Mass Cytometry

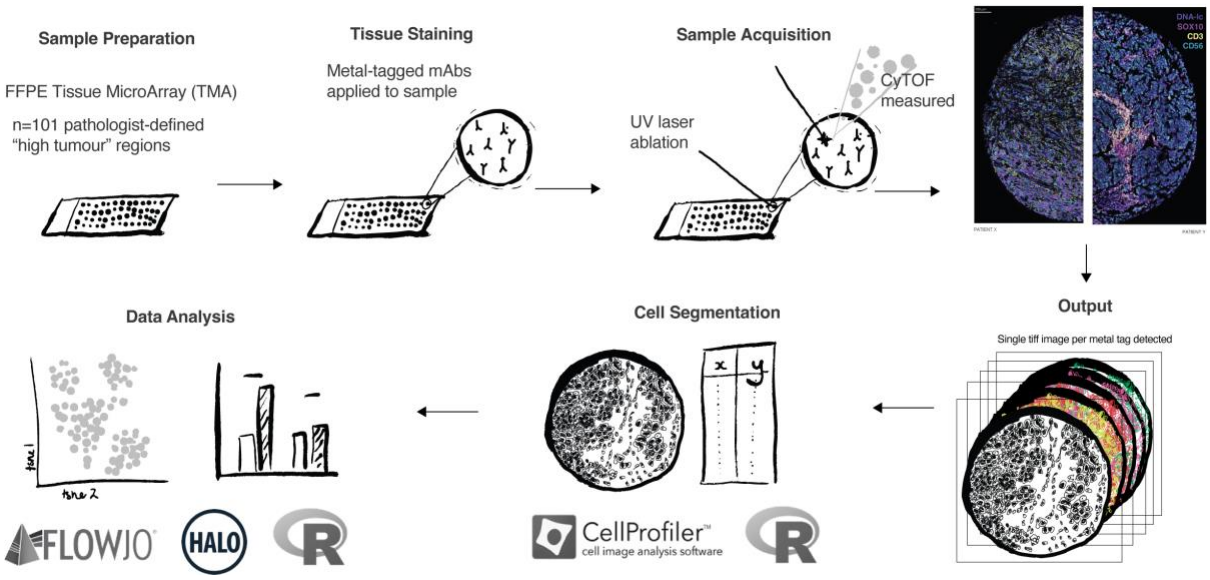

Figure 2.1 Imaging Mass Cytometry Experimental Workflow. Formalin-fixed paraffin embedded 'high-tumour' tissue microarray with areas from 100 nodal melanoma patients. 42 metal-tagged antibodies were applied to sample before sample acquisition using Hyperion Imaging Mass Cytometer to measure cytometry by time-of-flight (CyTOF). Representative image of two patient cores with DNA (blue) SOX10 (magenta) CD3 (yellow) and CD56 (cyan). Each sample output consists of a multi-image tiff (OME-TIFF). Cell segmentation was performed by two methods using cell profiler and spicy R package from A/Prof Ellis Patrick and Farhan Ameen (University of Sydney). Individual cell information was exported and input into further analysis software for clustering and statistical analysis. Images original.

2.4.1 Tissue Staining

Slides were baked at 60°C for 60 minutes before de-waxing in xylene for 10 minutes and rehydrating through a graded series of ethanol solutions (100%, 95%, 70%, 50%) for 5 minutes each, as detailed in Table 2.3. Slides were transferred to TBS-T Table 2.3, dried, and tissue was encircled using a wax pen (Dako, Jena, Germany). Antigen retrieval was then performed by placing slides in a plastic or glass jar filled with AR9 buffer (Table 2.3), the jar was then placed in a microwave at full power (100% on a 700W output microwave) until liquid boiled, and subsequently microwaved for 15 minutes at 20% power. Slides were cooled at room temperature in jar for 30-60 minutes, then washed for 10 minutes in TBS-T before slide was dried and wax pen encircled the tissue. Tissue was then washed again for 10 minutes in DPBS (Table 2.3) before blocking with Casein Block (Akoya Biosciences, Table 2.3) for 45 minutes at 37°C in a humidifying chamber. Primary staining was first performed for SOX-10 protein staining using mouse anti-human SOX10 (Table 2.5) diluted 1:50 in antibody diluent (Akoya Biosciences, Table 2.3) for 45 minutes at RT. Slides were then washed twice in TBS-T for 2 minutes before secondary antibody anti-mouse AF647 diluted 1:50 in DPBS (Table 2.3) for 30

minutes at RT. Slides were again washed twice in TBS-T for 2 minutes at RT. Slides were then incubated with metal tagged antibodies per table 2.7 at 4°C overnight in a humidified chamber. The following morning, slides were washed twice in 0.1% Triton-X in DPBS (Table 2.3) for 8 minutes, followed by two 8-minute washes in DPBS. Tissue was then stained with DNA intercalator (Table 2.6) for 30 minutes at RT, washed twice with ddH2O for 5 minutes each, and let air dry for 30 minutes at RT.

2.4.2 Tissue Ablation

Samples were acquired using Hyperion Imaging Mass cytometer (Standard Biotools) by pulsed laser ablation at 200Hz which atomises metal ions bound to tissue to then be analysed by time-of-flight mass cytometry.

2.4.3 Preliminary Analysis

Each tissue microarray (TMA) sample core was exported as mass cytometry files (TXT, multipage TIFF, OME-TIFF, MCD) which was loaded into MCD viewer (v1.0.560.6, Standard Biotools) software for exportation as single TIFF images, for visualisation, quality control and to produce representative images.

2.4.4 Cell segmentation (Cell Profiler) and targeted cell phenotyping

Cell segmentation was subsequently performed using Cell Profiler (open source) using single-colour TIFF images. Each core/patient sample is then exported as a comma separated value (csv) file that contains each ‘cell’ as a data point with *x,y* coordinates and marker expression. We then imported this csv into FlowJo software and manually gated cell populations according to phenotypic expression. Box and whisker plots were used to visualise data. Box lines correspond to 25th percentile, median, and 75th percentile, and whiskers extend to minimum and maximum points. All data points are shown.

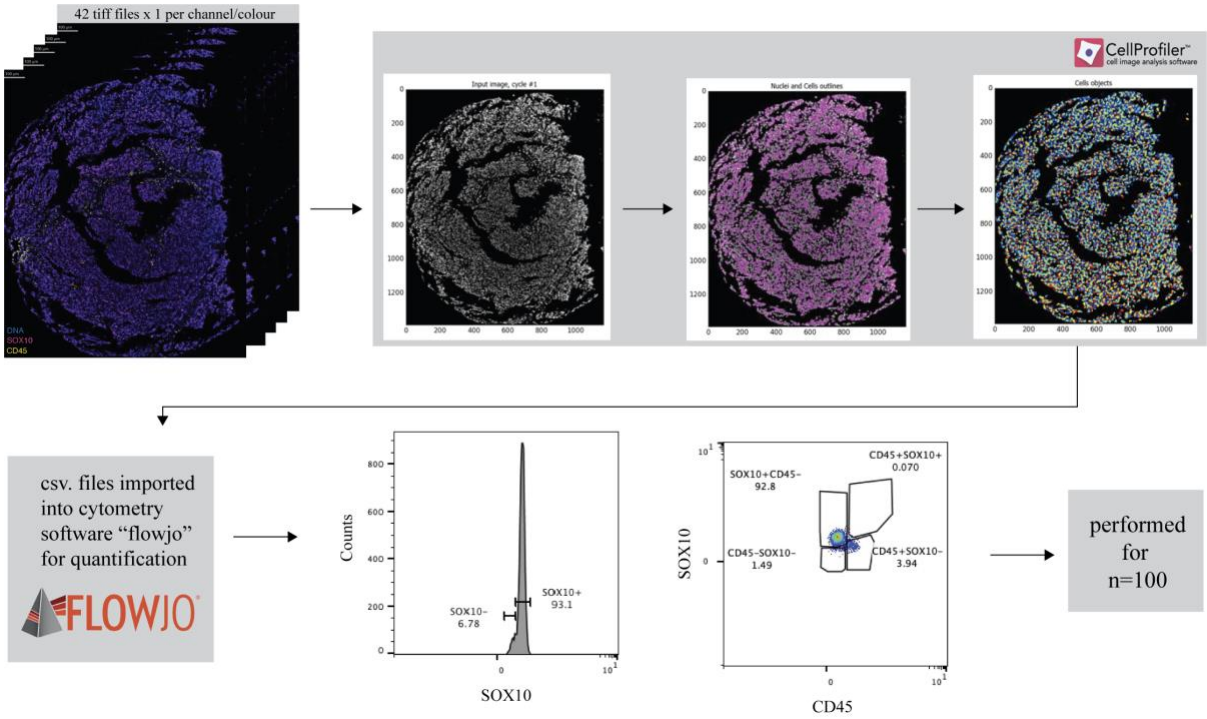

Figure 2.2 Imaging Mass Cytometry Analysis Workflow. Visualisation of analysis pipeline described in section 2.4.4. Each sample ablated by IMC consisted of 42 individual images that were loaded into cell segmentation software and cell segmentation was performed for each individual sample. Data was exported and loaded into cytometry analysis software for manual phenotyping.

2.4.5 Cell segmentation, supervised clustering and spatial analysis

Spatial Analysis was performed in collaboration with Dr Ellis Patrick and Farhan Ameen (School of Mathematics and Statistics, University of Sydney). Cell segmentation was performed using *simpleseg* package (*Bioconductor*) (Canete, 2024). Data was transformed using arcsine function, followed by post-segmentation data trim (removing top and bottom 1% of data) and normalisation of data to calculate mean values per sample.

Table 2.6 IMC Reagents

Reagent	Details	Company
Triton-X	Diluted in PBS	Cell Signalling Technologies
DNA-Intercalator (DNA-Ir)	Diluted 1:100 in PBS	Standard Biotools

Table 2.7 IMC Antibodies

Metal	Antibody	Clone	Concentration (µg/mL)	Company
89Y	alpha-SMA	1A4	1	

Metal	Antibody	Clone	Concentration (μg/mL)	Company
113In	Vimentin	D21H3	2	
115In	CD11c	D3V1E	3.991	
139La	pan-cytokeratin	SPM115	1	
141Pr	CD20	H1	4	
142Nd	HH3	polyclonal	4.015	
143Nd	CD45RA	HI100	4.004	
144Nd	Myeloperoxidase	E1E71	7.992	
145Nd	CD103	EPR4166	3.009	
146Nd	CD8a	D8A8Y	3.51824	
147Sm	Podoplanin	polyclonal	1.999	
148Nd	CD16	EPR1678	8	
149Sm	CADM1	polyclonal	5	
150Nd	IDO	D5J4E	8	
151Eu	CD274/PD-L1	E1L3N	2	
152Sm	CD13	498001	4.006	
153Eu	CD68	KP1	2	
154Sm	VISTA	D1L2G	7.98	
155Gd	CD31	MEC13.1	4	
156Gd	CD183/CXCR3	49801	1	
158Gd	T-bet	D6N8B	6	
159Tb	CD197	polyclonal	8.01	
160Gd	CD14	EPR3653	2	
161Dy	FXIIIa	polyclonal	7.68	
162Dy	FoxP3	polyclonal	4	
163Dy	CD279/PD1	EPR4877	2.001	
164Dy	CD45RO	D6I3M	3.992	
165Ho	OX40	E9U70	3.99	
166Er	CD45	D9M8I	1.994	
167Er	CD66a	YTH71.3	1	
168Er	Ki67	B56	1.997	
169Tm	Lag-3	02G40	1.0015	
170Er	CD3	polyclonal	4.61	Standard Biotools
171Yb	Granzyme B	EPR8260	8.026	

Metal	Antibody	Clone	Concentration (μg/mL)	Company
172Yb	Cy5	CY5-15	4	
173Yb	CD4	EPR6855	4	
174Yb	HLA-DR	EPR3692	0.9995	
175Lu	ICOS	D1K2T	10.0175	
176Yb	CD56	EPR2566	4	
209Bi	DC SIGN	polyclonal	1	
191Ir	DNA Intercalator		1.25ng/mL	
193Ir	DNA Intercalator		1.25ng/mL	

2.5 RNAscope *in situ* hybridisation

2.5.1 Tissue Preparation

Formalin-Fixed Paraffin Embedded (FFPE) tissue sections were baked at 60°C for 60 minutes. Slides were placed in xylene for 10 minutes (Table 2.3.1) and subsequently rehydrated using an ethanol gradient (100%, 95%, 70%, 50%) for 5 minutes each. Antigen retrieval (AR) was performed using RNAScope Target Retrieval Buffer (Table 2.3.1) using 100% power on 700W microwave until boiling point, followed by 15 minutes at 20% power. Samples were set at RT for ~1 hour to equilibrate. Samples were placed in ddH_2O for 2 minutes in a coplin jar before being removed and wax pen (Dako) traced around tissue area on slide, and ddH_2O pipetted gently onto tissue. Three washes were performed with ddH_2O, before endogenous peroxides quenched with 3% hydrogen peroxide (Table 2.3) for 30 minutes. Slides were washed three times with ddH_2O before Protease Plus (Table 2.3) was applied to permeabilise tissue and placed in humidifying chamber for 30 minutes at RT.

2.5.2 *In situ* hybridisation

RNAscope probe was warmed up to 40°C before being applied to sample tissue. Sample slides were then placed within a humidifying chamber with extra water and placed within a 40°C oven to hybridise for 120 minutes, checking at 30-minute intervals to ensure tissue had not dried out. Slides were removed from oven and tissue was washed three times in RNAscope wash buffer (Table 2.8) for 2 minutes each. Amplification #1 reagent (Table 2.8) was pipetted onto sample (volume variable, required only to cover tissue) and incubated in humidifying chamber at 40°C for 30 minutes. Slides were then washed three times in RNAscope wash buffer

for 2 minutes each, before Amplification #2 reagent was placed onto tissue and sample incubated for 15 minutes at 40°C. Slides were again washed three times in RNAscope wash buffer for 2 minutes each, and Amplification #3 reagent was placed onto tissue and sample incubated for 30 minutes at 40°C. Slides were washed three times using RNAscope wash buffer for 2 minutes each, and Amplification #4 Reagent was applied for 15 minutes and slides incubated again in humidifying chamber for 30 minutes at 40°C. Slides were washed 3 x 2 minutes with RNAscope wash buffer and selected OPAL© TSA Fluorophore (1:1000) (Table 2.4) was applied to sample and incubated for 10 minutes at RT. Slides were washed 3 x 2 minutes with RNAscope wash buffer and counterstained with DAPI (Cell Signalling) and mounted with Prolong Diamond (Life Technologies) and stored at 4°C in the dark until imaged.

2.5.3 Controls

Positive and negative control probes, unstained sample controls and single colour TSA fluorophore controls were stained alongside test slides and imaged with samples (Table 2.8). Universal negative control probe from ACD Bio is an RNAscope probe targeting the bacterial DapB gene from the *Bacillus subtilis* strain SMY, a soil bacterium.

2.5.4 Imaging

RNAscope stained samples were imaged on Mantra fluorescent microscope (Akoya Biosciences/PerkinElmer) at the Australian Centre Microscopy & Microanalysis (ACMM) Facility at the University of Sydney using Mantra imaging software.

2.5.5 Data analysis

RNAscope quantification was performed using RNAscope Image Analysis Module in HALO (Indica Systems). This module detects both number of dots and intensity of dots in conjunction with protein markers, allowing individual cell detection of transcripts. This information was exported into GraphPad Prism for statistical analysis and to generate graphical data. Box and whisker plots were used to visualise data. Box lines correspond to 25th percentile, median, and 75th percentile, and whiskers extend to minimum and maximum points. All data points are shown.

Table 2.8 RNAscope® Reagents

Reagent	Company	Details
RNAscope® 2.5 HD Reagent Kit - Brown Cat # 322300	ACD Bio	Containing: 3% Hydrogen Peroxide, Protease Plus, RNAscope® Antigen Retrieval Buffer, RNAscope® Wash Buffer: 50X Buffer Stored at 4°C and heated to 40 ˚C to dissolve before aliquoting and diluting 1:50 in dH_2O to make working concentration
IFN-γ mRNA Probe	ACD Bio	Cat #310501
IL-10 mRNA Probe	ACD Bio	Cat #602051
Negative Control Probe	ACD Bio	Cat #320871

2.6 Xenium *in situ* Hybridisation

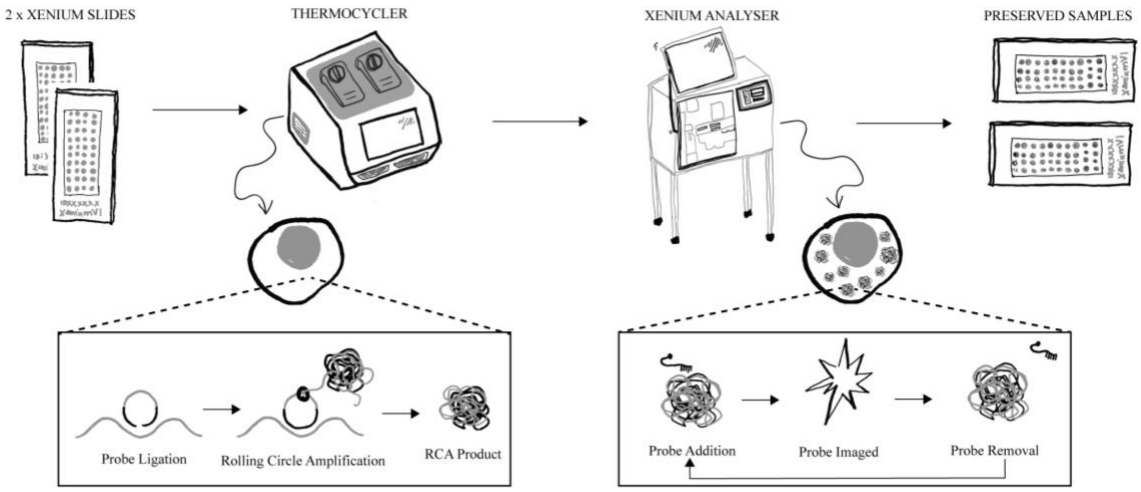

Figure 2.3 Xenium *in situ* Experimental Workflow. FFPE tissue samples mounted on custom 10X Xenium slides. Tissue de-crosslinking, probe hybridisation, ligation, and amplification was performed within C1000 thermocycler. Imaging was performed by cyclic application and removal of fluorescent probes to image all markers. Samples were preserved and further experiments able to be performed.

2.6.1 Tissue Preparation

Tissue cutting and mounting was performed by Dr Rachael Ireland at the Charles Perkins Centre Histology Facility (University of Sydney). FFPE samples mounted on Xenium slides were prepared according to 10X protocol Xenium *in situ* for FFPE – Tissue Preparation Guide (CG000578, revision C). For samples to be able to be acquired successfully on Xenium Instrument Analyzer (10X Genomics), tissue was cut from a pre-scored FFPE block and section split in water bath and mounted onto two separate Xenium (10X Genomics) slides to

accommodate the larger size of the full TMA sample area compared to the restricted sample area of the Xenium slide (12mm x 24mm). Before cutting, TMA block was soaked in cold water to rehydrate tissue and was scored using a surgical blade into two rectangular areas that would separate once cut with the microtome. This was to allow section to fit on Xenium slide without blocking fiducials needed for image registration. This was tested on a blank block prior to experimental samples. Slides were subsequently let dry at room temperature face-up to ensure no water was trapped under tissue, before being placed in an open thermocycler at 42°C for 3 hours. Slides was then placed in a plastic falcon tube containing desiccator overnight, to prepare for hybridisation on day 2.

2.6.2 Tissue deparaffinization

Xenium Human Multi-Tissue and Cancer kit, containing 377 gene targets was purchased from 10X Genomics in February 2024. Full gene list summarised in Table 2.10. Custom Xenium slides with mounted samples were placed face-up on Xenium Cassette Adaptor (10X Genomics) to bake in C1000 thermocycler at 60°C for 120 minutes with lid open. Slides were then left to cool on bench for ~10 minutes before being transferred to a chemical fume hood for tissue deparaffinisation. Slides were gentle immersed in xylene jar #1 for 10 minutes, before being placed in xylene jar #2 for a further 10 minutes. Slides were then placed in five consecutive jars of ethanol (Table 2.3) for 3 minutes each at the following concentrations: 100%, 100%, 96%, 96%, 70%, before a final wash in nuclease-free water (Table 2.9) for 20 seconds before being removed from fume hood.

2.6.3 Tissue decrosslinking

Xenium sample slides were placed within custom xenium cassettes to ensure a physical seal around tissue area, or ‘well’, allowing liquid to be placed on and washed off tissue. Slides were first washed with 500µL of PBS (Table 2.3), followed by 500µL of decrosslinking buffer (Table 2.9) on both wells, and a new cassette lid was attached to the Xenium cassette to ensure no cross-contamination. Samples were then placed back into the thermal cycler and decrosslinking program was commenced (22°C ‘hold’, 80°C for 30 minutes, 22°C for 10 minutes, 22°C ‘hold’).

2.6.4 Hybridisation

After decrosslinking, slides were removed from thermocycler, washed with 500µL of PBS-T (Table 2.3) three times for 1 minute. Probe Hybridisation Mix (containing 377 probes within hybridisation buffer and TE buffer, Table 2.9) was added to samples before they were placed within thermocycler with the lid on, and the following settings were commenced: a 50°C 'hold', 16-24hour/overnight at 50°C, followed by a 50°C 'hold'.

2.6.5 Post-hybridisation wash and ligation

Slides were removed from thermocycler and placed on a flat, clean work surface, cassette lid disposed, and sample was washed twice with 500µL PBS-T per slide for 1 minute each before Xenium-post hybridisation wash buffer (Table 2.9) was added to both wells and placed on the C1000 thermocycler for 30 minutes at 37°C. Following this, samples were washed with 500µL of PBS-T three times at RT before 500µL of Ligation Mix (Table 2.9) was added to both samples, and Xenium cassette replaced. Samples were placed within sealed thermocycler and ligation incubation commenced (120 minutes at 37°C).

2.6.6 Tissue amplification

Following tissue ligation, slides were washed three times with PBS-T for 1 minute at RT, and 500µL of Amplification Master Mix (Table 2.9) was applied to each slide and placed in the thermocycler for amplification at 30°C for 120 minutes. Slides were then washed with 500µL of TE Buffer (Table 2.9) for 1 minute and repeated twice more for a total of three washes.

2.6.7 Autofluorescence Quenching

Slides were then washed three times with 1000µL of PBS for 1 minute each, before 500µL of Diluted Reducing Agent B (Table 2.9) was applied to both samples and incubated for 10 minutes at RT. Following this, samples were washed with 1000µL of 70% ethanol (Table 2.3), followed by two further washes with 100% ethanol (Table 2.3) for 1 minute each. Autofluorescence solution was then applied to samples and incubated for 10 minutes at RT in the absence of light. Three washes were performed with 1000µL of 100% ethanol and no further solution added before being placed in the open thermocycler and dried for 5 minutes at 37°C.

2.6.8 Nuclear Staining

Slides were washed for 1 minute at RT in the dark with 1000µL of PBS, followed by a second wash with 1000µL of PBS-T for 2 minutes in the dark. 500µL of Xenium Nuclei Staining Buffer (Table 2.3) was then added to each slide and incubated for 1 minute in the dark at RT. Samples were then washed three times with 1000µL of PBS-T for 1 minute at RT in the dark. A final 1000µL of PBS-T was added, cassette lid placed on samples before proceeding to imaging.

2.6.9 Imaging

Imaging was performed on the Xenium Analyzer (10X Genomics) at Sydney Cytometry in the Charles Perkins Centre (CPC) at the University of Sydney. Cassettes were loaded into the appropriate slots in the Xenium Analyzer along with objective wetting consumable, and four buffers: (1) deionized water, (2) Xenium sample wash buffer A (3) Xenium sample wash buffer B and (4) Xenium Probe Removal Buffer, according to machine instructions. Decoding Reagent module A and B, two foil covered 96 well plates, were also loaded into machine. Four field of views were selected per slide, resulting in 8 total field of views. Final required information, including panel information and slide numbers were loaded into the Xenium Analyser, and automated imaging was commenced, which lasts between 2 and 4 days.

2.6.10 Data analysis

This analysis pipeline is discussed further in section 5.3.3. Supervised cell clustering of xenium data was performed in R Studio (v.2023.06.0+421) using *Seurat* and *FuseSOM* packages (Willie, 2024, Hao et al., 2024). Cell identities containing cluster number were then loaded back into Xenium Explorer (v2) to extract sample data by manually annotating tumour cores. The number of cells in each cluster was then calculated as a proportion of total cells per tumour core. Samples of suitable quality were imported into GraphPad Prism for statistical analysis and to generate graphical data. Box and whisker plots were used to visualise data. Box lines correspond to 25th percentile, median, and 75th percentile, and whiskers extend to minimum and maximum points. All data points are shown.

Table 2.9 Xenium *in situ* Hybridisation Reagents

Reagent		**Company**
Xenium Human Multi-Tissue and Cancer Gene Expression Panel Cat #: 10X-1000626	Human Multi-Tissue and Cancer Gene Expression Panel Probes	10X Genomics
Xenium Slides & Sample Prep Reagents Cat #: 10X- 1000460	2 Xenium Slides	
	Probe Hybridisation Buffer	
	Post Hybridization Wash Buffer	
	Ligation Buffer	
	Ligation Enzyme A	
	Ligation Enzyme B	
	Amplification Mix	
	Amplification Enzyme	
	Reducing Agent B	
	Autofluorescence Mix	
	FFPE Tissue Enhancer	
	Nuclei Staining Buffer	
	Perm Enzyme B	
Xenium Decoding Consumables Cat #: 10X-1000487	Module A Plate	
	Module B Plate	
Xenium Decoding Reagents Cat #: 10X-10000461	Decoding Reagent Module A	
	Decoding Reagent Module B	
Nuclease Free Water	Used to prepare tissue to prevent RNA contamination	Thermo Fisher

Table 2.10 Xenium *in situ* Gene Panel

Gene	**Ensembl ID**	**# p**	**Gene**	**Ensembl ID**	**# p**	**Gene**	**Ensembl ID**	**# p**
ABCC11	ENSG00000121270	4	DERL3	ENSG00000099958	8	MS4A4A	ENSG00000110079	8
ACE2	ENSG00000130234	8	DES	ENSG00000175084	4	MS4A6A	ENSG00000110077	8
ACKR1	ENSG00000213088	8	DIRAS3	ENSG00000162595	8	MTRNR2L11	ENSG00000270188	8
ACTA2	ENSG00000107796	4	DMBT1	ENSG00000187908	4	MYBPC1	ENSG00000196091	8
ACTG2	ENSG00000163017	8	DNAAF1	ENSG00000154099	8	MYC	ENSG00000136997	8
ADAM28	ENSG00000042980	8	DNASE1L3	ENSG00000163687	8	MYH11	ENSG00000133392	4
ADAMTS1	ENSG00000154734	8	DPEP1	ENSG00000015413	3	MYLK	ENSG00000065534	8
ADGRE1	ENSG00000174837	8	DPT	ENSG00000143196	8	MZB1	ENSG00000170476	6
ADGRL4	ENSG00000162618	8	DST	ENSG00000151914	8	NAT8	ENSG00000144035	4
ADH1C	ENSG00000248144	4	DUSP2	ENSG00000158050	6	NKG7	ENSG00000105374	2
ADH4	ENSG00000198099	4	ECSCR	ENSG00000249751	8	NPDC1	ENSG00000107281	5

Gene	Ensembl ID	# p	Gene	Ensembl ID	# p	Gene	Ensembl ID	# p
ADIPOQ	ENSG00000181092	4	EDN1	ENSG00000078401	8	NTN4	ENSG00000074527	8
AGER	ENSG00000204305	4	EDNRB	ENSG00000136160	8	OGN	ENSG00000106809	8
AGR3	ENSG00000173467	8	EGFL7	ENSG00000172889	3	OPRPN	ENSG00000171199	8
AHSP	ENSG00000169877	6	EGFR	ENSG00000146648	4	PCNA	ENSG00000132646	8
AIF1	ENSG00000204472	7	EHF	ENSG00000135373	8	PCOLCE	ENSG00000106333	4
ALAS2	ENSG00000158578	8	ELF5	ENSG00000135374	8	PCP4	ENSG00000183036	5
ALDH1A3	ENSG00000184254	8	EPCAM	ENSG00000119888	4	PCSK2	ENSG00000125851	8
AMY2A	ENSG00000243480	8	ERBB2	ENSG00000141736	3	PDCD1	ENSG00000188389	2
ANGPT2	ENSG00000091879	8	ERG	ENSG00000157554	8	PDGFRA	ENSG00000134853	8
ANPEP	ENSG00000166825	4	ESR1	ENSG00000091831	8	PDGFRB	ENSG00000113721	8
APCDD1	ENSG00000154856	8	FAS	ENSG00000026103	8	PDPN	ENSG00000162493	8
APOA5	ENSG00000110243	8	FBLN1	ENSG00000077942	4	PEBP4	ENSG00000134020	6
APOBEC3A	ENSG00000128383	8	FBN1	ENSG00000166147	8	PECAM1	ENSG00000261371	8
APOLD1	ENSG00000178878	8	FCER1A	ENSG00000179639	8	PGR	ENSG00000082175	8
AQP2	ENSG00000167580	3	FCGR1A	ENSG00000150337	8	PLA2G7	ENSG00000146070	8
AQP3	ENSG00000165272	2	FCGR3A	ENSG00000203747	8	PLAC9	ENSG00000189129	4
AQP8	ENSG00000103375	7	FCN1	ENSG00000085265	8	PLCG2	ENSG00000197943	8
AQP9	ENSG00000103569	8	FCN2	ENSG00000160339	5	PLD4	ENSG00000166428	8
AR	ENSG00000169083	8	FGFBP1	ENSG00000137440	8	PLIN4	ENSG00000167676	4
ARFGEF3	ENSG00000112379	8	FGFBP2	ENSG00000137441	8	PMP22	ENSG00000109099	8
ASCL1	ENSG00000139352	4	FGL2	ENSG00000127951	8	PPARG	ENSG00000132170	8
ASCL3	ENSG00000176009	7	FHL2	ENSG00000115641	8	PPP1R1A	ENSG00000135447	8
ASPN	ENSG00000106819	8	FKBP11	ENSG00000134285	5	PPP1R1B	ENSG00000131771	7
BAMBI	ENSG00000095739	8	FOXA1	ENSG00000129514	4	PPY	ENSG00000108849	2
BANK1	ENSG00000153064	8	FOXI1	ENSG00000168269	8	PRDM1	ENSG00000057657	8
BASP1	ENSG00000176788	8	FOXJ1	ENSG00000129654	4	PRF1	ENSG00000180644	7
BBOX1	ENSG00000129151	4	FOXP3	ENSG00000049768	7	PRG4	ENSG00000116690	4
BCL2L11	ENSG00000153094	8	FSTL3	ENSG00000070404	8	PROX1	ENSG00000117707	8
BMX	ENSG00000102010	8	FXYD2	ENSG00000137731	4	PTGDS	ENSG00000107317	4
BTNL9	ENSG00000165810	7	GATA2	ENSG00000179348	8	PTN	ENSG00000105894	8
C15orf48	ENSG00000166920	3	GATM	ENSG00000171766	4	PTPRC	ENSG00000081237	8
C1orf162	ENSG00000143110	8	GCG	ENSG00000115263	4	PVALB	ENSG00000100362	5
C1orf194	ENSG00000179902	4	GDF15	ENSG00000130513	1	RAMP2	ENSG00000131477	4
C20orf85	ENSG00000124237	3	GEM	ENSG00000164949	8	RAPGEF3	ENSG00000079337	8
C5orf46	ENSG00000178776	6	GHRL	ENSG00000157017	4	RBP5	ENSG00000139194	8
C6orf118	ENSG00000112539	8	GKN2	ENSG00000183607	4	RERGL	ENSG00000111404	8
C7	ENSG00000112936	4	GLIPR1	ENSG00000139278	8	RETN	ENSG00000104918	1
CA4	ENSG00000167434	5	GLYATL1	ENSG00000166840	4	RGS16	ENSG00000143333	8
CAPN8	ENSG00000203697	8	GNG11	ENSG00000127920	8	RIDA	ENSG00000132541	4
CAV1	ENSG00000105974	4	GNLY	ENSG00000115523	5	RND1	ENSG00000172602	8

Gene	Ensembl ID	# p	Gene	Ensembl ID	# p	Gene	Ensembl ID	# p
CAVIN1	ENSG00000177469	8	GPC1	ENSG00000063660	6	RTKN2	ENSG00000182010	8
CAVIN2	ENSG00000168497	8	GPC3	ENSG00000147257	8	S100A1	ENSG00000160678	4
CCDC39	ENSG00000284862	8	GPR183	ENSG00000169508	8	S100A12	ENSG00000163221	5
CCDC78	ENSG00000162004	3	GPRC5A	ENSG00000013588	8	SCGB2A1	ENSG00000124939	6
CCL19	ENSG00000172724	3	GPX2	ENSG00000176153	4	SCGN	ENSG00000079689	8
CCL27	ENSG00000213927	2	GYPA	ENSG00000170180	8	SELE	ENSG00000007908	8
CCL5	ENSG00000271503	5	GYPB	ENSG00000250361	1	SELL	ENSG00000188404	8
CCNB2	ENSG00000157456	8	GZMA	ENSG00000145649	8	SEMA3C	ENSG00000075223	8
CCR2	ENSG00000121807	8	GZMB	ENSG00000100453	4	SERPINB2	ENSG00000197632	8
CCR7	ENSG00000126353	8	GZMK	ENSG00000113088	8	SERPINB3	ENSG00000057149	8
CD14	ENSG00000170458	8	HAMP	ENSG00000105697	4	SERPINB9	ENSG00000170542	8
CD163	ENSG00000177575	4	HAVCR2	ENSG00000135077	8	SFRP2	ENSG00000145423	4
CD19	ENSG00000177455	8	HEMGN	ENSG00000136929	8	SFRP4	ENSG00000106483	4
CD1A	ENSG00000158477	8	HEPACAM2	ENSG00000188175	8	SFTA2	ENSG00000196260	6
CD1C	ENSG00000158481	8	HES4	ENSG00000188290	1	SH2D3C	ENSG00000095370	8
CD1E	ENSG00000158488	8	HIGD1B	ENSG00000131097	5	SLAMF1	ENSG00000117090	8
CD2	ENSG00000116824	8	HLA-DQB2	ENSG00000232629	8	SLAMF7	ENSG00000026751	8
CD247	ENSG00000198821	8	HMGCS2	ENSG00000134240	4	SLC18A2	ENSG00000165646	8
CD27	ENSG00000139193	5	HPGDS	ENSG00000163106	8	SLC22A8	ENSG00000149452	8
CD274	ENSG00000120217	8	HPX	ENSG00000110169	3	SLC26A2	ENSG00000155850	8
CD28	ENSG00000178562	8	IGF1	ENSG00000017427	8	SLC26A3	ENSG00000091138	8
CD300E	ENSG00000186407	8	IGSF6	ENSG00000140749	8	SLC4A1	ENSG00000004939	7
CD34	ENSG00000174059	8	IL1R2	ENSG00000115590	8	SMIM24	ENSG00000095932	8
CD3D	ENSG00000167286	5	IL1RL1	ENSG00000115602	8	SMYD2	ENSG00000143499	8
CD3E	ENSG00000198851	8	IL2RA	ENSG00000134460	8	SNAI1	ENSG00000124216	6
CD4	ENSG00000010610	8	IL3RA	ENSG00000185291	8	SNCA	ENSG00000145335	4
CD5L	ENSG00000073754	8	IL7R	ENSG00000168685	8	SNCG	ENSG00000173267	2
CD68	ENSG00000129226	3	INMT	ENSG00000241644	8	SNTN	ENSG00000188817	8
CD69	ENSG00000110848	8	INS	ENSG00000254647	3	SOX17	ENSG00000164736	8
CD70	ENSG00000125726	2	IRF8	ENSG00000140968	8	SOX18	ENSG00000203883	3
CD79A	ENSG00000105369	4	KCNK3	ENSG00000171303	8	SOX2	ENSG00000181449	8
CD83	ENSG00000112149	8	KCNMA1	ENSG00000156113	8	SPDEF	ENSG00000124664	6
CD86	ENSG00000114013	8	KIT	ENSG00000157404	8	SPI1	ENSG00000066336	2
CD8A	ENSG00000153563	8	KLK11	ENSG00000167757	5	SPIB	ENSG00000269404	8
CD93	ENSG00000125810	8	KLRB1	ENSG00000111796	8	SRPX	ENSG00000101955	8
CDH16	ENSG00000166589	4	KLRC1	ENSG00000134545	8	SST	ENSG00000157005	3
CDK1	ENSG00000170312	8	KLRD1	ENSG00000134539	8	STC1	ENSG00000159167	8
CENPF	ENSG00000117724	8	KNG1	ENSG00000113889	3	STC2	ENSG00000113739	8
CFAP53	ENSG00000172361	8	KRT20	ENSG00000171431	4	STEAP4	ENSG00000127954	8
CFB	ENSG00000243649	8	KRT7	ENSG00000135480	3	TAC1	ENSG00000006128	8

Gene	Ensembl ID	# p	Gene	Ensembl ID	# p	Gene	Ensembl ID	# p
CFHR1	ENSG00000244414	4	LAG3	ENSG00000089692	5	TAT	ENSG00000198650	4
CFHR3	ENSG00000116785	8	LAMP3	ENSG00000078081	8	TBX3	ENSG00000135111	8
CFTR	ENSG00000001626	8	LGI4	ENSG00000153902	4	TCF15	ENSG00000125878	3
CHGA	ENSG00000100604	4	LGR5	ENSG00000139292	4	TCF4	ENSG00000196628	8
CLCA1	ENSG00000016490	8	LIF	ENSG00000128342	8	TCIM	ENSG00000176907	8
CLCA2	ENSG00000137975	8	LILRA4	ENSG00000239961	8	TCL1A	ENSG00000100721	7
CLEC10A	ENSG00000132514	8	LILRA5	ENSG00000187116	4	TENT5C	ENSG00000183508	8
CLEC14A	ENSG00000176435	8	LILRB2	ENSG00000131042	8	TFF2	ENSG00000160181	4
CLEC4E	ENSG00000166523	8	LILRB4	ENSG00000186818	4	TFPI	ENSG00000003436	8
CLECL1	ENSG00000184293	7	LPL	ENSG00000175445	4	THAP2	ENSG00000173451	8
CLIC6	ENSG00000159212	8	LTBP2	ENSG00000119681	8	THBS2	ENSG00000186340	4
CNN1	ENSG00000130176	6	LY6D	ENSG00000167656	2	THY1	ENSG00000154096	8
COCH	ENSG00000100473	8	LY86	ENSG00000112799	8	TIMP4	ENSG00000157150	8
COL17A1	ENSG00000065618	8	LYVE1	ENSG00000133800	8	TM4SF18	ENSG00000163762	8
COL5A2	ENSG00000204262	8	MALL	ENSG00000144063	8	TM4SF4	ENSG00000169903	4
CPA3	ENSG00000163751	4	MAMDC2	ENSG00000165072	8	TMC5	ENSG00000103534	8
CRHBP	ENSG00000145708	4	MARCO	ENSG00000019169	4	TMEM100	ENSG00000166292	8
CRISPLD2	ENSG00000103196	8	MCEMP1	ENSG00000183019	8	TMEM174	ENSG00000164325	8
CSF2RA	ENSG00000198223	8	MCF2L	ENSG00000126217	8	TMEM52B	ENSG00000165685	4
CSF3	ENSG00000108342	7	MDM2	ENSG00000135679	8	TNC	ENSG00000041982	8
CTLA4	ENSG00000163599	8	MEDAG	ENSG00000102802	8	TNFRSF13B	ENSG00000240505	5
CTSG	ENSG00000100448	3	MEF2C	ENSG00000081189	8	TNFRSF17	ENSG00000048462	8
CTSK	ENSG00000143387	8	MEST	ENSG00000106484	8	TNFRSF9	ENSG00000049249	8
CXCL10	ENSG00000169245	8	MET	ENSG00000105976	8	TOP2A	ENSG00000131747	4
CXCL2	ENSG00000081041	8	MFAP5	ENSG00000197614	8	TRAC	ENSG00000277734	8
CXCL6	ENSG00000124875	8	MKI67	ENSG00000148773	8	TREM2	ENSG00000095970	7
CXCL9	ENSG00000138755	8	MLANA	ENSG00000120215	3	TSPAN19	ENSG00000231738	8
CXCR4	ENSG00000121966	8	MLPH	ENSG00000115648	8	UBE2C	ENSG00000175063	4
CYP1A1	ENSG00000140465	8	MMRN1	ENSG00000138722	8	UMOD	ENSG00000169344	3
CYP2A7	ENSG00000198077	8	MMRN2	ENSG00000173269	8	UPK3B	ENSG00000243566	4
CYP2B6	ENSG00000197408	8	MNDA	ENSG00000163563	8	VCAN	ENSG00000038427	8
CYP2F1	ENSG00000197446	8	MPEG1	ENSG00000197629	8	VSIG4	ENSG00000155659	8
CYP3A4	ENSG00000160868	4	MRC1	ENSG00000260314	4	VWA5A	ENSG00000110002	8
CYP4B1	ENSG00000142973	8	MS4A1	ENSG00000156738	8	VWF	ENSG00000110799	8
CYTIP	ENSG00000115165	8	MS4A2	ENSG00000149534	8			

*** adapted from 10X Genomics "Xenium_hMulti_v1_metadata", accessed March 2024**

2.7 Phenocycler Fusion (PCF)

2.7.1 Tissue Preparation

All PCF staining and imaging was performed by PhD candidate Xinyu Bai (Melanoma Institute, University of Sydney) with my assistance. After acquiring samples in the Xenium, one of the two slides (Xenium slide 2) were removed and performed antigen retrieval in AR 9 buffer performed (Table 2.3) in a pressure cooker with ~1L of ddH_2O for 20 minutes and left to equilibrate to RT for at least 30 minutes. Slides were then placed into a glass coplin jar containing ddH_2O for two minutes, washed twice in two coplin jars containing hydration buffer (Akoya Biosciences) for two minutes each. Slides were then equilibrated in staining buffer (Akoya Biosciences) for 20-30 minutes.

2.7.2 Tissue Staining

Antibody cocktail containing antibodies listed in Table 2.7.1 (made up in Blocking Buffer according to Phenocycler Fusion Protocol PD-000011 REV I; Akoya Biosciences) was applied to slide and covered with a 2cm x 3cm piece of parafilm and incubate for 3 hours at RT in a humidifying chamber. After this incubation, slides were washed twice in staining buffer (Akoya Biosciences) and fixed for 10 minutes in Fixing solution (1.6% PFA in Storage Buffer (Akoya Biosciences). Slides were then washed 3x in PBS for 30 seconds each before being submerged in ice cold methanol for 5 minutes at 4°C and subsequently washed three times in PBS. Phenocycler Fixative Reagent (Akoya Biosciences) was applied to sample for 20 minutes and subsequently washed three times with PBS and stored in staining buffer until acquisition on Phenocycler Fusion.

2.7.3 PCF Imaging

Reporter plates were prepared containing all reporters on Cy3, Cy5 and Cy7 according to Table 2.11. Immediately prior to PCF run, the flow cell was attached to the stained slide using the PCF flow cell assembly and application device (Akoya Biosciences). The PCF instrument was then set up with the PhenoImager software, priming performed, and the experimental slide with flow cell was attached and PhenoCycler multicycle run initiated. Representative PCF images were produced using QuPath (v0.5.1) (Bankhead et al., 2017).

Table 2.11: Phenocycler Fusion Antibodies

Cycle	Cy3		Cy5		Cy7	
	Marker	**Dilution**	**Marker**	**Dilution**	**Marker**	**Dilution**
1	BLANK					
2	CD27-c	1:50	TIM3-c	1:50		
3	TBET-c	1:50	CD1c-c	1:50		
4	SOX10-c	1:20	IDO1	1:200		
5	CD8	1:200	CD4	1:200	CD20	1:400
6			CD68	1:200	CD31	1:200
7	CD45RO	1:200	ICOS	1:400	HLA-A	1:200
8			CD11c	1:400	SMA	1:200
9	CD34	1:200	MITF-c	1:50	Vimentin	1:200
10	CD39	1:100	FOXP3	1:200	HLA-E	1:100
11	CD14	1:200	HLA-DR	1:400		
12	VISTA	1:100	PD-L1	1:100		
13	GZMB	1:100	CD3e	1:200	MLANA-c	1:50
14	CD38	1:200	PD-1	1:200		
15	CD163	1:200	CD45	1:200		
16	CD141	1:200	LAG3	1:100		
17	Ki-67	1:200	Collagen IV	1:200		
18	S100B-c	1:200	TCF7-c	1:100		
19	B2M-c	1:200	PMEL-c	1:100		
20	BLANK					

c = conjugated by Xinyu Bai

2.8 Hematoxylin and eosin-staining

2.8.1 H&E Staining

H&E staining was performed with the assistance of Xinyu Bai performed in a fume hood at the Melanoma Institute Australia in CPC, based on their optimised H&E staining protocol for FFPE melanoma tissues. All solutions were contained in plastic staining coplin jars and stored according to relevant regulations**.** All jars of milliQ dH_2O described were fresh containers unless otherwise stated. Staining was performed at RT. Slides for staining were immersed in three consecutive jars filled with milliQ dH_2O for 1 minute each, followed by Hematoxylin for 3 minutes, and then washed again in three separate jars of milliQ dH_2O for 1 minute each. Slide was stained in blueing solution (Table 2.12) for 1 minute, before being washed in milliQ dH_2O for 1 minute. Slides were then placed in an increasing ethanol gradient by being placed in

consecutive jars containing 50%, 70%, 95%, 95% for 1 minute each. Slides were then placed in eosin for 45 seconds for counterstaining, followed by immersion in xylene for 2 minutes. Slides were then mounted using mounting media covered with a coverslip and stored at RT in the dark until imaging.

2.8.2 H&E Imaging

Imaging was performed by Dr Rachael Ireland on the Zeiss Axio Scan Z1 at the Australian Centre for Microscopy and Microanalysis at the CPC, University of Sydney.

Table 2.12 Hematoxylin and Eosin (H&E) Staining Reagents

Reagent	**Source**
Hematoxylin	Sigma-Aldrich
Eosin	Sigma-Aldrich
Blueing Solution	Hurst Scientific
milliQ	Thermo Fisher Scientific

3 Detailed phenotyping of myeloid populations within metastatic melanoma reveals PD-L2+ myeloid cells are associated with response to anti-PD-1 therapy (manuscript in preparation for submission)

The data generated from the work involved in this chapter has been collated into a manuscript that is being prepared for publication.

Detailed phenotyping of myeloid populations within metastatic melanoma reveals PD-L2+ myeloid cells are associated with response to anti-PD-1 therapy

Authors: Ruth O Allen[1,2], Annie T Tasker[2,3], Moomal Tasneem[1,2], Grace H Attrill[1,2,3] Felix Marsh-Wakefield[4], Susan Shead[1], James S Wilmott[1,2,3], Ben Roediger[5], Richard A Scolyer[1,2,3,6], Georgina V Long[1,2,3,7,8], Umaimainthan Palendira[1,2,3]*, Angela L Ferguson[1,2,4]*

Affiliations

[1] Faculty of Medicine and Health, The University of Sydney, Sydney, NSW, Australia

[2] Charles Perkins Centre, The University of Sydney, Sydney, NSW, Australia

[3] Melanoma Institute Australia, The University of Sydney, Sydney, NSW, Australia

[4] Centenary Institute, The University of Sydney, Sydney, NSW, Australia

[5] Novartis Institutes for BioMedical Research

[6] Department of Tissue Pathology and Diagnostic Oncology, Royal Prince Alfred Hospital and NSW Health Pathology, Sydney, New South Wales, Australia

[7] Royal North Shore Hospital, Sydney, New South Wales, Australia.

[8] Mater Hospital, North Sydney, New South Wales, Australia

* contributed equally

Corresponding Authors: Angela Ferguson, a.ferguson@sydney.edu.au or Mainthan Palendira, umaimainthan.palendira@sydney.edu.au

Keywords

Metastatic Melanoma; Myeloid Cells; anti-PD-1; immunotherapy; VISTA.

Abstract

To understand mechanisms of response and resistance to immune checkpoint inhibitors (ICIs) in metastatic melanoma, we need greater knowledge of the diverse cell types in the tumour microenvironment. Using flow and mass cytometry (CyTOF) we profile immune cell populations in metastatic melanoma tumour dissociates. This study extensively profiled the immune infiltrates present in metastatic melanoma tumours and identified 11 phenotypically distinct and functionally relevant myeloid cell subsets. Importantly, we define a distinct PD-L2-expressing myeloid cell present in greater proportions within the tumours of PD-1 responders compared to non-responders. We also profile the expression pattern of novel

immunotherapy target VISTA across these immune populations in metastatic melanoma. This study presents a detailed understanding of the immune infiltrate present in the tumours of metastatic melanoma patients and identifies unique myeloid cells present, including a PD-L2+ myeloid population associated with patient response to immunotherapy.

3.1 Introduction

Despite the relative success of anti-CTLA-4 and anti-PD1 checkpoint blockade therapies (ICI) and most recently anti-PD-1 and anti-LAG3 combination immunotherapy for metastatic melanoma, there remains a large proportion of patients who do not respond to these treatments or develop resistance to them (Tawbi et al., 2021). All these treatment strategies primarily target T cells with the aim of reinvigorating their functional capacity to boost tumour clearance. Whether targeting other cell types could complement these therapies remain unknown, however, a major hurdle is the lack of clarity on various immune cell phenotypes and the expression patterns of potential target molecules within the TME.

Recent advances in cellular and molecular profiling technologies have enabled a greater understanding of the constituents of the tumour microenvironment (TME) and their likely role in anti or pro-tumour activities. However, the role of myeloid cells within the TME has remained poorly characterized, owing to the large heterogeneity of these cells. Recent single cell transcriptomics data has revealed that macrophages are highly heterogenous in tumour tissue, and challenges remain to consistently identify the same cell subsets across different patient cohorts (Hume et al., 2023, Lin et al., 2024a, Liu et al., 2024, Li et al., 2023b). Therefore, there is an unmet need to develop strategies for identifying various myeloid cells that could be applied across different patient cohorts.

It is imperative that we understand the phenotypic diversity of myeloid cells and what this might suggest about their functional role within the tumour to be able to target these cells with immunotherapy (Mantovani et al., 2021). One strategy that is being considered to bolster checkpoint blockade success is to manipulate myeloid cells within the TME. One relevant immune receptor for such strategy is V-domain Immunoglobulin Suppressor of T Cell Activation (VISTA). VISTA is an established inhibitory receptor and is expressed widely across both healthy and diseased tissues, plays an important homeostatic role in the human body (Thakkar et al., 2022). VISTA emerged as a possible target for immune checkpoint

blockade therapy due to its homology to PD-L1. However, work in recent years has shown VISTA signalling is distinct from PD-1 and PD-L1 pathways, making it an attractive candidate for combination therapy (Kakavand et al., 2017, Ruggieri et al., 2022). Reported ligands of VISTA include PSGL-1, VSIG-3, and VSIG-8 (Shekari et al., 2023). In cancer, VISTA is expressed on a variety of immune and tumour cells, in particular myeloid cells and monocytes (Li et al., 2021) (Yuan et al., 2021). As with most solid tumour cancers, VISTA has been reported as being associated with both positive and negative clinical outcomes in melanoma (Zong et al., 2022, Zong et al., 2020, Ma et al., 2022, Long et al., 2022, Ruggieri et al., 2022, Zapała et al., 2022, Wang et al., 2023a, Liu et al., 2023).

We reasoned that receptor based immune profiling of the TME using cytometry methods could provide a useful strategy for particularly identifying cells with complex phenotypes such as myeloid cells. We have developed a panel of antibodies that enabled us to identify 11 myeloid populations within metastatic melanoma tumours by flow cytometry. We have also validated this approach using mass cytometry on a different cohort of patients. Importantly, here we have applied this approach to identify myeloid cells that are associated with response to anti-PD-1 therapy. In addition, we also map the expression pattern of VISTA to understand the potential implications of blocking its interactions with its ligands.

3.2 Materials and Methods

Flow Cytometry

Study ethics

All tissue was acquired for research with approval from the Sydney Local Health District Human Ethics Review Committee (protocol no X15-0454 and 2019/ETH06874), and informed consent from each patient and from the MIA Biospecimen Tissue Bank.

Sample preparation and staining

Cryopreserved single cell tumour dissociates were thawed in a 37°C water bath. Cells were treated in ACK lysis buffer (Gibco) for 1 minute at RT to lyse red blood cells. Cells were then stained with fluorochrome-conjugated antibodies for 30 minutes at 4°C (Table 2.2). If intracellular staining was performed, cells were resuspended in Fix/Perm buffer (BD Pharmingen) and incubated for 40 minutes at 4°C in the absence of light to permeabilise the cells. Cells were then washed in Perm/Wash buffer (BD Pharmingen) and intracellular

antibodies were applied to cells and samples incubated for 40 minutes at 4°C in the absence of light. Following staining, cells were fixed for 30 minutes on ice in 4% PFA in FACS buffer (Table 2.2). Cells were centrifuged at 1455 rcf for 4 minutes at 4°C, the supernatant was discarded, and the cells resuspended in FACS buffer. All samples were stored at 4°C while awaiting analysis.

Sample Acquisition

Stained samples and controls were analysed on a BD five laser LSR Fortessa (Sydney Cytometry, the University of Sydney). Unstained cells and single colour controls were run with each experiment, as well as fluorescence Minus One (FMO) controls for all intracellular markers (Table 2.2) to determine changes in background fluorescence when permeabilising the cells. Live/dead stain, Zombie Aqua^{TM} Fixable Viability Kit (Table 2.1) was applied to separate unstained cells to use as a cell viability control as intracellular staining protocol impacts the reliability of this staining.

Flow Cytometry Data Analysis

Data collected was analysed using FlowJo v10. GraphPad Prism was used to analyse quantitative data from FlowJo analysis and generate graphical data. Box and whisker plots were used to visualise data. Box lines correspond to 25th percentile, median, and 75th percentile, and whiskers extend to minimum and maximum points. All data points are shown.

The gating strategy (supp. Figure 3.1) used to define unique myeloid cell populations was established after extensive testing in our lab. An auto-fluorescent (AF) macrophage population, previously excluded by the CD3-CD19- gate therefore a CD3-CD19-AF+ gate was adopted to exclude lymphocytes and include this population. Cells were gated as HLA-DR+, and CD11c+ cells were further defined into macrophage and DC subsets. CD1c and CD141 were employed to define classical DC subsets cDC1 and cDC2s. After cycling through multiple markers including CD1a, CD11a, CD38, CD169, CD209 and CD303, cell-surface marker CD13 was used to separate macrophage and dendritic populations due to the definition it gave to subsets and its established role in phagocytosis in macrophages and dendritic cells (Villaseñor-Cardoso et al., 2013). Macrophage activation marker CD206 was used to further delineate macrophage populations not only because of the established use in the literature but also because it has been associated with prognosis in solid tumours (Liu et al., 2022a, Debacker et al., 2021, Roussel et al., 2017). The HLA-DR+CD11c- populations were separated according to CD14 expression

(CD11c- Monocytes) and CD1c expression (deemed 'Tumour Infiltrating Myeloid Cells' or TIM1 and TIM2). Live Dead (Zombie Aqua) stain was run on separate samples as intracellular staining protocol impacts the reliability of this staining. Values reported in text are mean values unless stated otherwise, and ± indicates standard error of mean (SEM) value.

Cytometry by Time of Flight (CyTOF)

Study Design and Experimental Details

Data in figures 3.3 and 3.4 was produced by reanalysing CyTOF data from a previously published melanoma study investigating the prevalence of various checkpoint targets in melanoma progression (Edwards et al., 2019). This study was performed under ethics review committee approval (protocol no X17-0312) and patients' informed consent. 18 fresh tumour biopsies were taken from 18 patients with either stage III or stage IV melanoma. All patients had never received proport systemic treatment, and the tumour biopsy site had not been treated with radiotherapy, topical or intralesional therapy. Full experimental details are included in published manuscript (Edwards et al., 2019).

CyTOF Data Analysis

All manual gating was performed in FlowJo (v10.5.2). Gating of novel myeloid populations performed as per representative gating strategies (Figure 3.3A & 3.4A). FI-tSNE plots (Linderman et al., 2019) in Figure 3.3 were generated using *spectre* package (Ashhurst et al., 2022) on CD45+CD3-CD20-HLA-DR+ cells from 7 of the patients profiled with identical CyTOF panels in Figure 3.4. Statistical analysis and data visualisation was performed in GraphPad Prism. In box and whisker plots included, box lines correspond to 25th percentile, median, and 75th percentile, and whiskers extend to minimum and maximum points. All data points are shown. Uncorrected Dunn's test was performed to determine statistical differences between proportions of myeloid cell populations. Uncorrected Fisher's least significant difference (LSD) test performed with single pooled variance to test statistically significant differences in myeloid populations in PD-1 responders and non-responders. Mann-Whitney test was performed to determine differences in expression of markers in individual cell populations. Values reported in text are mean values unless stated otherwise, and ± indicates standard deviation (SD).

3.3 Results

T_H1 CD4 T cells and γδ T cells are dominant lymphocyte populations within metastatic melanomas.

Although the cellular composition of metastatic melanoma is well characterised in comparison to many other cancers, there is much we still do not know about the diversity of the immune compartment. To address this, we employed multi-parameter flow cytometry to profile the immune compartment of 31 metastatic melanoma tumours excised from patients that had no prior therapies (treatment-naïve). These tumours were surgically excised before treatment from multiple sites: lymph node (81%, n=25), subcutaneous (13%, n=4), adrenal gland (3%, n=1) and brain (3%, n=1). 42% of the cohort was female (n=13) and 58% male (n=18). Quantification of major lymphocyte populations as a proportion of live single cells showed that CD4 T cells were the dominant immune population, comprising an average of 25.1% of live single cells (±19.19%), followed by γδ T cells (22.1% ± 26.2), CD8 T cells (16.7% ± 21.5), B cells (14.7% ± 22.2) (Figure 3.1A). To determine whether this cellular composition was impacted by the site of tumour, we compared lymph node metastasis against cutaneous metastasis and found no significant differences (Figure 3.1B). In addition, the cellular composition was also independent of sex of the patients (supplementary figure 3.1)

Unbiased clustering (tSNE) of the data led to B cells, CD8 T cells, CD4 T cells and yd T cells clusters (Figure 3.1C) demonstrating large phenotypic diversity. We therefore further defined our T cell populations into 11 sub-populations in order to more accurately profile metastatic melanoma. Further characterisation of CD8+ T cells using tissue-residency markers CD69 and CD103 revealed 39% (± 24.8) of CD8+ T cells were CD69+CD103-, 22.4% (± 21.6) were CD69+CD103+, and the remaining CD8 T cells were CD69-CD103- (28.9% ± 24.8) (Figure 3.1D), suggesting that only a third of the CD8+ T cells could be circulating cells. We then further classified CD4+ T cells into four functional subsets based on the expression of key transcription factors namely T_H1 (Tbet+RORγt-), T_H2 (GATA3+), T_H17 (RORγt+Tbet-) and T_H17.1 cells (Tbet+RORγt+) (Annunziato et al., 2007) (Basdeo et al., 2017). All subsets were present within these tumours, however T_H1 cells were the most dominant CD4+ T cell subset comprising an average of 33.9% (± 19.1) of CD4 T cells (Figure 3.1E). Characterisation of the gamma delta (γδ) T cell population into delta chain subtypes using Vδ1 and Vδ2 showed that the vast majority were Vδ1+Vδ2- (mean 84.7% ±8.8) (Figure 3.1F). Together, we saw a large

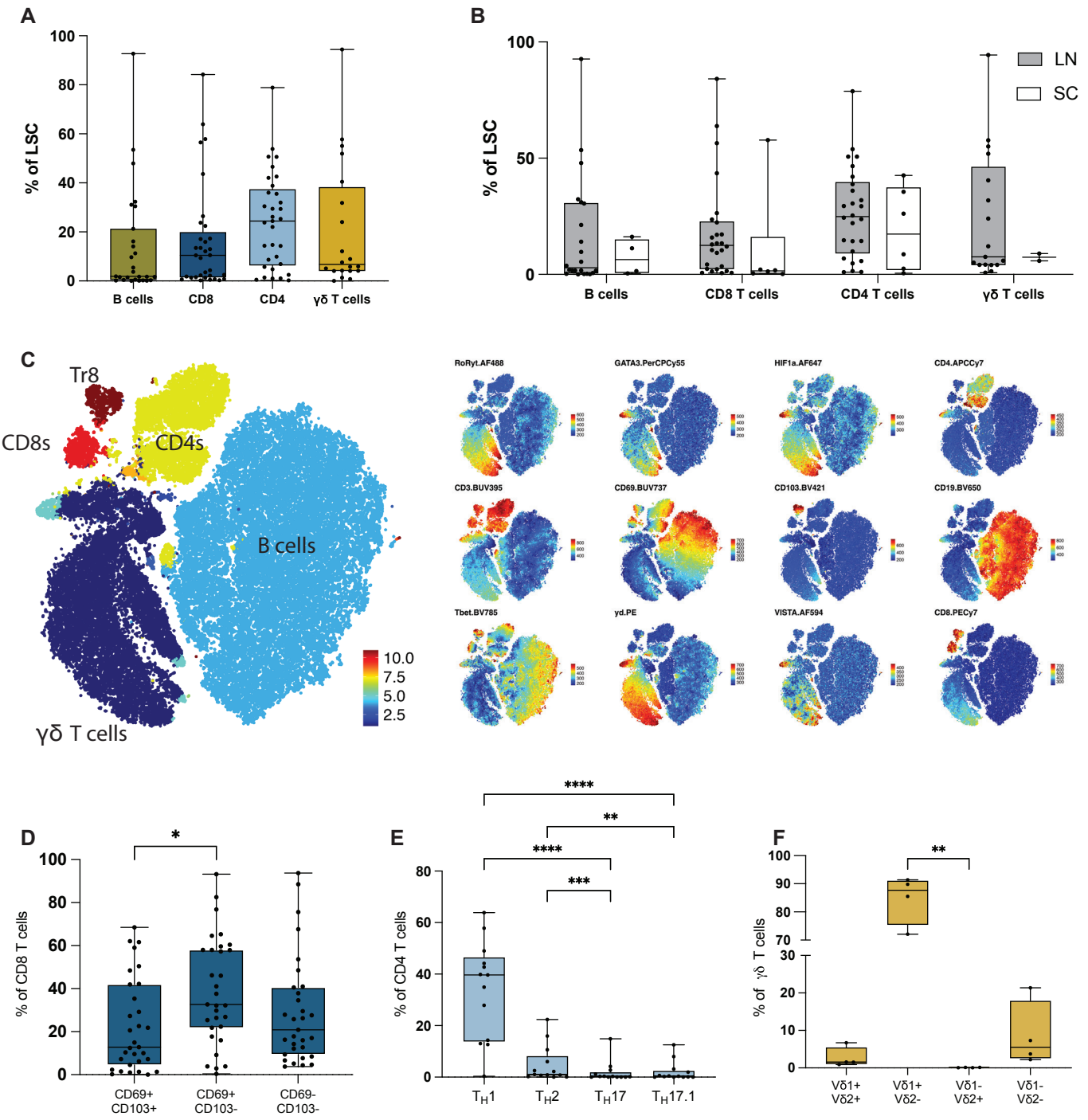

Figure 3.1 B and T cell populations and subsets in metastatic melanoma tumour tissue. Tumours from treatment-naïve metastatic melanoma patients (n=36) were analysed using flow cytometry to define 20 distinct cell populations. **(A)** Proportions of B cells, CD8+ T cells, CD4+ T cells and γδ cells in melanoma (n=36) **(B)** Mean proportions of B cells, CD8+ T cells, CD4+ T cells and γδ cells in metastatic melanoma compared between tumour location, lymph node associated (n=19, grey) or subcutaneous (n=5, white). **(C)** FlowSOM lymphocyte metaclusters identified by individual FitSNE plots (RORγt, GATA3, HIF1α, CD4, CD3, CD69, CD103, CD19, T-bet, γδ, VISTA, CD8). B cells (aqua), CD4 T cells (yellow) CD8 T cells (red) and Tr8 cells (maroon) and γδ T cells (dark blue). Plots generated using n=7 patients. **(D)** Proportions of CD8+ T cell subsets CD103+CD69+, CD103+CD69-, and CD103-CD69- cells. **(E)** CD4 T cell subsets T_H1, T_H2, T_H17, $T_H17.1$ cells as a proportion of total CD4+ T cells. **(F)** γδ T cell subsets separated into subsets defined by expression of Vδ 1 and Vδ2 expression. Mann-Whitney tests performed to determine statistical significance. p<0.0332(*), p<0.0021(**), p<0.0002(***), p<0.0001(****).

phenotypic diversity in the lymphocyte populations that was not associated with sex or site of metastasis (supplementary figure 3.1).

Phenotypically diverse myeloid cells with varying expression of checkpoint receptors are present within metastatic melanomas.

Despite the important role innate cells play in tumour control, they are poorly characterised in human tumours. We therefore sought to define the unique myeloid populations (defined as CD45+CD3-CD19-HLA-DR+ cells) and their phenotypes within metastatic melanomas using multi-parameter flow cytometry. By cycling through several known myeloid cell markers, we identified a core panel that could be used to identify different populations of myeloid cells within metastatic melanoma tumours using flow cytometry. This gating strategy revealed 4 phenotypically distinct macrophage populations, four dendritic cell populations, 2 tumour induced myeloid cells, and a monocyte population. Following gating for CD45+CD3-CD19-HLA-DR+CD11c+, CD14+ cells were defined as macrophages, and four subpopulations (Mϕ1-Mϕ4) were defined according to CD13 and CD206 expression (Figure 3.2A, B). Dendritic cells were defined first as CD45+CD3-CD19-HLA-DR+CD11c+CD14-, and subsequently gated using CD1c, CD13 and CD141 expression to define two inflammatory dendritic cell (iDC) populations, as well as conventional dendritic cell type 1 population (cDC1) and conventional dendritic cell type 2 population (cDC2s). CD11c- innate cells were then defined according to CD14 and CD1c expression to produce three populations. We quantified these 11 populations across our 31 tumour dissociates and detected them as proportions of live single cells (supplementary figure 3.2) and of the innate cell compartment (CD45+CD3/CD19-HLA-DR+) (Figure 3.2C, D). As expected, overall myeloid cells constituted a small proportion of live single cells within these tumours.

Macrophages were present at varying levels within metastatic tumours, with Mϕ1 comprising a mean proportion of 5.3% (± 6.2), Mϕ2 cells 6.3% (± 7.1), Mϕ3 cells 4% (± 5.1) and Mϕ4 (± 5.5) of innate cells within tumours (Figure 3.2C). Dendritic cells were also present at varying percentages in our cohort; CD13+ iDCs made up 5.9% (± 7), CD13- iDCs made up 8.1% (± 8.9), cDC1s at 4.7% (± 6) cDC2s 9.1%± 15.7 (Figure 3.2C). The largest subsets were the CD11c- cells, with CD11c- monocytes making up 5.8% (± 6.6), TIM1 cells 16.7% (± 25.8) and TIM2 cells the largest average proportion at 22.4% (± 21) (Figure 3.2C). Figure 3.2D summarises the mean values described here to visualise the myeloid compartment. We again

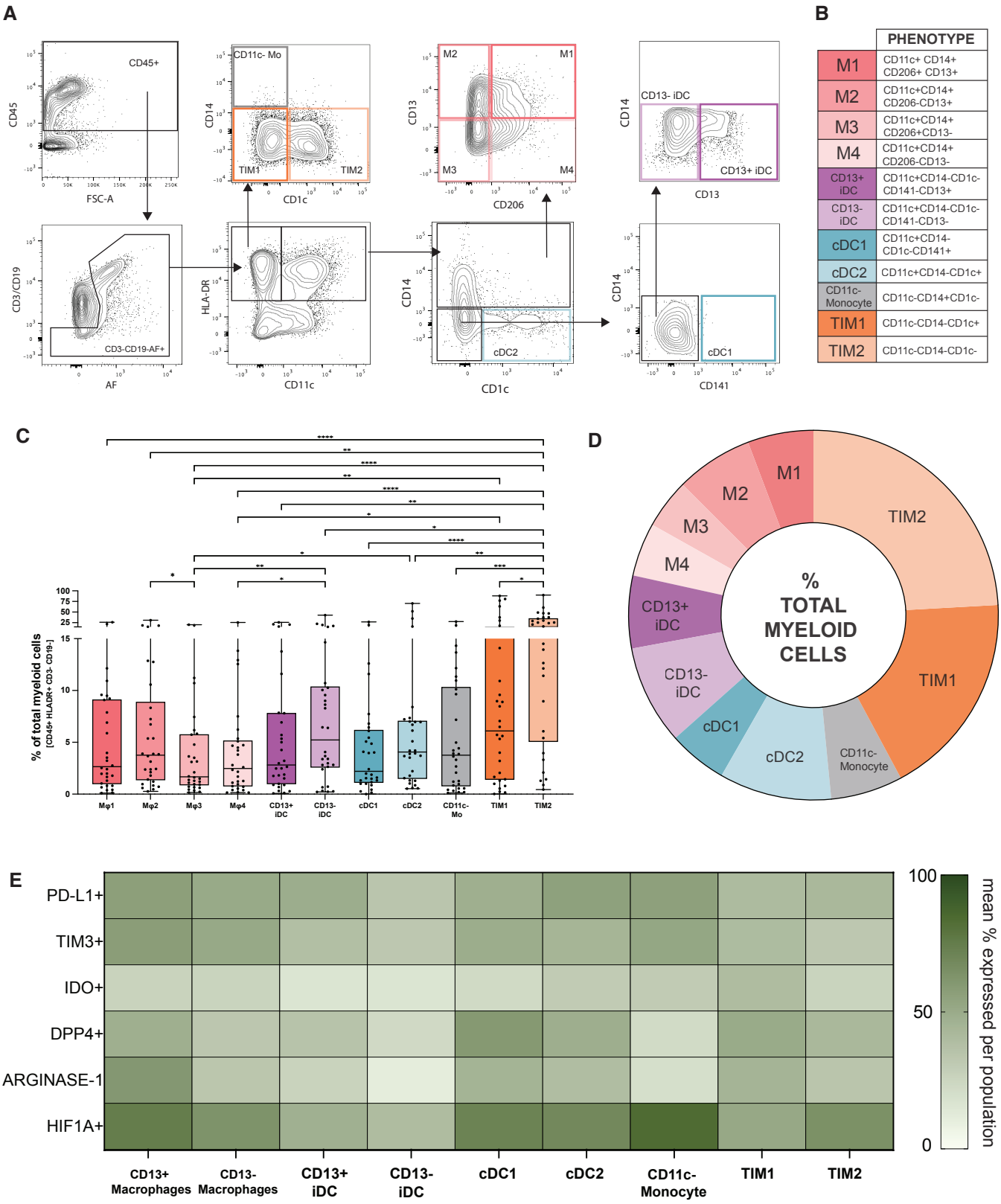

Figure 3.2 Metastatic melanoma tissue contains phenotypically diverse and distinct myeloid cell subsets with varying expression of immune checkpoint and modulatory markers. 22 metastatic melanoma tumours were processed and analysed using flow cytometry. **(A)** Gating strategy to define myeloid cells in melanoma with annotated phenotypes detailed in **(B)** Phenotypic markers used to define macrophages (Mϕ1, Mϕ2, Mϕ3, Mϕ4), Dendritic cells (iDC separated by CD13 expression, cDC1 & cDC2) monocytes (CD11c- Monocyte) and myeloid cells (TIM1, TIM2) **(C)** Populations defined in (A) and (B) calculated as a proportion of all myeloid cells (CD45+HLADR+CD3-CD19-) Statistical significance determined by non-parametric Friedman test with multiple comparisons $p < 0.01$ included in graph (n=22) **(D)** Visualisation of myeloid cells as proportions of CD45+HLA-DR+CD3-CD19- cells using mean values (n=22) **(E)** Heatmap of mean percentage expressing immune-modulatory and checkpoint markers, PD-L1 (n=13), TIM-3 (n=10), IDO (n=9), DPP4 (n=13), Arginase-1 (n=11) and HIF1α (n=3) on myeloid cell populations.

tested if the presence of myeloid cell subsets as well as total CD45+CD3-CD19- cells differed when our cohort was separated by sex and site of metastasis and observed no differences (supplementary figure 3.1).

We then sought to understanding the role of these cell populations within the tumour by determining the expression of checkpoint receptors PD-L1, TIM-3, IDO and the regulator of chemokine expression, DPP4. One possible regulatory element that could impact T cell recruitment to tumours is DDP4, which cleaves and inactivates T cell recruiting chemokines such as CXCL9, CXCL10 and CXCL11 (Casrouge et al., 2012, Remm et al., 2016). In addition, we also measured the metabolic potential of the cells through their expression of Arginase-1 and HIF1α. PD-L1 and TIM-3 was expressed at low to moderate levels across the myeloid compartment, while IDO and Clec9A also had low expression across all subtypes (Figure 3.2E). The proportion of DPP4+ cells was highest on cDC1s (60% ±39.9), cDC2s (48.6% ± 38.6), TIM1 (50.5% ± 37.4) and CD13+ macrophages (48.3% ± 40) compared to other myeloid cells, suggesting that even if these cells produce CXCL9, CXCL10 or CXCL11, they may not be able to recruit T cells (Figure 3.2E). Similar trends were observed for Arginase-1, with CD13+ macrophages averaging 60.7% (± 36.1), 45.4% (±41.5) cDC1s, and 45.2% (± 27.8) of TIM1 cells expressing Arginase-1 (Figure 3.2E). HIF1α had the most varied expression across the myeloid compartment (Figure 3.2E). Myeloid populations with the most HIF1α+ percentages were CD11c- Monocytes (83.9%), CD13+ macrophages (75%) and cDC1s (71.7%) (Figure 3.2E).

Validation of myeloid cell phenotypes within metastatic melanoma tumours using mass cytometry

Having established a strategy for identifying various myeloid cells within metastatic melanoma tumours, we wanted to validate these cell phenotypes using a different method in a different cohort of patients. We investigated the myeloid compartment in detail on an already published cohort where suspension mass cytometry was used (Edwards et al., 2019). We gated and quantified the same 11 myeloid populations across 17 treatment naïve metastatic melanoma tumour biopsy specimens (Figure 3.3A).

We were able to identify all 11 myeloid populations within this validation cohort (Figure 3.3). The proportions of different cell populations were, however, highly variable as seen previously.

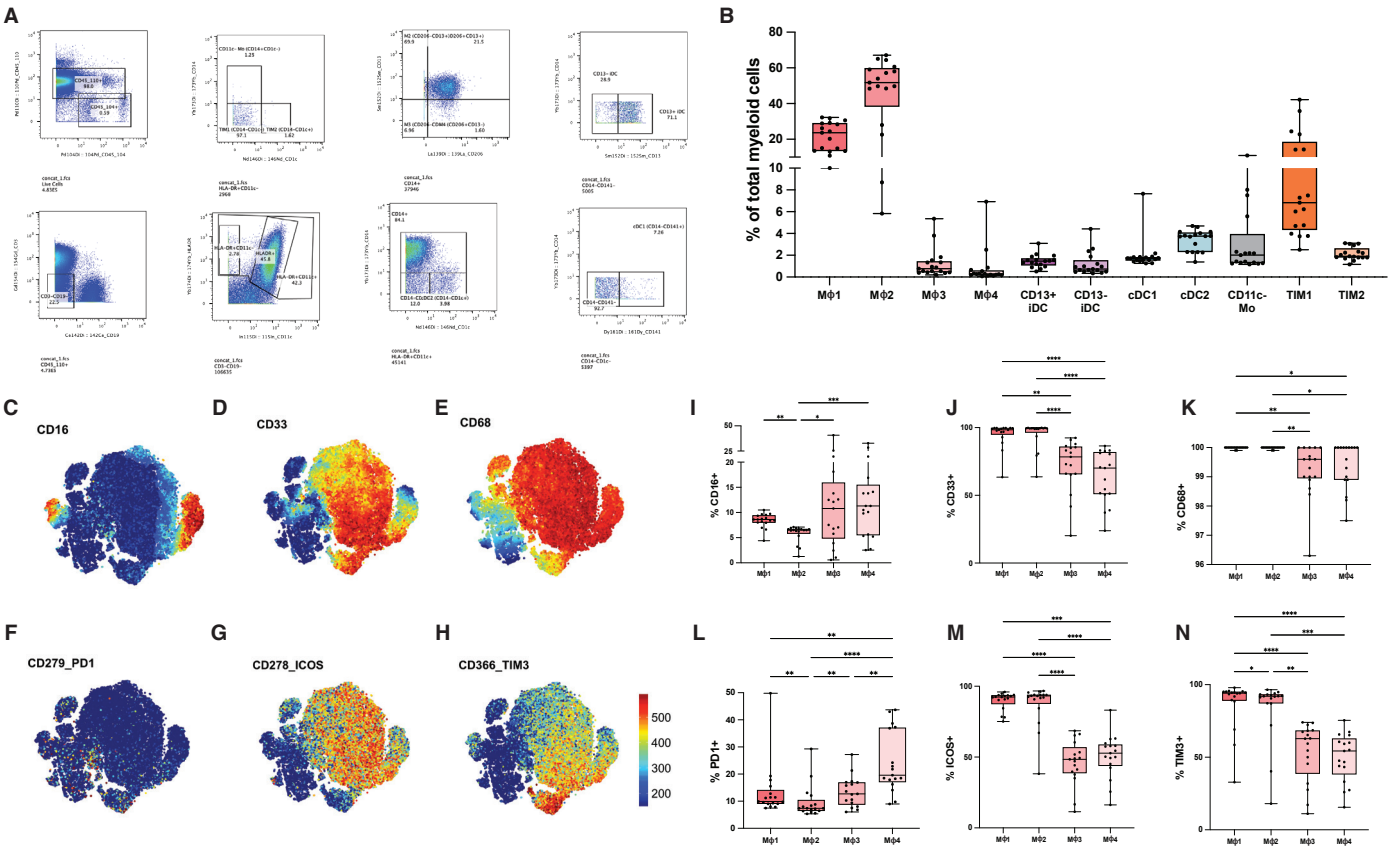

Figure 3.3 Myeloid populations in melanoma identified using CyTOF (A) Representative gating strategy for the identification of myeloid subsets identified in Figure 3.2 replicated in CyTOF data. Plots exported from FlowJo (FlowJo LLC, BD) **(B)** Quantification of myeloid cell populations as a proportion of HLA-DR+ cells (n=20). tSNE map of **(C)** CD16 **(D)** CD33 **(E)** CD68 **(F)** PD-1 (CD279) **(G)** ICOS (CD278) **(H)** TIM-3 on all HLA-DR+ cells (n=20). Percentage of macrophages (Mϕ1, Mϕ2, Mϕ3, Mϕ4) expressing **(I)** CD16 **(J)** CD33 **(K)** CD68 **(L)** PD-1 **(M)** ICOS and **(N)** TIM-3. Uncorrected Dunn's test for multiple comparisons performed. p<0.0332(*), p<0.0021(**), p<0.0002(***), p<0.0001(****).

Mϕ2 cells made up the highest proportion of HLA-DR+ myeloid cells in this cohort at 46.98% (±19.04), followed by Mϕ1s with an average of 21.56% (±8.04) (Figure 3.3B). TIM1 cells made up 12.41% (±11.97). Amongst DC populations, cDC2s were the largest population (3.40% ± 0.96) as seen in the discovery cohort followed by cDC1 population (2.01% ±1.47) (Figure 3.3B). We also found comparable proportions of CD11c- Mo (3.13% ± 2.97) and TIM2 cells (2.14% ±0.58) (Figure 3.3B).

As CyTOF enabled a larger panel of antibodies, we were able to use the high-dimensional dataset to further determine the heterogeneity of the 11 myeloid subsets. tNSE mapping of HLADR+ myeloid cells demonstrated that CD16, CD33, CD68 as well as checkpoint markers PD-1, PD-L1, PD-L2, ICOS and TIM-3 have varied expression across the macrophages, dendritic cells, CD11c- monocytes and TIM1 and TIM2 cells, demonstrating that these subsets were indeed heterogenous (Figure 3.3C-N). We then used these markers to determine differences between each of the 4 macrophage subsets identified in this study. Interestingly, CD68, a widely used marker for macrophages was highly expressed on all 4 subsets although some Mϕ3 and Mϕ4 cells had lower expression (Figure 3.3E, K). Expression of CD33, ICOS and TIM-3 showed a similar pattern between Mϕ1 and Mϕ2 but different levels in Mϕ3 and Mϕ4 while the latter two shared similar expression pattern (Figure 3.3D, G-H, J, M-N). Importantly, PD-1 had a significantly different level of expression between all four macrophage populations, with the highest expression recorded on Mϕ4s (mean % values; Mϕ1 = 13.48 ± 9.96, Mϕ2 = 9.72 ± 6.11, Mϕ3 = 13.49 ± 5.60, Mϕ4 = 24.14 ± 11.32) (Figure 3.3F, L).

Myeloid cells expressing PD-L2 in metastatic melanoma tumours are associated with response to immune checkpoint blockade therapy

Myeloid cell populations, particularly macrophages have been associated with response to immune checkpoint inhibitors (ICIs) (Lee et al., 2023, Xiao et al., 2023). We therefore wanted to determine whether any of the 11 myeloid populations identified in this study could be associated with response to ICI. The validation cohort used in this study also consisted of patients who went on to receive either PD-1 monotherapy (n=13) or PD-1 + CTLA-4 combination therapy (n=5). These patients were then grouped into responders and non-responders according to RECIST criteria (Seymour et al., 2017, Schwartz et al., 2016).

All 11 myeloid cell populations were identified in all patients irrespective of response, however, as expected, their numbers were low (Figure 3.4A). Interestingly, patients who subsequently responded to PD-1 monotherapy had significantly less Mϕ2 and significantly more TIM1 cells when compared to those who did not respond (Figure 3.4A, p=<0.0001, Uncorrected Fisher's LSD test). There were no significant differences seen in the remaining 9 myeloid populations (Figure 3.4A). To determine whether the expression patterns of key immune checkpoints differed between responders and non-responders we next examined for PD-1, PDL-1, PDL-2 (Figure 3.4B-G) on the two myeloid cell populations that were present in different numbers in ICI responders. This showed that the proportion of TIM1 cells expressing PD-L2 was significantly higher in the tumours of responders when compared to non-responders (p=0.0349, Mann-Whitney test) (Figure 3.4G). There were no differences in the expression of PD-1 or PD-L1 on these cells (Figure 3.4E, F). We also found no significant differences in the expression of PD-1, PD-L1 and PD-L2 on Mϕ2 populations between responders and non-responders (Figure 3.4B-D). Together, these data demonstrate a potential role for PD-L2+ TIM1 cells in response to anti-PD-1 therapy.

VISTA expression is restricted to subsets of immune cells and correlates with the expression of HIF-1α

Developing alternative targets for immune checkpoint blockade therapies is critical. VISTA is a checkpoint receptor that has an important regulatory role in both lymphocytes and myeloid cells. As such, it is the target of 4 clinical trials in solid tumours, yet the expression of VISTA and its binding partners are not fully understood. Using multi-parameter flow cytometry, we found amongst lymphocytes, a subset of cells expressed VISTA with highest expression on B cells (32.8% ± 36.6), followed by CD4 T cells (15.1% ± 41.5) (Figure 3.5A). Within the effector CD4+ T cell populations, $T_H17.1$s had the greatest proportional VISTA expression of quantified CD4 T cell subsets (69% ± 32.1), followed by T_H2s (56.8% ± 35.2) and T_H17s (53.72% ± 33.8). Interestingly, T_H1 cells, were found to express the least (22.9% ± 31.7) (Figure 3.5B). In comparison, amongst the CD8+ T cell subsets, 9.7% (±16.7) of CD69+CD103+ CD8 T cells expressed VISTA, followed by 13.8% (±17.1) of CD69+CD103- CD8 T cells and 19.7% (± 28) of the remaining (CD69-CD103-) CD8 T cells (Figure 3.5C). VISTA expression was also highly variable across myeloid cell populations with the highest on Mϕ1 cells (42.8% ± 22.7), followed by Mϕ3s (34.1% ± 22.9) Mϕ2s

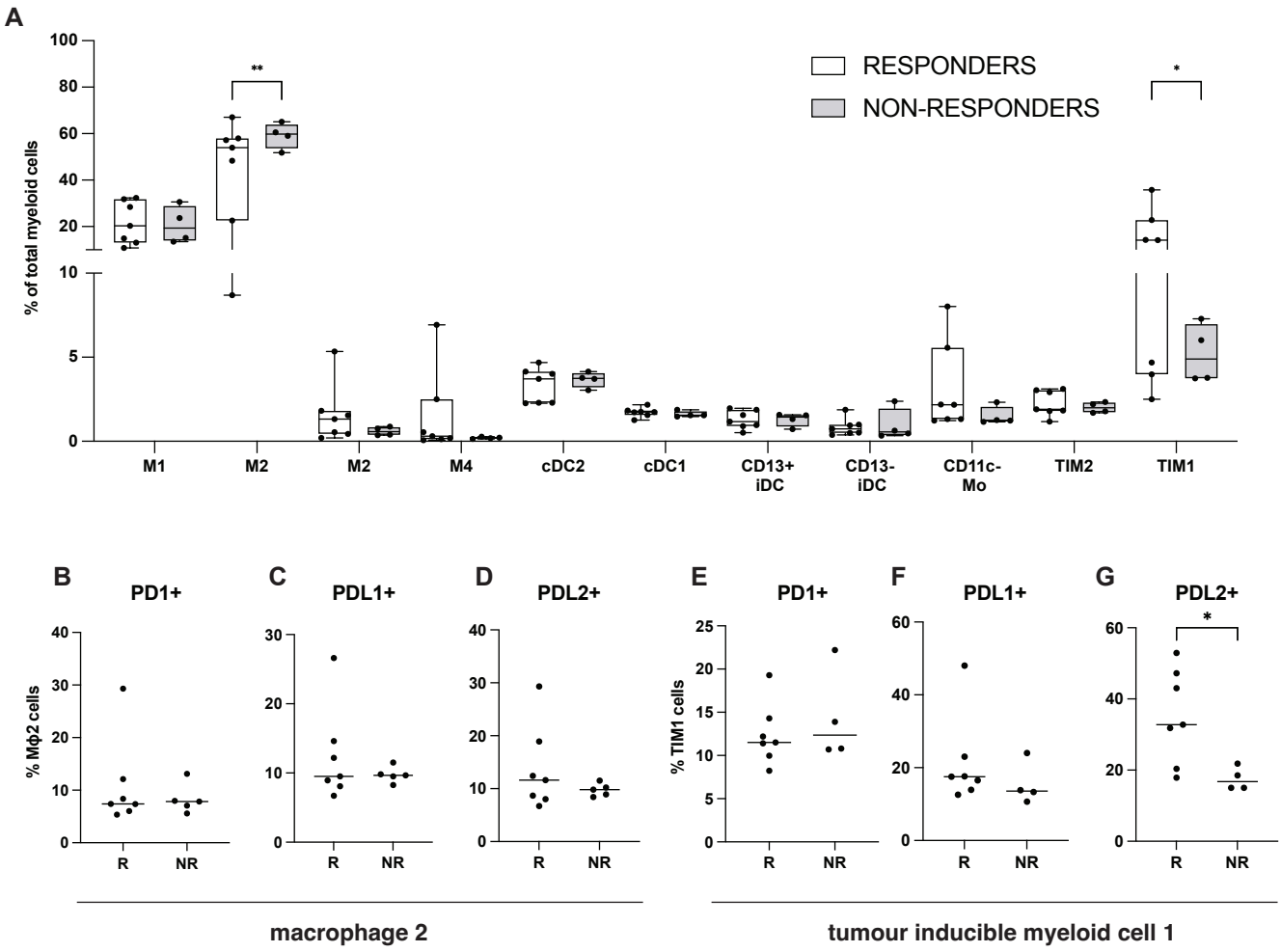

Figure 3.4 PD-L2+ myeloid cells are high in tumours of PD-1-responders (A) Proportions of myeloid populations identified in Figure 3.3 compared between PD-1 immunotherapy responders (n=7) and non-responders (n=4). Fishers LSD test performed to determine statistical differences. p<0.0332(*), p<0.0021(**), p<0.0002(***), p<0.0001(****). Percentage of **(B)** PD-1+ **(C)** PD-L1+ and **(D)** PD-L2+ MΦ2 (CD13+CD206-) cells and **(E)** PD-1+ **(F)** PD-L1+ and **(G)** PD-L2+ TIM1 (HLADR+CD11c-CD14-CD1c-) cells compared between PD-1 monotherapy responders (R, n=7) and non-responders (NR, n=4). Mann-Whitney test performed to compare ranks. p<0.0332(*), p<0.0021(**), p<0.0002(***), p<0.0001(****).

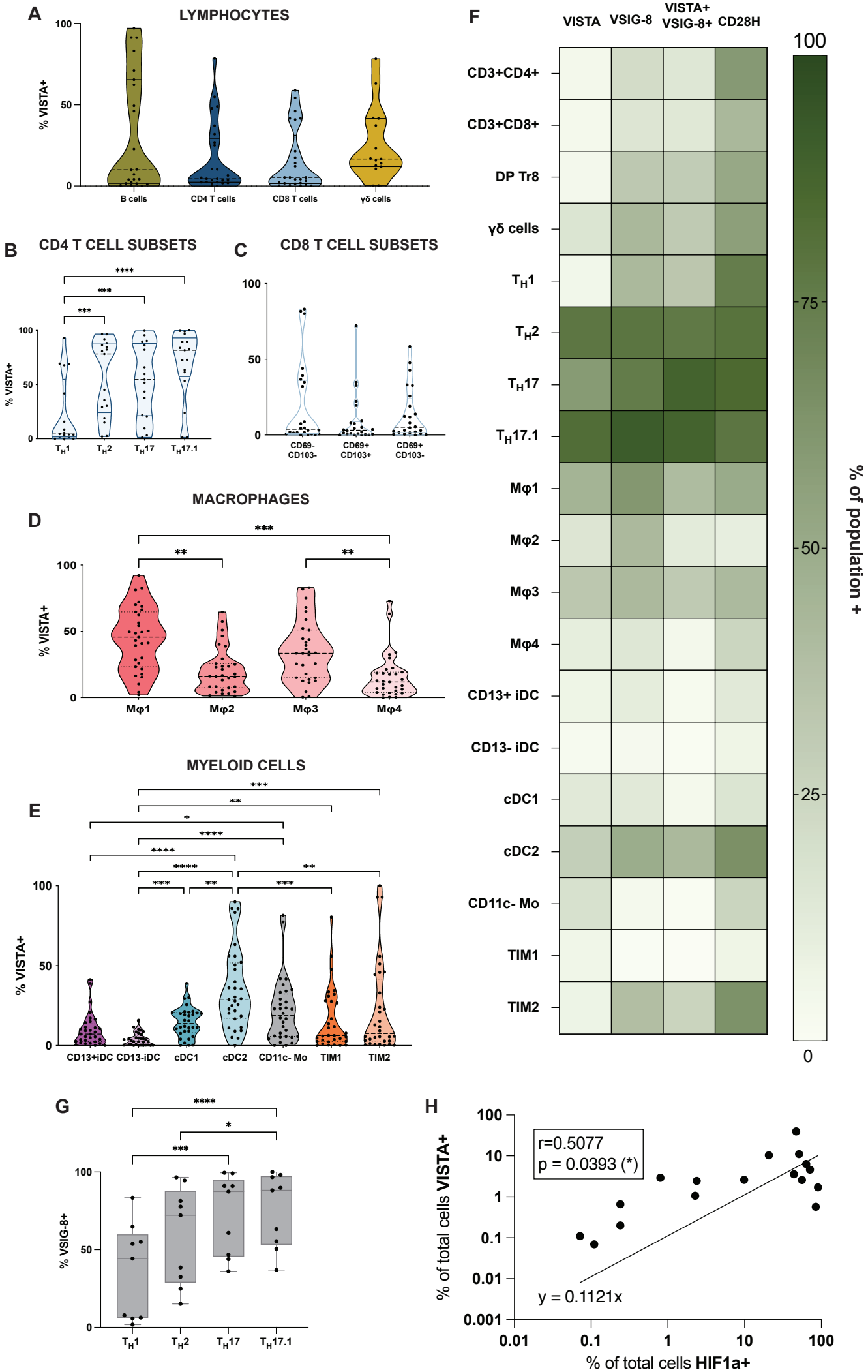
A
LYMPHOCYTES
% VISTA+
B cells
CD4 T cells
CD8 T cells
γδ cells
B
CD4 T CELL SUBSETS
C
CD8 T CELL SUBSETS
CD69- CD103-
CD69+ CD103+
CD69+ CD103-
D
MACROPHAGES
Mφ1
Mφ2
Mφ3
Mφ4
E
MYELOID CELLS
CD13+iDC
CD13-iDC
cDC1
cDC2
CD11c- Mo
TIM1
TIM2
F
VISTA
VSIG-8
VISTA+ VSIG-8+
CD28H
CD3+CD4+
CD3+CD8+
DP Tr8
γδ cells
CD13+ iDC
CD13- iDC
cDC1
cDC2
CD11c- Mo
TIM1
TIM2
% of population +
G
% VSIG-8+
H
r=0.5077
p = 0.0393 (*)
y = 0.1121x
% of total cells VISTA+
% of total cells HIF1a+

Figure 3.5 Mapping the VISTA expression of immune infiltrates in treatment-naïve metastatic Melanoma tumours. Percentage of **(A)** B cells (n=17), CD4 T cells (n=29), CD8 T cells (n=29) and γδ T cells (n=17) **(B)** T_H1, T_H2, T_H17 and $T_H17.1$ cells (n=21) **(C)** CD69-CD103- CD8 T cells, CD69+CD103+ CD8 T cells, CD69+CD103- CD8 T cells (n=29) **(D)** macrophages (n=12) and **(E)** Dendritic Cell and Monocytes (n=12) that express VISTA as determined by flow cytometry. **(F)** Heat-map displaying normalised mean percentage of VISTA (n=24), VISTA-binding partner VSIG-8 (n=12) and B7-family member CD28-H (n=12) on cells phenotypes displayed on y axis. **(G)** Percentage of T_H1, T_H2, T_H17 and $T_H17.1$ cells expressing VSIG-8 (n=21).Uncorrected Dunn's test for multiple comparisons performed. $p<0.0332$(*), $p<0.0021$(**), $p<0.0002$(***), $p<0.0001$(****). **(H)** Non-parametric spearman correlation with simple linear regression of percentage of VISTA+ cells and percentage of HIF1α+ cells in melanoma patients, spearman R value = 0.5007, exact two-tailed p value = 0.0393 Line calculated using simple linear regression (n=17).

(19.1% ±17.1) and Mϕ4s (13.9% ± 13.3) (Figure 3.5D). VISTA expression was low on DCs with the exception of cDC2s (32.1% ± 22.4) (Figure 3.5E).

In order to better understand the role of VISTA expression within tumours, we next wanted to determine the expression pattern of its ligands VSIG-8 and CD28-H (also known as TMIGD2 and IGPR-1) (Molloy, 2016) (Rahimi et al., 2012). Mirroring the expression pattern of VISTA, we found $T_H17.1$ cells had the highest proportion of VSIG-8 expressing cells within the CD4 T cell compartment (75.5%±24), followed closely by T_H17 cells (72.9% ± 25.7), T_H2 cells (59.2% ±31.4) and $T_H1$cells (35.9% ±30.8) (Figure 3.5F, G). A similar pattern was observed for the expression of CD28-H (Figure 3.5F). We next wanted to understand why VISTA expression was highly heterogenous within the tumours, we examined the expression of VISTA regulator HIF-1α (Deng et al., 2019). We found the total percentage of VISTA+ cells correlated with the percentage of total HIF1α expressing cells ($p=0.0393$, $r=0.5077$), suggesting that VISTA expression could be associated with hypoxic conditions (Yuan et al., 2021, Deng et al., 2019) (Figure 3.5H). Finally, to determine whether VISTA expression was associated with the location within tumours, we performed mIHC on FFPE metastatic melanoma tumour tissue. This showed that VISTA was equally expressed within and outside of tumour regions (supplementary figure 3.3). Together here we demonstrate how detailed immune phenotyping can be used to map the expression of immune checkpoint receptors.

3.4 Discussion

Despite the increasing evidence showing critical roles for myeloid cells in tumour development and control, they remain poorly characterized in many solid tumours. A major challenge is the heterogeneity of these cells within tumours. Recent studies using single cell transcriptomic approaches are slowly unravelling the complex heterogeneity of these cells, however, challenges remain in cross-validating cell populations using genotype/phenotype data across different studies. Here, we used the traditional flow cytometry approach and identified 11 myeloid populations, which includes 4 DC subsets and 4 macrophage populations. We detected these 11 populations in all 30 patients examined at varying proportions. Importantly, we used a different approach, mass cytometry, on a different cohort of patients to validate these findings and found all 11 cell populations consistently across different cohorts. We also applied this strategy to identify a population of myeloid cells we call tumour-induced myeloid (TIM) cells

(CD45+HLA-DR+CD14-CD1c+) that were significantly higher in patients who responded to anti-PD-1 treatment. Interestingly, these cells also expressed a much higher proportion of PD-L2 in responders to ICI therapy when compared to non-responders.

Dendritic cells play a pivotal role in anti-tumour immunity from recruitment of T cells to antigen presentation and activation of tumour-specific responses (Cabeza-Cabrerizo et al., 2021). Two major cell subsets have been identified in human tumours, namely conventional DC type 1 and type 2 (cDC1 and cDC2). While both conventional DC subsets have been implicated in tumour control, cDC1 are critical for cross-presentation and activation of tumour specific cytotoxic T cell responses (Saito et al., 2022). By contrast, cDC2 have been mainly implicated in the activation of helper T cells and their differentiation into Th1 cells (Hatscher et al., 2021, Leal Rojas et al., 2017). Therefore, both cDC1 and cDC2 are likely to play a critical role in tumour control. Our data shows there are higher proportions of cDC2 when compared to cDC1 in metastatic melanoma. We also find Th1 CD4 T cells to be a dominant lymphocyte population within these tumours, further supporting the potential role of cDC2 population. Recent studies however have found heterogeneity in cDC2 populations as well, further dividing them into DC2 and DC3 subsets (Villani et al., 2017). We also found increased levels of DPP4 (CD26) on cDC1 population within metastatic melanomas, which might impede their ability to recruit T cells. DPP4 cleaves and inactivates CXCL-9, CXCL-10 and CXCL-11, three chemokines involved in the recruitment of T cells to sites of inflammation through their receptor CXCR3 (Zuo et al., 2023, Tian et al., 2023)

While DC phenotypes have remained reasonably consistent across many tumour types, defining macrophage cell phenotypes has been challenging. Over-simplification of the diversity of these cells led to two commonly used subsets, namely M1 and M2. However, there is enough evidence showing that this sub-setting strategy is inaccurate and does not reflect the continuum of differentiation states of macrophages found within human tumours. Here we defined macrophages based on the expression of CD13 and CD206, and this led to identification of at least 4 different subsets, which we have named Mϕ1 – Mϕ4 subsets. One group that sought to develop a panel to define human macrophages appropriately included CD13 and CD206 within their panel as they also found these markers differentiated macrophage populations in response to different stimuli (Liu et al., 2022a). While the differences between the 4 cell subsets identified in this study were purely based on their

phenotypes and our data does not support any functional differences, we were able to consistently identify these cell populations across all patients from two different cohorts. Importantly, our data also shows a high degree of heterogeneity in all four macrophage subsets. When we examined data from CyTOF, clear and varying expression levels of CD16, PD-1, ICOS and TIM-3 were noted, which supports the heterogeneity of these populations.

In addition to these known myeloid cell populations, we also identified two myeloid populations that we have termed tumour-induced myeloid cells 1 and 2 (TIM1 and TIM2). One of the key features that differentiated these cells from DCs is the lack of CD11c expression, which is associated with conventional DCs (See et al., 2017). Both of these cell populations also lacked the expression of CD14, a marker associated with monocyte-derived macrophages. Together TIM1 and TIM2 populations were identified in all patients from both discovery and validation cohorts and made up of 10-40% of all HLA-DR+ myeloid cells within tumours, suggesting that they occupy a reasonable proportion of myeloid cells within metastatic melanoma. These two cell populations also expressed high levels of PD-L1 and IDO.

We also explored the potential role of the 11 myeloid cell populations by determining the association between their numbers and response to checkpoint blockade immunotherapy. Linking cell populations to clinical outcomes is one potential way of determining their contribution to tumour control. We found Mϕ2 population to be significantly higher on pre-treatment biopsies of non-responders when compared to responders, suggesting that these cells could be involved in regulation rather than anti-tumour immune activities. Future studies are required to identify their exact role. Phenotypically, these Mϕ2 cells express very little PD-1, PD-L1 and PD-L2. However, these cells expressed high levels of CD33, TIM-3, CD68 and ICOS. By contrast, responders had significantly higher proportions of TIM1 cells and the expression levels of PD-L2 on these cells was also significantly higher in responders. This suggests that the TIM1 cell population is likely to contribute towards tumour control in metastatic melanoma. Further functional studies are required to determine their exact role TIM1 cells play within the tumour. It is important to note that the validation cohort used was a different group of treatment naïve patient samples which impacts results interpretation and methodological validation in regard to cohort differences.

We then wanted to profile immune checkpoint markers established to be well expressed across the myeloid compartment. We saw that VISTA was expressed across T cells, B cells, myeloid cells and DCs. This was in line with current literature that reports VISTA expression is highest on myeloid cells and macrophages, and engagement of VISTA-expressing cells with cells expressing VISTA ligands leads to a suppressive immune environment (Broughton et al., 2019, Li et al., 2024). Although T_H2, T_H17 and $T_H17.1$ cells made up a small proportion of total cells, VISTA was also expressed on more than half of the cells quantified in these cell populations. T_H2, T_H17 and $T_H17.1$ cells have been associated with tumour progression in melanoma, as well as tumour control (Aspord et al., 2013, Zennadi et al., 2001, Nevala et al., 2009, McCarter et al., 2005, Chen and Gao, 2019, Lomax et al., 2017, Pan et al., 2023).

Despite some evidence for VISTA expression as a good prognostic factor in tumours, there is also a body evidence to suggest that VISTA on macrophages plays a suppressive/pro-tumour role (Lin et al., 2024b, Rannikko and Hollmén, 2024, Noelle et al., 2023). It is evident that metabolic changes in the tumour can also drive tumour progression. Hypoxia, or reduced cellular oxygen availability, is a known condition of tumour microenvironments as tumour cells consume oxygen at an increased rate, thus depriving resident immune cells of oxygen which results in altered cellular function and exhaustion (Hu et al., 2022). Our data found that the proportion of VISTA+ cells correlated with HIF1α expression across 17 patients. This was unsurprising as VISTA expression and hypoxia are tightly linked. HIF1α binds to the VISTA promotor directly and upregulates VISTA expression on myeloid cells in murine models (Deng et al., 2019). It is also known that VISTA engages with PSGL-1, one of the known ligands of VISTA, at an acidic pH due to high histidine content. This means that VISTA is much more biologically active in acidic conditions such as those induced by hypoxia, often found within TME (Johnston et al., 2019). Further to this, one group developed an anti-VISTA mAb that targeted the histidine-rich epitope of VISTA, and this was able to successfully restore T cell responsiveness (Johnston et al., 2019). It is also clear that hypoxia drives resistance to immunotherapy (Kopecka et al., 2021). Together, these data demonstrate that there are multiple pathways that regulate VISTA expression in the TME. Understanding what immune cell populations express VISTA and what this suggests about the function of VISTA, will allow us to harness the potential of anti-VISTA therapy.

One of the major limitations of experimental approaches that rely on single cell tissue dissociates is the potential loss of cells during the tissue dissociation process (Steinert et al., 2015). It has become evident that particularly some myeloid cells are susceptible during tissue dissociation processing and therefore could be underrepresented in the data. With spatial biology platforms becoming more reliable, future studies will need to explore these cell populations further using intact tissues.

A

Sex	n	% cohort
F	13	42%
M	18	58%

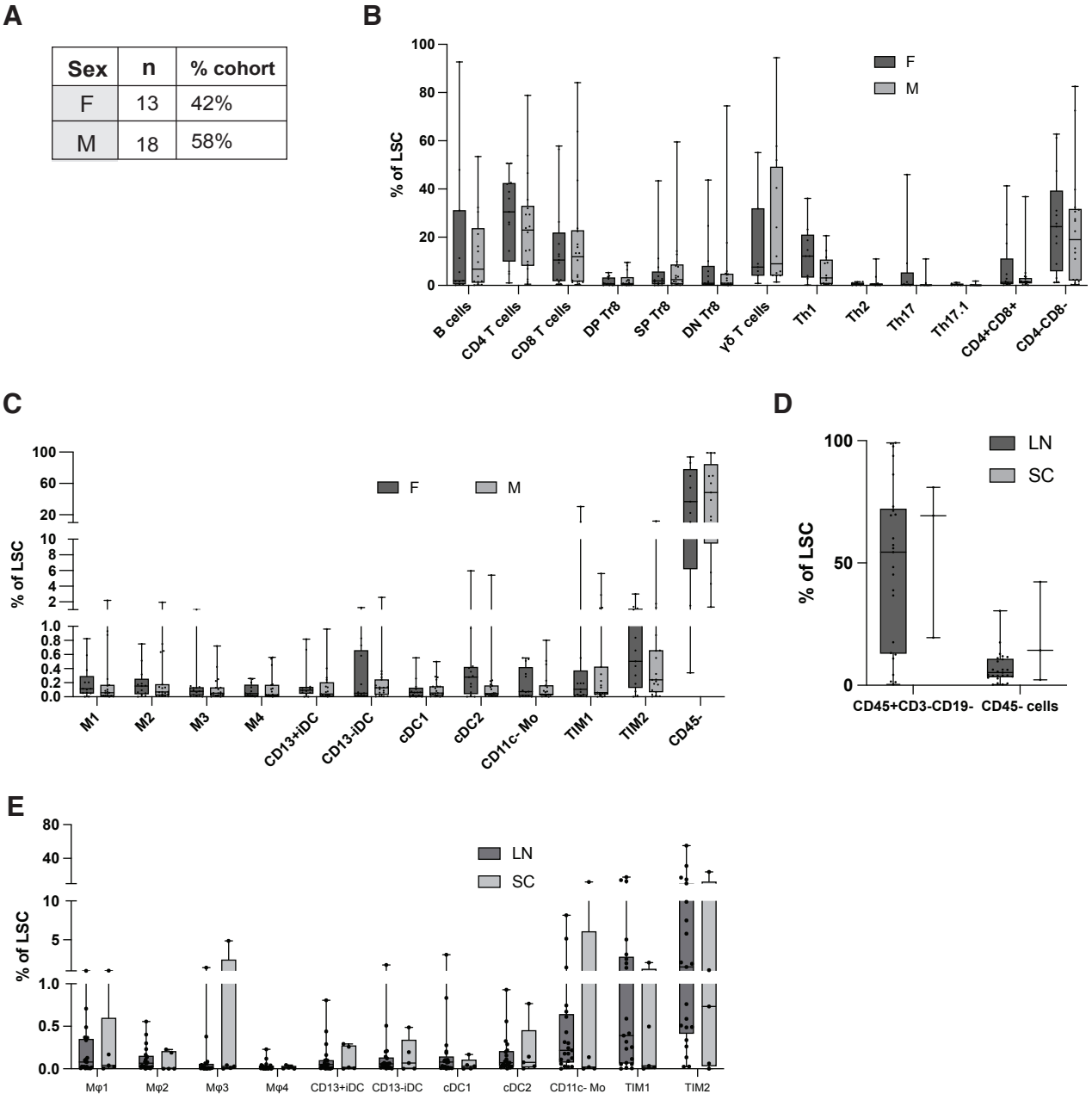

Supplementary Figure 3.1 Proportions of immune cells do not differ between male and female patients or between tumour location. (A) Table detailing cohort spread of M and F patients. Proportions of **(B)** lymphocytes and **(C)** myeloid cells in patients grouped by sex. Proportions of **(D)** innate cells and CD45- cells and **(E)** macrophages (Mϕ1, Mϕ2, Mϕ3, Mϕ4), Dendritic cells (iDC separated by CD13 expression, cDC1 & cDC2) monocytes (CD11c- Monocyte) and myeloid cells (TIM1, TIM2) compared between tumour location, lymph node associated (n=19, grey) or subcutaneous (n=5, white). Fisher's LSD test performed to determine statistical significance, $p < 0.01$ included in graph

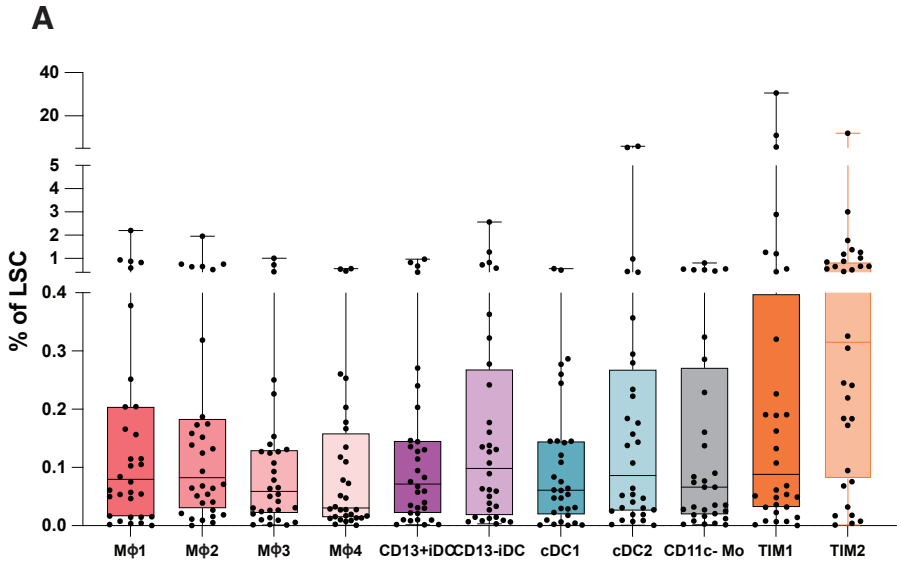

B

	PHENOTYPE
M1	CD11c+ CD14+ CD206+ CD13+
M2	CD11c+CD14+ CD206-CD13+
M3	CD11c+CD14+ CD206+CD13-
M4	CD11c+CD14+ CD206-CD13-
CD13+ iDC	CD11c+CD14-CD1c- CD141-CD13+
CD13- iDC	CD11c+CD14-CD1c- CD141-CD13-
cDC1	CD11c+CD14- CD1c-CD141+
cDC2	CD11c+CD14-CD1c+
CD11c- Monocyte	CD11c-CD14+CD1c-
TIM1	CD11c-CD14-CD1c+
TIM2	CD11c-CD14-CD1c-

Supplementary Figure 3.2 Metastatic melanoma tissue contains phenotypically diverse and distinct myeloid cell subsets with varying expression of immune checkpoint and modulatory markers. (A) Macrophages (Mϕ1, Mϕ2, Mϕ3, Mϕ4), Dendritic cells (iDC separated by CD13 expression, cDC1 & cDC2) monocytes (CD11c- Monocyte) and myeloid cells (TIM1, TIM2) represented as a proportion of live single cells (LSC) from 22 metastatic melanoma solid tumour process and analysed using flow cytometry. Statistical significance determined by non-parametric Friedman test with multiple comparisons $p < 0.01$ included in graph. **(B)** Markers used to define cell phenotypes in (A).

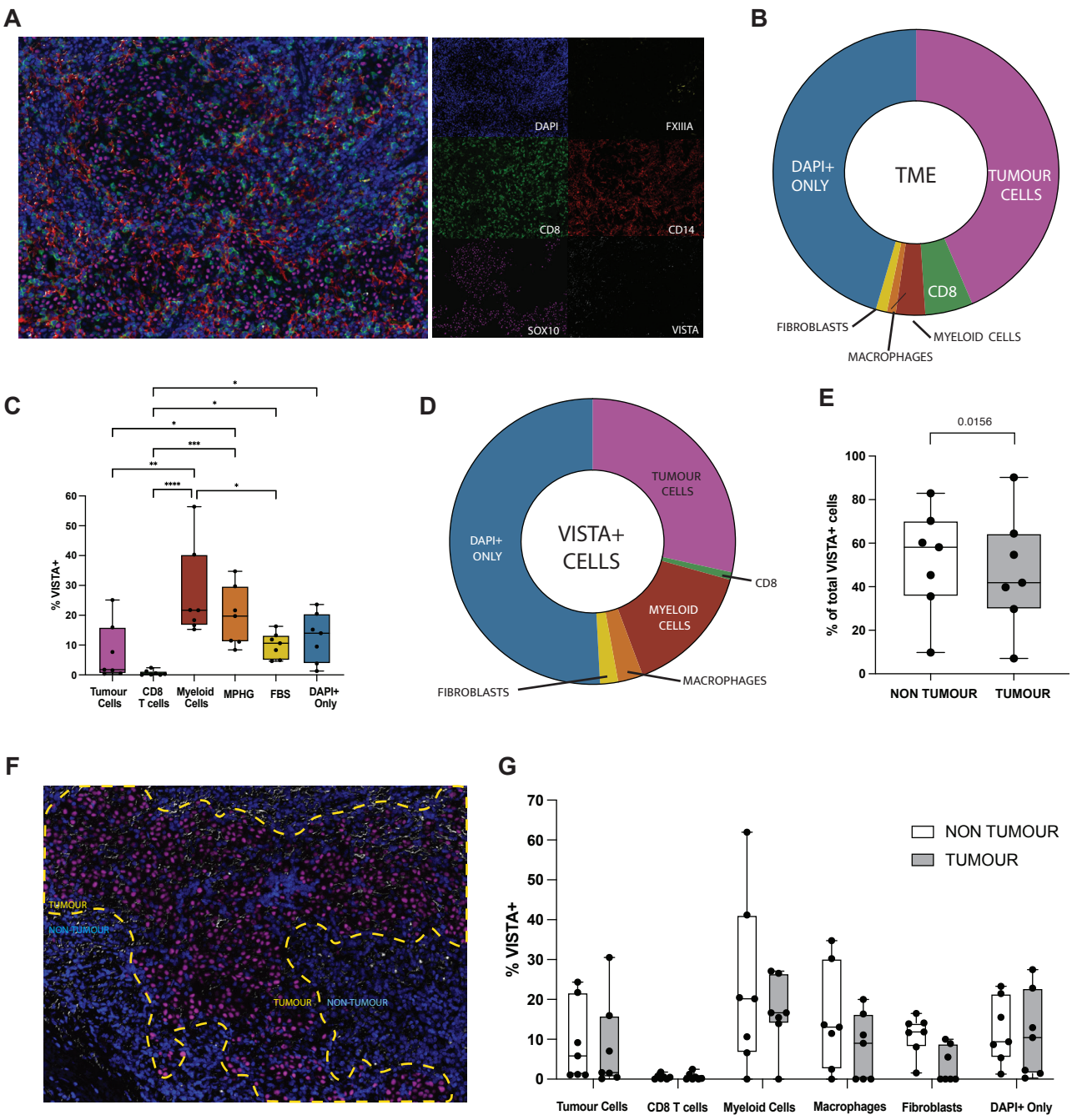

Supplementary Figure 3.3 VISTA in tumour tissue is primarily expressed on immune cells. **(A)** Representative staining of mIHC of metastatic melanoma with single colour images of VISTA (white), FXIIIA (yellow), CD8 (green), CD14 (red) and SOX10 (magenta) and counterstained with DAPI (blue). **(B)** Tumour Cells (SOX10+), CD8+ T cells (CD8+SOX10-), macrophages (CD14+FXIIIA+), myeloid cells (CD14+FXIIIA-) and fibroblasts (FXIIIA+CD14-) were identified and quantified as a proportion of nucleated cells (n=7). Cells present were also defined as VISTA+/- and **(C)** average proportions of VISTA+ cells were identified in metatstatic melanoma. Uncorrected Dunn's test performed to determine statistical significance (n=7). **(D)** Mean percentage of myeloid cells, macrophages, fibroblasts, tumour cells, CD8+ T cells and undefined cells (DAPI+SOX10-CD8-FXIIIA-CD14-) that were VISTA+ in metastatic melanoma tumour tissue. **(E)** VISTA+ cells present in tumour regions (defined by SOX10+) and non-tumour regions (SOX-10-), Mann-Whitney tests performed to determine statistical significance. p=0.0156 (n=7) **(F)** representative image of VISTA+ cells and identification of tumour and non-tumour regions. Dotted line represents border of 'tumour' (SOX10+ staining) and 'non-tumour'. **(G)** VISTA+ proportions of myeloid cells, macrophages, fibroblasts, tumour cells and CD8+ T cells present in tumour (T) and non-tumour (NT) regions. Uncorrected Fishers LSD performed to determine differences in proportions between tumour and non-tumour regions (n=7).

4 Mapping the cellular landscape of metastatic melanoma tumours

4.1 Introduction

Understanding the immune landscape of metastatic melanoma is a field that has been developing for many years. However, acquiring good quality human tissue with enough replicates is a major hurdle. Additionally, in an era of systemic therapy, there are very few chances to fully map the immune landscape of tumour samples from untreated metastatic melanoma patients. We were given an opportunity in collaboration with Professor Angela Hong to conduct a high-parameter analysis on tumours from human melanoma patients enrolled in clinical trial ANZMTG 01.02/TROG 02.01/NCT00287196. Due to these patients being enrolled in a clinical trial, we can use the extensive clinical information collected from the trial to assist our analysis. Additionally, as these patients were recruited between 2003 and 2007 when there was no use of any systemic therapies, this remains a 'clean' cohort, difficult to obtain in other ways. This is therefore an excellent cohort to profile pre-treatment predictors of patient response. The data obtained in this investigation may also be applicable to clinical melanoma treatment strategies.

To make the most of these invaluable samples, we sought to map extensively the tumour microenvironment in metastatic melanoma using high-parameter approaches. The ability to visualise the content of tumours and map the cellular interactions is critical for understanding the role of TME. Achieving this depends on technologies that provide ultra high-plex tissue imaging. There are multiple platforms using different technologies to achieve this. However, only some of these platforms enable the use of formalin-fixed paraffin embedded (FFPE) tissues. Due to fixation, the ability to use monoclonal antibodies to identify cellular markers is often compromised. Our group, in particular Dr Angela Ferguson, has optimised over 40 antibodies for use in Imaging Mass Cytometry (IMC). A typical data set generated from these platforms are high-dimensional in nature and require a complex analysis process. Starting off with cell segmentation, a fundamental step that is used to define cell boundaries all the way to mapping individual cellar interactions are key part of such analysis. Therefore, various methodologies could be used to develop the analytical pipeline for such high-dimensional datasets.

In this chapter, we explore different methodologies for analysing data generated from Imaging Mass Cytometry. IMC uses metal conjugated antibodies to detect cellular markers. In the

second part of this chapter, we apply this approach to interrogate the role of immune and non-immune cells in the TME. We performed IMC on a TMA comprising cores from lymph node metastases from 100 treatment-naïve melanoma patients. These cores were selected from high-tumour regions by a clinical pathologist. These samples were used to profile the immune microenvironment as the diversity and plasticity of melanoma cells is well known and there is an increasing need to be able to understand and categorise these cell states (Cheng et al., 2024). Using clinical outcomes as a measure of favourable/unfavourable outcomes, we determine which cellular contents were associated with such outcomes.

4.2 Materials and Methods

4.2.1 Imaging Mass Cytometry

Imaging Mass Cytometry (IMC) was performed as detailed in section 2.4.

4.3 Results

4.3.1 Clinical Cohort

260 patients were recruited across Australia, New Zealand, the Netherlands and Brazil to the phase 3 randomised controlled trial for adjuvant lymph-node field radiotherapy versus observation only in patients with melanoma at high risk of further lymph-node field relapse after lymphadenectomy between March 20th 2002 and September 21st 2007 [ANZMTG 01.02/TROG 02.01] (Henderson et al., 2015, Burmeister et al., 2012). Following lymphadenectomy, patients were randomised to receive either adjuvant stereotactic radiotherapy (48Gy in 20 fractions within 12 weeks of surgery), or observation. Participants, including those giving treatment, were not blinded to treatment allocation. Patients were assessed every 3 months from randomisation for 2 years, and subsequently followed up every 6 months until 5 years from randomisation, then yearly with final follow-up date November 2011. The primary endpoint was lymph-node field relapse (as a first relapse) and 18% of patients in the radiotherapy-treated group relapsed within 5 years, compared to 33% within the control group (no radiotherapy given, observation only) (Henderson et al., 2015). Secondary endpoints were overall survival and relapse-free survival, and the trial reported 5-year survival as 40% in the adjuvant radiotherapy group compared to 45% in the observation only group (Henderson et al., 2015). In both the initial report and the 6-year follow up it was concluded that adjuvant radiotherapy improved local (or lymph-node field) relapse but had no impact on

survival. These studies, along with others, form the basis of current recommendations for radiotherapy treatment in patients that do not respond or are ineligible for systemic therapies.

Professor Angela Hong provided our team with tissue-microarrays containing high-tumour, peri-tumour, and tumour infiltrating lymphocyte 1mm^2 cores from 100 patients from this cohort, chosen to represent patient characteristics of the larger cohort (Table 4.1). In this study we have analysed the high-tumour tissue microarray only. This cohort was comprised of 52 patients allocated to adjuvant radiotherapy, and 48 patients to observation only (Figure 4.1). Thus, of the 53 patients that were alive at the end of follow up, 16 had relapsed, and 24 were given radiotherapy. Of the 47 patients that had died, 47 of them had relapsed, and 26 of them had been given radiotherapy.

Lymph-node field site, status of primary lesion, number of positive nodes, and extranodal spread (none, limited or extensive) was assessed in the clinical trial using multivariate analysis (Burmeister et al., 2012). Of the prognostic criteria assessed, extranodal spread was identified as the only independent risk factor for lymph-node field relapse (Hazard Ratio 0.56, 95% CI 0.32-0.98, p=0.041) (Burmeister et al., 2012). Within our cohort, we recorded 51 patients with either limited or extensive extranodal spread, and 49 patients with no extranodal spread (Figure 4.1).

4.3.2 Established alternate methods for the analysis of high-parameter imaging mass cytometry data

4.3.2.1 Method 1: Mapping the cellular landscape of tumours using supervised cell segmentation and manual phenotyping

This first study aimed at mapping the cellular landscape of tumours by taking different approaches. IMC-stained tumour samples from 100 melanoma patients were acquired using the Hyperion Imaging System (Standard Biotools) at the CPC Sydney Cytometry Facility (Figure 4.2). The author and research team were blinded to the outcomes for the duration of the analysis period to reduce risk of bias. One the preliminary analyses were completed, the author was unblinded to assess the impact of the TME on clinical outcomes which consisted of relapse (no relapse or relapse) and survival (alive or dead).

Table 4.1 Clinical trial ANZMTG 01.02/TROG 02.01/NCT00287196 patient details

		Project Cohort (n=100)		Clinical Trial Cohort (n=217)	
		Adjuvant Radiotherapy (n=52)	Observation (n=48)	Adjuvant Radiotherapy (n=109)	Observation (n=108)
Sex	**Male**	41 (79%)	35 (73%)	83 (73%)	81 (75%)
	Female	11 (21%)	13 (27%)	26 (24%)	27 (25%)
Age at Random-isation	**Median (IQR; range)**	59 (22-80)	55 (26-85)	59 (47-69)	56 (45-68)
ECOG performance status	**0**	34 (65%)	28 (58%)	77 (71%)	74 (69%)
	1	18 (35%)	20 (42%)	32 (29%)	34 (31%)
Lymph node field	**Head and neck**	14 (27%)	13 (27%)	29 (27%)	30 (28%)
	Axilla	22 (42%)	16 (33%)	45 (41%)	44 (41%)
	Groin	16 (31%)	19 (40%)	35 (32%)	34 (31%)
Node maximum diameter	**Great than 4cm**	26 (50%)	30 (63%)	64 (59%)	66 (61%)
	Less than 4 cm	26 (50%)	18 (38%)	45 (41%)	42 (39%)
Extent of Extra nodal Spread	**None**	27 (52%)	22 46%)	51 (47%)	56 (52%)
	Limited	14 (27%)	15 (31%)	36 (33%)	35 (32%)
	Extensive	11 (21%)	11 (23%)	22 (20%)	17 (16%)
Primary Site	**Head and Neck**	9 (17%)	8 (17%)	18 (17%)	20 (19%)
	Trunk	15 (29%)	8 (17%)	30 (28%)	22 (20%)
	Arm	6 (12%)	7 (15%)	15 (14%)	16 (15%)
	Leg	11 (21%)	16 (33%)	26 (24%)	25 (23%)
	Unknown	11 (21%)	9 (19%)	20 (18%)	25 (23%)
Use of Interferon	**None**	52 (100%)	48 (100%)	105 (96%)	103 (95%)
	Planned or started at random-isation	0 (0%)	0	4 (4%)	5 (5%)

IQR = Interquartile Range**, ECOG** = Eastern Cooperative Oncology Group

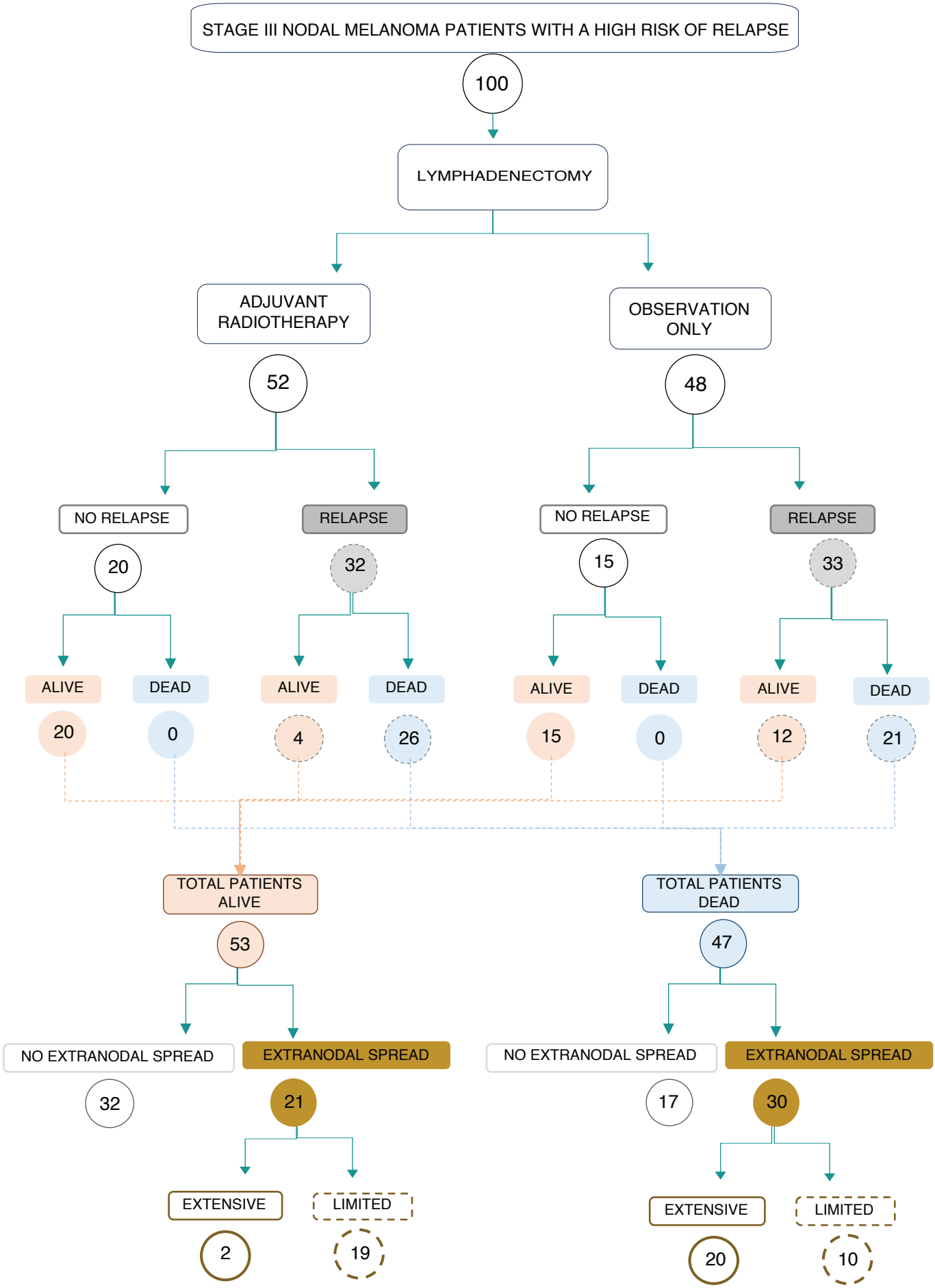
STAGE III NODAL MELANOMA PATIENTS WITH A HIGH RISK OF RELAPSE
100
LYMPHADENECTOMY
ADJUVANT RADIOTHERAPY
52
OBSERVATION ONLY
48
NO RELAPSE
20
RELAPSE
32
NO RELAPSE
15
RELAPSE
33
ALIVE
20
DEAD
0
ALIVE
4
DEAD
26
ALIVE
15
DEAD
0
ALIVE
12
DEAD
21
TOTAL PATIENTS ALIVE
53
TOTAL PATIENTS DEAD
47
NO EXTRANODAL SPREAD
32
EXTRANODAL SPREAD
21
NO EXTRANODAL SPREAD
17
EXTRANODAL SPREAD
30
EXTENSIVE
2
LIMITED
19
EXTENSIVE
20
LIMITED
10

Figure 4.1 Patient cohort flowchart from randomisation to primary outcomes. Patients were enrolled in the randomised control trial 'Adjuvant Radiotherapy versus observation alone for patients at risk of lymph node field relapse after therapeutic lymphadenectomy for melanoma' (ANZMTG 01.02/TROG 02.01/NCT00287196). From the 250 patients in this trial, 101 patient samples were included in this study. This smaller cohort was designed to represent patient characteristics of the total cohort. These stage III nodal melanoma patients were classified as having a high risk of relapse and thus after lymphadenectomy were randomly allocated to either adjuvant radiotherapy (n=52) at the nodal site or observation only (no radiotherapy) (n=49). The two primary outcomes within the trial were relapse and death, and these patients were grouped accordingly. Of the multiple patient features recorded in the trial, extranodal spread was determined to be an independent prognostic indicator of relapse. Patients either had no extranodal spread or extranodal spread (limited or extensive).

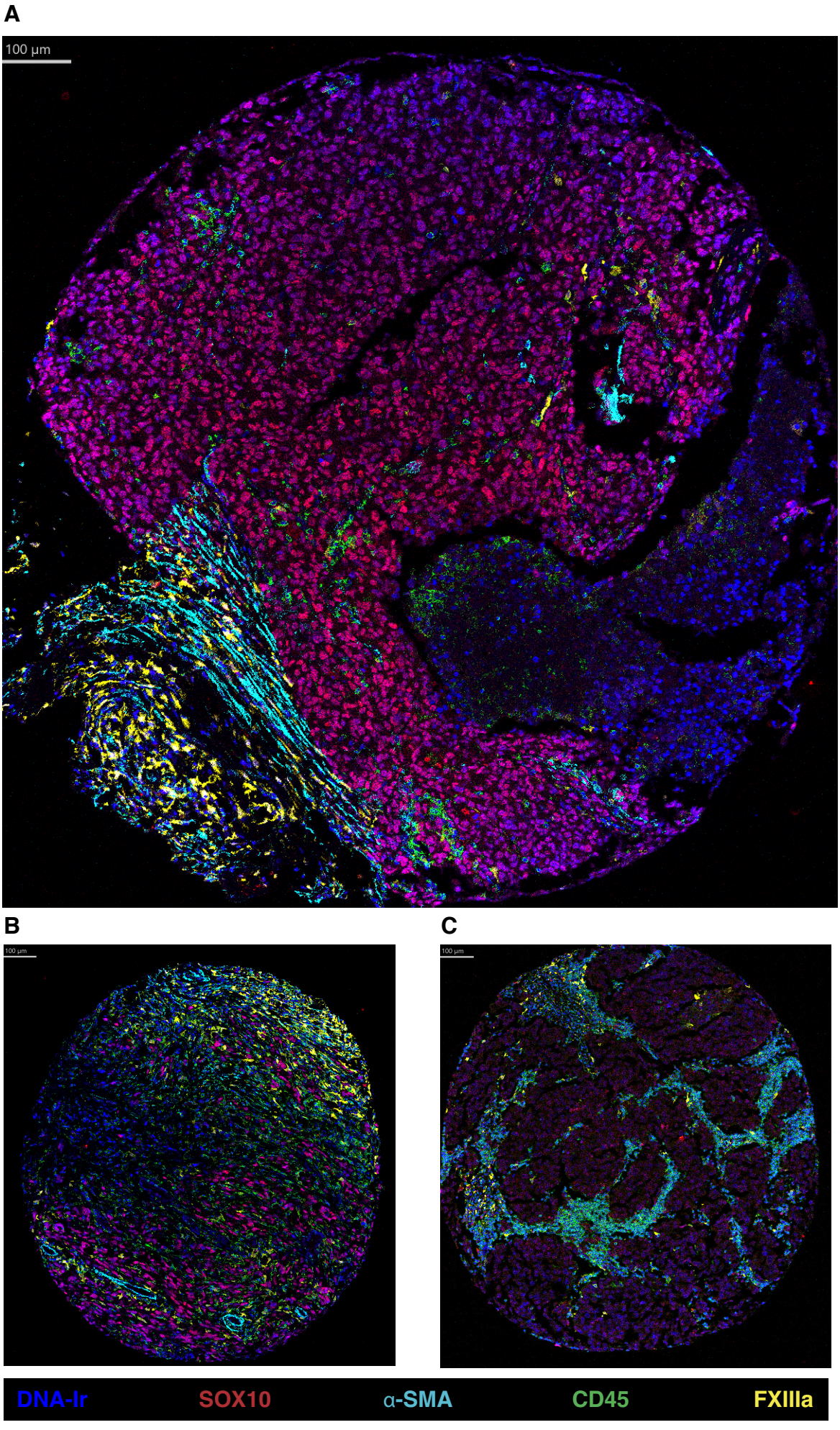
A
100 µm
B
100 µm
C
100 µm
DNA-Ir
SOX10
α-SMA
CD45
FXIIIa

Figure 4.2 Imaging Mass Cytometry staining of metastatic melanoma tumours. Imaging mass cytometry IMC was performed on pathologist-defined high-tumour regions of FFPE tumour tissue from treatment-naïve metastatic melanoma patients. IMC antibody panel detailed in Table 2.7. **(A) (B)** and **(C)** show three separate tumour cores with DNA-Ir (blue) SOX10 (red) αSMA (cyan) CD45 (green) and FXIIIa (yellow) channels overlayed for visualisation. MCD viewer used to generate images. Scale bar = 100 μm.

Cell segmentation was performed using Cell Profiler software (Stirling et al., 2021). Cells were individually identified based on nuclear markers (DNA-Ir) and cell surface markers. To quantify cell populations, objects identified as cells were exported from cell profiler and inputted into cytometry gating software FlowJo (FlowJo LLC, BD) and subsequently classified or 'gated' into cell phenotypes detailed in Figure 4.3. These populations were then calculated as percentage of total cells within sample as well as number of cells per mm^2 of tumour tissue analysed. Samples containing duplicate (n=10) or triplicate (n=2) cores on the tissue microarray were averaged for each patient.

We calculated that CD8 T cells averaged 2.86% (±4.68) of total cells, and mean density of 212 cells/mm^2 (±349.1) across the entire cohort (Figure 4.4A, B). CD4 T cells made up the largest proportion of lymphocytes, averaging 3.63% (±4.55) of all cells and recording density of 332.4 cells/mm^2 (±543.6) (Figure 4.4A). Within the helper T cell subsets, CD4 subsets T-regulatory (T_{REG}) cells and T-helper cell type-1 (T_H1) cells made up 3.05% (±3.94) and 0.34% (±0.55) of cells and 278.8 cells/mm^2 (±461.2) and 27.46 cells/mm^2 (±46.83) respectively (Figure 4.4A). B cells comprised 2.66% (±6.45) of total cells with an average density of 272.6 cells/mm^2 (±690) (Figure 4.4A).

Innate cells in melanoma were also quantified. We saw monocytes (defined as HLA-DR+CD11c+CD14+FXIIIA-) comprised 0.03% (±0.12) of cells and average 2.29 cells/mm^2 (±9.28) (Figure 4.4B). Macrophages (defined as HLA-DR+CD11c+CD14+FXIIIA+) made up 0.09% (±0.21) at a density of 5.88cells/mm^2 (±12.14) (Figure 4.4B). We found that most of these macrophages expressed CD16, and as such, CD16+ macrophages (HLA-DR+CD11c+CD14+FXIIIA+CD16+) were quantified at 0.08% (±0.22) of total cells and had a density of 5.44cells/mm^2 (±15.03) (Figure 4.4B). Neutrophils averaged 0.22% (±0.84) of cells and were present at a density of 15.24 cells/mm^2 (±73.43) (Figure 4.4B). Natural Killer (NK) cells made up 0.74% (±1.45) of all cells and mean density was 29.94 cells/mm^2 (±95.21) (Figure 4.4B).

Non-leukocytes were negative gated for tumour cell marker SOX10 and leukocyte marker CD45 expression (Figure 4.2 & Table 4.2). Fibroblasts (defined as CD31-FXIIA+) made up 5.7% (±10.6) of total cells and average density of 331.1 cells/mm^2 (±411.6) (Figure 4.4B).

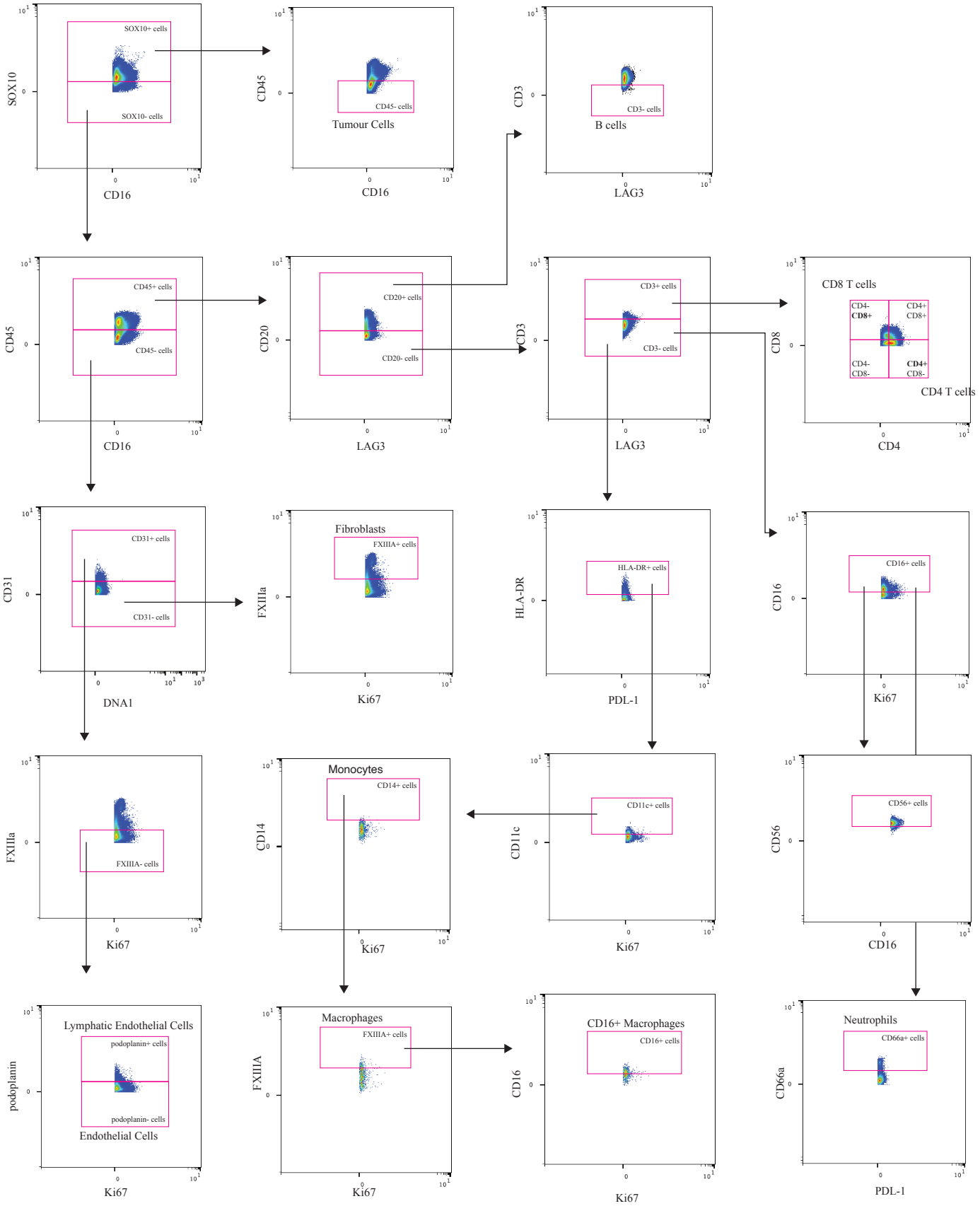

Figure 4.3 Gating strategy for identifying cells in the TME of metastatic melanoma. Representative gating strategy employing positive/negative gating for the identification of immune and tumour cells in treatment naïve metastatic melanoma. IMC images were input into Cell Profiler for cell segmentation before exported and input into FlowJo for phenotypic gating. Phenotypes are as detailed in Table 4.2. All graphs exported from FlowJo software (FlowJo LLC).

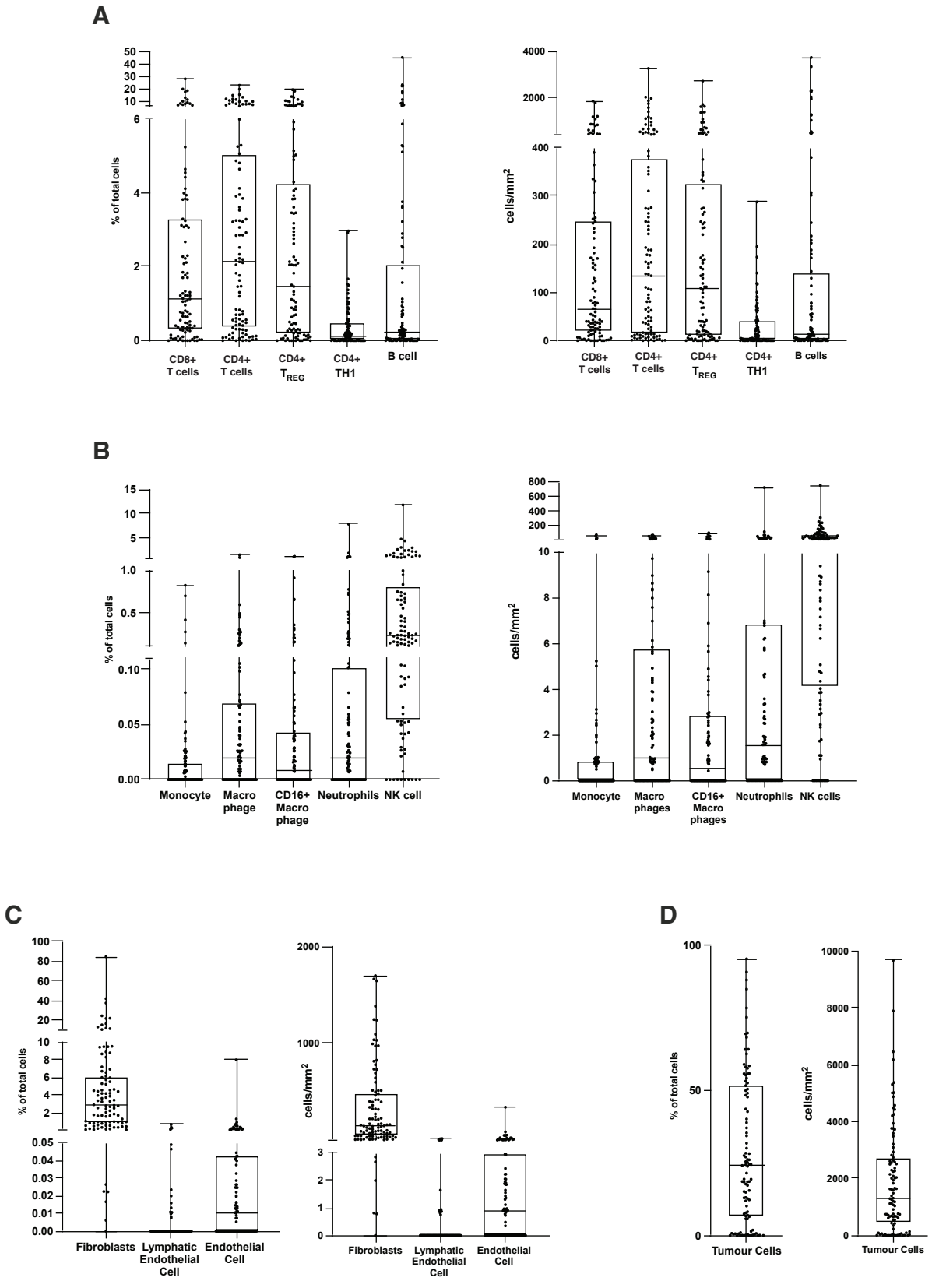

Figure 4.4 Cellular composition of metastatic melanoma tumours. IMC was used to ablate high-tumour regions of treatment naïve metastatic melanoma patients to assess immune phenotypes associated with clinical outcomes. Images produced from IMC underwent supervised cell segmentation (Cell Profiler) and manual gating (FlowJo). Proportion and densities of **(A)** CD8 T cells, CD4 T cells, TREG cells, TH1 cells and B cells **(B)** Monocytes, macrophages, CD16+ macrophages, neutrophils and NK cells **(C)** fibroblasts, lymphatic endothelial cells and endothelial cells and **(D)**tumour cells. Cell phenotypes detailed in Table 4.2. Full gating strategy including negative selection gates is detailed in Figure 4.3.

Table 4.2: Markers employed to define cell phenotypes in manual gating

Cell	**Phenotype**
CD8 T cells	SOX10-CD45+CD20-CD3+CD8+
CD103+ CD8 T cells	CD20-CD3+CD8+ CD103+
Cytotoxic CD8 T cells	CD20-CD3+CD8+Granzyme-B+
Ki67+ (proliferating) CD8 T cells	CD20-CD3+CD8+Ki67+
CD4 T cells	CD20-CD3+CD4+
FOXP3+ CD4+ T cells ($T_{REG}S$)	CD20-CD3+CD4+FOXP3+
Tbet+ CD4 T cells (T_H1s)	CD20-CD3+CD4+T-bet+
Ki67+ (proliferating) CD4 T cells	CD20-CD3+CD4+
B cells	CD3-CD20+
Ki67+ (proliferating) B cells	CD3-CD20+Ki67+
NK cells	CD20-CD3-CD16+CD56+
Neutrophils	CD20-CD3-CD16+CD66a+
Monocytes	SOX10-CD45-CD3-CD20-HLADR+CD11c+
Macrophages	SOX10-CD45-CD3-CD20+HLADR+CD11c+CD14+FXIIIA+
CD16+ macrophages	SOX10-CD45-CD3-CD20-HLADR+CD11c+CD14+ FXIIIA+CD16+
Lymphatic endothelial cells	SOX10-CD45-CD31+ FXIIIA- podoplanin+
Endothelial cells	SOX10-CD45-CD31+ FXIIIA- podoplanin-
Fibroblasts	SOX10-CD45-CD31-FXIIIA+
Tumour Cells	CD45-SOX10+
Ki67+ (proliferating) Tumour Cells	CD45-SOX10+Ki67+

Lymphatic endothelial cells (CD31+FXIIIA-podoplanin+) averaged 0.02% (±0.08) of all cells and recorded average density of 0.84 cells/mm^2 (±3.02) (Figure 4.4B). Endothelial cells/non-lymphatic endothelial cells made up 0.16% (±0.82) of total cells and 8.26 cells/mm^2 (±35.9) (Figure 4.4B). Unsurprisingly, tumour cells made up the major component of our high-tumour region samples, recording an average of 29.16% (±25.8) of all samples and density of 1886 cells/mm^2 (±1917) (Figure 4.4B).

4.3.2.2 Method 2: Using an assisted AI-platform to map the cellular landscape of tumours

To compare and validate our phenotypic analysis using cell profiler and FlowJo, we used HALO software (Highplex Fluorescence Module v3.3.2541) to segment and phenotype 19 patient samples with key cell phenotypic markers and restricted the number of tissue markers to 10 of the 42 markers available from IMC. These patients were selected before the author was unblinded. Of these patients, 8 patients relapsed and died, and 11 patients did not relapse and were alive at follow-up.

HALO analysis uses nuclear expansion and membrane markers to define cell boundaries with adjustable inputs from the user. In this way it is an assisted AI cell segmentation and analysis software that can also calculate spatial interactions between cell phenotypes. We employed DNA-Ir as our nuclear stain, SOX10 as our tumour marker and HLADR, CD3, CD4, CD8, CD14, CD11c, Tbet and FXIIIa as immune cell markers to define 8 cell phenotypes (Figure 4.5B, C). All immune cells were SOX10-. Cells were then annotated based on their phenotype. For example, CD4 T cells were CD3+CD4+ and T_H1 cells were CD3+CD4+Tbet+. CD8 T cells were CD3+CD8+, and Tbet+ CD8 T cells were defined as CD3+CD8+Tbet+. We wanted to classify myeloid populations that were defined in Chapter 3 of this study, and as such, had three myeloid populations: a general myeloid cell (HLADR+CD11c+CD14-), macrophages (HLADR+CD11c+CD14+FXIIIA+) and CD11c- monocytes (HLADR+CD11c-CD14+FXIIIA-). Tumour cells were defined as SOX10+CD4-CD8-.

Using this method to analyse tumour and immune cells within the selected 19-patient cohort, we found that CD4 T cells made up 5.83% (±9.94) of cells and CD8 T cells made up 3.30% (±6.9) of all cells. T_H1s and Tbet+ CD8 T cells made up 0.61% (±1.1) and 0.52% (±0.74) respectively (Figure 4.5B). Myeloid cells recorded 1.11% (±1.56), macrophages 0.63%

A

Cell Phenotypes

CD4 T cells	SOX10-CD3+CD4+
TH1 CD4 T cells	SOX10-CD3+CD4+T-bet+
CD8 T cells	SOX10-CD3+CD8+
Tbet+ CD8 T cells	SOX10-CD3+CD8+T-bet+
Myeloid Cell	HLADR+CD11c+CD14-
Macrophage	HLADR+CD11c+CD14+FXIIIA+
CD11c- Monocyte	HLADR+CD11c+CD14+FXIIIA-
Tumour Cells	SOX10+CD4-CD8-

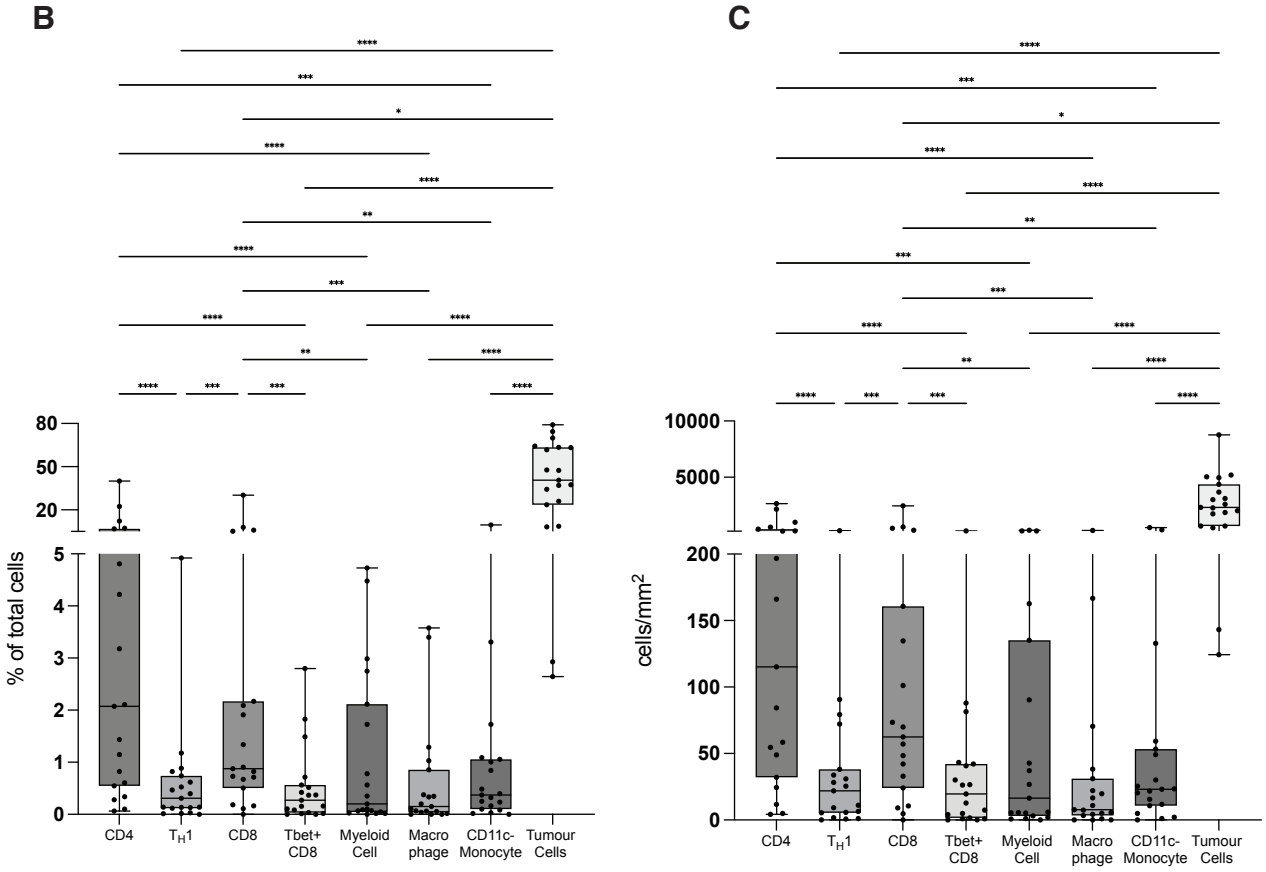

Figure 4.5 Tumour and immune cells in metastatic melanoma identified using assisted cell analysis software. 22 tumour cores from 19 patients were ablated using IMC and images were imported into HALO (Indica Systems) for cell segmentation and phenotypic analysis **(A)** For HALO analysis, phenotypes were defined using using DNA-Ir, SOX10, CD3, CD4, T-bet, CD8, HLA-DR, CD11c, CD14, and FXIIIA. All cells quantified were DNA-Ir. Quantification of these cell populations are shown, calculated as **(B)** percentage of total cells and **(C)** cells/mm^2. (n=19). Uncorrected Dunn's multiple comparison test performed to compare ranks. p value; 0.01234(ns), 0.0032(*), 0.0021 (**), 0.0002 (***), <0.0001 (****). (n=19).

(±1.08) and CD11c- monocytes 1.11% (±2.2) of cells (Figure 4.5B). Tumour cells averaged 41.78% (±5.7) of all cells (Figure 4.5B).

In a similar trend when we quantified cell densities, we saw CD4 T cells averaged 421 cells per mm^2 (±744.9) and CD8 T cells averaged 242.8 cells/mm^2 (±559.3) (Figure 4.5C). T_H1s and Tbet+ CD8 T cells averaged 37.35 cells/mm^2 (±57.78) and 34.61 cells/mm^2 (±53.45) respectively (Figure 4.5C). Myeloid cells averaged 67.50 cells/mm^2 (±93.29), macrophages 36.14 cells/mm^2 (±69.94) and CD11c- monocytes 69.90 cells/mm^2 (±132.1) (Figure 4.5C). Tumour cells averaged 2796 cells per mm^2 (±2188) with densities recorded between 124.3 and 8761 cells per mm^2 across the 19 samples tested (Figure 4.5C).

4.3.2.3 Method III: Unsupervised Clustering

The major benefit from high-dimensional datasets will be to perform unbiased analysis whereby cellular landscape could be mapped without preconceived phenotypes. Using unsupervised cell segmentation and clustering methods in collaboration with A/Prof Ellis Patrick and Farhan Ameen (University of Sydney), we were able to analyse our imaging mass cytometry data to both validate and compare with our other methods of analysis. Cell segmentation was performed using *simpleseg* R package and assessed by the candidate for accuracy. Data was normalised using square root transformation and the top and bottom 1% was 'trimmed' to minimise junk. Representative sample images and cell segmentation mask is shown for reference (Figure 4.6A-C).

Cells were then clustered using FuseSOM using markers established by previous analysis: CD45, CD3, CD4, FOXP3, CD8a, CD20, HLA-DR, CD11c, CD14, FXIIIa, CD66a, CD56, CD31, podoplanin, panCK and SOX10 (Figure 4.6D, E). 14 clusters were determined to be optimal using the 'elbow method' and assessing if the cells identified by these clusters were biologically correct and distinct. This work was done in collaboration with bioinformaticians and applied statisticians A/Prof Ellis Patrick and Farhan Ameen (The University of Sydney). The 'elbow method' employs a graphical visualisation using the within-clusters sum of squares on the y axis with the number of clusters on the x axis. The k value that corresponds in the 'elbow' of this plot is deemed the optimal number of clusters (Zhao, 2022, Edy et al., 2020). Using various visualisations including heatmaps of normalised expression values for each cluster, we labelled clusters as cell phenotypes according to marker expression (Figure 4.6D-

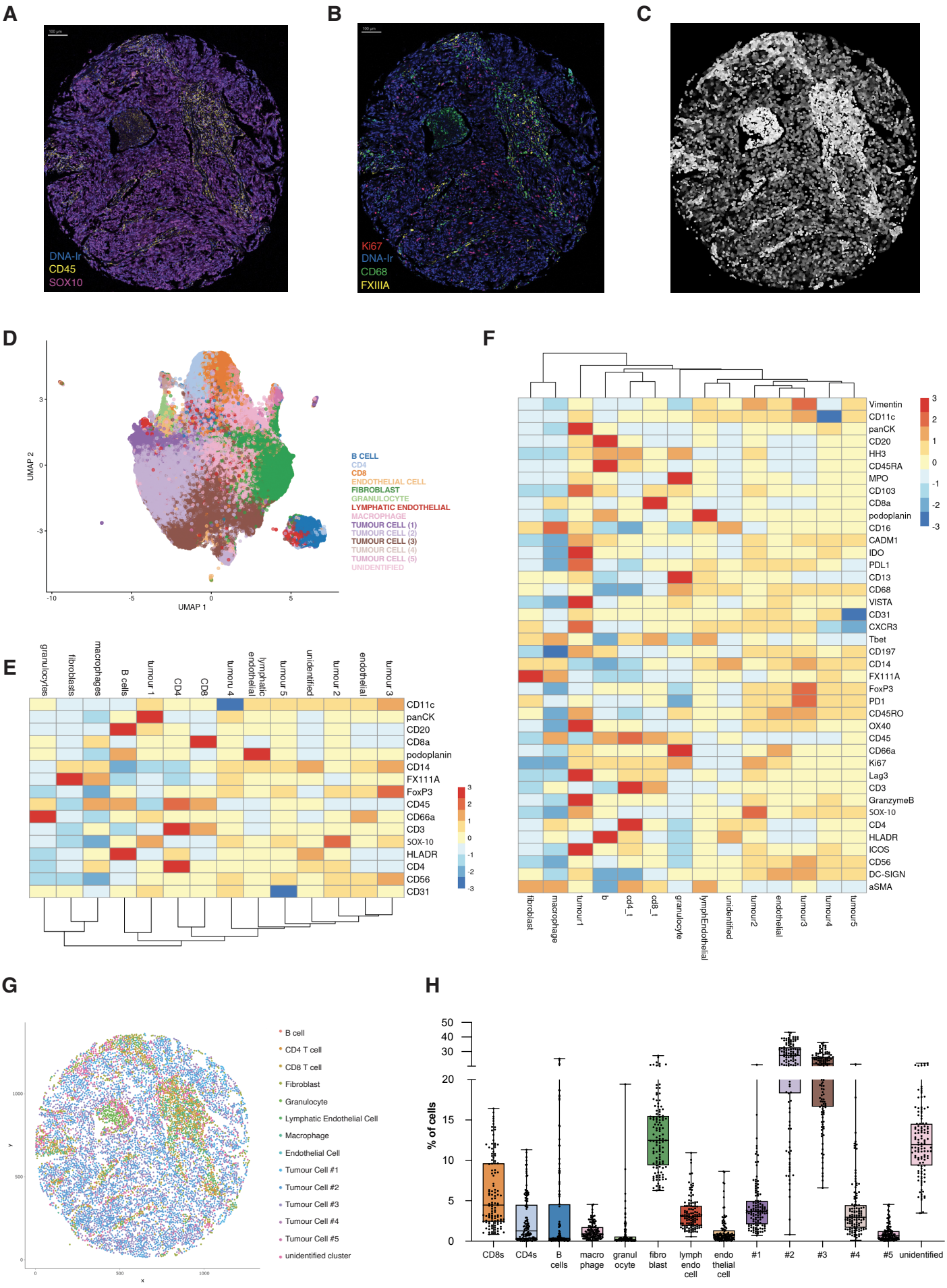
A
DNA-Ir
CD45
SOX10
B
Ki67
DNA-Ir
CD68
FXIIIA
C
D
UMAP 2
UMAP 1
B CELL
CD4
CD8
ENDOTHELIAL CELL
FIBROBLAST
GRANULOCYTE
LYMPHATIC ENDOTHELIAL
MACROPHAGE
TUMOUR CELL (1)
TUMOUR CELL (2)
TUMOUR CELL (3)
TUMOUR CELL (4)
TUMOUR CELL (5)
UNIDENTIFIED
E
granulocytes
fibroblasts
macrophages
B cells
tumour 1
CD4
CD8
tumour 4
lymphatic endothelial
tumour 5
unidentified
tumour 2
endothelial
tumour 3
CD11c
panCK
CD20
CD8a
podoplanin
CD14
FX111A
FoxP3
CD45
CD66a
CD3
SOX-10
HLADR
CD4
CD56
CD31
F
Vimentin
CD11c
panCK
CD20
HH3
CD45RA
MPO
CD103
CD8a
podoplanin
CD16
CADM1
IDO
PDL1
CD13
CD68
VISTA
CD31
CXCR3
Tbet
CD197
CD14
FX111A
FoxP3
PD1
CD45RO
OX40
CD45
CD66a
Ki67
Lag3
CD3
GranzymeB
SOX-10
CD4
HLADR
ICOS
CD56
DC-SIGN
aSMA
fibroblast
macrophage
tumour1
b
cd4_t
cd8_t
granulocyte
lymphEndothelial
unidentified
tumour2
endothelial
tumour3
tumour4
tumour5
G
B cell
CD4 T cell
CD8 T cell
Fibroblast
Granulocyte
Lymphatic Endothelial Cell
Macrophage
Endothelial Cell
Tumour Cell #1
Tumour Cell #2
Tumour Cell #3
Tumour Cell #4
Tumour Cell #5
unidentified cluster
H
% of cells
CD8s
CD4s
B cells
macro phage
granul ocyte
fibro blast
lymph endo cell
endo thelial cell
#1
#2
#3
#4
#5
unidentified

Figure 4.6 Supervised clustering performed on metastatic melanoma biopsies reveals 14 distinct cell populations. Unbiased clustering was performed using primary identification markers (CD45, SOX10, CD11c, panCK, CD20, CD8a, podoplanin, CD14, FXIIIA, FOXP3, CD66a, CD3, HLADR, CD4, CD56, CD31). Example IMC channel overlay of **(A)** DNA-Ir (blue), CD45 (yellow) and SOX10 (magenta) signal and **(B)** DNA-Ir (blue) Ki67 (red), CD68 (green) and FXIIIa (yellow). Image produced using MCD viewer. **(C)** Cell mask showing cell outlines as detected by segmentation algorithm applied to sample shown in (A). **(D)** UMAP performed for visualisation of cell clustering. All cells within all samples are combined and clustering is performed on the whole cohort. Each dot within the UMAP is a single cell and coloured according to cluster identified. **(E)** Heatmap displaying normalised expression values of markers used for clustering on all 14 cell clusters identified. **(F)** Heatmap displaying normalised expression values of all markers used in experiment on all 14 cell clusters identified. **(G)** Visual reconstruction of representative sample shown in (A) and (B) showing cells as individual dots using plotly R package. Cell 'dots' were mapped using x and y coordinates of each cell identified using cell segmentation using original IMC multi-tiff image output. **(H)** Cell clusters displayed as a proportion of all cells in all samples analysed (n=100).

F). Clusters were visualised on each sample using the plotly package (Sievert, 2020) and exported for manual inspection by the author to ensure it was representing the raw images correctly (representative plot Figure 4.6G).

We also quantified these identified cell clusters as a percentage of total cells (Figure 4.6H). The CD8 T cell cluster occupied an average of 4.47% (±4.36) of cells, CD4 T cell cluster made up 1.27% (±2.95) and B cell cluster 0.36% (±6.11) (Figure 4.6H). Macrophages, granulocytes and fibroblasts made up 1.25% (±0.97), 0.85% (±2.13) and 13% (±4.39) of all cells respectively. Lymphatic endothelial cells made up 3.42% (±2) of cells, and endothelial cells made up 1.22% (±1.66) (Figure 4.6H). Tumour cells were defined according to positive SOX10 expression, and the 5 clusters identified were numbered accordingly. Tumour cell clusters #2 and #3 made up the majority of tumour cells in our samples averaging 25.26% (±10.44) and 21.45% (±6.74) respectively (Figure 4.6H). Tumour cell #1 averaged 4.36% (±3.2) of cells, #4 3.94% (±3.5) and #5 0.98% (±1.01) (Figure 4.6H). We also had an unidentified cell type cluster that made up between 3 and 22% of cells within a sample (mean = 12.21% (±4.18)) (Figure 4.6H).

4.3.3 Spatial analysis reveals how immune and tumour cells interact in metastatic melanoma high-tumour regions

One of the major advantages of using an unbiased approach is the ability to map spatial interactions within our samples. We therefore wanted to investigate how cell phenotypes interacted with each other within the TME. Spatial interactions were investigated in collaboration with A/Prof. Ellis Patrick and Farhan Ameen (University of Sydney)

We used *spicyR* (bioconductor) package to test for spatial relationships between pairs of cell phenotypes in spatial omics technologies such as imaging mass cytometry (Canete et al., 2022). The relationship between cell phenotypes identified in Figure 4.6 was thus quantified and visualised in ‘bubbleplots’ using *spicyR* (Figure 4.7). Figure 4.7A summarises the amount of interaction or avoidance, a normalised value, of each cell cluster with every other cell cluster in high-tumour regions of metastatic melanoma. This data revealed some interesting cellular interactions that have not been previously appreciated. As expected, CD8 T cells interact with tumour cells displaying various phenotypes. Surprisingly, CD4 T cells are not seen interacting with tumour cells. Instead, CD4 T cells largely interact with CD8 T cells, macrophages and B

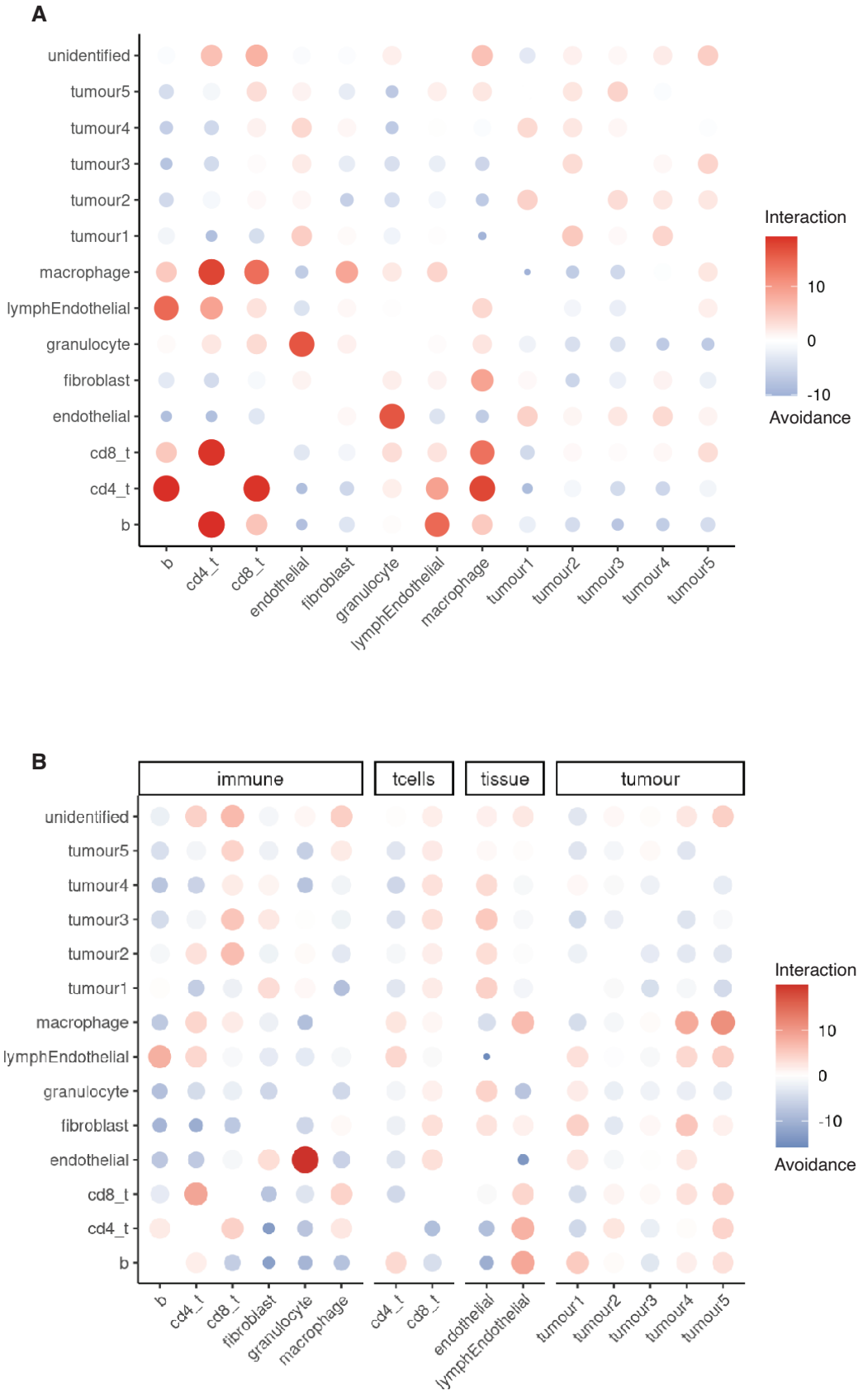

Figure 4.7 Spatial interactions within high-tumour areas of treatment naïve metastatic melanoma. Visualisation of interactions between clusters identified in Figure 4.5D identified using **(A)** 'spicyR' R package (Bioconductor) and **(A)** *statial* R package (Bioconductor) to map average interactions (attraction or avoidance) in melanoma metastases. Dot size and colour corresponds to interaction or avoidance value (n=100).

cells (Figure 4.7A). Macrophages are closely associated with CD4 T cells, and CD8 T cells to a lesser degree (Figure 4.7A). B cells and lymphatic endothelial cells also appear to be located close to each other (Figure 4.7A).

To test how cell clusters behave in relation to their cell classification or 'grouping', we employed the *statial* R package (bioconductor), an R package developed by our collaborator Farhan Ameen to address the plastic nature of cell states in the tissue (Ameen F, 2024). This package tests the behaviour of a population of cells when compared to their closest cell phenotypes. By classifying cell clusters within a 'parent' population, e.g. all tumour cells, *statial* calculates how the 'child' population deviates from the spatial behaviour of the 'parent' population (Ameen F, 2024). Each dot or 'bubble' in Figure 4.7B indicates how this cell interaction is spatially located in the child cluster compared to the parent. Applying this to the cell clusters identified in Figure 4.6, B cell, CD4 and CD8 T cell, fibroblasts, granulocytes and macrophage clusters were grouped as 'immune' cells, CD4 and CD8 T cells also separately grouped as 'T cells', endothelial and lymphatic endothelial cells as 'tissue' or structural cells and tumour cells 1-5 as 'tumour' cells (Figure 4.7B). According to this analysis, cell clusters within the immune cell parent population interact very differently with the tumour microenvironment. This suggests that not all immune populations behave the same way when it comes to spatial interactions within melanoma tumours. Comparing interactions only within the immune compartment, for example, interactions between granulocytes and endothelial cells are much higher when compared to any other immune populations' interactions with endothelial cells (Figure 4.7B). Comparing only T cells, this analysis also suggests that both

CD4 and CD8 T cells behave differently within melanoma tumours. CD8 T cells are most closely located near tumour cells, CD4 T cells and macrophages, while CD4 T cells are most closely located with macrophages, lymphatic endothelial cells and B cells (Figure 4.7B). Looking at endothelial cells and lymphatic endothelial cell interactions within the tumour, it appears that endothelial cells are more localised to tumour cells, and lymphatic endothelial cells are more closely associated with immune cells (Figure 4.7B). Tumour cells appear to all interact similarly with the TME, however tumour cells 4 and 5 are more closely associated with macrophages compared to other tumour cells (Figure 4.7B).

4.3.4 Applying a different approach to understand the role of the TME and its impact on clinical outcomes

Having established different methods for analysis, we adopted two approaches for the rest of the work in this chapter, namely manual gating (method I) and unbiased approach (method III) as we were confident in the accuracy of these approaches as well as their efficiency to enable scalability. We used these approaches to understand how mapping the immune landscape of TME could help understand the role of immune cells associated with clinical outcomes and determine whether biomarkers of treatment response could be developed using this approach.

4.3.5 Tumour composition did not differ between treatment allocations

Samples used in this study were acquired from a clinical trial where the effect of radiotherapy was assessed (as detailed in section 4.2.1). As an initial test, we wanted to determine whether the baseline tumour cellular composition (prior to radiotherapy) was significantly different between patients selected for radiotherapy and patients in the control arm. We saw no differences between the densities of all cells, CD8 T cells, CD4 T cells, B cells, monocytes, macrophages or NK cells between patients allocated to adjuvant radiotherapy and observation alone (Figure 4.8A-G). Although there was a slightly higher density of tumour cells in patients that went on to receive radiotherapy within our cohort, the difference did not reach statistical significance ($p=0.0920$) (Figure 4.8H). These data suggest that there was no inherent bias in the selection of patients for treatment.

4.3.6 Higher immune and non-lymphoid cells in high-tumour regions of treatment naïve metastatic melanoma tumours are associated with survival

In order to maximise the use of these data, we combined both the treatment arm (radiotherapy treated) and control arm (observation only) in our analysis. We then applied survival as a measure to determine whether the cellular content of the TME was associated with better patient survival. As the trial established that adjuvant radiotherapy had no effect on survival (Burmeister et al., 2012, Henderson et al., 2015), we reasoned that it would be an appropriate clinical outcome to base this on. From the data available it was clear that radiotherapy would not have impacted patient survival.

CD8 T cells were found to be significantly higher in patients that were alive at follow-up when compared to those who were deceased (Figure 4.9). CD8 T cells averaged 3.98% of total cells

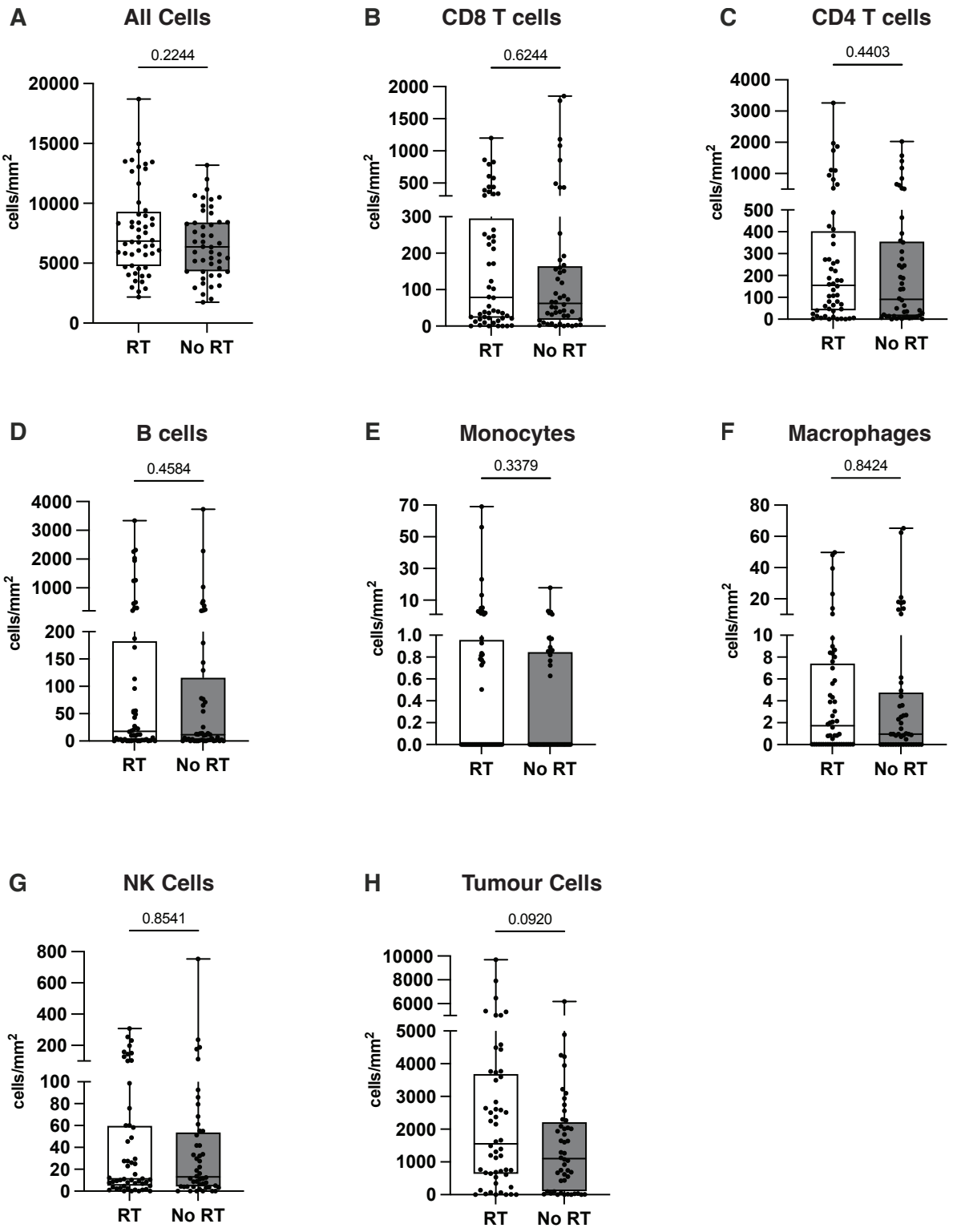

Figure 4.8 No differences in tumour composition between patients treated with adjuvant radiotherapy and no radiotherapy. IMC was used to ablate high-tumour regions of treatment naïve metastatic melanoma patients to assess immune phenotypes associated with clinical outcomes. Images produced from IMC underwent supervised cell segmentation (Cell Profiler) and manual gating (FlowJo). Densities of **(A)** all cells detected **(B)** CD8 T cells **(C)** CD4 T cells **(D)** B cells **(E)** monocytes **(F)** macrophages **(G)** NK cells and **(H)** tumour cells in patients allocated to adjuvant radiotherapy treatment (n=52) or no radiotherapy (observation only) (n=48). Cell phenotypes detailed in Table 4.2. Full gating strategy is detailed in Figure 4.3. Mann-Whitney two-tailed test performed to determine statistical differences.

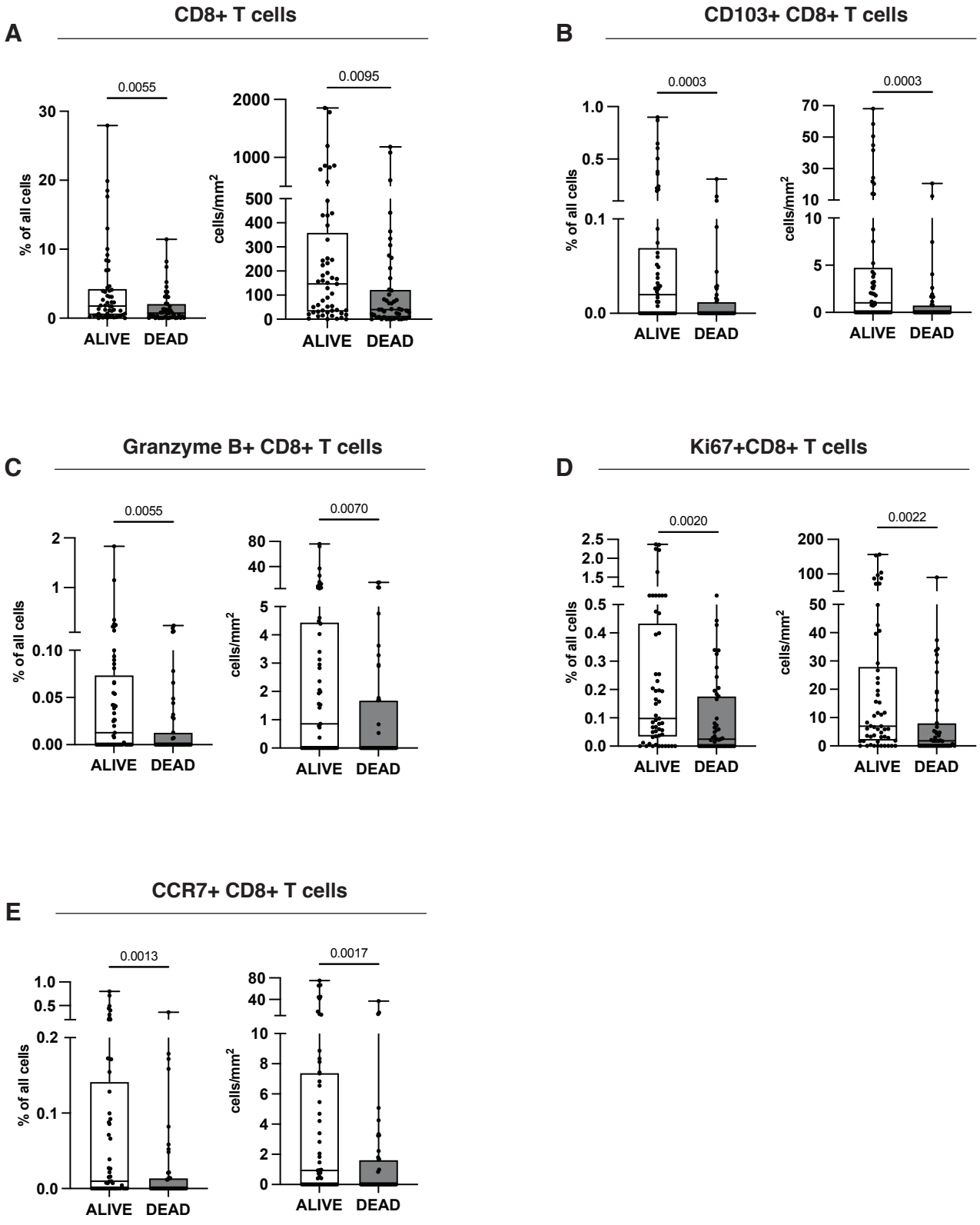

Figure 4.9 Higher quantities of CD8+ T cells in tumour regions are associated with survival in metastatic melanoma. IMC was used to ablate pathologist-defined high-tumour regions of treatment naïve metastatic melanoma patients to assess immune phenotypes associated with survival. Images produced from IMC underwent cell segmentation (Cell Profiler) and manual gating (FlowJo). Proportion and density of **(A)** CD8+ T cell **(B)** CD103+ CD8+ T cell **(C)** Granzyme B+ CD8+ T cell **(D)** Ki67+CD8+ T cells and **(E)** CCR7+ CD8+ T cells were compared between patients that were alive (n=53) or dead (n=47) at clinical follow up. Cell phenotypes detailed in Table 4.2. Full gating strategy is detailed in Figure 4.3. Mann-Whitney test was performed to determine statistical significance.

and 278.4 cells per mm^2 patients in were alive compared to 1.61% of all cells and 137.1 cells per mm^2 in patients who were deceased at follow-up (Figure 4.9A). The same trend was observed for CD8 T cells subsets CD103+CD8 T cells, Granzyme B+ CD8 T cells, CCR7+ CD8 T cells and Ki67+ CD8 T cells (Figure 4.9B-E).

CD4 T cells were also significantly higher in patients who were alive (4.34% of all cells and 386.3 cells per mm^2) compared to 2.83% of cells and 271.6 cells of mm^2 in patients that died (Figure 4.10A). CD4 T cell subsets T_{REG}s, T_H1 cells Ki67+ CD4 T cells and CCR7+ CD4 T cells were also recorded as significantly higher in patients that survived (Figure 4.10B-E).

Patients that survived had significantly more B cells (3.74% of all cells, 402.6 cells per mm^2) compared to those that were dead at follow-up (1.43% of all cells, 126 cell/mm^2) (Figure 4.11A). Similarly, proliferating (Ki67+) B cells were significantly higher in patients that survived (22.9% of all cells, 28.89 cells per mm^2) compared to those that did not (7.38% of all cells, 7.38 cells per mm^2) (Figure 4.11B).

Despite the myeloid compartment making up a relatively low proportion of total cells, we saw distinct differences in myeloid cells when patients were separated by survival outcome. Monocytes, classified as HLADR+CD11c+CD14+FXIIIA- cells, were significantly higher in patients that survived, making up 0.041% of cells and 2.96 cells per mm^2 density, compared to 0.020% of cells and 1.53 cells per mm^2 in those that did not survive (Figure 4.12A). Although macrophage proportions or density was not recorded as significantly different between survival outcomes, CD16+ macrophages (classified as HLADR+CD11c+CD14+FXIIA+CD16+ cells) were significantly higher in patients that were alive (0.11% of cells, 7.376 cells per mm^2) compared to patients that had died (0.04% of all cells, 3.259 cells per mm^2) (Figure 4.12B, C). There were no differences in proportions or densities of NK cells or neutrophils between patients (Figure 4.1D, E).

Both lymphatic endothelial cells (CD31+FXIIIA-podoplanin+) and non-lymphatic endothelial cells (CD31+FXIIIA-podoplanin-) were significantly higher in patients that were alive at follow-up (Figure 4.13A, B). Lymphatic endothelial cells made up an average of 0.02% of cells and 1.2 cells per mm^2 compared to 0.01% of cells and 0.45 cells per mm^2 in patients that died (Figure 4.13A). Non-lymphatic endothelial cells made up 0.26% and 13.23 cell per mm^2 compared to 0.05% and 2.65 cells per mm^2 in patients that died (Figure 4.13B). We saw no

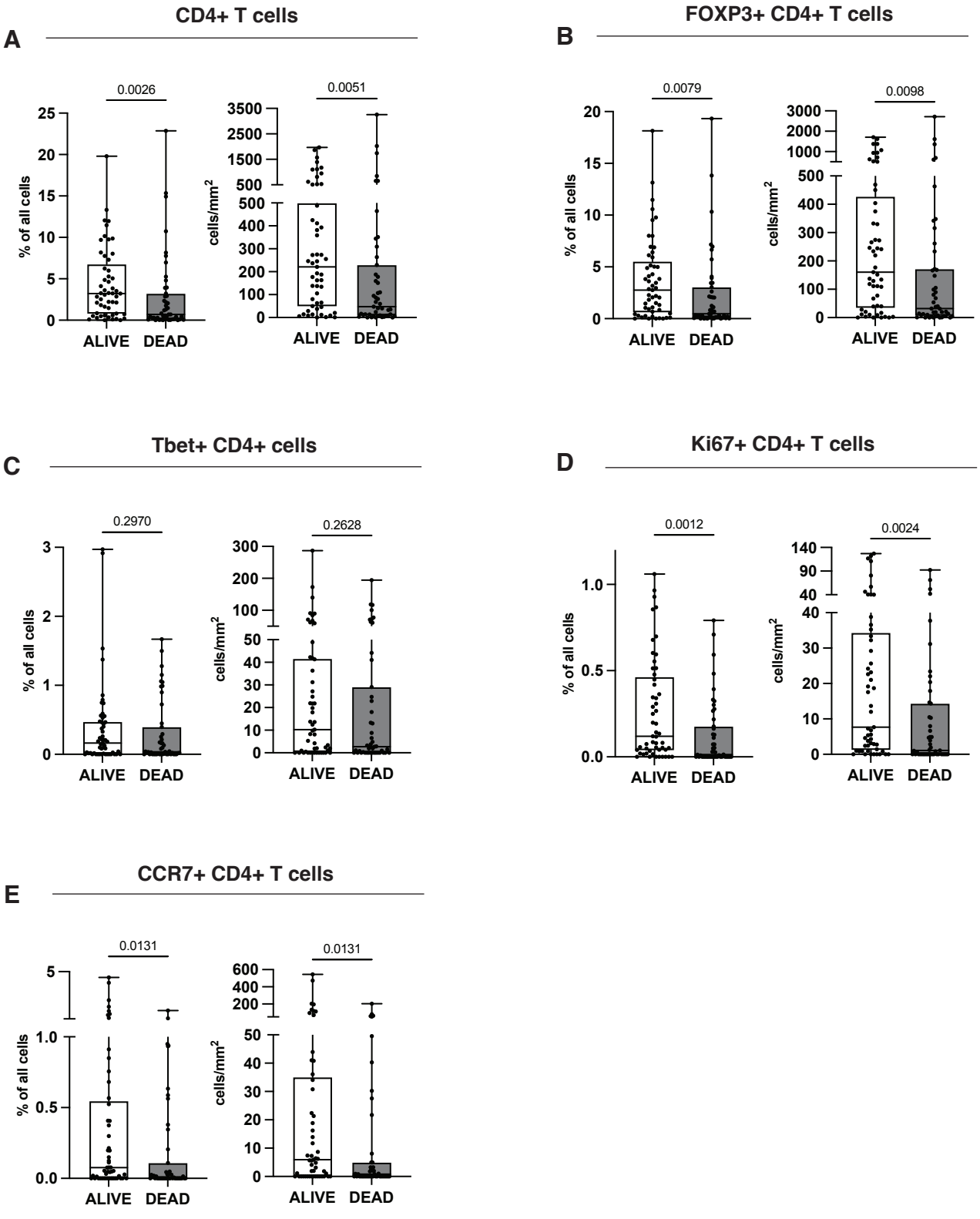

Figure 4.10 Higher quantities of CD4 T cells in tumour regions are associated with survival in metastatic melanoma. IMC was used to ablate pathologist-defined high-tumour regions of treatment naïve metastatic melanoma patients to assess immune phenotypes associated with survival. Images produced from IMC underwent cell segmentation (Cell Profiler) and manual gating (FlowJo). Proportion and density of **(A)** CD4 T cells **(B)** FOXP3+ CD4+ T cells (T_{REG}s) **(C)** Tbet+ CD4+ T cells (T_H1s) **(D)** Proliferating CD4 T cells and **(E)** CCR7+ CD4 T cells were compared between patients that were alive (n=53) or dead (n=47) at clinical follow up. Cell phenotypes detailed in Table 4.2. Full gating strategy is detailed in Figure 4.3. Mann-Whitney test was performed to determine statistical significance.

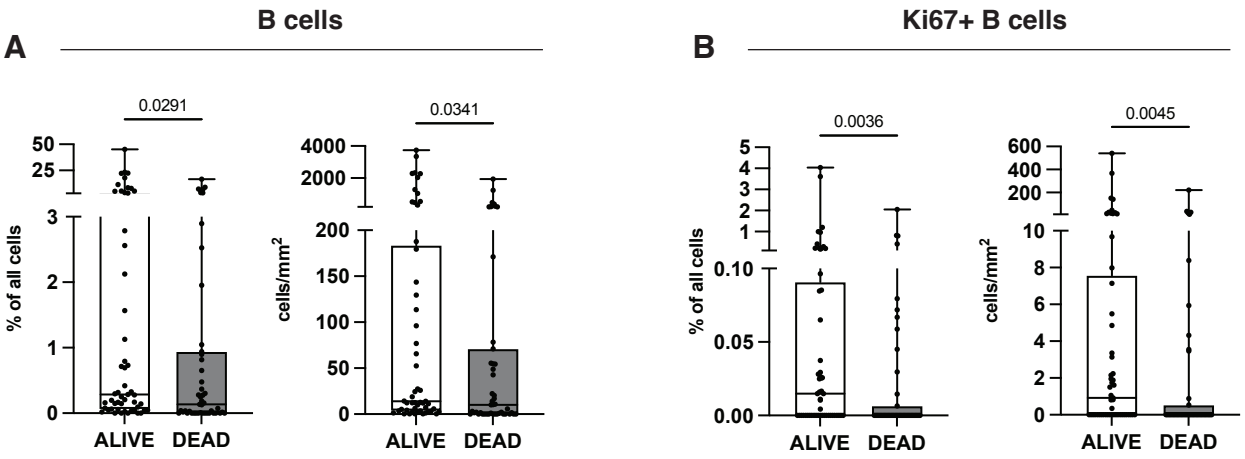

Figure 4.11 Higher quantities of B cells in tumour regions are associated with survival in metastatic melanoma. IMC was used to ablate pathologist-defined high-tumour regions of treatment naïve metastatic melanoma patients to assess immune phenotypes associated with survival. Images produced from IMC underwent cell segmentation (Cell Profiler) and manual gating (FlowJo). Proportion and density of **(A)** B cells and **(B)** Ki67+ B cells were compared between patients that were alive (n=53) or dead (n=47) at clinical trial end point. Cell phenotypes detailed in Table 4.2. Full gating strategy is detailed in Figure 4.3. Mann-Whitney test was performed to determine statistical significance.

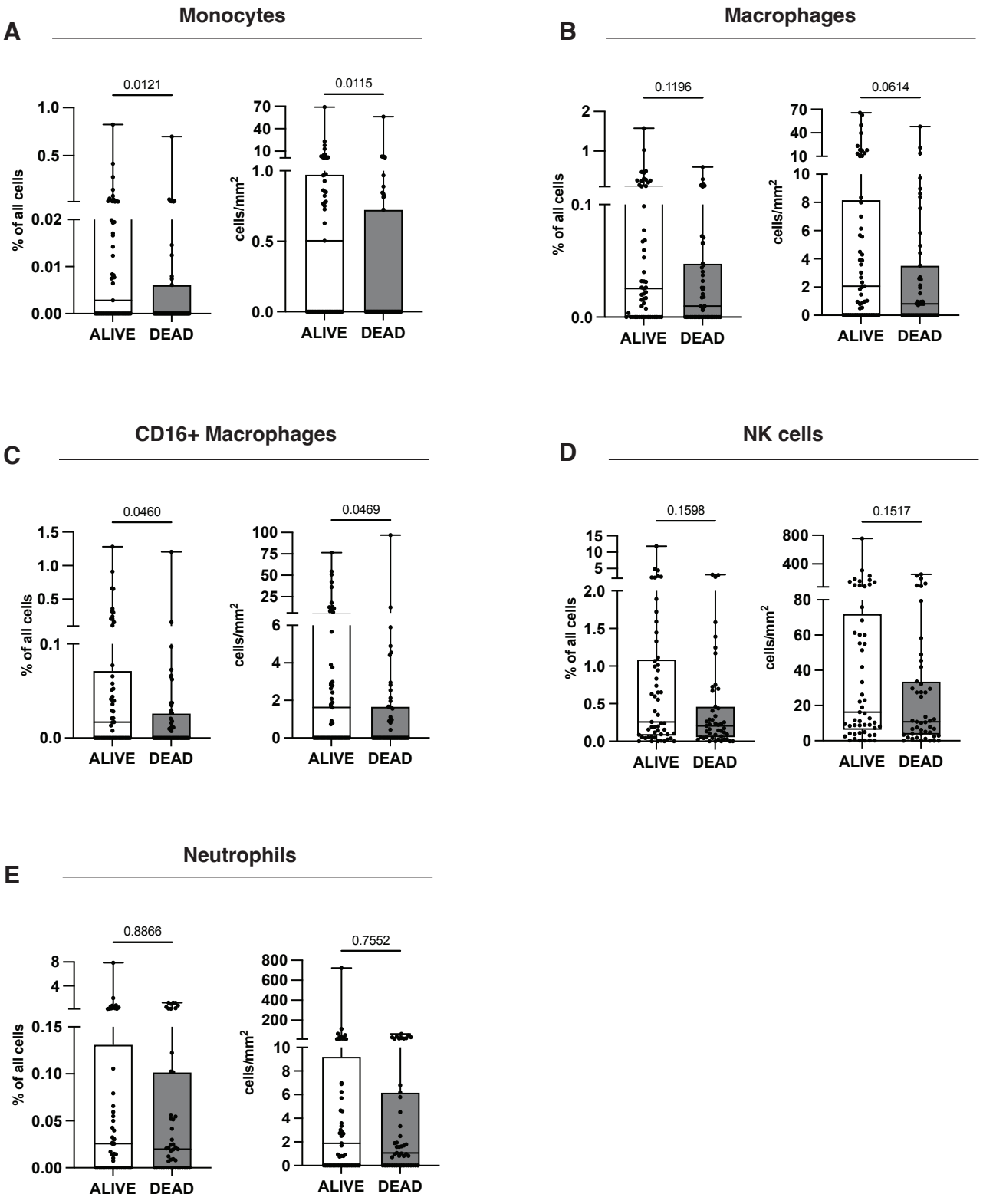

Figure 4.12 Quantities of innate immune cells in tumour regions are not associated with survival in metastatic melanoma patients. IMC was used to ablate pathologist-defined high-tumour regions of treatment naïve metastatic melanoma patients to assess immune phenotypes associated with survival. Images produced from IMC underwent cell segmentation (Cell Profiler) and manual gating (FlowJo). Proportion and density of **(A)** monocytes **(B)** macrophages **(C)** CD16+ macrophages **(D)** NK cells and **(E)** neutrophils were compared between patients that were alive (n=53) or dead (n=47) at clinical trial end point. Cell phenotypes detailed in Table 4.2. Full gating strategy is detailed in Figure 4.3. Mann-Whitney test was performed to determine statistical significance.

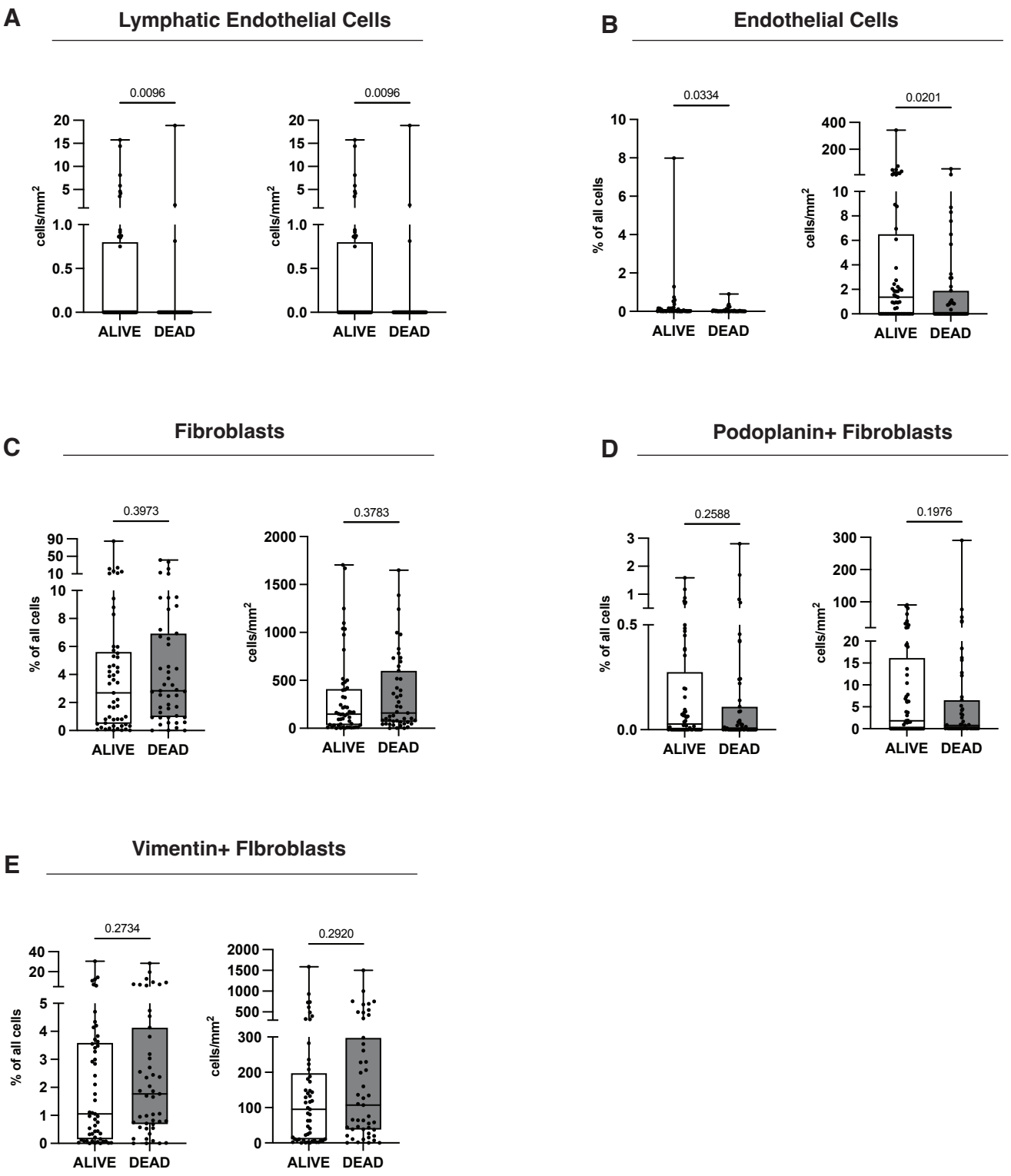

Figure 4.13 Higher quantities of non-leukocytes in tumour regions are associated with survival in metastatic melanoma patients. IMC was used to ablate pathologist-defined high-tumour regions of treatment naïve metastatic melanoma patients to assess immune phenotypes associated with survival. Images produced from IMC underwent cell segmentation (Cell Profiler) and manual gating (FlowJo). Proportion and density of **(A)** lymphatic endothelial cells **(B)** endothelial cells **(C)** fibroblasts **(D)** podoplanin+ fibroblasts and **(E)** vimentin+ fibroblasts were compared between patients that were alive (n=53) or dead (n=47) at clinical follow up. All non-leukocytes were pre-gated as SOX10-CD45-. Cell phenotypes detailed in Table 4.2. Full gating strategy is detailed in Figure 4.3. Mann-Whitney test was performed to determine statistical significance.

differences in Fibroblasts, podoplanin+ Fibroblasts or Vimentin+ Fibroblasts between patients that were alive or dead at follow-up (Figure 4.13C-E). We also saw no differences in any tumour cell population between patients that were alive or dead at follow-up (Figure 4.14).

To further investigate cell types associated with survival, we separated 5 patients determined to have a survival time of greater than 3 years within the observation only cohort (n=48). We found no differences in CD8 T cells, CD4 T cells, B cells, Macrophages, NK cells, monocytes, T_H1 cells or tumour cell density in patients that survived more than 3 years compared to less than 3 years (Figure 4.15A-E, G-I). Interestingly, T_{REG}s (FOXP3+ CD4+ cells) had a higher density in patients who had a survival of less than 3 years (255 cells per mm^2) compared to 54.4 cells permm^2 in patients that survived more than 3 years, although this difference was not significant (p=0.0789, Mann-Whitney test) (Figure 4.15F).

As it was highlighted in the clinical trial that extranodal spread was an independently bad prognostic indicator, we sought to understand why this may be the case, and if the answer lay in the immune cell milieu of the tumours. We found no differences in cell density between patients of extranodal spread status (Figure 4.16A). CD8, CD4 T cell densities are significantly higher in patients with extranodal spread that were alive at follow-up, however we do not observe this between alive and dead in patients that had no extranodal spread (Figure 4.16B, C). We also saw this trend for CD4 subset T_{REG}s (Figure 4.16E). There is a trend toward higher B cell density is higher patients alive at follow-up with both extranodal spread and no extranodal spread, and this difference approached significance for patients with extranodal spread (p=0.0991) (Figure 4.16E). Monocytes were marginally higher in patients with no extranodal spread who were alive at follow-up (0.06 cells per mm^2) compared to those who were dead at follow-up (0.039 cells per mm^2) (Figure 4.16F). Similarly, monocytes were higher in patients with extranodal spread that were alive (0.094 cells per mm^2) compared to those that died (0.050 cells per mm^2), however these differences were not significant (Figure 4.16F). Macrophages were higher in alive patients that had no extranodal spread (alive = 7.26 cells per mm^2; dead = 2.29 cells per mm^2) compared to those that had extranodal spread (alive = 9.03 cells per mm^2; dead = 4.23 cells per mm^2) (Figure 4.16G). NK cells were lower in alive patients without extranodal spread (43.55 cells per mm^2) compared to dead in patients without extranodal spread (54.66 cells per mm^2), while those with extranodal spread that were alive at follow-up had more NK cells than those that were dead at follow-up (alive = 92.27 cells per mm^2, dead = 24.45 cells per mm^2 p=0.0794) (Figure 4.16H). Tumour cell densities showed no

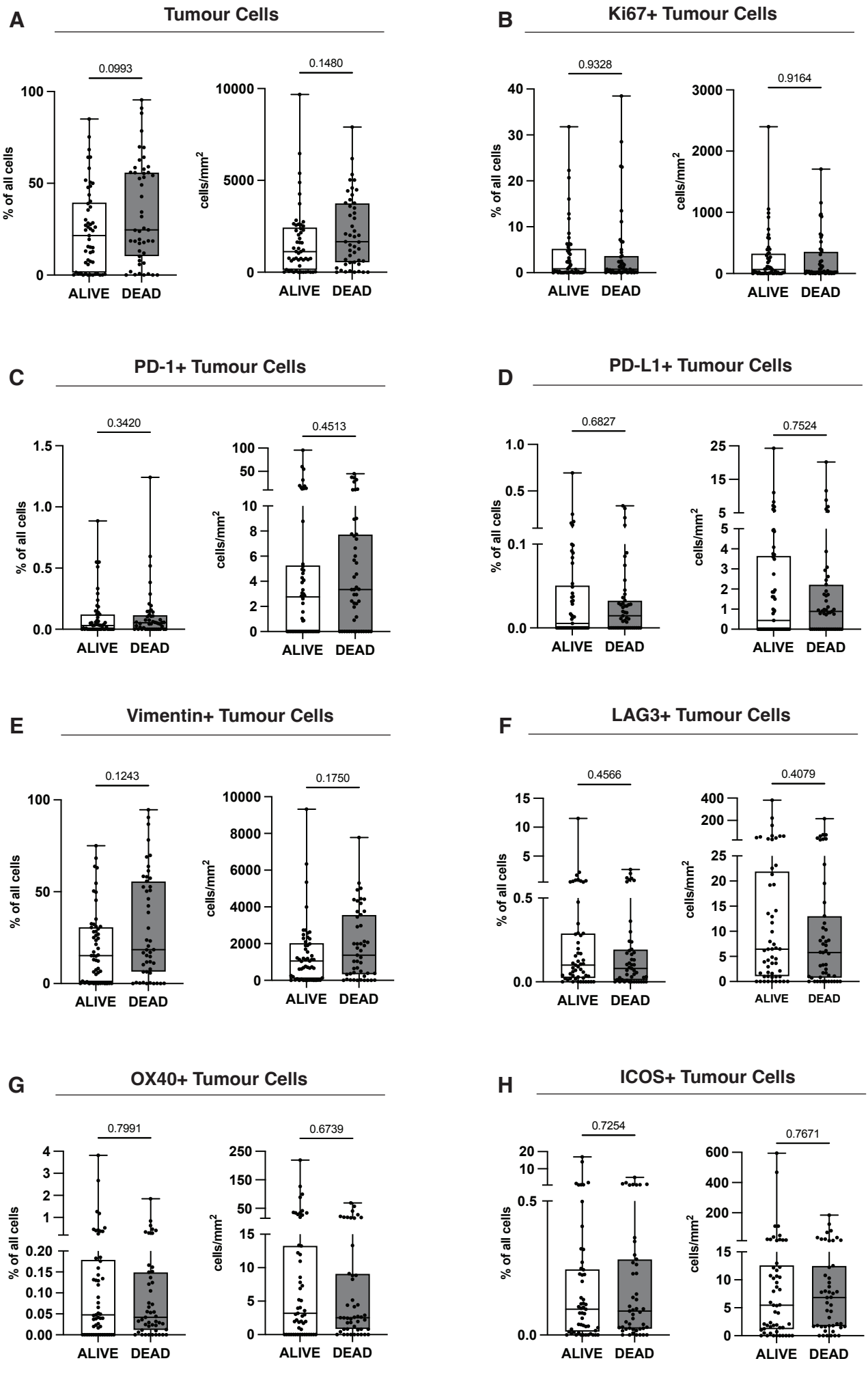
A
Tumour Cells
0.0993
0.1480
% of all cells
cells/mm2
ALIVE
DEAD
B
Ki67+ Tumour Cells
0.9328
0.9164
C
PD-1+ Tumour Cells
0.3420
0.4513
D
PD-L1+ Tumour Cells
0.6827
0.7524
E
Vimentin+ Tumour Cells
0.1243
0.1750
F
LAG3+ Tumour Cells
0.4566
0.4079
G
OX40+ Tumour Cells
0.7991
0.6739
H
ICOS+ Tumour Cells
0.7254
0.7671

Figure 4.14 Tumour cells in tumour regions are not associated with survival in metastatic melanoma patients. IMC was used to ablate pathologist-defined high-tumour regions of treatment naïve metastatic melanoma patients to assess immune phenotypes associated with survival. Images produced from IMC underwent supervised cell segmentation (Cell Profiler) and manual gating (FlowJo). Proportion and density of **(A)** tumour cells **(B)** Ki67+ tumour cells **(C)** PD1+ tumour cells **(D)** PDL1+ tumour cells **(E)** Vimentin+ tumour cells **(F)** LAG3+ tumour cells **(G)** OX40+ tumour cells and **(H)** ICOS+ tumour cells were compared between patients that were alive (n=53) or dead (n=47) at clinical trial end point. Cell phenotypes detailed in Table 4.2. Full gating strategy is detailed in Figure 4.3. Mann-Whitney test was performed to determine statistical significance.

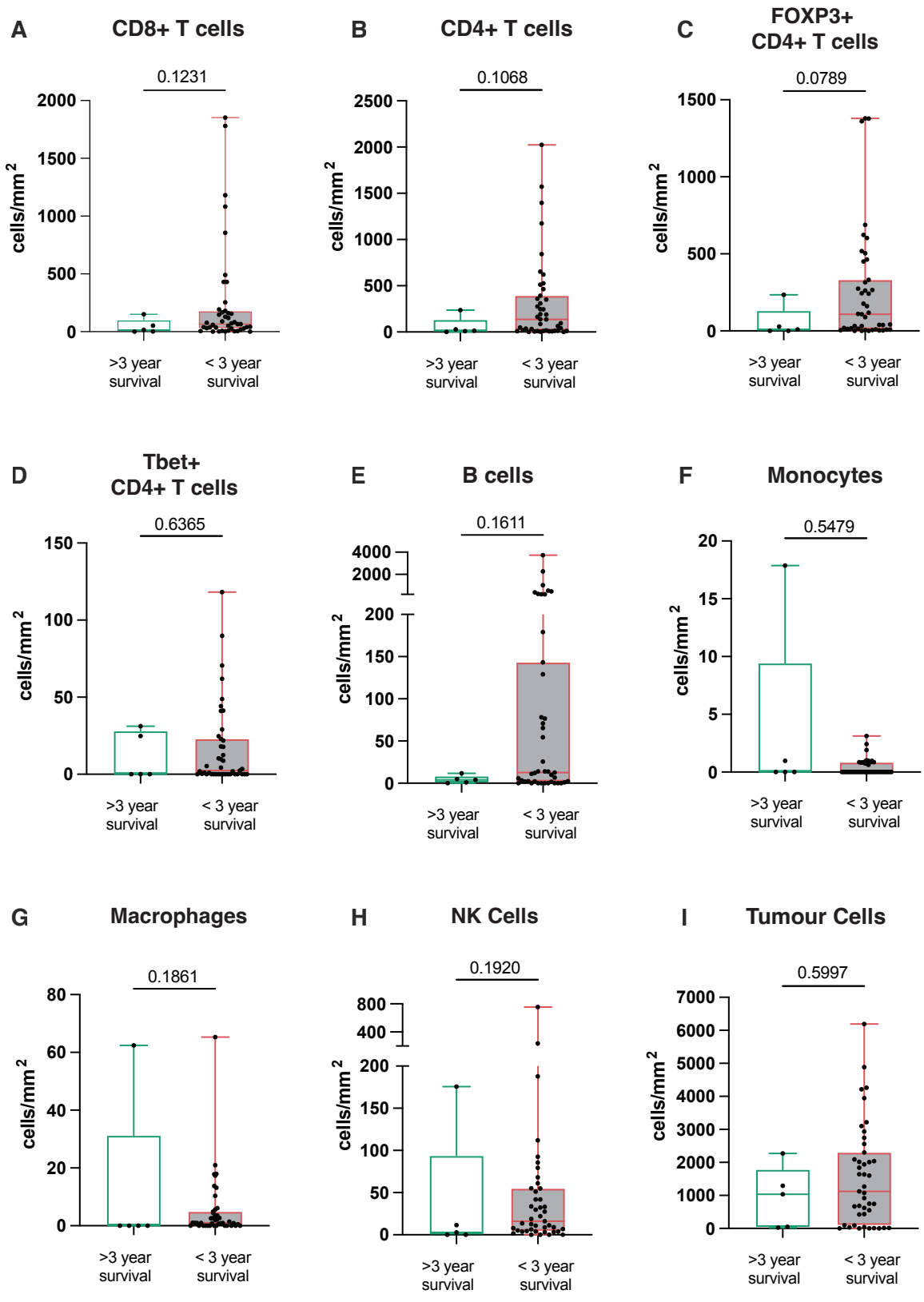

Figure 4.15 Cell populations associated with longer survival in metastatic melanoma patients. Density of **(A)** CD8 T cells, **(B)** CD4 T cells, **(C)** FOXP3+ CD4 T cells, **(D)** Tbet+ CD4+ T cells, **(E)** B cells, **(F)** monocytes, **(G)** macrophages, **(H)** NK cells and **(I)** tumour cells compared between patients not treated with radiotherapy with a survival time greater than 3 years since randomisation (n=5) to those that had less than 3 years survival (n= 43). Cell phenotypes detailed in Table 4.2. Full gating strategy is detailed in Figure 4.3. Mann-Whitney test performed to compare ranks between groups with exact, two-tailed p values reported.

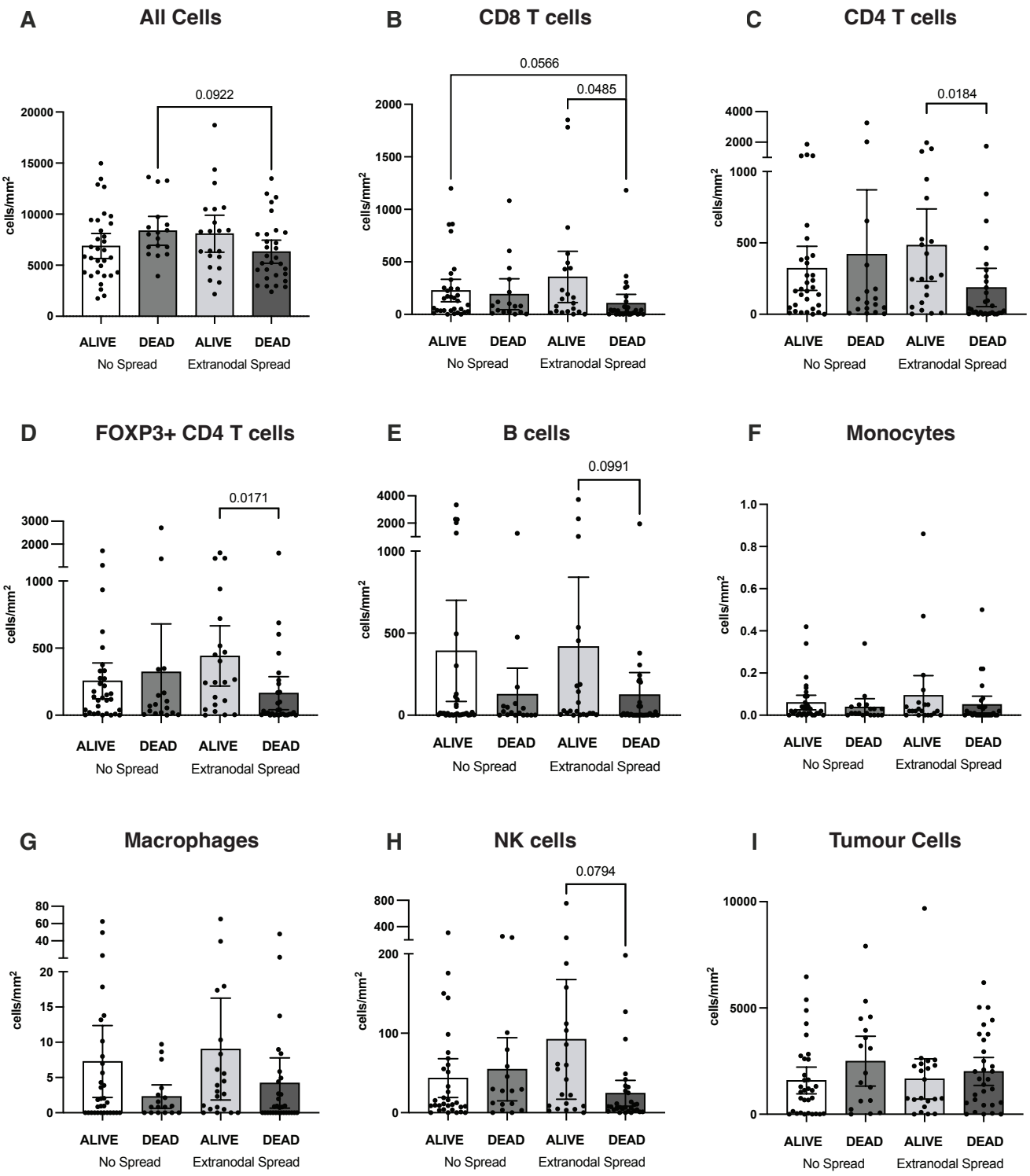

Figure 4.16 Immune and tumour cell densities of patients separated by extranodal spread status and survival. IMC was used to ablate pathologist-defined high-tumour regions of treatment naïve metastatic melanoma patients to assess immune phenotypes associated with clinical outcomes. Images produced from IMC underwent cell segmentation (Cell Profiler) and manual gating (FlowJo). Density of **(A)** all cells, **(B)** CD8 T cells, **(C)** CD4 T cells, **(D)** FOXP3+ CD4 T cells, **(E)** B cells, **(F)** monocytes, **(G)** macrophages, **(H)** NK cells and **(I)** tumour cells between patients that had no extra nodal spread (alive n=32, dead n=17) and those that had either limited or extensive extranodal spread (alive n=21, dead n=30). Cell phenotypes detailed in Table 4.2. Full gating strategy is detailed in Figure 4.3. Dunn's multiple comparison test performed to compare ranks with p values < 0.1 included on graph.

significant differences between survival outcomes when patients were grouped by extranodal spread status (Figure 4.16I).

4.3.6.1 Validation of the impact of the TME on clinical outcome used unbiased approach (Method III)

Having mapped the immune landscape using the unbiased approach to determine the impact of the TME on clinical outcomes, we next aimed to validate these findings using an unbiased approach. We then tested the differences in proportions of each cell cluster between alive and dead patients to establish phenotypes associated with survival using the proportions test contained in R *stats* package. Table 4.3 outlines the mean proportions of each cluster and the p value computed by R using the Pearson's chi-squared test. We saw that CD8 T cells, lymphatic endothelial cells and unidentified cell cluster were all significantly higher in patients that survived compared to those who died (Table 4.3). Tumour cell #5 and #2 were significantly lower in patients alive at follow-up (Table 4.3). There were no differences in proportions of CD4 T cells, B cells, macrophages, granulocytes, fibroblasts, endothelial cells, or tumour cells #1, #3 and #4 (Table 4.3).

4.3.7 Low presence of immune and non-lymphocytic cells in high-tumour regions of treatment naïve metastatic melanoma tumours are associated with relapse

4.3.7.1 Manual Gating

We next determined the impact of the TME on relapse. Of the samples analysed in this study, 48 patients relapsed, and 52 patients did not show any signs of relapse (median follow-up time was 3.3 years). We therefore determined what impact the TME had on relapse by comparing cell populations between patients that relapsed and those that did not.

As outlined above, cell data was exported from cell profiler and gated using gating strategy in Figure 4.3, before being quantified as both percentage of total cells within sample, and cells per mm^2. CD8 T cells, CD103+CD8 T cells, proliferating CD8 T cells and CCR7+ CD8 T cells were found to be significantly higher in patients that relapsed compared to those who did not (Figure 4.17A-B, D-E). Interestingly, Granzyme B+ CD8 T cells were not different between patients that relapsed and those that did not relapse (Figure 4.17C).

Table 4.3 Proportions of cell clusters identified in Figure 4.6 compared between patients alive or dead at clinical trial end point.

Cell Cluster	Alive [Mean value]	Dead [Mean Value]	p value	Adjusted p value
CD8 T cells	0.069	0.048	0.0056	0.056
Lymphatic Endothelial Cells	0.038	0.029	0.012	0.056
Tumour Cell #5	0.0077	0.012	0.015	0.056
Unidentified Cluster	0.13	0.11	0.016	0.056
Tumour Cell #2	0.23	0.27	0.03	0.084
B cells	0.042	0.028	0.18	0.42
Fibroblast	0.13	0.14	0.21	0.42
Macrophage	0.013	0.011	0.25	0.42
Tumour Cell #3	0.21	0.22	0.27	0.42
Tumour Cell #1	0.045	0.041	0.47	0.66
Granulocyte	0.0094	0.0075	0.62	0.79
Endothelial Cells	0.038	0.041	0.74	0.85
Tumour Cell #4	0.012	0.013	0.79	0.85
CD4 T cells	0.026	0.025	0.85	0.85

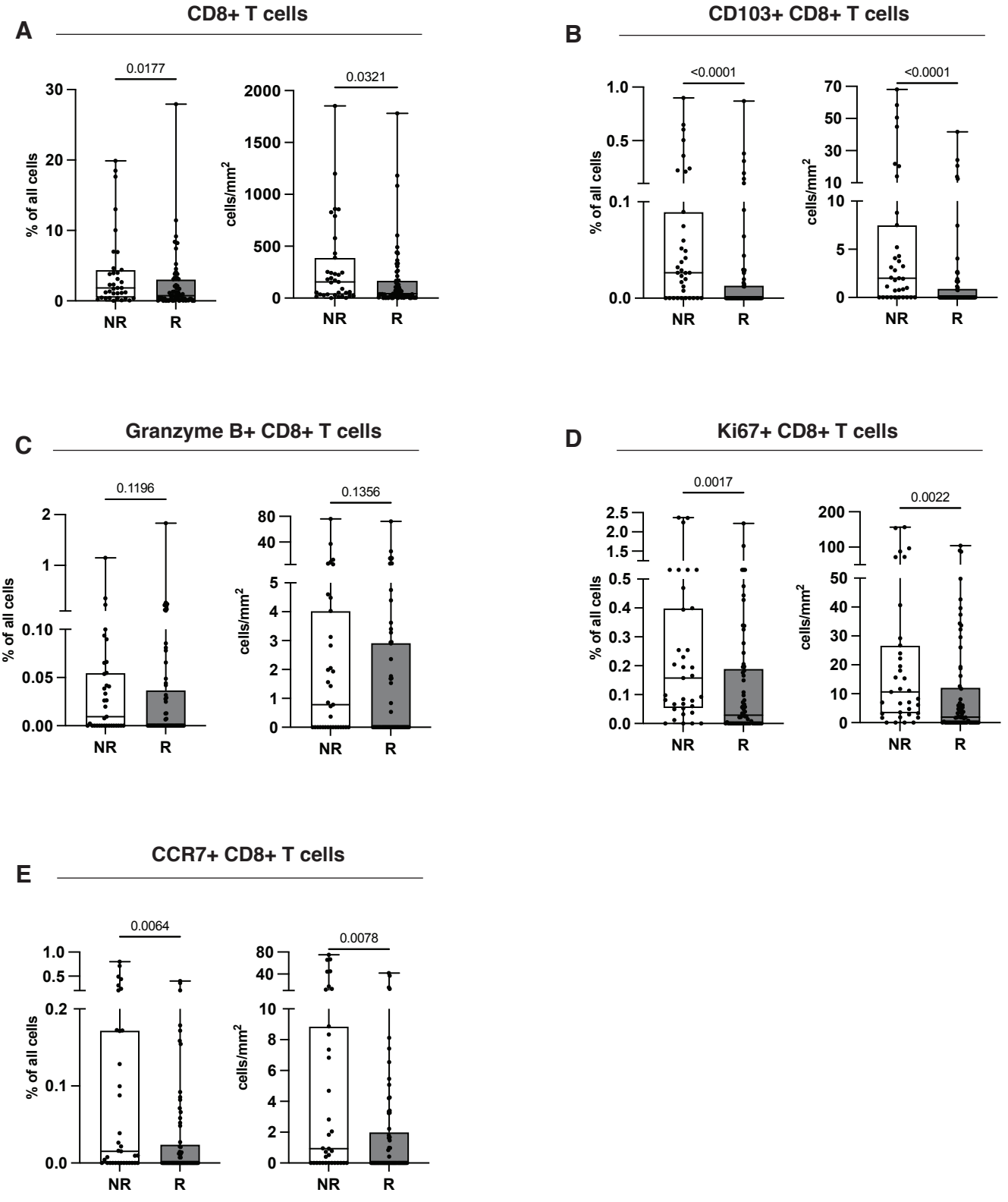

Figure 4.17 Higher quantities of CD8+ T cells in tumour regions are associated with no relapse in metastatic melanoma. IMC was used to ablate pathologist-defined pathologist-defined high-tumour regions of treatment-naïve metastatic melanoma patients to assess immune phenotypes associated with relapse. Images produced from IMC underwent cell segmentation (Cell Profiler) and manual gating (FlowJo). Proportion and density of **(A)** CD8 T cell **(B)** CD103+ CD8 T cell **(C)** Granzyme B+ CD8 T cell **(D)** Ki67+CD8 T cells and **(E)** CCR7+ CD8 T cells were compared between patients that did not relapse (NR, n=35) and those that did relapse (R, n=65). Cell phenotypes detailed in Table 4.2. Full gating strategy is detailed in Figure 4.3. Mann-Whitney test was performed to determine statistical significance.

There was a trend towards a higher proportion of CD4 T cells in patients that did not relapse compared to those that did, although this was not significant (p=0.0550) (Figure 4.18A). However, CD4 T cell density was significantly higher in patients that relapsed compared to patients that did not relapse (p=0.0496, Mann-Whitney test) (Figure 4.18A). There were no differences in levels or density of T_{REG} or T_H1 cells (TBET+CD4+) between groups (Figure 4.18B-C). Proportions and densities of both proliferating CD4 T cells and CCR7+ CD4 T cells were significantly higher in patients that did not relapse (Figure 4.18D-E).

There were no differences in baseline levels of overall or proliferating B cells between patients that did not relapse and those that did (Figure 4.19). Similarly, innate immune cell populations and non-leukocytes were present in similar numbers and density when patient groupings were split by relapse outcome (Figure 4.20 & Figure 4.21). We also saw no difference in tumour cells between patients that were alive or dead at follow-up (Figure 4.22).

4.3.7.2 Unbiased clustering

As performed in section 4.3, we again used R stats package to test the differences in proportions of each cell cluster between patients that relapsed and those that did not to establish phenotypes associated with relapse. Macrophages were significantly higher in patients that did not relapse, while Tumour cell #5 was present in significantly higher numbers in patients that did relapse (Table 4.4). CD8 T cells were higher in patients that did not relapse; however, this was not significant (p=0.092) (Table 4.4). There were no differences in proportions of CD4 T cells, B cells, macrophages, granulocytes, fibroblasts, lymphatic endothelial cells, endothelial cells, or Tumour cells #1, #2, #3 or #4 (Table 4.4).

4.3.8 Impact of radiotherapy on (local) relapse

The clinical trial cohort assessed in this study reported that adjuvant radiotherapy improved local relapse (Henderson et al., 2015, Burmeister et al., 2012). Relapses in the lymph node field were more frequent in the observation group, and the 5-year cumulative incidence of lymph node field relapse as a site of first relapse was 18% in the adjuvant radiotherapy group compared to 33% in the observation group (Henderson et al., 2015). We wanted to confirm that there were no differences in the pre-treatment milieu of patients in the context of relapse, beyond establishing there were no differences between treatment allocations in Figure 4.7. To do this, we compared CD4 T cells, CD8 T cells, B cells, macrophages, NK and tumour cell

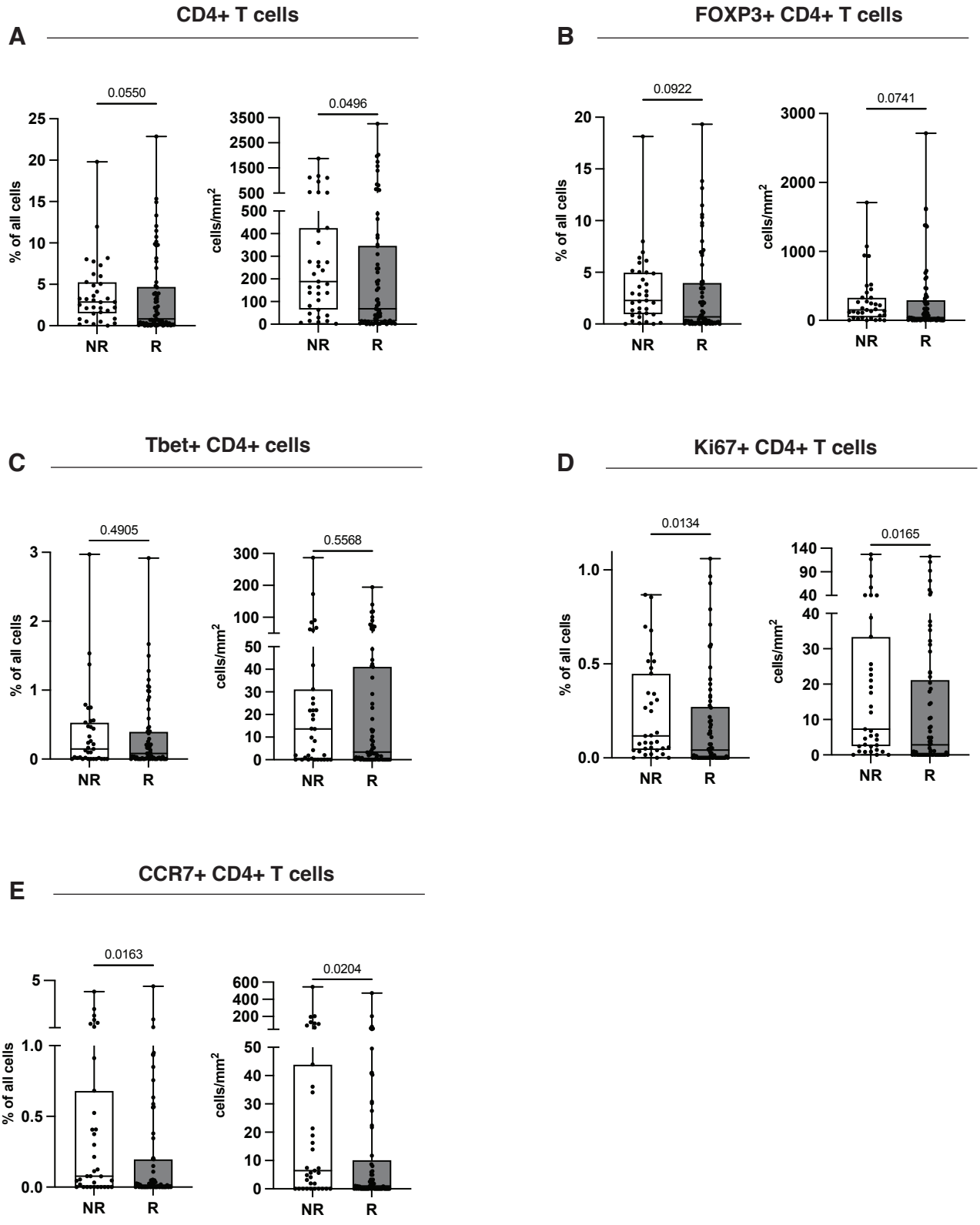

Figure 4.18 Higher quantities of CD4 T cells in tumour regions are associated with no relapse in metastatic melanoma. IMC was used to ablate pathologist-defined high-tumour regions of treatment naïve metastatic melanoma patients to assess immune phenotypes associated with relapse. Images produced from IMC underwent cell segmentation (Cell Profiler) and manual gating (FlowJo). Proportion and density of **(A)** CD4 T cells **(A)** FOXP3+ CD4 T cells **(A)** Tbet+ CD4 T cells **(A)** Ki67+CD4 T cells **(A)** CCR7+ CD4 T cells cells were compared between patients that did not relapse (NR, n=35) and those that did relapse (R, n=65). Cell phenotypes detailed in Table 4.2. Full gating strategy is detailed in Figure 4.3. Mann-Whitney test was performed to determine statistical significance.

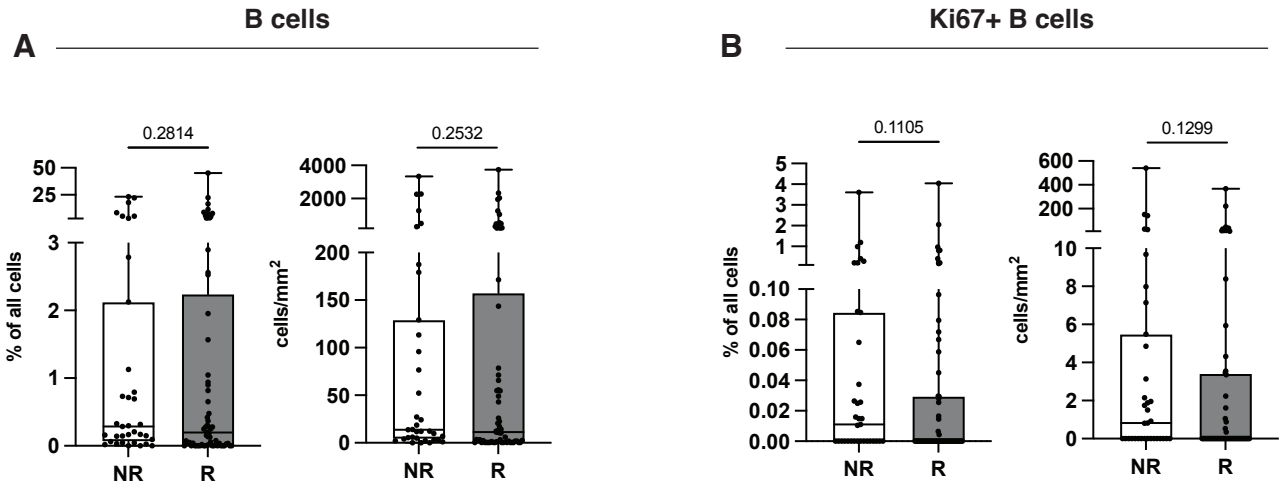

Figure 4.19 B cell quantities in tumour regions are not associated with relapse in metastatic melanoma. IMC was used to ablate pathologist-defined high-tumour regions of treatment naïve metastatic melanoma patients to assess immune phenotypes associated with relapse. Images produced from IMC underwent cell segmentation (Cell Profiler) and manual gating (FlowJo). Proportion and density of **(A)** CD20+ B cells and **(B)** Ki67+ B cells were compared between patients that did not relapse (NR, n=35) and those that did relapse (R, n=65). Cell phenotypes detailed in Table 4.2. Full gating strategy is detailed in Figure 4.3. Mann-Whitney test was performed to determine statistical significance.

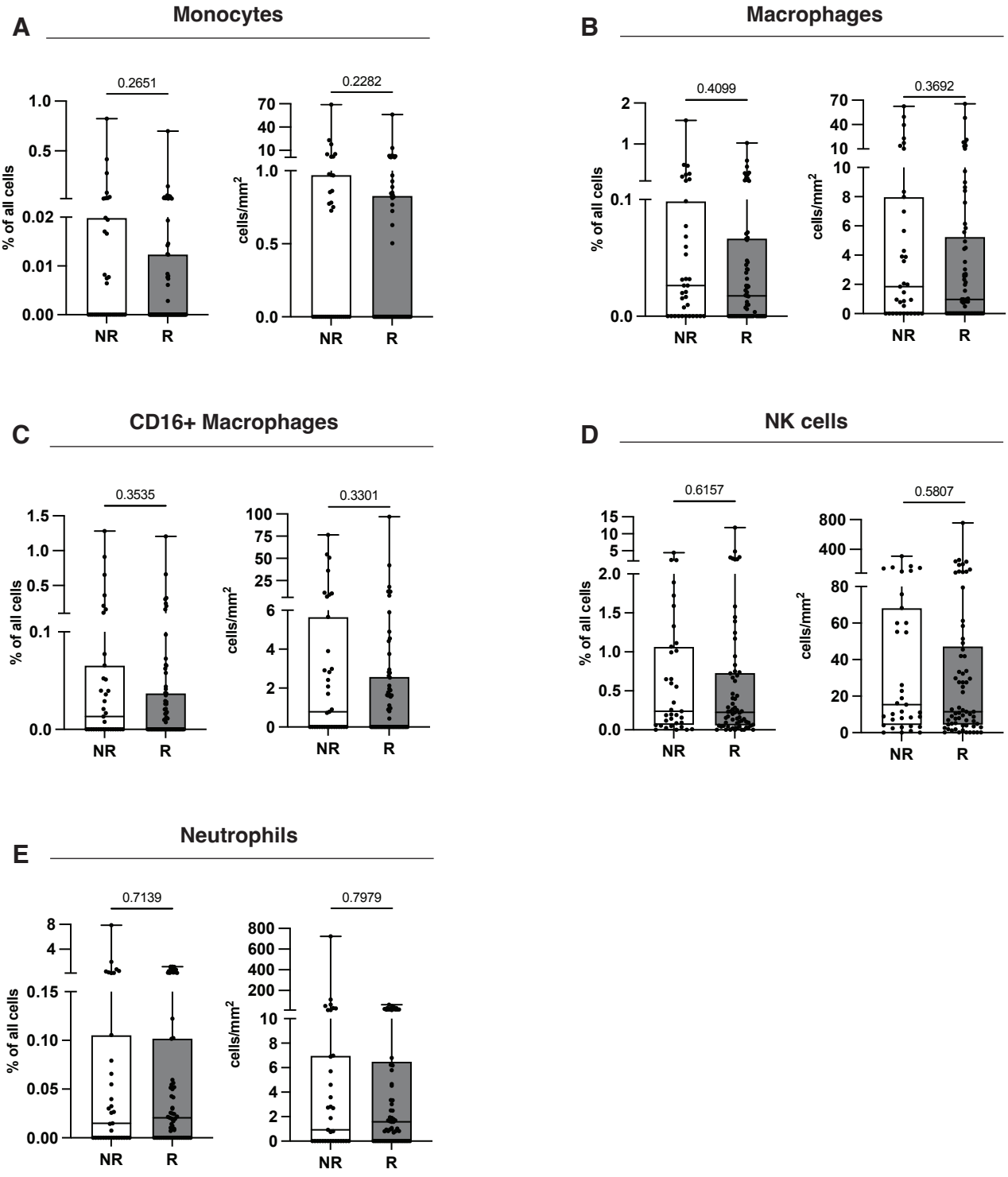

Figure 4.20 Quantities of innate immune cells in tumour regions are not associated with relapse in metastatic melanoma. IMC was used to ablate pathologist-defined high-tumour regions of treatment-naïve metastatic melanoma patients to assess immune phenotypes associated with relapse. Images produced from IMC underwent cell segmentation (Cell Profiler) and manual gating (FlowJo). Proportion and density of **(A)** monocytes **(B)** macrophages **(C)** CD16+ macrophages **(D)** NK cells and **(E)** neutrophils were compared between patients that did not relapse (NR, n=35) and those that did relapse (R, n=65). All innate cells were pre-gated as SOX10-CD45+CD20-CD3-. Cell phenotypes detailed in Table 4.2. Full gating strategy is detailed in Figure 4.3. Mann-Whitney tests were performed to determine statistical significance.

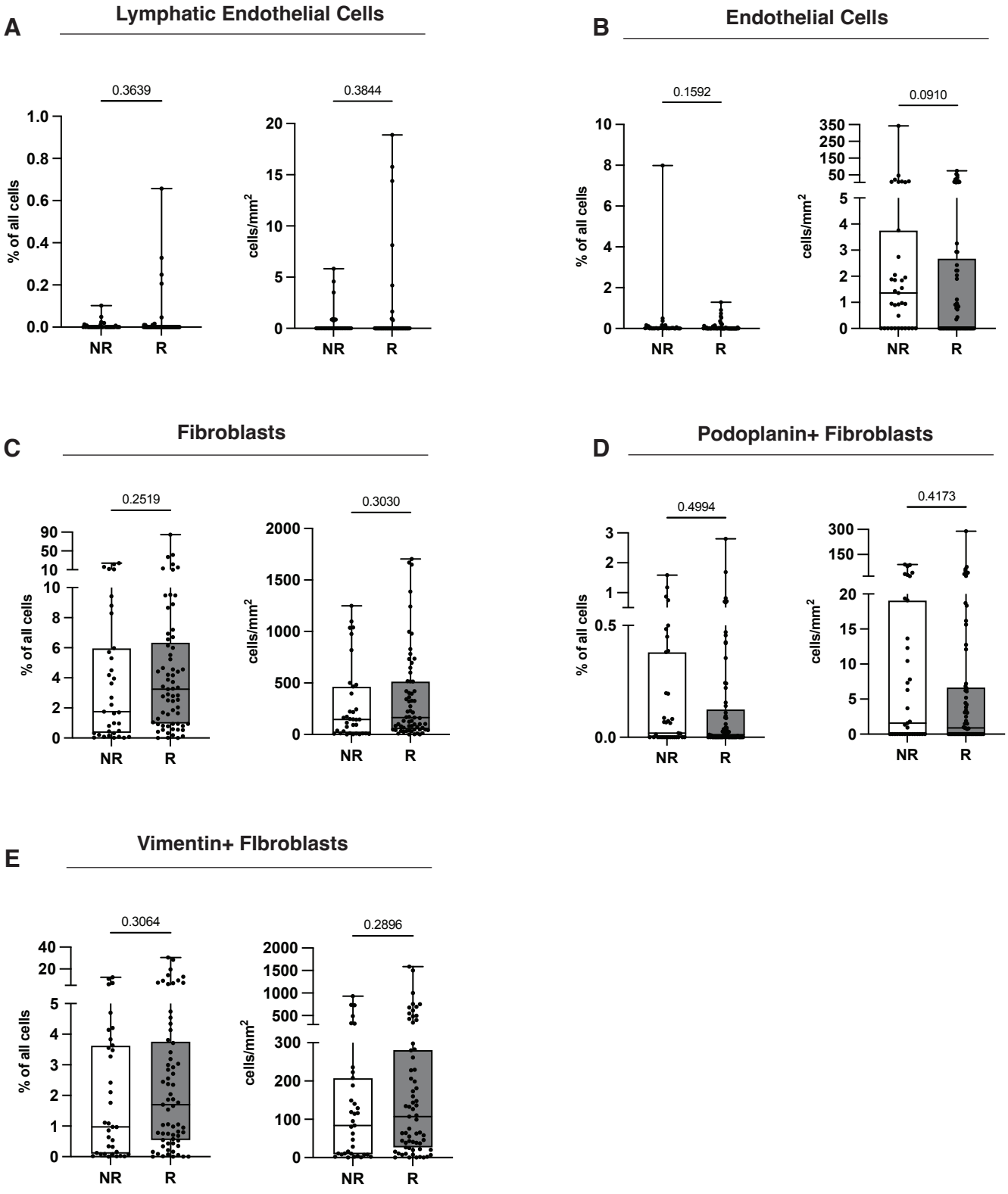

Figure 4.21 Quantities of non-leukocytes in tumour regions are not associated with relapse in metastatic melanoma patients. IMC was used to ablate pathologist-defined high-tumour regions of treatment-naïve metastatic melanoma patients to assess immune phenotypes associated with relapse. Images produced from IMC underwent cell segmentation (Cell Profiler) and manual gating (FlowJo). Proportion and density of **(A)** lymphatic endothelial cells **(B)** endothelial cells **(C)** fibroblasts **(D)** podoplanin+ fibroblasts and **(E)** vimentin+ fibroblasts were compared between patients that did not relapse (NR, n=35) and those that did relapse (R, n=65). All non-lymphoid structural cells were pre-gated as SOX10-CD45-. All non-lymphoid structural cells were pre-gated as SOX10-CD45-. Cell phenotypes detailed in Table 4.2. Full gating strategy is detailed in Figure 4.3. Mann-Whitney test was performed to determine statistical significance.

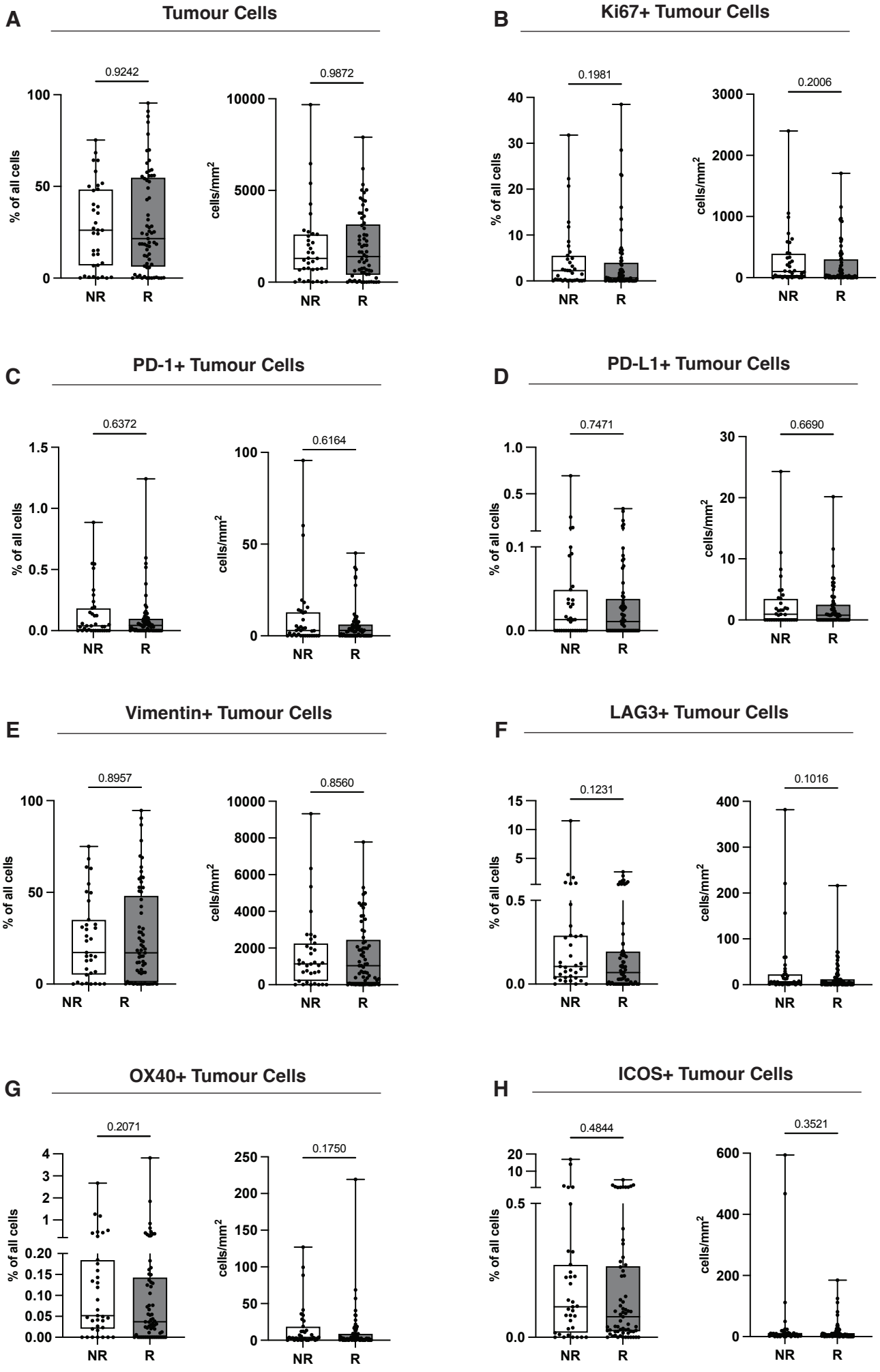
A
Tumour Cells
0.9242
0.9872
% of all cells
cells/mm2
NR
R
B
Ki67+ Tumour Cells
0.1981
0.2006
C
PD-1+ Tumour Cells
0.6372
0.6164
D
PD-L1+ Tumour Cells
0.7471
0.6690
E
Vimentin+ Tumour Cells
0.8957
0.8560
F
LAG3+ Tumour Cells
0.1231
0.1016
G
OX40+ Tumour Cells
0.2071
0.1750
H
ICOS+ Tumour Cells
0.4844
0.3521

Figure 4.22 Tumour cell quantities in tumour regions are not associated with relapse in metatstatic melanoma. IMC was used to ablate pathologist-defined high-tumour regions of treatment naïve metastatic melanoma patients to assess immune phenotypes associated with relapse. Images produced from IMC underwent cell segmentation (Cell Profiler) and manual gating (FlowJo). Proportion and density of **(A)** tumour cells **(B)** Ki67+ tumour cells **(C)** PD1+ tumour cells **(D)** PDL1+ tumour cells **(E)** Vimentin+ tumour cells **(F)** LAG3+ tumour cells **(G)** OX40+ tumour cells **(H)** ICOS+ tumour cells were compared between patients that did not relapse (NR, n=35) and those that did relapse (R, n=65). Tumour cells were pre-gated as CD45-CD3- and SOX10+. Cell phenotypes detailed in Table 4.2. Full gating strategy is detailed in Figure 4.3. Mann-Whitney test was performed to determine statistical significance.

Table 4.4 Proportions of cell clusters identified in Figure 4.6 compared between patients that relapsed and those that did not at clinical trial end point.

Cell Cluster	No Relapse [Mean value]	Relapse [Mean Value]	p value	Adjusted p value
Tumour Cell #5	0.0062	0.011	0.0011	0.015
Macrophage	0.016	0.011	0.014	0.098
CD8 T cells	0.069	0.055	0.092	0.34
Tumour Cell #2	0.23	0.26	0.11	0.34
Fibroblast	0.12	0.13	0.12	0.34
Tumour Cell #1	0.051	0.04	0.16	0.37
Lymphatic Endothelial Cells	0.037	0.033	0.33	0.66
CD4 T cells	0.029	0.024	0.39	0.68
Granulocyte	0.011	0.0072	0.45	0.7
Tumour Cell #4	0.011	0.013	0.59	0.83
Tumour Cell #3	0.22	0.21	0.77	0.89
B cells	0.037	0.035	0.83	0.89
Unidentified Cluster	0.12	0.12	0.83	0.89
Endothelial Cells	0.04	0.039	0.89	0.89

populations between patients that did not relapse and those that did in both observation only (no radiotherapy) (NR n=15; R n=33) and radiotherapy patient groups (NR n=20; R n=32).

We report no differences in proportions or densities of CD8 T cells, CD4 T cells or B cells in patients that did not relapse compared to those that did, for both treatment groups (Figure 4.23). We also saw no differences in macrophage and NK cell proportions and densities between patients that did not relapse and those that did (Figure 4.24). Similarly, tumour cells were no different between patients that did not relapse and those that did in both the observation and radiotherapy groups (Figure 4.25) These data suggest that at baseline there were no differences between the patients who subsequently received radiotherapy (treatment arm) and those who did not (control arm).

As Henderson et al. (2015) reported the impact of radiotherapy on local relapse only, we then compared immune and tumour cell densities between patients that had distant relapse (only), local relapse (only) or no relapse for both treatment allocations (Figure 4.26). Patients that had a combination of local, in transit and distant relapse were excluded from this comparison. There were no significant differences for immune cells (Figure 4.26A) or tumour cells (Figure 4.26B) when comparing patients that had a distant relapse, a local relapse or no relapse in both radiotherapy and observation groups.

4.3.8.1 Spatial analysis reveals innate and non-immune cell interactions distinguish patients who survived longer

We next wanted to use spatial information to compare how cell interactions in the TME differ between good and bad patient outcomes. Each dot or 'bubble' is coloured according to attraction (red) or avoidance (blue). Dot size corresponds to the negative log10 of p-value calculated on the difference between alive and dead patients (Figure 4.27A) or relapse versus no relapse patients (Figure 4.28A). A black circle indicates that the p-value calculated is less than 0.05.

Using these methods, we see that both endothelial cells and lymphatic endothelial cells cluster together significantly more in patients alive at follow up (Figure 4.27A). Lymphatic endothelial cells also avoid endothelial cells significantly more in patients who were alive at follow-up (Figure 4.27A). Additionally, macrophages avoid endothelial cells significantly more in

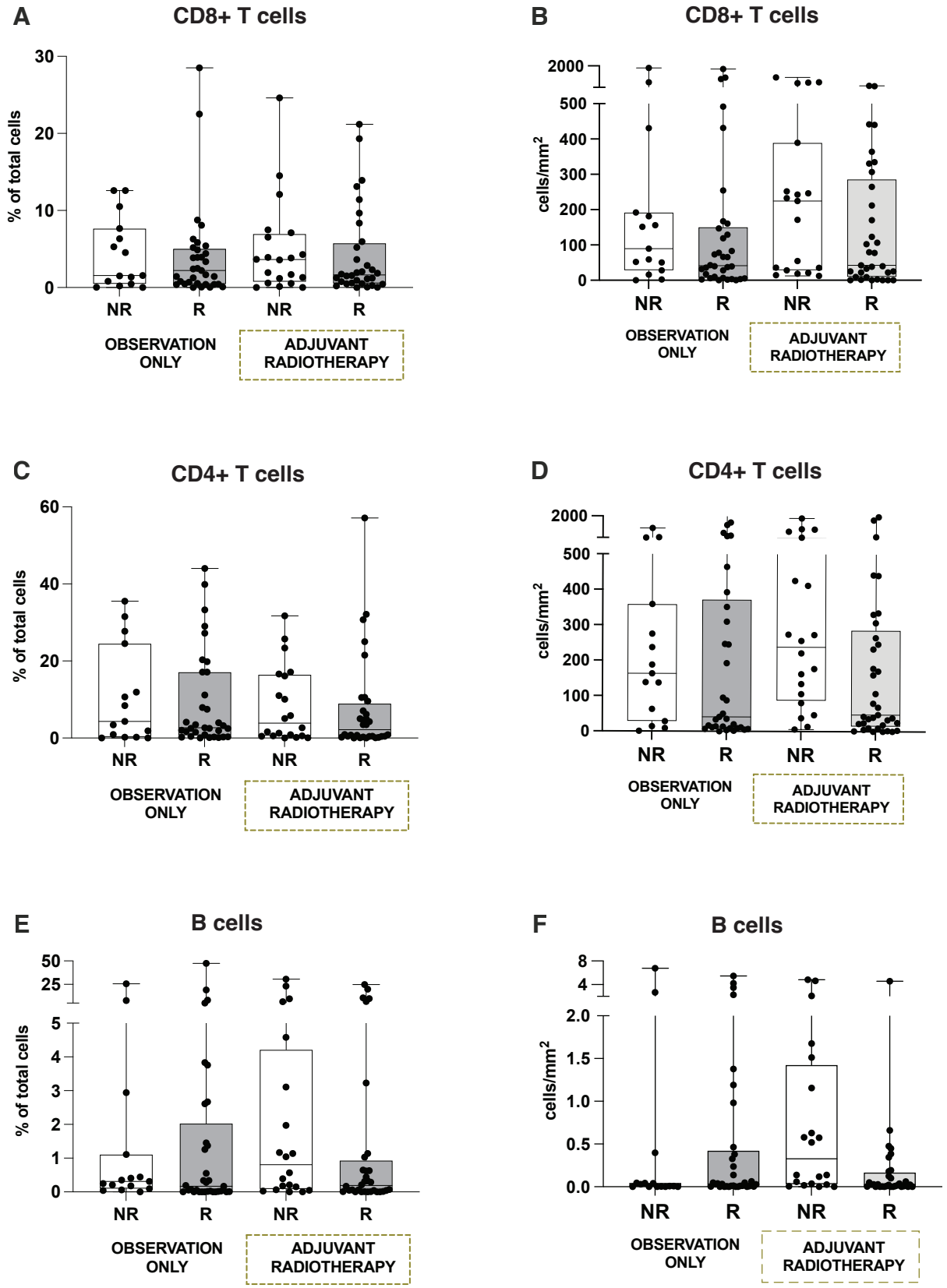

Figure 4.23 Tumour quantities of lymphocytes are not significantly different between treatment allocation and relapse conditions. Proportion of **(A)** CD8 T cells, **(C)** CD4 T cells, **(E)** CD20+ cells and density of **(B)** CD8 T cells, **(D)** CD4 T cells and **(F)** CD20+ B cells compared between those that were allocated observation only and did not relapse (NR n=15) and relapsed (R n=33), and those that were allocated adjuvant radiotherapy and did not relapse (NR n=19) and those that did relapse (R n=34). Cell phenotypes detailed in Table 4.2. Full gating strategy is detailed in Figure 4.3. Dunn's multiple comparison test performed to compare ranks.

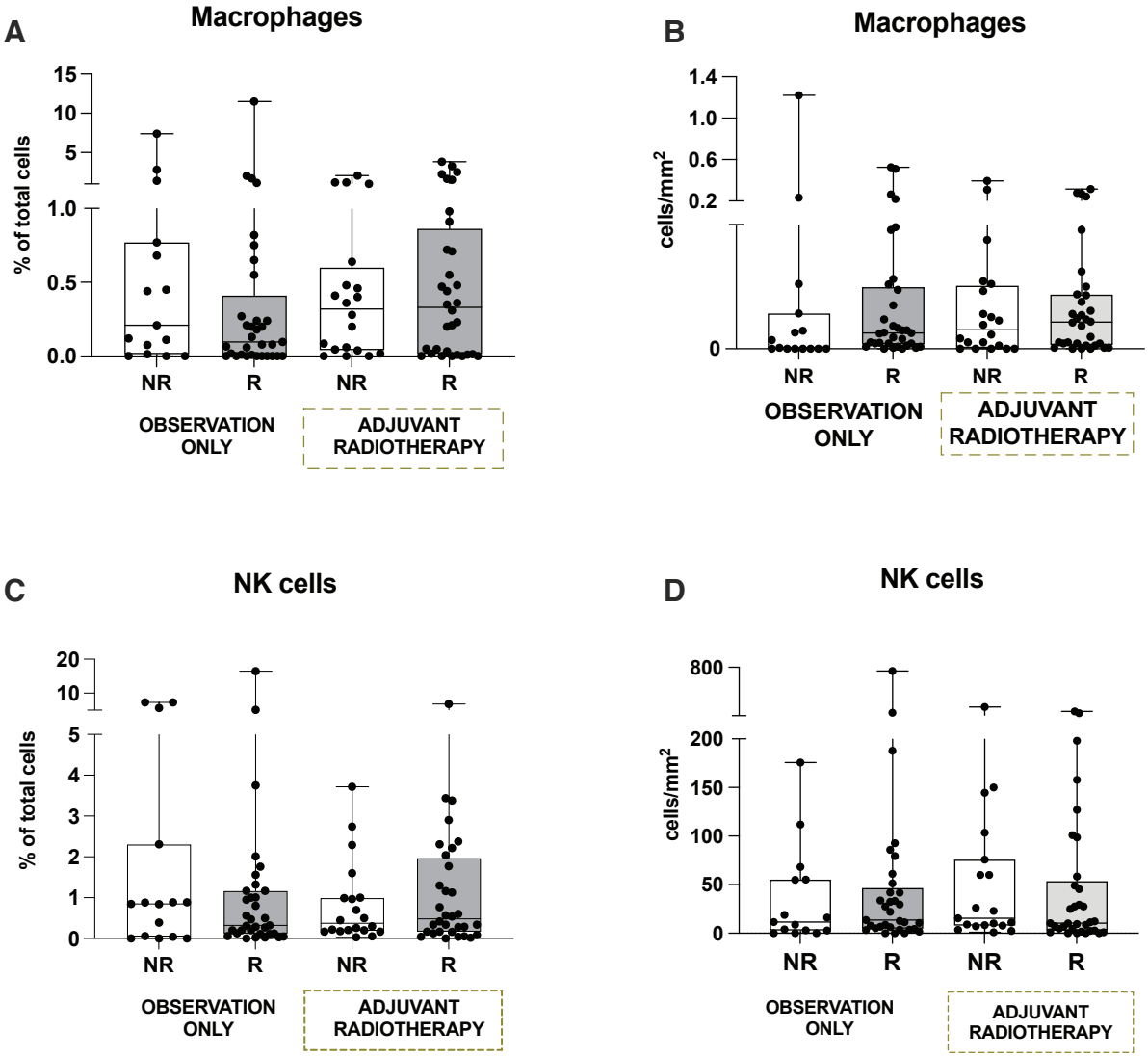

Figure 4.24 Tumour quantities of innate immune cells in are not significantly different between treatment allocation and relapse conditions. Proportion of **(A)** macrophages **(C)** NK cells and density of **(B)** macrophages and **(D)** NK cells compared between those that were allocated observation only and did not relapse (NR n=15) and relapsed (R n=33), and those that were allocated adjuvant radiotherapy and did not relapse (NR n=19) and those that did relapse (R n=34). Cell phenotypes detailed in Table 4.2. Full gating strategy is detailed in Figure 4.3. Dunn's multiple comparison test performed to compare ranks.

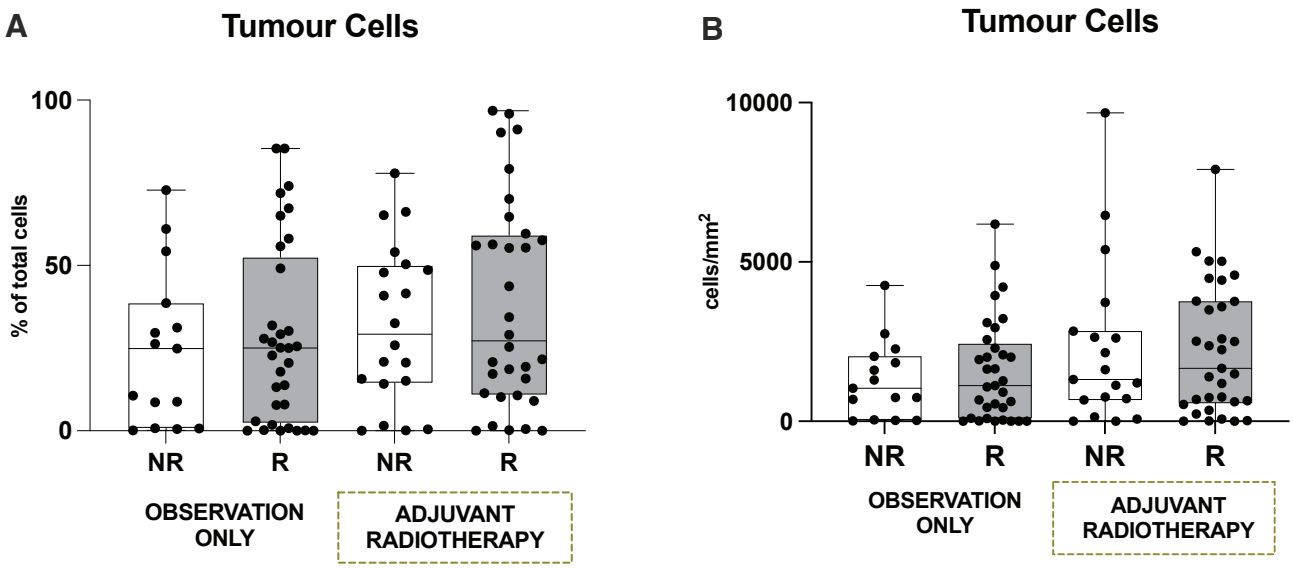

Figure 4.25 Tumour quantities of tumour cells are not significantly different between treatment allocation and relapse conditions. (A) Proportion and **(B)** density of tumour cells compared between those that were allocated observation only and did not relapse (NR n=15) and relapsed (R n=33), and those that were allocated adjuvant radiotherapy and did not relapse (NR n=19) and those that did relapse (R n=34). Cell phenotypes detailed in Table 4.2. Full gating strategy is detailed in Figure 4.3. Dunn's multiple comparison test performed to compare ranks.

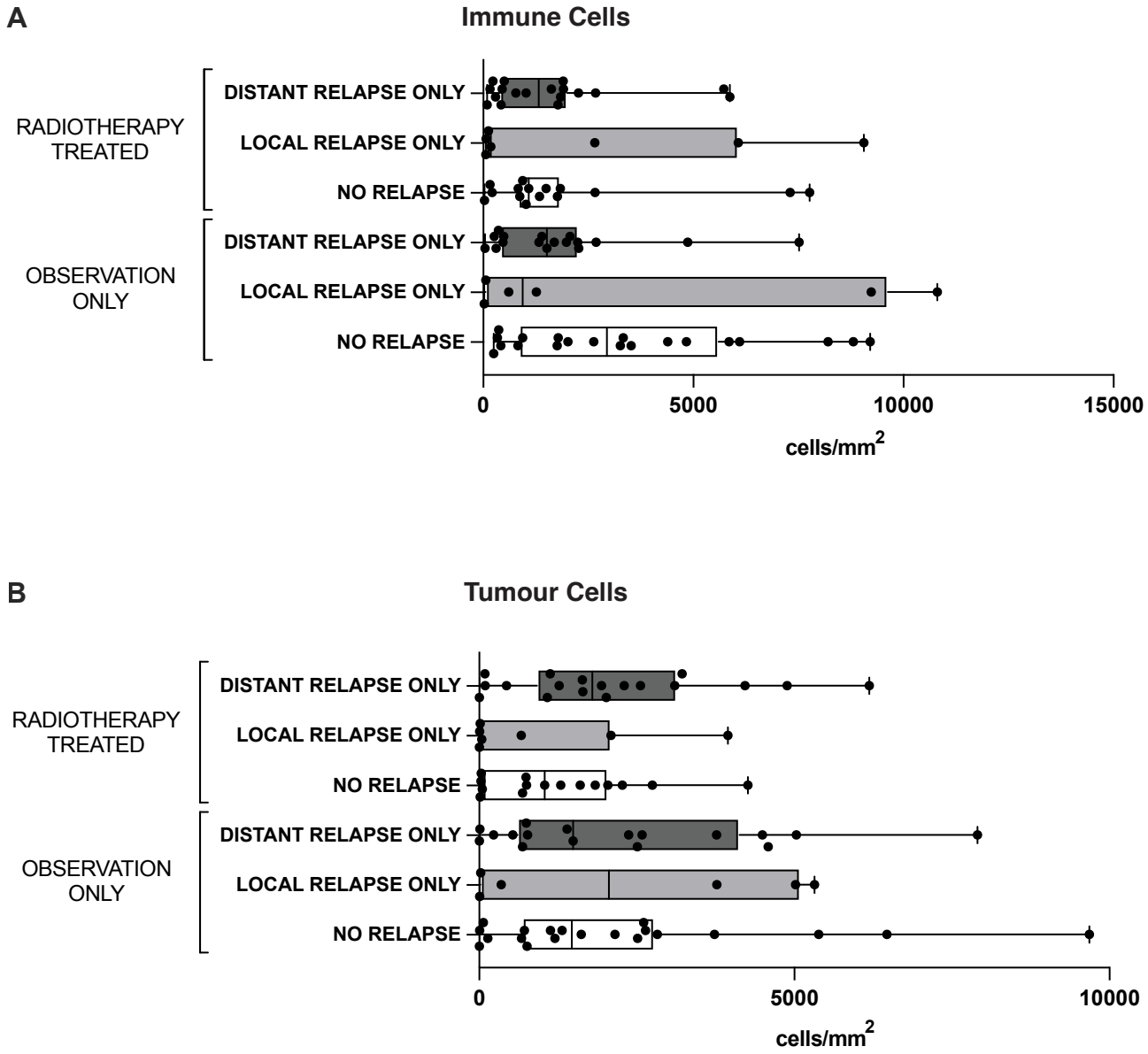

Figure 4.26 Immune and tumour cell density does not differ between relapse location or treatment allocations. IMC was used to ablate high-tumour regions of treatment naïve metastatic melanoma patients to assess immune phenotypes associated with clinical outcomes. Images produced from IMC underwent cell segmentation (Cell Profiler) and manual gating (FlowJo). Denisty of **(A)** Immune cells (CD45+SOX10-) and **(B)** Tumour Cells (SOX10+CD45-) is compared between patients allocated to radiotherapy and who had distant relapse only (n=17), local relapse only (n=6) or no relapse (n=20), or observation and went on to have distant relapse only (n=18), local relapse only (n=7) or no relapse (n=15). Patients who had a multiple different relapse locations were excluded from this analysis. Kruskal-Wallis test for statistical significance was performed (approximate p value = 0.3499). Cell phenotypes detailed in Table 4.2. Full gating strategy is detailed in Figure 4.3.

A

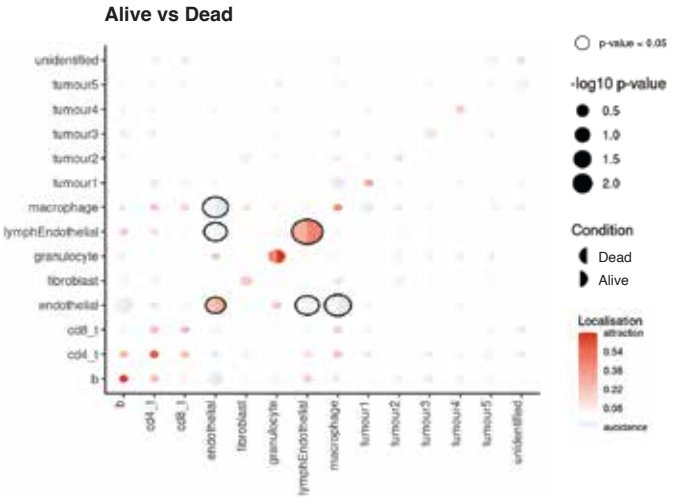

B

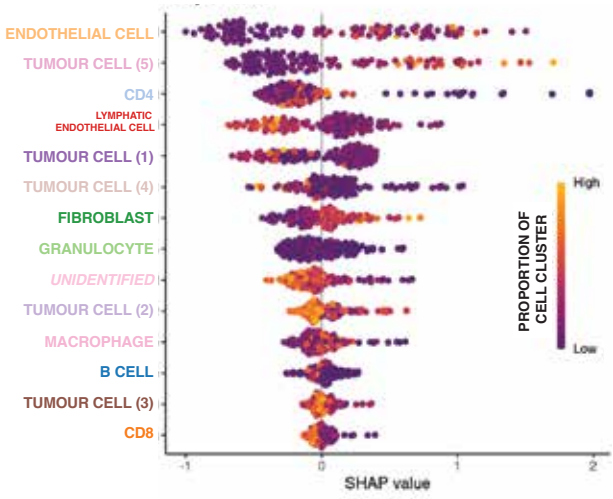

C

Lymphatic Endothelial Cell + Tumour #4

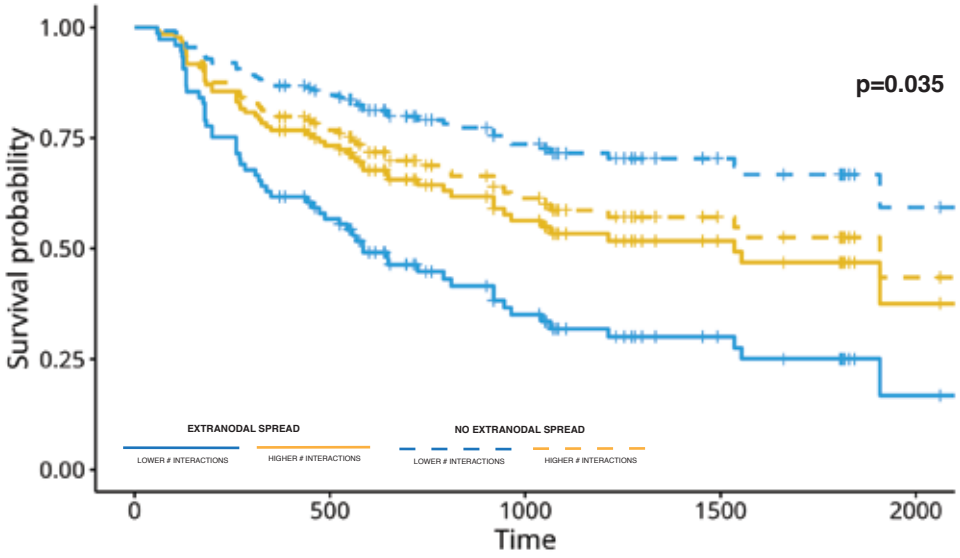

D

Fibroblast + Macrophages

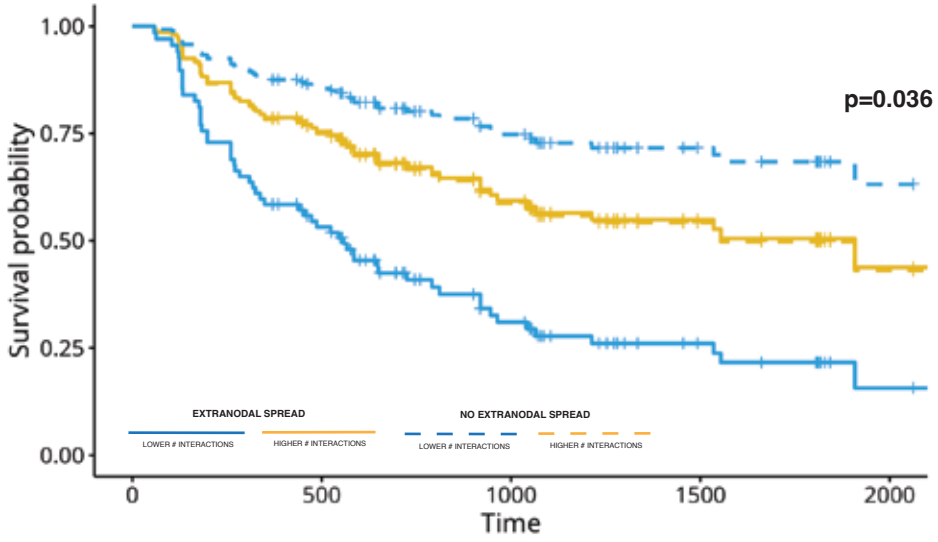

Figure 4.27 Spatial interactions associated with survival within high-tumour areas of treatment naïve metastatic melanoma. (A) Visualisation of intereactions between clusters identified in Figure 4.6 using *spicyR* R package (Bioconductor) separated by patients who were alive (n=53) and dead (n=47). Survival plots of patients grouped according to **(B)** SHAP plot showing factors that contribute to a shorter 'time-to-relapse" calculated using shapviz R package. Using this model, a positive SHAP value indicates that if a patient has this cell population (high/low proportions as indicated), this patient is more likely to relapse earlier. **(C)** Number of interactions between lymphatic endothelial cells and tumour cell #4 and **(D)** fibroblasts and macrophages, grouped by patients with extranodal spead low interactions (solid blue line), extranodal spread high interactions (solid yellow line), no extranodal spread low interactions (dashed blue line) and no extranodal spread high interactions (yellow dashed lines). Number of interactions above average were labelled 'high' and those below average 'low'. All significant interactions between cell types in patients separated by survival summarised in table 4.5.

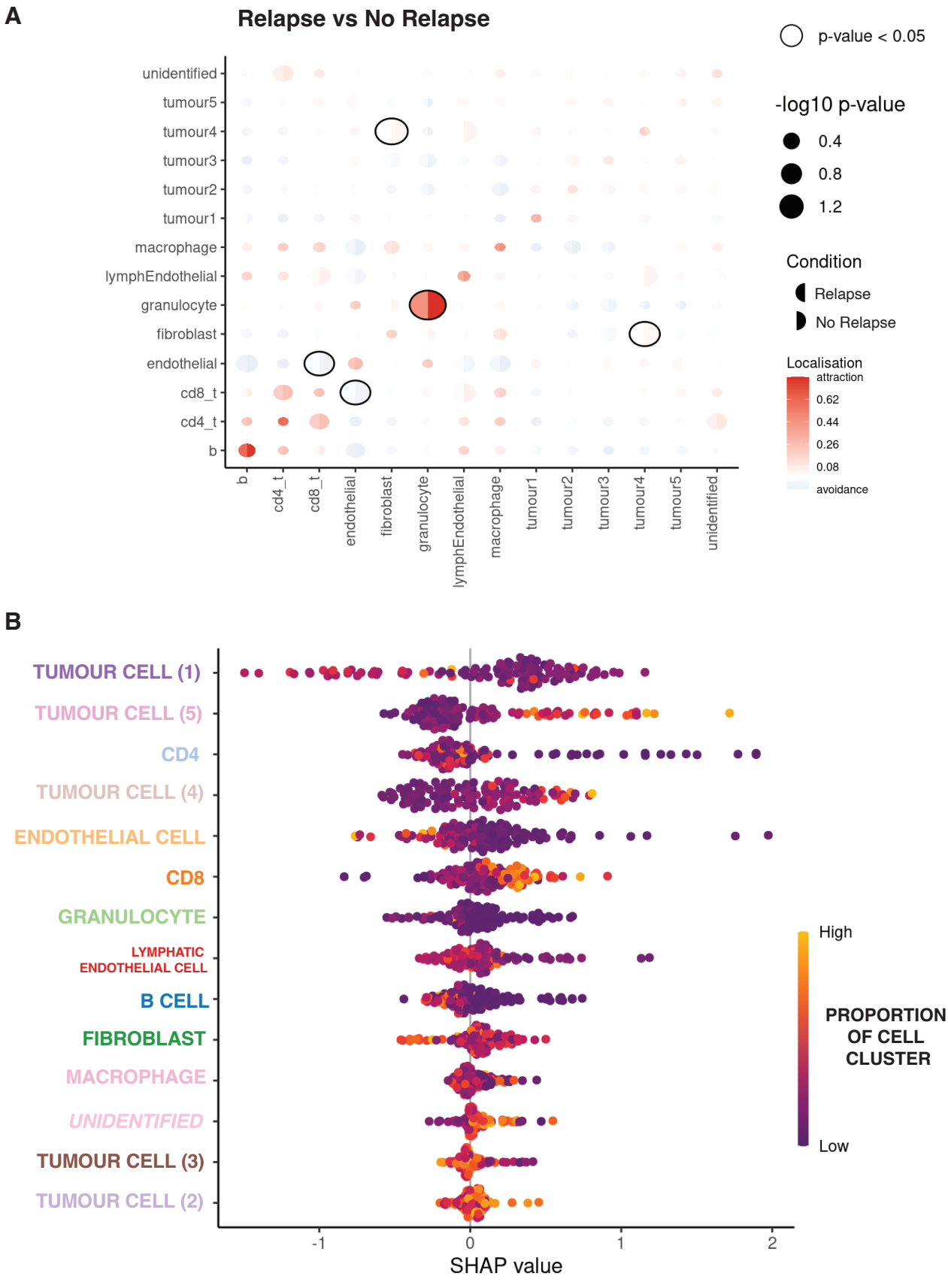

Figure 4.28 Spatial interactions associated with relapse within high-tumour regions of treatment-naïve metastatic melanoma. (A) Visualisation of intereactions between clusters identified in Figure 4.6 using *spicyR* R package (Bioconductor) separated by patients experiencing no relapse (n=35) and relapse (n=66) **(B)** SHAP plot exemplifying factors that contribute to a shorter 'time-to-relapse" calculated using shapviz R package. Using this model, a positive SHAP value indicates that if a patient has this cell population (high/low proportions as indicated), this patient is more likely to relapse earlier.

patients alive at follow-up when compared to the interactions in those that did not survive (Figure 4.27A).

To investigate the impact of the TME on how quickly a patient relapses, we conducted a 'time-to-event' test by calculating Shapely Additive Explanations (SHAP) values using R package *shapviz* (Lundberg and Lee, 2017). This package produces a model to best represent the outcome tested, by entering the time-to-event for each patient. The SHAP value is calculated using these inputs by producing a model that best fits the data given. In this SHAP plot, we are assessing the impact of each of the 14 clusters identified in Figure 4.5 on the time-to-death. Each dot represents one patient. As such, if the SHAP value for this patient is high (further to the right on the plot), the model predicts that that patient will have a shorter time-to-event. The colour of the dot indicates if it was a high (yellow) or low (purple) proportion of this cell type that contributed to the model.

Using this information to interpret the SHAP plot shown in Figure 4.27D, we can deduce that, according to this model, a patient with a high proportion of endothelial cells within high-tumour regions will have a shorter time-to-death. It also predicts that higher proportions of tumour cell #5 result in a shorter-time-to-death (Figure 4.27B). Very low proportions of CD4 T cells, low proportions of lymphatic endothelial cells and low proportions of Tumour cell 1 and 4 may also lower your time-to-death (Figure 4.27B). Proportions of fibroblasts, granulocytes, unidentified cluster, tumour cell 2, macrophages, B cells, Tumour cell 3 and CD8 do not impact time to death in this model (Figure 4.27B).

To investigate the impact of extranodal spread and cell interactions on survival, we compared all cell interactions shown in Figure 4.27A by conducting a pairwise statistical analysis to test if there are spatial relationships that contribute to patient outcome that is not explained by survival or extranodal spread alone. Significant interactions produced by this test are summarised in Table 4.5.

In order to visualise these results, we have plotted the top two significant interactions as survival plots (Figure 4.27C, D). Patients are first separated into extranodal spread (dashed line) or no spread (solid line), and within these groups, high (yellow) and low (blue) interactions.

We saw that patients with no extranodal spread and a high number of interactions between lymphatic endothelial cells and tumour cell #4 had the highest survival probability, followed by patients with extranodal spread that had a low number of interactions (Figure 4.27C). We then see that this relationship flips for patients with extranodal spread, as the lowest survival probability is recorded for patients with extranodal spread with a low number of interactions between lymphatic endothelial cells and tumour cell number 4, compared with those who had a high number of interactions (Figure 4.27C).

The second most significant interaction identified was the interaction between fibroblasts and macrophages (Table 4.5). Separating the cohort out into the four groupings outlined above, we saw patients with no extranodal spread and a low number of interactions between fibroblasts and macrophages had the highest survival probability (Figure 4.27D). However, a patient with high number of interactions between fibroblasts and macrophages has a very similar survival probability regardless of extranodal spread status, shown by the overlapping dashed and filled in yellow lines (Figure 4.27D). The lowest survival probability is recorded for patients with no extranodal spread that have a low number of interactions between fibroblasts and macrophages.

4.3.8.2 Spatial analysis reveals immune, tumour and structural cells associated with relapse

Comparing spatial interactions between patients that relapsed and those that did not using spicyR, we found that granulocytes are significantly more attracted to each other in patients that did not relapse compared to those that did (Figure 4.28A). We also found that tumour cell #4 is significantly closer to fibroblasts in patients that do not relapse, and endothelial cells avoid each other significantly more in patients that did not relapse (Figure 4.28A).

We again used a SHAP plot (detailed in section 4.2.8.1) to identify proportions of cell clusters identified in Figure 4.5 that contribute to a patients' time-to-relapse (Figure 4.28B). This analysis suggests that having a low proportion of tumour cell #1, a high proportion of tumour cell #5, and a moderate to high proportion of tumour cell #4 will result in a shorter time-to-relapse (Figure 4.28B). It also suggests that having a low proportion of both CD4 T cells and endothelial cells will result in a quicker time-to-relapse (Figure 4.28B).

4.4 Discussion

In this study, we sought to identify methods to analyse IMC data that were accurate, economically efficient, and accessible for basic science researchers. By collaborating with specialist clinicians and bioinformaticians, we were able to employ methods that incorporated clinical information such as how long a patient took to relapse or die, factors such as extranodal spread as well as in depth spatial analysis that looked for relationships between cells and allowed comparison of the entire tumour landscape.

Cell segmentation is one of the first steps performed in high dimensional tissue analysis, and as such, inaccurate segmentation impacts all further analysis. Common issues with cell segmentation include over and under segmentation, accurately detecting clumped and irregularly shaped cells, and ensuring that tissue containing cell types of different morphologies are detected accurately. In this chapter, three different cell segmentation approaches were taken. I will discuss the advantages as well as the issues encountered with each method. Cell profiler was one of the first free cell segmentation tools, developed to be able to process a large amount of image-based data in less time and with less sophisticated computers than previously available in order to meet the needs of researchers in biology (Carpenter et al., 2006, Kamentsky et al., 2011). Cell segmentation in cell profiler is performed by first identifying the primary object such as the nucleus, followed by secondary object, often the cell boundaries with flexible parameters to be able to detect cells with many different morphologies. The algorithm uses thresholding to identify objects within acceptable size parameters that the user inputs. Once the cell objects are identified, the mean intensity of the markers are measured in the cell, and in this study were exported as a csv file for downstream analysis in FlowJo and R. This approach took considerable time as each sample was inspected and analysed individually. An AI-based cell segmentation program HALO (Indica Labs) was also used to analyse a small number of patient samples to compare with other programs used in this study (Figure 4.5). As this is a commercial program, there is little information available regarding the specific algorithms used to identify cells. However, it does require the user to detail a marker as nuclear, cytoplasmic or membranous, and to input a range of acceptable nuclei and cell size. Despite the assistance of inbuilt algorithms, it is not feasible to analyse more than 10 markers across multiple samples due to the time and tissue staining experience required to perform manual thresholding for each marker. The trade-off with this approach is that it results in accurate analysis, as the researcher performing the analysis has examined the samples in detail and has picked up errors or artifacts. The third cell segmentation method in this study was performed

by *simpleseg*, an R package developed to identify cells using watershed-based segmentation methods (Canete, 2024). This method did not require any manual input beyond identifying nuclear stains (DNA-Ir). This approach will not work for all tissue types but has been shown to produce accurate results in melanoma and squamous cell carcinoma (SCC) (Ferguson et al., 2022). The candidate inspected the cell segmentation masks for accuracy and was satisfied. This approach was extremely time efficient, and the code is publicly available with forums, allowing for collaboration between researchers.

Cells were identified in this study by either cell-targeted analysis to identify phenotypes well established in the literature, or by supervised clustering methods. The first approach, manual gating, successfully identified cell types, and we found some of these populations differed between patients when grouped by outcome. As this approach may introduce bias from the scientist, as we only 'see what we are looking for', we also performed supervised clustering of the same data. We were able to identify similar populations using this method, and we also found differences in these cell populations between patients grouped by outcome. Differences between these two approaches may be attributed to different cell segmentation methods (discussed previously), smaller populations not identified by whole-experiment analysis as well as immune and tumour cell heterogeneity. Performing either approach alone would have resulted in fewer outcome-related features identified and a narrower understanding of the TME. In conclusion, identifying cell populations in human tissue using high-parameter data requires the researcher to look at the data through multiple methods. The multiple methods used in this study allowed us to produce a detailed and robust picture of the tumour microenvironment in metastatic melanoma.

Producing interpretable, accurate and reproducible data from high-parameter experimental approaches such as IMC requires a strong collaboration between basic science researchers, bioinformaticians and clinicians. It also requires increased skill development and support in coding skills for basic science researchers that until recently, has not been required. This skill development and collaboration is better achieved by open source, transparent methods that employ R or Python as they often allow for alterations to tailor to specific needs. In contrast, 'closed-box' systems like HALO may keep up with changes in the field with development of new modules and program updates, these often do not meet the specific needs of researchers or are implemented too late to be useful. Additionally, inexpensive analysis approaches are far more accessible for researchers, particularly when experiments like IMC are already extremely

costly. For these reasons, open-sourced, customisable analysis pipelines developed with bioinformaticians and inspected for accuracy are the most sustainable approaches to address clinical questions from tissue samples.

Our study found many novel cell phenotypes and cell interactions in the treatment-naïve metastatic melanoma TME associated with improved patient prognosis i.e. patients that survived and did not relapse. Our data mirrored the understanding in the field that the TME of metastatic melanoma is made up of a heterogeneous mix of T cells, B cells, innate cells, structural cells and tumour cells. We mapped the TME across 100 patients using 42 protein markers, an approach that, until now, has only been done using a small number of markers. The differences in proportions of cell types between the approaches reported in this study can be attributed to the use of alternate cell segmentation approaches, phenotype identification, and statistical analysis. We set out to perform different analysis approaches to identify the method that most accurately represented the data, was able to be visualised in the tissue samples, and was able to address questions regarding clinical outcomes. However, these data alone are simply quantities of cells present, and without spatial understanding, we can only deduce part of the biology of metastatic melanoma. When we investigated the spatial data, we saw a much more comprehensive understanding of the TME of metastatic melanoma.

Overall, we saw that the TME of metastatic melanoma is made up of a large proportion of T cells, NK cells, fibroblasts and tumour cells as well as B cells, macrophages, monocytes, neutrophils and endothelial cells. When we looked at what cells interacted most across all patients, we saw some interesting results. CD4 and CD8 T cells were located closely together, along with B cells, and these cells also interacted closely with macrophages (Figure 4.7A). This was not surprising as all samples were lymph-node metastasis, and human lymph nodes contain high proportions of T and B cells (Krishnamurty and Turley, 2020). Lymphatic endothelial cells were located closest with B cells and CD4 T cells. Granulocytes and endothelial cells interacted mostly with each other compared to any other cell. Tumour cells interact mostly with other tumour cells, and tumour cell #4 and #5, characterised by a lack of expression of checkpoint markers seen in tumour cells #1, #2 and #3 including PD-L1, PD-1, IDO, OX40 (Figure 4.6F). Tumour cells #4 and #5 also interacted more with immune cells than tumour cells #1, #2 and #3 (Figure 4.7).

Although CD4 T cells are present in higher proportion in nodal melanoma samples, CD8 T cells are often attributed as the most important anti-tumour cell. Our analysis suggests that CD4 T cells are more important than CD8 T cells in tumour control as revealed by the SHAP analysis where lower CD4 T cell numbers were associated with shorter time to death. Comparing CD4 and CD8 T cell interactions across the whole cohort highlighted that CD4 T cells were more closely located with B cells, lymphatic endothelial cells and macrophages rather than direct contact with tumour cells. CD4 T cells provide help through soluble mediators such as cytokines that shape the local environment towards pro or anti-tumour immunity (Poncette et al., 2022, Xie et al., 2023, Speiser et al., 2023). Recently, multiple groups have demonstrated the important anti-tumour roles of CD4 T cells in melanoma (Kruse et al., 2023, Oliveira et al., 2022, Bawden et al., 2024). We also saw that endothelial cells and granulocytes were closely located together in our samples. This makes sense as tumour tissue often undergoes fibrosis and vascular dysfunction via the interplay between endothelial cells, neutrophils and platelets (Dehghani and Panitch, 2020, Zhang et al., 2023).

When we examined the impact of the TME on clinical outcomes, it was clear that 'immune rich' tumours were associated with survival. Patients that survived had a more activated, proliferating and functional immune compartment. This was shown by the higher number of both overall and proliferating lymphocytes as well as a higher tissue resident (CD103+), cytotoxic (granzyme B+) in patients that survived according to our targeted cell analysis (Figure 4.9). The CD8 T cell cluster identified by unbiased clustering also expressed Ki67, T-bet and CD103, suggesting it was a proliferating tissue-resident effector CD8 T cell (Rovira et al., 2016, Li et al., 2013, Kao et al., 2011). Unsurprisingly, this CD8 T cell cluster was significantly higher in patients that were alive at follow-up compared to those that died ($p=0.0056$, Table 4.3). Similarly, patients that did not relapse had more CD4 and CD8 T cells, tissue-resident CD103+ CD8 T cells and proliferating CD4 and CD8 T cells (Figure 4.16 & Figure 4.17). Together our data clearly demonstrates the link between inflamed tumours and patient survival or relapse. One of the key findings from this study is the behavioural aspect of the spatial data. We found that CD8 T cell behaviour, when compared to other immune cells, was completely different and there were closer interactions with tumour cells. This suggests that the TME factors that determine cell location are likely to be different for CD8 T cells and other immune cells. Although chemokines such as CXCL-9, 10 and 11 play a key role in the recruitment of T cells to the tumours, the behaviour of CD8 T cells was different from that of CD4 T cells, suggesting potential differences even between the two T cell populations. Within

melanoma tumours, CD4 T cells were found to largely interact with CD8 T cells, macrophages and B cells.

In our data we saw CD16+ macrophages were present in higher numbers in patients in patients alive at clinical trial conclusion when compared to those who were deceased (Figure 4.11). In support of this, the macrophage population identified by clustering was higher in patients that did not relapse, suggesting an important anti-tumour function for this subset (Table 4.3). This macrophage population also expressed CD45, FXIIIA, CD16, T-bet, CD14 and CD8 (Figure 4.5). The expression of CD16+ macrophages have been identified as an important biomarker of response to ICI in melanoma patients, as well as important for anti-tumour functionality of monocytes (Lee et al., 2023, van Ravenswaay Claasen et al., 1992, Yeap et al., 2016, Adegoke et al., 2023). This study adds important evidence of anti-tumour macrophage phenotypes to the field.

Despite seeing no differences in proportions of granulocytes between patients that relapsed and those that did not (Figure 4.11 & Table 4.4), granulocytes were clustered together more closely in patients that did not relapse (Figure 4.26A). A higher neutrophil/lymphocyte ratio is associated with worse outcomes in melanoma, and both neutrophil infiltration and neutrophil extracellular traps (NETs) have been associated with necrosis in melanoma (Pinto-Paz et al., 2021, Weide et al., 2023, Dabrosin et al., 2019). The capabilities of neutrophils to elicit anti-tumoral responses is known to exist but are less clearly known at this time (Yan et al., 2023). One group investigated the impact of NETs in melanoma in vitro assays and saw that NETs inhibited tumour cell migration and contributed to melanoma cell death and necrosis. (Schedel et al., 2020).

This work highlighted the complex roles of endothelial cells within the TME of metastatic melanoma. Lymphatic endothelial cells were significantly higher in patients that survived in both our targeted analysis ($p=0.0096$, Figure 4.12A) as well as our alternate unbiased analysis approach in ($p=0.012$, Table 4.3). Our targeted analysis also found endothelial cells were increased in patients that survived (Figure 4.12). Interestingly, we saw that a higher proportion of endothelial cells and a low proportion of lymphatic endothelial cells contributed to shorter survival time, while a lower proportion of endothelial cells contributed to a shorter time to patient relapse (Figures 4.27 & 4.28). We then looked at the way endothelial cells were interacting with other cells within the TME to try and contextualise these results. We saw that

lymphatic endothelial cells clustered together, and endothelial cells clustered together in patients that survived, mirroring our proportional results stated earlier (Figure 4.27). Perhaps more surprising, we found that macrophages and endothelial cells were avoiding each other significantly more in patients that survived, and lymphatic endothelial cells were avoiding endothelial cells significantly more in patients that survived (Figure 4.26A). We also saw that endothelial cells avoid CD8 T cells significantly more in patients that did not relapse compared to those that did (Figure 4.27A). This could suggest this endothelial cell cluster is suppressive and drives the tumour microenvironment towards this suppressive phenotype when it interacts with other cells such as macrophages and CD8 T cells. This is supported by the expression of inhibitory checkpoints such as PD-L1, as PD-L1-expressing tumour endothelial cells induce suppression of CD8 T cells via PD-L1/PD-1 interaction (Yu et al., 2023, Dieterich et al., 2017, Taguchi et al., 2020).

Unsurprisingly, as our samples were high-tumour regions, tumour cells made up the largest proportion of cells within a sample across all our analytical approaches (Figure 4.4 - 4.5). When we compared tumour cell populations between patient outcomes using the manual identification of cell populations, we saw no differences in tumour cell proportion or density (Figure 4.13 & Figure 4.21). However, two of the five tumour cell clusters identified using the unbiased approach in this project were found to be significantly different between patients separated by relapse and survival outcome. This shows the importance of considering a multitude of approaches to investigating the tumour microenvironment to find predictors of outcome.

Tumour cell #1 was characterised by high expression of checkpoint receptors e.g. ICOS, Lag3, OX40, VISTA, IDO and PD-L1 (Figure 4.5F). This tumour cell appears to be associated with better patient outcomes. This may be because tumour cell #1 avoids macrophages, CD4 and CD8 T cells more than any other tumour cell, thus limiting the ability of it to drive an exhausted phenotype in these CD8 T cells (Figure 4.7). Tumour cell #2 was found to be significantly higher in patients dead at follow-up compared to alive ($p=0.03$). Tumour cell #2 had a high expression of Ki67 and vimentin, a protein associated with mesenchymal cells and increased metastasis in melanoma (Kuburich et al., 2022, Paulin et al., 2022, Qendro et al., 2014). Tumour cell #3 was not associated with any clinical outcome.

Higher proportions of tumour cell #4 appears to result in a shorter time to relapse but a lower proportion of tumour cell #4 is associated with shorter time to death (Figure 4.26B & Figure 2.7B). We know that across all patients, tumour cell #4 is located closest to endothelial cells, macrophages, fibroblasts and tumour cell #1 (Figure 4.7). The average distance between tumour cell #4 and fibroblasts was significantly higher in patients that relapsed compared to those that did not, despite no differences in proportions of these cells (Figure 4.28, Table 4.4). More interactions between tumour cells and fibroblasts are associated with tumour cell invasion and ECM remodelling in multiple cancers, including melanoma (Yamaguchi and Sakai, 2015, Ziani et al., 2017, Zhou et al., 2020, Liu and Mak, 2022). Additionally, lymphatic endothelial cell interactions with tumour cell #4 was identified as an interaction that had a complex interplay with extranodal spread status and survival (Figure 4.26C). In patients with extranodal spread more interactions between lymphatic endothelial cells and tumour cell #4 was associated with better survival probability, while in patients with no extranodal spread this same interaction was associated with worse survival probability. CD56 expression on tumour cells, as seen on tumour cell #4, has been seen in melanoma and has also been shown to mediate tumour cell binding with endothelial cells (Zocchi et al., 1993, Steppert et al., 2020, Geertsen et al., 1999). Although these findings did not identify an association of CD56 expression on endothelial cells with survival, it suggests that this interaction may be assisting dissemination of tumour cells from the site of metastasis within the lymph node to other distant sites, leading to disease progression. It does not, however, explain why this interaction may be a good thing for patients that already have extranodal spread.

Despite tumour cell #5 occupying a small proportion of total cells (mean = 0.98% of total cells, Figure 4.5H), it was present in significantly higher proportions in patients that died compared to those alive at follow-up ($p=0.015$), as well as in patients that relapsed compared to those that did not ($p=0.0011$). We also saw that a high proportion of tumour cell #5 was associated with a shorter time to both death and relapse (Figure 4.26B & Figure 2.7B). Tumour cell #5 in our data differs from the other tumour cell clusters by lack of expression of many of the proteins tested in IMC (Figure 4.5). This may be contributing to its association with bad outcomes, as expressing less checkpoint receptors or tumour cell associated markers may results in lower recognition by the immune system, resulting in tumour progression. These data clearly show that quantification alone is not enough to decipher underlying biology within tissues. We must look further to undercover relationships between cells to understand how tissue biology is linked with patient outcomes such as survival and relapse as discussed in this study.

There remain multiple limitations of this study. As this study was discovery work, we reported p values rather than adjusted p values when discussing proportional differences between patients. However, if these populations were investigated as possible clinical biomarkers, more stringent benchmarks would be required. Much of this study pursued immune and tumour cell phenotyping and subtyping. In this approach, we aimed to not simply identify cell populations, but to consider what this information provides us regarding functional roles and relationships in the TME. This approach attempts to avoid the common pitfalls of employing experiments that identify more and more markers without proper examination of the data produced. Further to this, identifying protein targets in FFPE tissue as performed in this chapter only depicts one 'snapshot in time'. It was for this reason that at the conclusion of this study we looked for complementary approaches to better appreciate the functional potential of individual cells.

In conclusion, this study identified multiple cellular phenotypes and relationships in the TME of metastatic melanoma by employing multiple methods to analyse high-parameter data. This study then applied these findings to identify cellular features that were associated with relapse and survival of melanoma patients.

5 Combining spatial transcriptomics and spatial proteomics to map the immune landscape of tumours

5.1 Introduction

In the previous chapter we developed methodology for mapping cellular interactions within tumours. Interaction was defined based on the distance between cells (<20um). While this provides a useful way to determine the interactions, the nature of such interactions are unknown. If the molecular pathways could be identified within cells that are involved in interactions, we will then be able to determine the nature of the interactions and how likely they contribute to pro or anti-tumour activities.

Understanding the cellular interactions that are within the TME therefore requires not only a single cell proteomics (e.g. IMC) approach, but also the mapping of molecular pathways at single cell resolution. As technology platforms become more and more available, pan-omics performed on a single slide could provide greater clarity on what each and individual cellular interactions could mean to tumour development, control and immune escape mechanisms. The use of spatial transcriptomics in the field of immunology has resulting in many exciting discoveries in the last few years (Janesick et al., 2023, Krausgruber et al., 2023, Grauel et al., 2020, Chen et al., 2020). Unfortunately, current spatial technologies have limitations and do not have the capacity to enable multi-omics on a single slide. Each omics will have to be done separately on different slides and then combined for analysis. This is a major drawback as overlay of protein staining with transcriptomics performed on different tissues sections may not be accurate.

The aim of this chapter was to develop methods to determine the molecular signatures of cells within the TME that could be combined with protein stains. Initial focus was on single mRNA stains combined with mIHC. We also develop methods for spatial transcriptomics using the 10X Xenium platform. This technology is new (released in 2024) and full protocols for using FFPE sections have not been validated. The panel used in this study included 377 gene targets that were selected for identifying cells in human tumour tissue. Targets are identified by specific probes hybridised to the target mRNA followed by rolling circle amplification and detection of the product through multiple imaging cycles. We used the Xenium *in situ* platform to analyse the same TMA used in chapter 4 that contained biopsies from high-tumour regions

of tumours from 100 metastatic melanoma patients to identify cells within the TME that were associated with relapse and survival. In performing this experiment on samples previously acquired using IMC we also aimed to compare the data obtained by both approaches. Finally, in this chapter, we also develop a protocol to combine transcriptomics with single cell proteomics (IMC) to enable both cellular and molecular mapping on the same tissue section.

5.2 Materials and Methods

5.2.1 Experimental Design of Xenium in situ hybridisation study

TMA used in this study was same as chapter 4. Ethics and cohort details are outlined in section 4.2.1. TMA was split across two custom xenium analyzer slides (10X genomics) and *in situ* hybridisation was performed over 2 days and imaged for 2 days immediately after staining. 10X Genomics published that the Xenium analysis protocol is non-destructive and as such, staining can be performed post-acquisition. Phenocycler fusion (PCF) antibody staining followed by H&E staining was performed on slide 1, and imaging mass cytometry was performed on slide 2. Slide 1 was stored for 24 hours before PCF staining was commenced. H&E staining was performed 6 days after PCF experiment. Slide 2 was stored at RT for 9 days before being stained for IMC. IMC staining was then performed as detailed in section 2.4.1. 12 out of the total 26 cores that remained on slide were chosen to ablate due to cost-benefit analysis, as some cores looked too damaged to risk expensive hours of ablation.

5.3 Results

5.3.1 In situ analysis of treatment naïve metastatic melanoma using RNAscope

After our robust characterisation of the immune milieu in metastatic melanoma (chapter 4), we wanted to develop protocols for identifying messenger RNA (mRNA) molecules within cells. One of the commonly used techniques for this purpose is RNAscope. A major advantage of this method is its ability to combine with OPAL technology that could generate high resolution images for analysis. We therefore optimised RNAscope with combination of 4-6 protein stains (OPAL mIHC).

5.3.1.1 Establishing protocols for the detection of multiple cytokines within the TME.

To delineate cell populations capable of pro- and anti-inflammatory cytokine production within the TME we altered RNAscope mRNA staining technique to be embedded in our OPAL multiplex staining protocol as detailed in section 2.5. IL-10 and IFN-γ were chosen as

pro- and anti-inflammatory cytokines due to their established roles in tumour progression (Figure 5.1, 5.2). We first optimised RNAscope within human tumour tissue by experimenting with pre-treatment protease conditions, probe hybridisation conditions, and TSA fluorophore dilutions, as well as performing relevant controls including RNAscope negative probe staining (Figure 5.3 A, B).

IFNG was successfully stained in melanoma tissue, first with a single OPAL colour (CD8) and DAPI (Figure 5.1A, B), and then in multiplex stains with CD3, CD8, CD56, SOX10 (Figure 5.1C). Cytokines such as IFN-g play a critical role in tumour control, however, are nearly impossible to stain for protein using IHC methods. Combining IFN-g RNAscope with immune markers therefore provides an opportunity to map cells that produce this cytokine. After multiple optimisations, we were able to clearly detect IFN-g within melanoma tumours. Co-staining with T cells markers CD3 and CD8 showed co-localisation of IFN-g within cells that expressed CD3 and CD8. Interestingly, our data also showed large populations of cells that were positive for IFN-g were not T cells (Figure 5.1), suggesting that a major source of intra-tumoral IFN-g is likely to be non-T cell immune populations such as NK cells.

In contrast to IFN-g, IL-10 is a regulatory cytokine. Existing data suggested that IL-10 could be a key cytokine in squamous cell carcinomas (SCC). *IL10* mRNA staining was therefore performed SCC specimen to determine if IL-10 production was linked to tumour progression. After multiple optimisation steps, we successfully detected IL-10 mRNA in cSCC specimen (Figure 5.2). Co-staining with CD3 and tumour cell marker CK5 showed that T cells were the major source of this cytokine within the TME (Figure 5.2A). 12 cutaneous SCC samples were stained with *IL10*, CD3, CK5 (tumour marker) and DAPI to determine whether presence of IL-10 was associated with poor clinical outcome. We quantified *IL10* using HALO RNAscope module and found no differences in the number or density of cells with *IL10* production potential between patients that did not progress (NP) and those that had disease progression (P) (Figure 5.2B, C).

5.3.2 Establishing analysis pipeline for spatial transcriptomics

Although RNAscope is a reliable method for the detection of mRNA, the number of different mRNA molecules that can be detected in a single assay is very limited. Fortunately, the technological advances in the past year have enabled ultra-high plex transcriptomics. We therefore switched to a new technology platform by 10X called Xenium. *Xenium in situ* is a

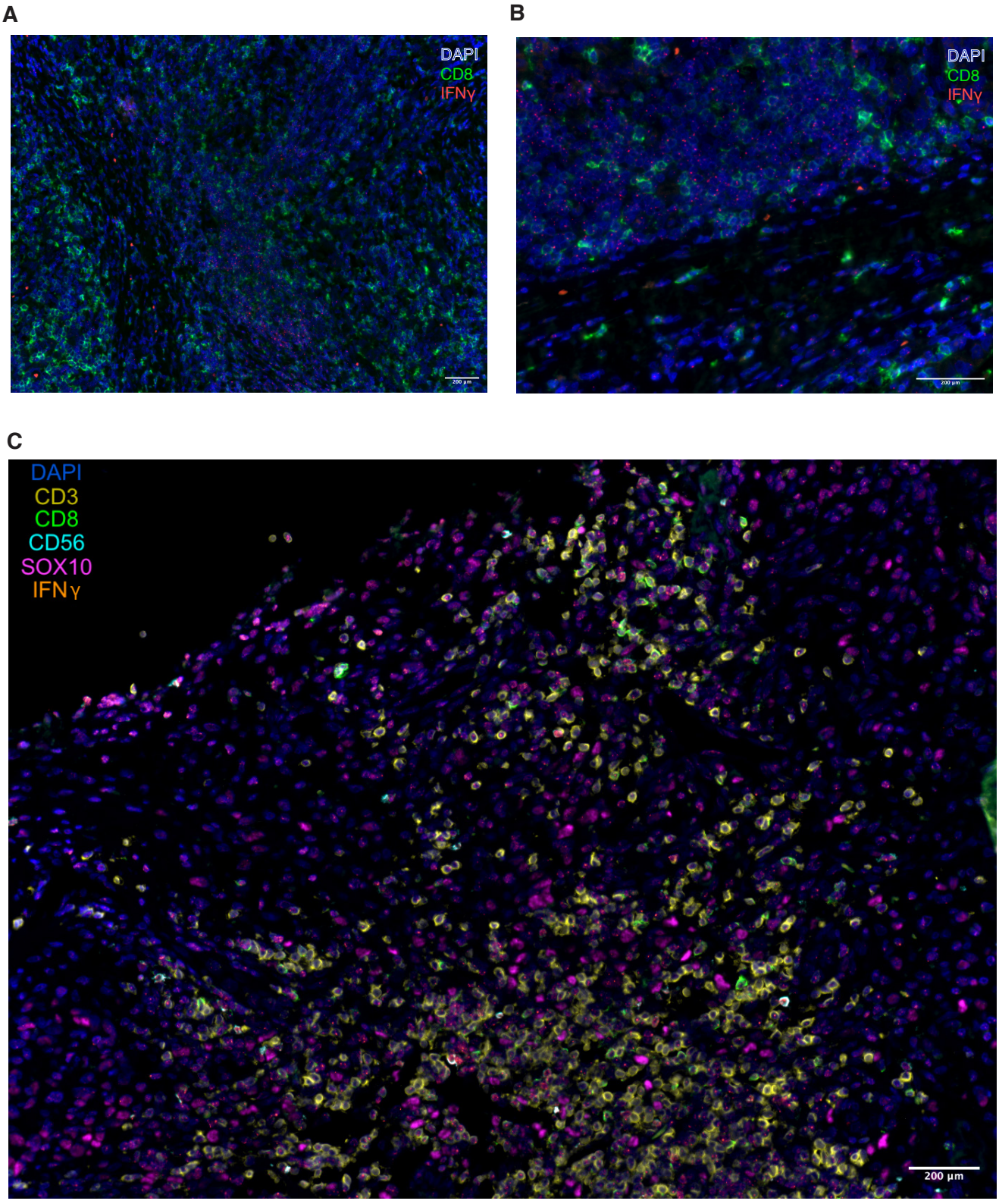

Figure 5.1 Cellular location of IFNγ in metastatic melanoma. IFNγ RNAscope staining was optimised in metastatic melanoma FFPE tissue to determine suitability and quantifiability of experimental approach. Representative image of IFNγ staining on metastatic melanoma sample with DAPI (blue) CD8 (green) and IFNγ RNA (red) at **A** 20x magnification and **B** 40x magnification. **C** Representative 20x magnification image of metastatic melanoma multiplex, stained with DAPI (blue), CD3 (yellow) CD8 (green) CD56 (SOX10), SOX10 (magenta) and IFNγ (orange punctate dots). All images were taken on Mantra Imaging System at the Australian Centre for Microscopy and Analysis. Unmixing performed using Inform v2.4.2 (Akoya Biosciences) Scale Bar = 200µM.

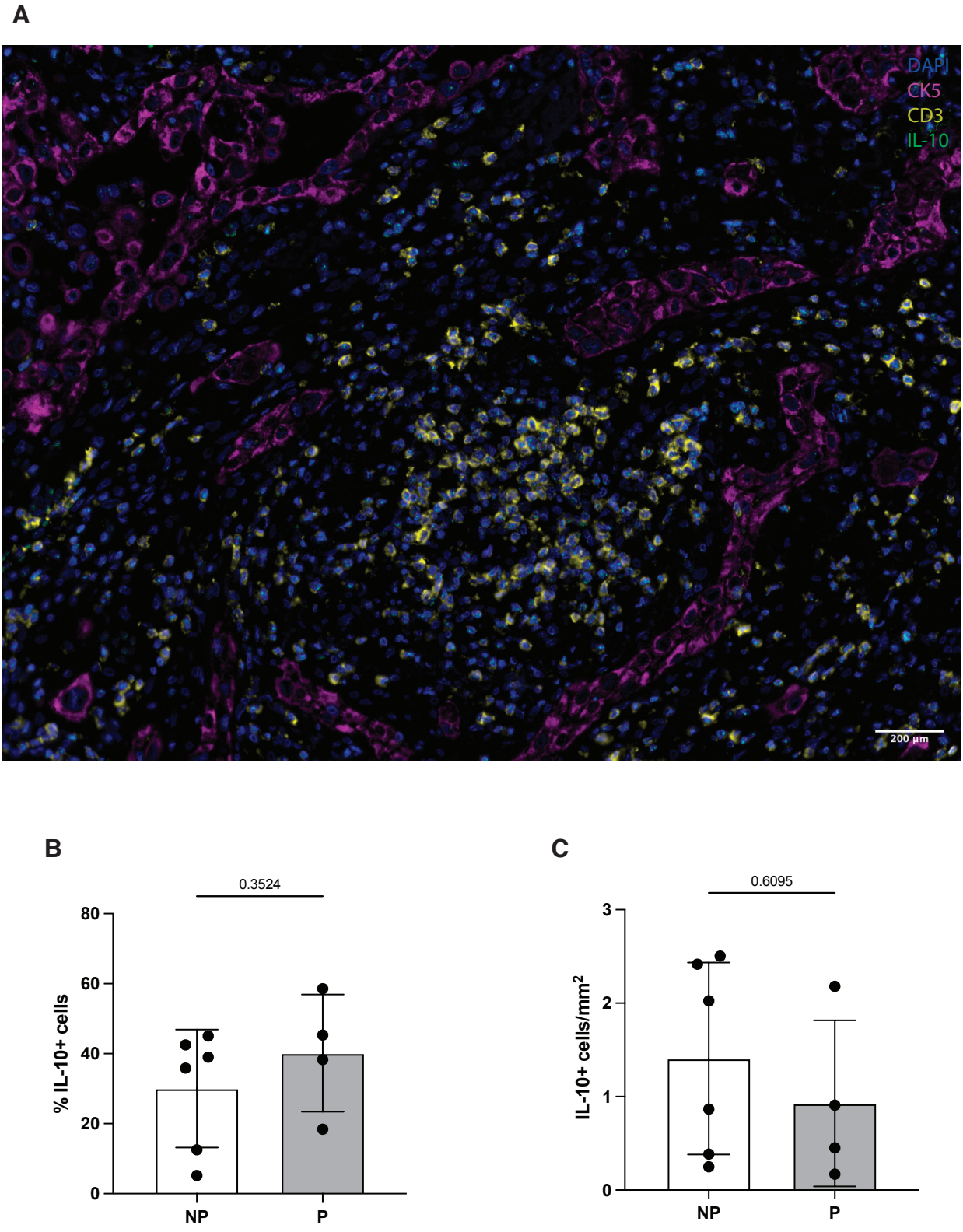

Figure 5.2 IL-10 transcripts do not differ between cutaneous SCC patients with and without disease progression. RNAScope was used to detect IL-10 transcripts alongside detection of tumour and immune protein markers in 10 patients with squamous cell carcinoma (non-melanoma skin cancer) that had no progression (NP, n=6) or disease progression (P, n=6). Regions of interest within whole section stained were quantified using HALO (Indica Labs) with specialised RNAScope quantification module. **(A)** Representative image of IL-10 staining in SCC (progressor) patient sample. Images were acquired on Mantra Imaging system (Akoya Biosciences) and exported using Inform as DAPI (blue) CK5 (magenta) CD3 (yellow) and IL-10 RNA (green). Quantification of IL-10+ cells as **(B)** a proportion of total cells within sample and **(C)** density, cells/mm^2. Mann-Whitney statistical test performed to determine significance. Images were taken on Mantra Imaging System at the Australian Centre for Microscopy and Analysis. Unmixing performed using Inform v2.4.2 (Akoya Biosciences) Scale Bar = 200µM.

A

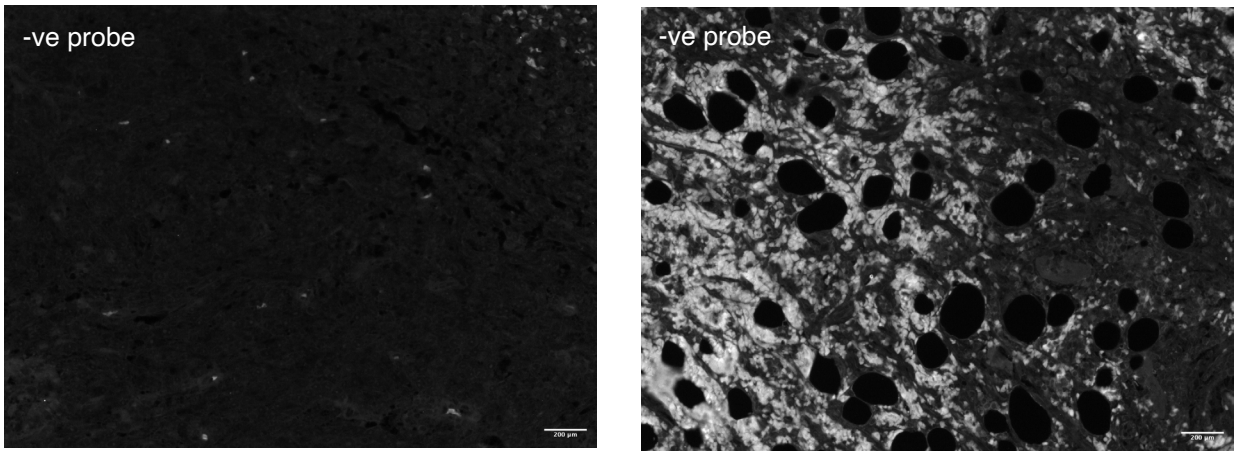

B

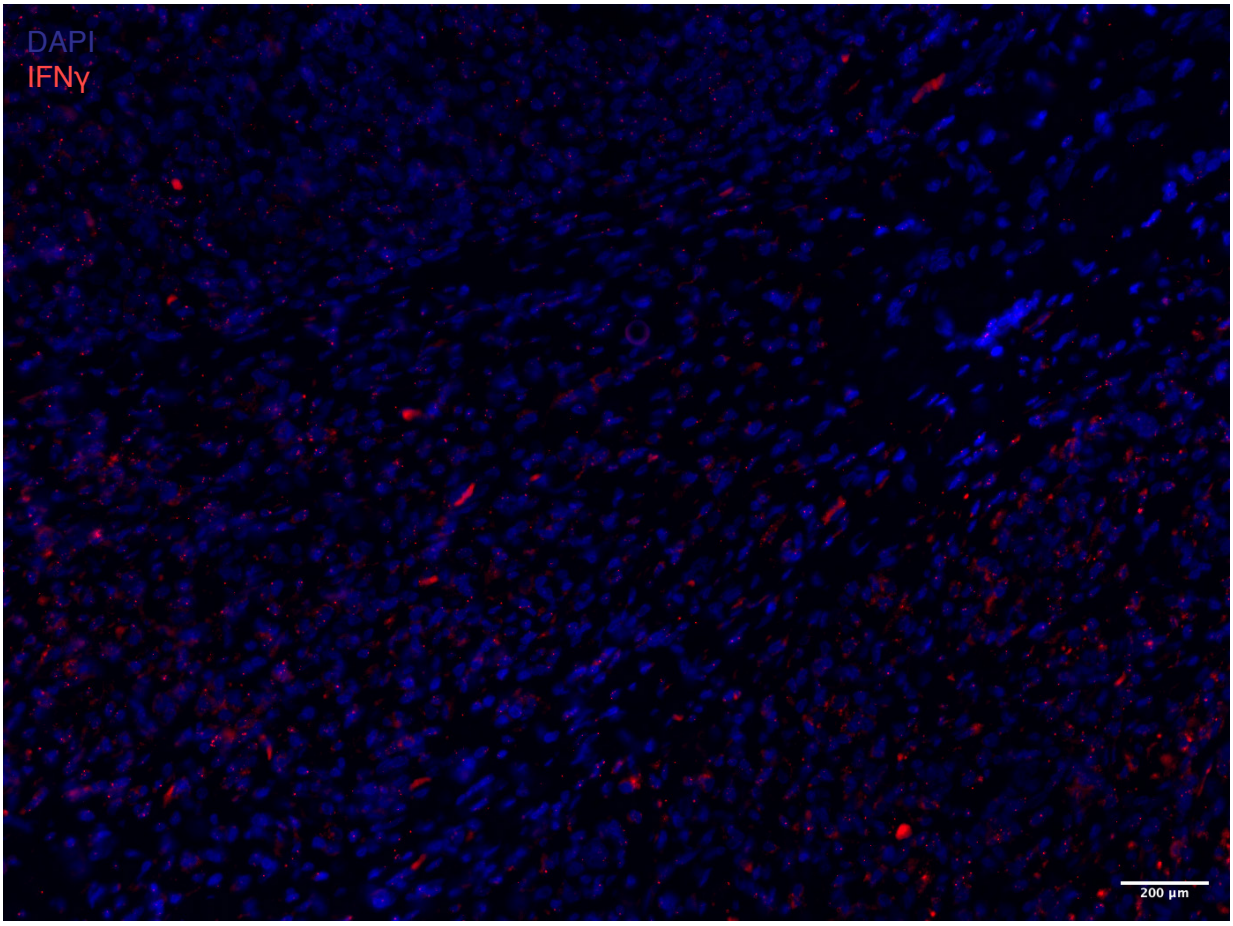

Figure 5.3 Representative staining of RNAscope negative control probe in metastatic melanoma samples. Images were acquired during experiments in **(A)** Two 20x images of negative probe control (PPIB) staining in 2020 on one melanoma patient FFPE tumour sample. **(B)** 20x Negative control probe staining performed in 2023 on metastatic melanoma tumour sample. All images were taken on Mantra Imaging System at the Australian Centre for Microscopy and Analysis. Unmixing performed using Inform v2.4.2 (Akoya Biosciences). Scale Bar = 200µM.

single cell spatial imaging platform that detects RNA transcripts in FFPE tissue and performs automated imaging and analysis using *Xenium Analyzer* instrument (Azevedo, 2024). The main aim was to establish a protocol and research pipeline for mapping both the cellular and molecular landscape of tumours. We employed this platform to characterise pre-treatment metastatic melanoma in the same cohort stained and characterised for tissue proteins in Chapter 4, we aimed to compare findings from both studies to enhance our understanding of the functional roles of immune and tumour cell subsets in melanoma. As our TMA was larger than the imageable area of the custom Xenium slide, the TMA was split across two slides. After tissue staining, the data was loaded into Xenium Analyzer and each slide was split into four regions resulting in a total of eight separate regions. Figure 5.4 and 5.5 display sample split across xenium slides with the DAPI stain taken before cyclic imaging was commenced.

5.3.2.1 Supervised clustering of single cell data

In order to be able to analyse all samples stained across both slides together, cell identities and transcripts detected were extracted from Xenium Explorer and collated as one Xenium file using Seurat package in R (Hao et al., 2024) (Figure 5.6). Cells were then clustered into 20 clusters using the top 8 expressed markers in clusters produced by xenium analyzer: *S100A1, MET, MLPH, MTRNR2L11, EDNRB, MS4A1, PTPRC, CXCR4, TRAC, CD79A, ALDH1A3, TNC, MEST, SEMA3C, PTN, VCAN, MLANA, CTSK, CXCL9, CCL5, FGFBP2, MAMDC2, MDM2, SNCA, CXCL10, AIF1, FCGR3A, PMP22, FGL2, CD83, GNG11, SRPX, BAMBI, SLC26A2, TCL1A, BANK1, COL5A2, FBN1, CD3E, CCL19, CD3D, CD2, MYC, SLAMF7, MZB1, PECAM1, TENT5C, MYLK, CD8A, NKG7, MS4A6A, CD68, DST* (Table 5.1). These markers were inputted into *FuseSOM* package (R studio), a correlation based self-organising map that allows characterisation of cell types in high plex imaging assays (Willie, 2024). Following cluster identification, differentially expressed transcripts were visualised as a heatmap (Figure 5.7).

Cell cluster identities were then re-loaded into Xenium analyzer and each sample core was selected separately to generate .csv files of cell identities within each sample area to calculate proportion and cell density of each cluster (Figure 5.8). Samples were only used in this analysis if they were deemed suitable quality, indicated by green or orange sample ID in Figures 5.4 and 5.5. We then used this data to compare cell clusters between patients grouped by survival (Figure 5.9) and relapse (Figure 5.10).

Table 5.1 Top-expressed markers across clusters

Cluster No.									
1	2	3	4	5	6	7	8	9	10
AIF1	CXCL9	AIF1	AIF1	AIF1	EDNRB	AIF1	ALDH1A3	ALDH1A3	AIF1
ALDH1A3	MLANA	ALDH1A3	ALDH1A3	ALDH1A3	MLANA	ALDH1A3	MLANA	MLANA	ALDH1A3
CD3E	MS4A1	CD3E	CXCL9	CXCL9	S100A1	CXCL9	TNC	PTPRC	CXCR4
CXCR4	PTPRC	CXCL9	CXCR4	FBN1	SNCA	FBN1	AIF1	CXCL9	FBN1
EDNRB	TNC	CXCR4	MLANA	FGL2	ALDH1A3	FGL2	CXCL9	EDNRB	MDM2
FBN1	ALDH1A3	FBN1	MS4A1	MDM2	MTRNR2L11	MLANA	DST	FGL2	MTRNR2L11
MDM2	MTRNR2L11	FGL2	MYLK	MLANA	MDM2	MS4A1	EDNRB	MEST	MYLK
MTRNR2L11	PECAM1	MDM2	PECAM1	MS4A1	MET	MTRNR2L11	FBN1	MYLK	PECAM1
MYLK	PMP22	MLANA	SLAMF7	MTRNR2L11	MYLK	MYLK	FGL2	PECAM1	PTPRC
PECAM1	S100A1	MTRNR2L11	SRPX	MYLK	SRPX	PECAM1	MS4A1	PMP22	S100A1

Cluster No.									
11	12	13	14	15	16	17	18	19	20
AIF1	ALDH1A3	AIF1	AIF1	AIF1	AIF1	ALDH1A3	AIF1	ALDH1A3	ALDH1A3
ALDH1A3	CXCL9	ALDH1A3	ALDH1A3	ALDH1A3	ALDH1A3	CXCL10	ALDH1A3	CCL5	CXCL9
CXCL10	MLANA	MTRNR2L11	CXCL9	CXCL9	FBN1	CXCL9	CCL5	CD3E	MLANA
CXCL9	MS4A1	PECAM1	EDNRB	EDNRB	FGL2	EDNRB	CXCL9	CXCL10	MS4A1
MS4A1	PECAM1	PTPRC	MLANA	MLANA	MDM2	FGL2	MLANA	CXCR4	PECAM1
MTRNR2L11	TNC	S100A1	MS4A1	MS4A1	MS4A1	MLANA	PTPRC	FBN1	TNC
MYLK	AIF1	SLAMF7	PECAM1	MZB1	MTRNR2L11	MS4A1	TNC	MDM2	TRAC
PECAM1	CD3E	SRPX	PMP22	PECAM1	MYLK	PECAM1	EDNRB	MLANA	AIF1
S100A1	CXCR4	TNC	TNC	SLAMF7	PECAM1	PTPRC	MS4A1	MS4A1	CCL5
SLAMF7	FBN1	TRAC	TRAC	TNC	S100A1	S100A1	MYLK	MTRNR2L11	CD3E

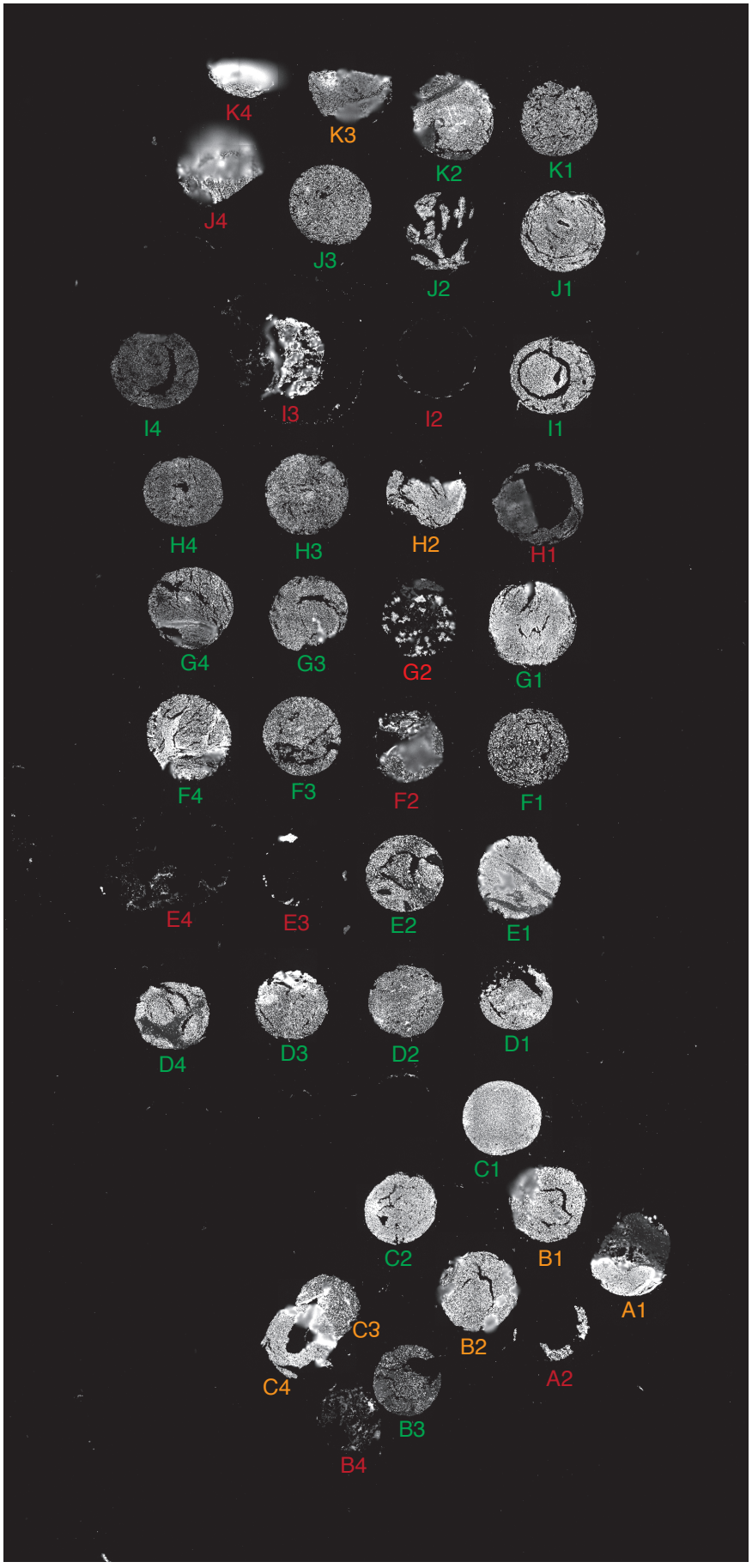

Figure 5.4 Xenium slide 1 pre-acquisition. Image taken by Xenium analyzer before imaging commenced. Samples cores are identified according to their coordinates in original TMA that was scored and split across two slides to adhere to restricted sample area. Sample labels are coloured according to sample quality: unable to be analysed/used (red), parts lost or obscured but remains useful and analysable (orange) and sample quality well-preserved (green).

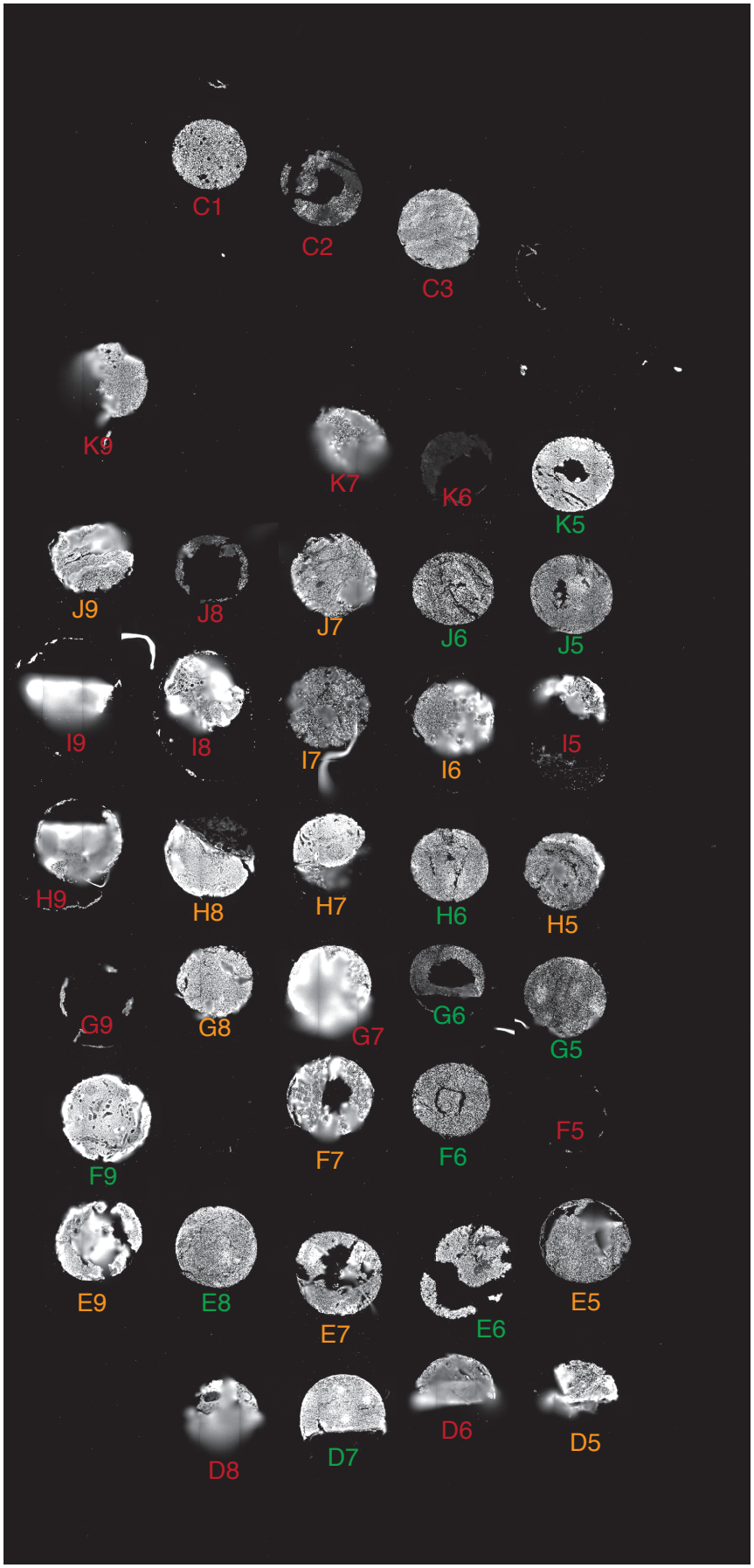

Figure 5.5 Xenium slide 2 pre-acquisition. Image taken by Xenium analyzer before imaging commenced. Samples cores are identified according to their coordinates in original TMA that was scored and split across two slides to adhere to restricted sample area. Sample labels are coloured according to sample quality: unable to be analysed/used (red), parts lost or obscured but remains useful and analysable (orange) and sample quality well-preserved (green).

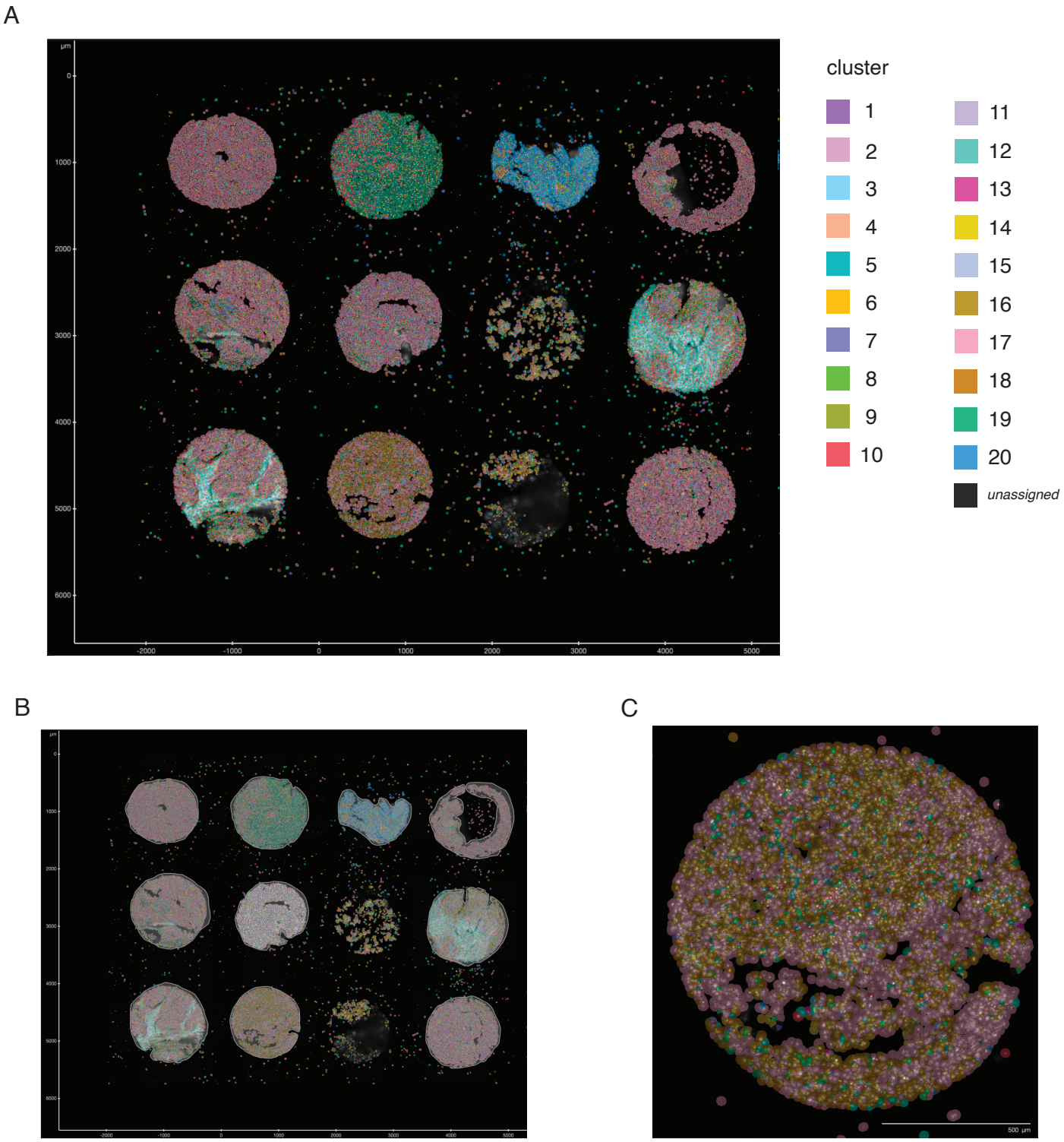

Figure 5.6 Representative Xenium *in situ* mRNA staining in metastatic melanoma tissue. Samples acquired by Xenium platform were loaded into Xenium Explorer 2 for visualisation and analysis. **(A)** Section of Xenium slide 1 showing transcripts and cell segmentation performed by Xenium algorithms overlayed on DNA stain (whiute). Clusters depicted are those identified by R clustering that were imported into Xenium analyzer for visulisation and to quantify cells per patient. **(B)** Identical regions as in (A) with each tumour sample manually circled (white outline) to demonstrate how data was collected per sample. **(C)** Sample F3 with cell clusters overlayed on nuclear stain (white). scale bar = 500µm.

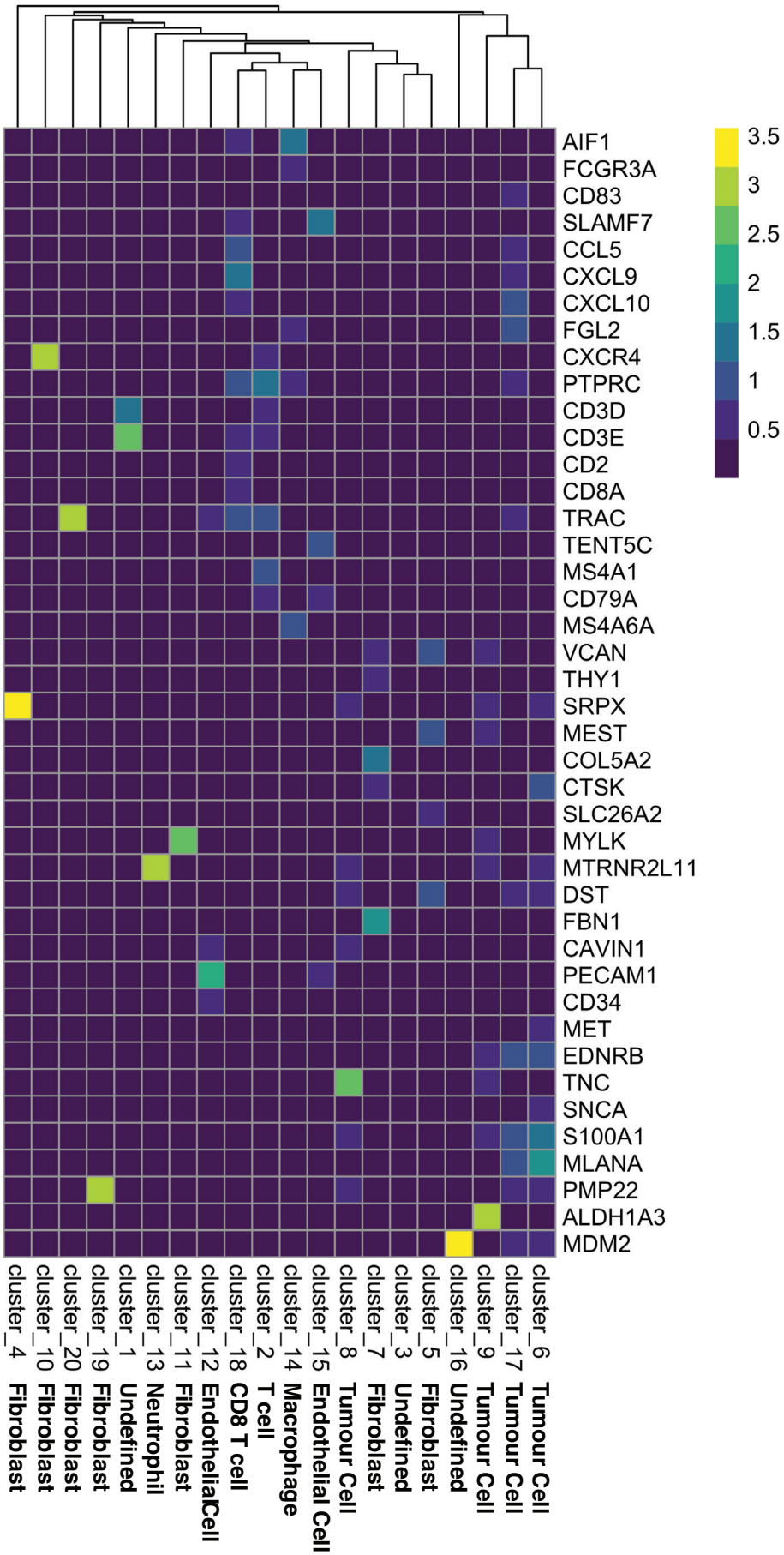

Figure 5.7 Heatmap of transcript expression across 20 clusters identified using supervised clustering. Top markers identified by xenium analzyer were used to perform whole-cohort clustering in R. Normalised and log-transformed transcript counts were input into FuseSOM R package (bioconductor) to produce 20 cell clusters, with hierarchical classification.

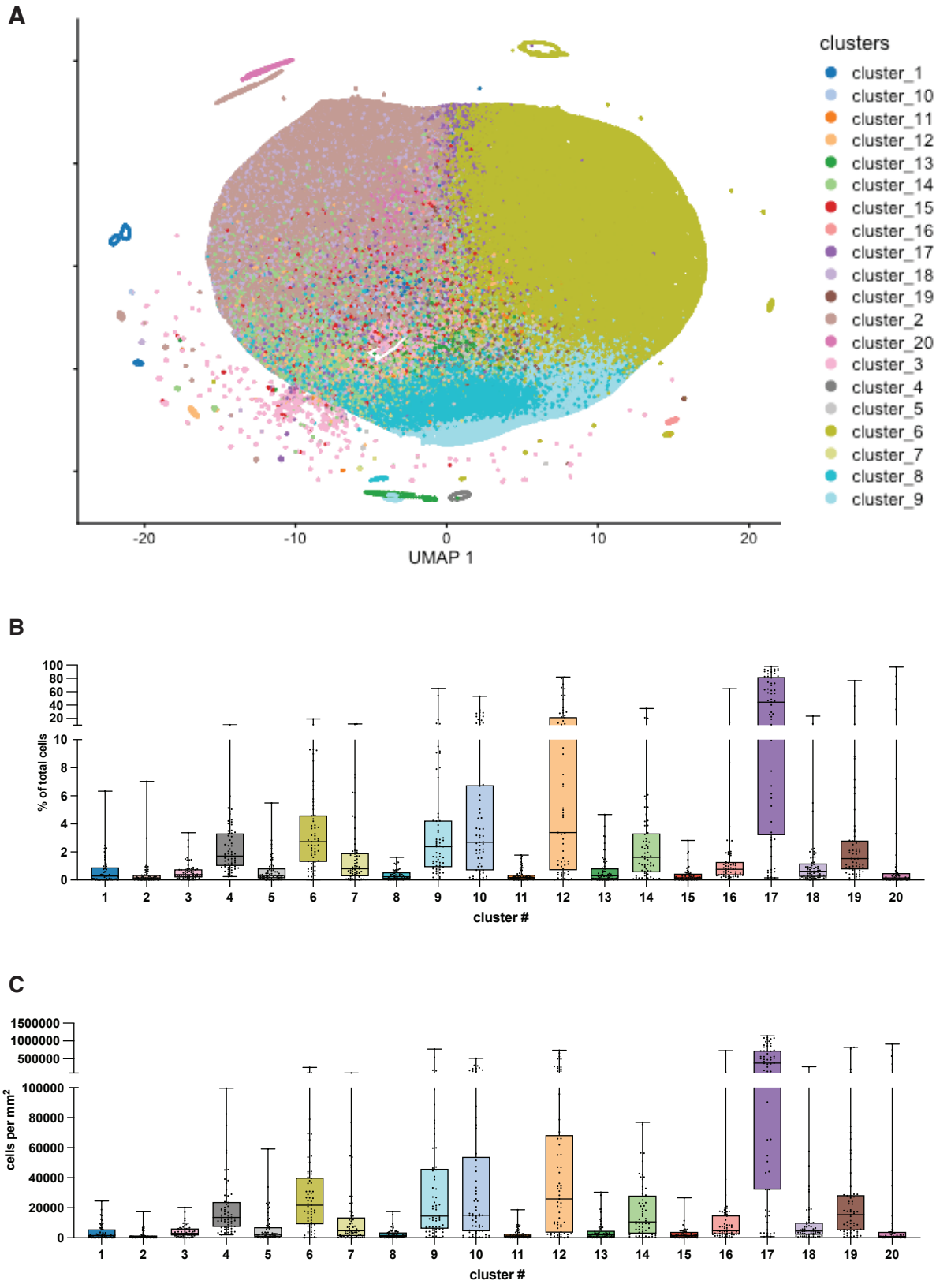

Figure 5.8 Cell clusters identified using supervised clustering. (A) UMAP performed on 20 cell clusters identified in R using FlowSOM (bioconductor). 61 out of 78 tumour cores stained and run through Xenium analyzer were determined appropriate for quantification (orange and green samples in Figures 5.4 and 5.5. Number of cells identified per cluster in each sample as **(B)** proportion of total cells and **(C)** density to calculate and visualise mean values.

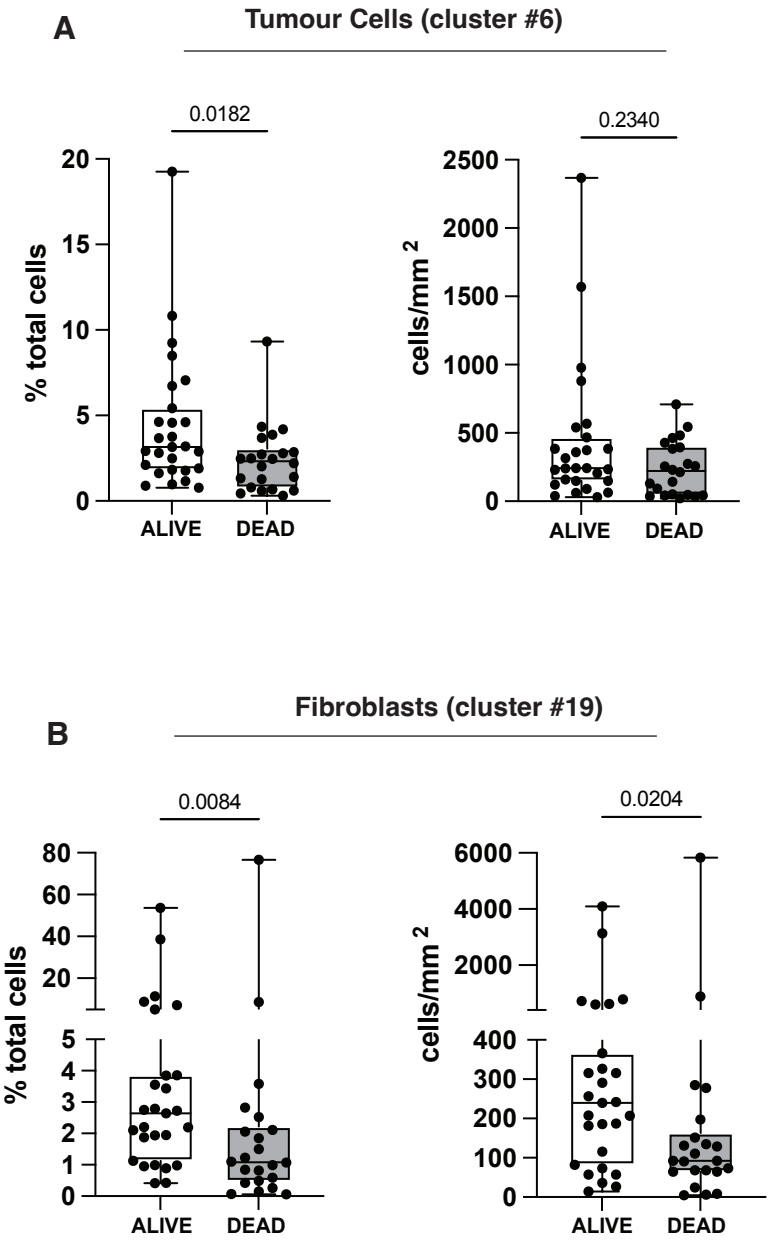

Figure 5.9 Cell clusters associated with survival in metastatic melanoma. Percentage and density of cells identified into clusters by supervised clustering were compared between patients that were alive (A, n=27) and those that died (D, n=22). 49 out of 78 tumour cores stained and run through Xenium analyzer were determined appropriate for quantification (orange and green samples in Figures 5.4 and 5.5. 4 of the 20 clusters tested differed significantly between survival outcomes and are shown here: **(A)** cluster 6, **(B)** cluster 19. Cluster phenotypes detailed in Figure 5.7. Mann-Whitney test performed to determine statistical significance.

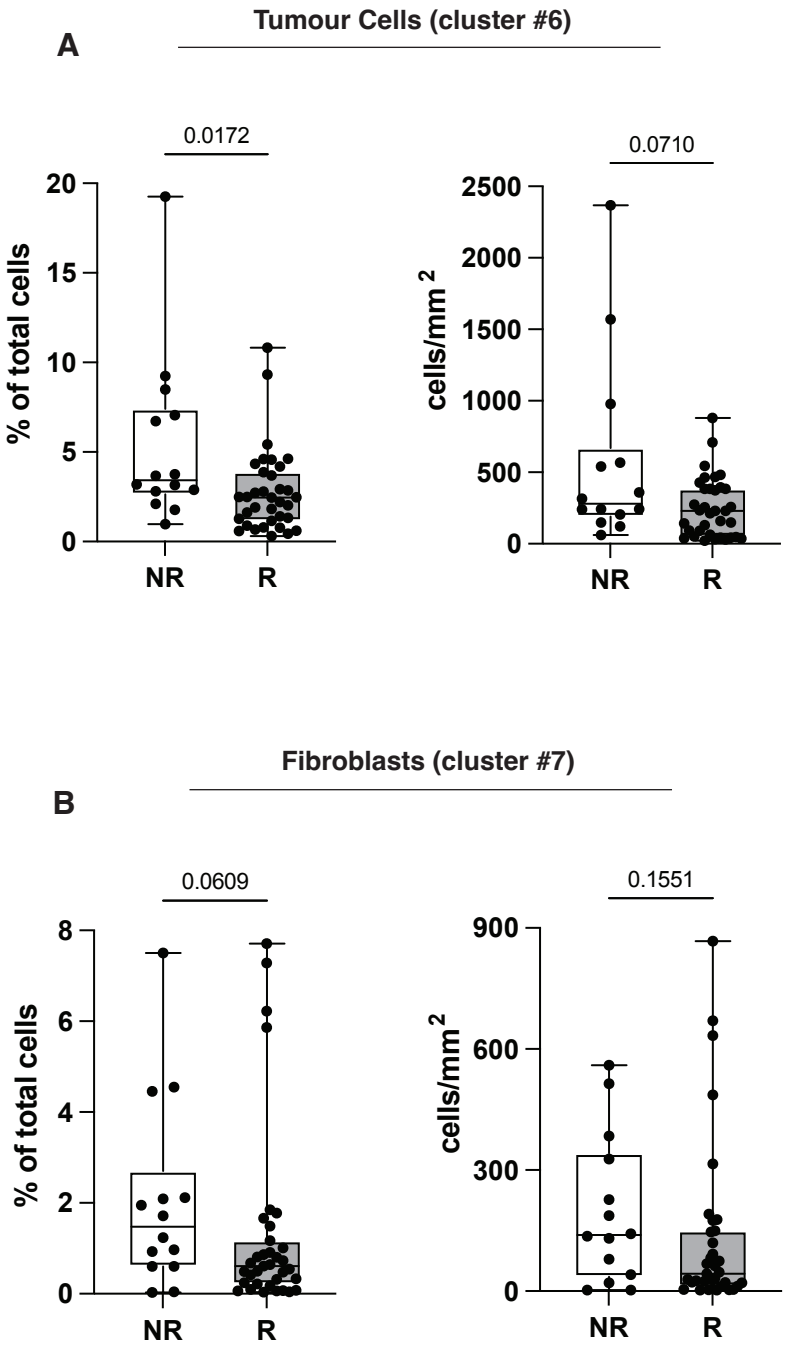

Figure 5.10 Cell clusters associated with relapse in metastatic melanoma. Percentage and density of cells identified into clusters by supervised clustering were compared between patients that relapsed (R, n=35) and those that had no relapse (NR, n=14). 49 out of 78 tumour cores stained and run through Xenium analyzer were determined appropriate for quantification (orange and green samples in Figures 5.4 and 5.5. 3 of the 20 clusters tested differed significantly between relapse outcomes: **(A)** cluster 6 and **(B)** cluster 7. Cluster phenotypes detailed in Figure 5.7. Mann-Whitney test performed to determine statistical significance.

5.3.2.2 Cluster annotation

Within these 20 clusters we were able to identify four tumour cell clusters, two T cell clusters, one macrophage cluster, one neutrophil cluster, 6 fibroblast clusters, two endothelial cell clusters. Three clusters were unable to be definitively identified and are labelled 'undefined' (Figure 5.7). These clusters were consistent with the fact that tumour areas selected for spatial transcriptomics were all from 'high' tumour regions. It is important to note however that the cell segmentation module within the Xenium Analyzer uses only DAPI staining to segment cells which can result in inaccurate cell segmentation and impact validity of cluster analysis. This issue has since been addressed by 10X Genomics with their release of an optional cell segmentation module that uses CD45, Vimentin and 18S protein staining along with DAPI to define nuclear and cell boundaries to improve Xenium cell segmentation (Xiaoyan Qian, 2024).

To delineate tumour cells, we assessed clusters for expression of *S100A1* (encodes A100 calcium binding protein-1) and *MLANA* (encodes Melan-A) as both are well established melanoma tumour cell markers (Karlsson et al., 2021). Clusters 8 and 9 expressed *S100A1*, and clusters 6 and 17 expressed both *MLANA* and *S100A1* and were therefore denoted tumour cells (Figure 5.7). Cluster 6 and 17 additionally expressed tumour cell associated transcripts *PMP22, MDM2, SCNA, EDNRB* and *DST* (Figure 5.7). These markers are largely associated with immunosuppressive mechanisms in melanoma. The PMP22-family encodes proteins related to cell migration, growth and metastasis, and has been implicated in both pro and anti-tumour roles in melanoma. In a human melanoma cell line, PMP22-family protein EMP2 was shown to induce apoptosis of melanoma cells (Wang et al., 2019). Conversely, in uveal melanoma, PMP22 family proteins have been associated with more aggressive phenotypes (Kaochar et al., 2018, Onken et al., 2006). *MDM2* expression in melanoma was linked with a de MDM2 expression was found to be associated with tumour thickness and invasion level in primary melanoma, and in metastatic melanoma is associated with a dedifferentiated phenotype (Yousef et al., 2022, Rajabi et al., 2012). *SCNA* codes for alpha-synuclein, a protein highly expressed in melanocytes and enriched in skin cancer. Alpha-synuclein expression in melanoma tumour cells is linked to increased cell motility, chemotherapy resistance, autophagy-mediated death resistance and immune suppression (Nandakumar et al., 2017, Niederberger et al., 2023, Shekoohi et al., 2021, Rodríguez-Losada et al., 2020, Singh et al., 2023, Matsuo and Kamitani, 2010). Endothelin receptor B, the protein coded by *EDNRB*, is

linked with earlier metastasis, decreased survival and immunosuppression in melanoma (Kumasaka et al., 2015, Smith et al., 2002). *DST* expression in melanoma has been associated with a lack of TH1 immune signatures, CD8 expression, early patient mortality, enhanced tumour cell proliferation and greater tumour burden (Salerno et al., 2016, Leick et al., 2019).

Immune cells were defined by expression of *PTPRC* (encoding CD45 protein), which included clusters 17, 14, 2 and 18 (Figure 5.7). As cluster 17 was already defined as a tumour cell and expression of *S100A1* and *MLANA* was higher than P*TPRC*, this cluster is likely due to inaccurate cell segmentation that has encompassed neighbouring immune cells. Cluster 14 was identified as a macrophage due to expression of macrophage markers *FGL2, AIF1* and as well as *FCGR3A* (encoding CD16) expression (Karlsson et al., 2021). Cluster 18 was identified as CD8 T cells due to expression of *CD8A, CD2, CD3D, CD3D*, and *TRAC*. This CD8 T cell cluster also expressed high levels of *CCL5, CXCL9* and *CXCL10*. Cluster 2 is labelled as a general T cell population due to expression of *CD3D, CD3E* and *TRAC*. Cluster 13 was classified as a neutrophil despite undetectable expression of *PTPRC* (CD45) due to high expression of pseudogene *MTRNR2L11* that has been reported in neutrophils (Karlsson et al., 2021).

Of the 12 non-immune, non-tumour cell clusters remaining, six were classified as fibroblasts (Figure 5.7). Cluster 5 expressed transcripts which have been reported on fibroblasts, macrophages, endothelial cells and granulocytes (Carthy et al., 2015, Künzli et al., 2016). However, *MEST* (mesoderm specific transcript) is only expressed on fibroblasts, and therefore cluster 5 was classified as a fibroblast population (Abbasi et al., 2020, Hasegawa et al., 2020). Cluster 7 was defined as a fibroblast due to *THY-1* (CD90) expression which can be expressed on a variety of cell types including thymocytes, smooth muscle cells and fibroblasts, but fibroblasts are the only cells that would be located in nodal metastases (Karlsson et al., 2021). *MYLK* (myosin light chain kinase) is mostly expressed in smooth muscle cells, but fibroblasts have been reported as expressing *MYLK* (Katoh et al., 2001). As cluster 11 did not express *PTPRC* (CD45), it was defined as a fibroblast. Cluster 19, 20, 10 and 4 were classified as fibroblasts, despite being defined by a single transcript (Figure 5.7). *PMP22* (peripheral myelin protein 22) is expressed in Schwann cells and fibroblasts and is essential for migration and adhesion of these cells (Lee et al., 2014). It is unlikely that melanocytes and Schwann cells would be present within metastatic tumours. As such, we classified cluster 19 as a fibroblast population. Although *TRAC* encodes T receptor alpha constant, it has been reported as

expressed on fibroblasts (Karlsson et al., 2021). Due to the lack of expression of any other markers, including T cell markers, we therefore classified cluster 20 as a fibroblast (Figure 5.7). *CXCR4* is widely expressed on immune cells as well as on structural cells including fibroblasts (Karlsson et al., 2021). Again, as cluster 10 did not express any other transcripts associated with immune cells, we classified it as a fibroblast population. *SRPX* has been shown to be upregulated in cancer-associated fibroblasts in ovarian cancer (Liu et al., 2019a, Feng et al., 2022) Again, as this cluster did not express endothelial cell markers and as this tissue does not typically contain melanocytes or smooth muscle cells, we denoted cluster 4 as a fibroblast cluster.

Cluster 15 and cluster 12 expressed endothelial cell marker *PECAM1* (CD31) and were thus classified as endothelial cells. Cluster 15 also expressed *MS4A6A, TENT5C* and *SLAMF7* (Figure 5.7). Cluster 12 also expressed endothelial cell marker *CD34*, as well as *CAVIN1* and *TRAC*.

The remaining clusters lacked detectable CD45 and tumour cell markers and expressed only a single marker, therefore unable to be defined due to this marker being non-exclusive to cell phenotypes (Figure 5.7). Cluster 16 expressed *MDM2*, a transcript encoding a protein ligase that mediates ubiquitination of p53, resulting in its degradation by the proteasome in the cell (Sparks et al., 2014, Marine and Lozano, 2010). Cluster 3 did not express any detectable transcripts. Cluster 1 expressed a high level of *CD3D* and *CD3E*, however this is unlikely to be a T cell cluster due to the lack of *PTPRC* (CD45) expression and more likely the result of inaccurate cell segmentation detecting adjacent T cells (Figure 5.7).

5.3.3 Application of spatial transcriptomics data

Due to time constrains, the spatial transcriptomic data could not be fully analysed during this candidature. However, we have developed some basic analysis pipeline to determine the applicability of this dataset.

5.3.3.1 Tumour cells make up the majority of high-tumour regions.

As expected, tumour cell clusters comprised the majority of cells detected in high-tumour regions of nodal melanoma tumours (Figure 5.8). We next quantified the proportion of each cluster to determine how similar the data was when compared to what was generated using

IMC (Chapter 4). Cluster 17 made up largest component of cells detected, reporting mean proportions of 42.15% and mean density of 3129 cells per mm^2 (Figure 5.8B, C). Cluster 9 made up 5.13% of cells and average density of 482.6 cells/mm^2, cluster 6 3.56% and 341.4 cells/mm^2 and cluster 8 0.37% and 29.52 cells/mm^2 (Figure 5.8B, C).

Endothelial cells made up a large proportion of tumour regions, with cluster 12 averaging 14.67% of total cells and 2213 cells/mm^2, and cluster 15 making up 0.3486% and 25.5 cells/mm^2 (Figure 5.8B, C). The six fibroblast clusters identified made up approximately 20% of high-tumour samples (Figure 5.8B, C). The largest fibroblast clusters were cluster 19 and 20, making up 4.86% and 5.93% of all cells respectively (Figure 5.8B, C). Cluster 4 averaged 0.69% of total cells, and cluster 5 averaged 0.69% (Figure 5.8B, C). Remaining fibroblasts clusters 10 and 11 made up 7.08% and 0.35% respectively (Figure 5.8B, C).

Macrophages (cluster 14) averaged 3.08% of cells and recorded mean density of 186.4 cells/mm^2 (Figure 5.8B, C). CD8 T cells (cluster 18) averaged 1.43% of cells within a sample, with a density of 93.95 cells/mm^2 (Figure 5.8B, C). All other T cells (cluster 2) made up 0.38% of cells and recorded cell density of 26.22 cells/mm^2. Neutrophil cluster (#13) made up an average of 0.70% of cells and a density of 76.61 cells/mm^2. Remaining proportion of cells recorded were made up of undefined cells, making up a total of less than 4% (clusters 1, 3, 16) (Figure 5.8B, C). Total cell density did not differ between patients when grouped by survival or relapse outcomes (data not shown).

5.3.3.2 Tumour cells, endothelial cells and fibroblasts are associated with survival in melanoma patients with high risk of relapse

We then wanted to examine if any of the cell phenotypes identified were associated with survival. To do this, we compared proportion and density of all 20 cell clusters between patients alive (n=27) or dead (n=22). We found two clusters that were significantly higher in patients that survived (Figure 5.9). Cluster 6, a tumour cell cluster recorded significantly higher proportions (mean values; A= 4.40%, D= 2.40%) in patients that survived (Figure 5.9A). Cluster 6 also had a trend to higher cell density in patients that survived; however, this was not significant (mean values; A= 424.1 cells/mm^2, D= 239.9 cells/mm^2) (Figure 5.9A). Cluster 19, a fibroblast population, was also significantly higher in patients that survived, shown by proportions (mean values; A= 6.23%, D= 4.99%) and densities (mean values; A= 508.8

cells/mm^2, D= 399.6 cells/mm^2) (Figure 5.9B). The remaining 18 clusters did not significantly differ in proportion or density in the TME of patients grouped by survival.

5.3.3.3 Tumour cells, T cells and fibroblasts are associated with lack of relapse in melanoma patients with high risk of relapse

We also wanted to determine if there were any cell clusters associated with patient relapse, so we compared the proportion and cell density of each cell cluster between patients that had no relapse (n=14) or relapse (n=35). We again found that tumour cell cluster (#6) proportions were significantly higher in patients that had no relapse (mean values; A= 5.36%, D= 2.76%) (Figure 5.10A). Cluster 6 cell density was also higher in patients that did not relapse, but this was not significant (mean values; A= 568.9 cells/mm^2, D= 250.4 cells/mm^2) (Figure 5.10A). Another fibroblast population, cluster 7, was found to be higher in patients with no relapse (mean proportions: A= 5.36%, D= 2.76%; mean densities: A= 196.8 cells/mm^2, D= 133 cells/mm^2), but this difference was not significant (Figure 5.10B). The remaining clusters did not differ between patients grouped by relapse (data not shown). These data suggest that tumour cell cluster 6 is strongly associated with better patient outcomes.

5.3.4 Establishing protocols for combined spatial transcriptomics and spatial proteomics

5.3.4.1 Post-in situ hybridisation proteomics reveals validity of non-ablative transcriptomic imaging

Both proteomics and transcriptomic data is required to accurately characterise cell phenotypes in human tissue (Zapalska-Sozoniuk et al., 2019). The advantage to being able to perform this on the same tissue section removes the inaccuracy and inefficiency of cross-experimental approaches such as registering images from serial sections. Current technology platforms such as Xenium do not enable the combination of both transcriptomics and protein staining on the same slides. We wanted to develop our own protocols where we could perform both omics on the same slide. At the time of experimental plan, there was no published data showing IMC or Phenocyler Fusion (PCF) performed on tissue previously stained and imaged using the xenium platform. After processing the samples through xenium, we tested both IMC and PCF platforms to determine whether ultra-high plex IHC could be performed. Finally, we also performed H&E staining on one of the slides stained for PCF to determine tissue integrity.

5.3.4.2 Imaging Mass Cytometry (IMC)

The advantage of using IMC is that the tissue staining process is completed in one step therefore tissue integrity is likely to be maintained. Following transcriptomic staining, we wanted to test if we could successfully perform imaging mass cytometry staining and analysis. Xenium slide 2 was stained using antibody panel identical to previous IMC experiment (Table 2.7). 12 tumour cores (11 patients) were stained, ablated and analysed (Figure 5.11A). Images were viewed in mcd viewer and imported into cell profiler for cell segmentation and exported for analysis in FlowJo as described in 2.4.4.

Employing the gating strategy previously outlined (Figure 4.3), we quantified lymphocytes, innate immune and non-immune cells to compare the validity of proportions to previously acquired IMC data and compared proportions with previous work (Figure 4.4). In this smaller cohort we calculated that B cells made up an average of 2.15% of all cells, CD8 T cells made up 0.48% and CD4 T cells made up 7.18% (Figure 5.11B). CD4 Tregs were measured at 6.95% of all cells and T_H1 cells made up 1.41% (Figure 5.11B). When we looked at innate populations and found NK cells, neutrophils and monocytes made up 0.01%, 0.002% and 0.017% of total cells, respectively (Figure 5.11B). Macrophages made up 0.017% and CD16+ macrophages made up 0.009% of all cells (Figure 5.11B). Fibroblasts were calculated as 11.32% of total cells (Figure 5.11B). While no lymphatic endothelial cells were quantified in these samples, we found endothelial cells averaged 0.004% of cells (Figure 5.11B). Tumour cells made up an average of 22.25% with a standard deviation of 27.48 (Figure 5.11B). While not all these mean values match exactly those reported in previous work, it is unlikely that a smaller cohort of 13 of samples randomly selected would fully represent a 100-patient cohort. (Chapter 4, Figure 4.3). Additionally, these values are within the range reported for the larger cohort as displayed in Chapter 4 (Figure 4.3).

We also compared the proportions of selected immune populations between patients who were alive (n=6) and those who were diseased (n=5). Even within this small cohort, similar to the data we obtained in chapter 4, we saw total CD4 T cells significantly increased in patients that survived (Figure 5.12B). Tregs, making up a large portion of total CD4 T cells, were also significantly higher in patients that survived as seen in chapter 4 (Figure 5.12D). We saw no differences in innate or non-immune cell populations between patients who were alive and

A

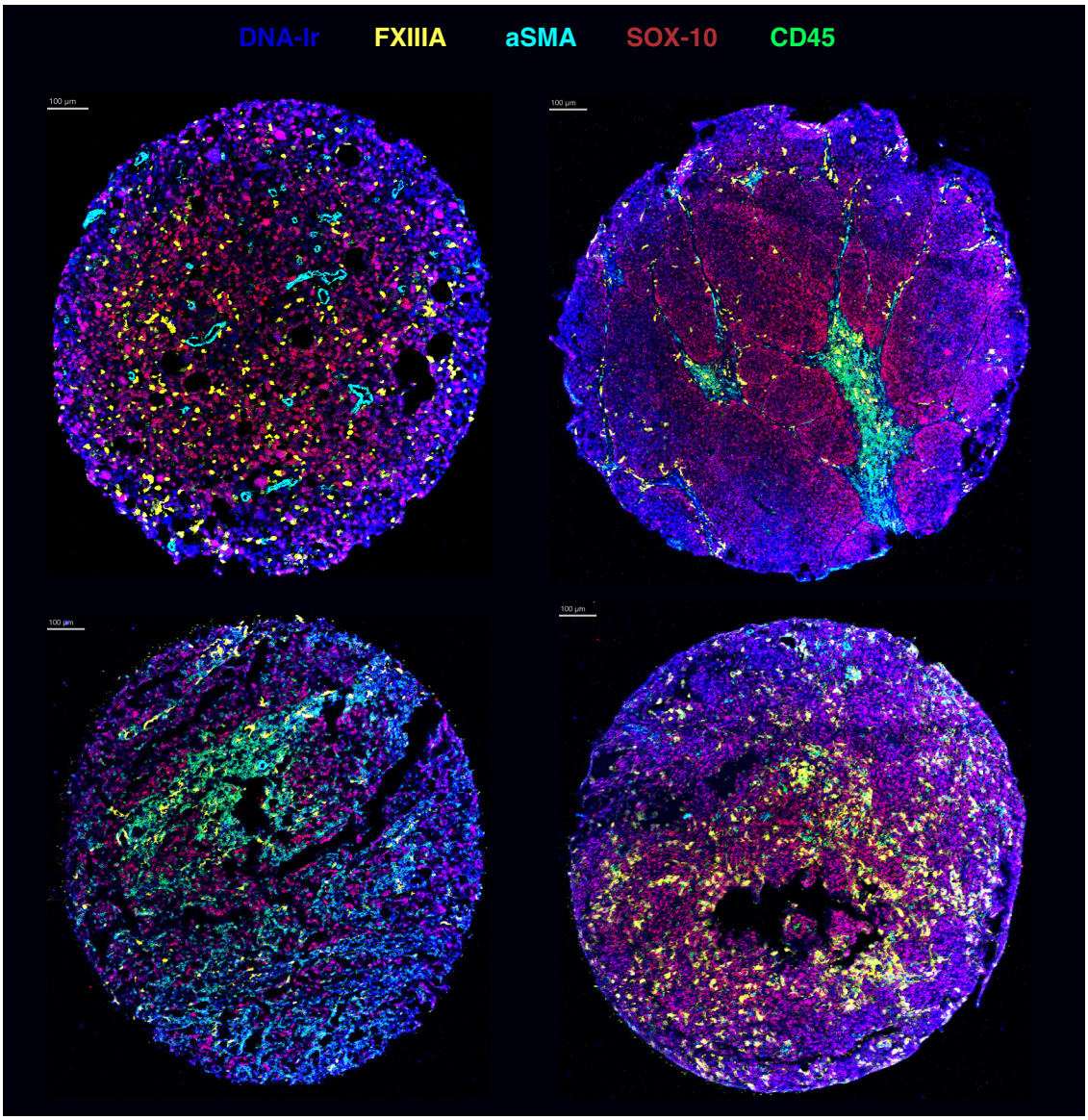
DNA-Ir
FXIIIA
aSMA
SOX-10
CD45
100 µm

B

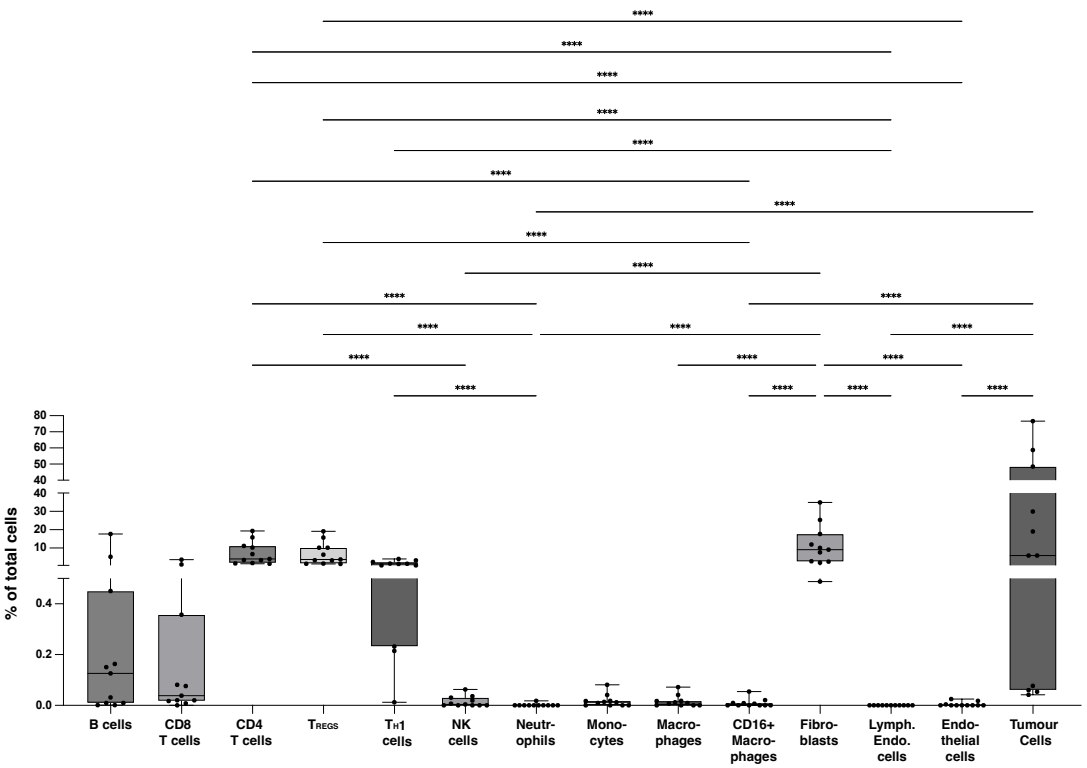
****
% of total cells
80
70
60
50
40
40
30
20
10
0.4
0.2
0.0
B cells
CD8 T cells
CD4 T cells
TREGS
TH1 cells
NK cells
Neutr-ophils
Mono-cytes
Macro-phages
CD16+ Macro-phages
Fibro-blasts
Lymph. Endo. cells
Endo-thelial cells
Tumour Cells

Figure 5.11 Imaging mass cytometry performed on tumour tissue following transcriptomic staining. Following mRNA staining of metastatic melanoma TMA, samples were stained with imaging mass cytometry antibodies and ablated to determine feasibilty of multiple stains. **(A)** Representative staining of 4/12 samples ablated by imaging mass cytometry. Images produced using MCD viewer. **(B)** Proportions of immune, non-immune and tumour cell populations identified using gating strategy defined in Figure 4.3 in patients assessed using IMC and quantified using Cell Profiler for segmentation and FlowJo for population quantification (n=12).Uncorrected Dunn's test to determine stastically significant differences between mean ranks. p values <0.0001(****) only included on graph.

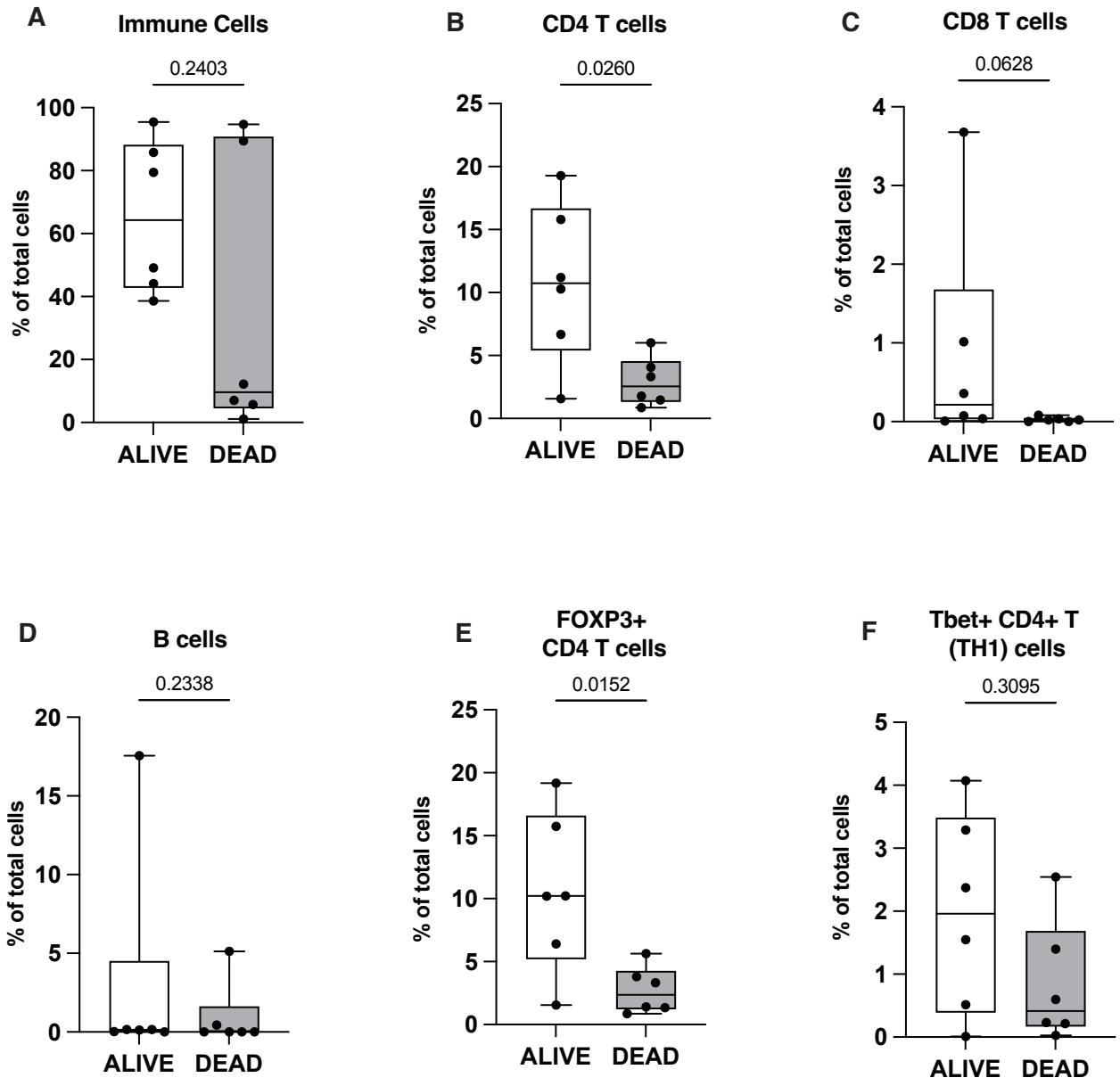

Figure 5.12 CD4 T cells are associated with survival in metastatic melanoma patients. A smaller patient cohort (11/100) were stained using imaging mass cytometry following transcriptomic (Xenium) staining and imaging. Percentage of **(A)** all immune cells, **(B)** CD4 T cells, **(C)** CD8 T cells, **(D)** B cells, **(E)** FOXP4+ CD4+ (regulatory) T cells and **(F)** Tbet+ CD4 T-Helper Type-1 cells as a proportion of total cells in patients alive (n=6) or dead (n=5). Mann-Whitney statistical test performed to determine significance.

those who were diseased (Figure 5.13 & 5.14), an observation mirrored in our previous findings.

5.3.4.3 PCF

After acquisition on Xenium analyzer, we also tested another tissue imaging platform called Phenocyler fusion (PCF, Akoya Biosciences). A major difference between IMC and PCF is that PCF relies on cyclical staining process that also involves multiple antigen retrieval steps could affect the tissue integrity. However, the image quality acquired through PCF is significantly greater when compared to those from IMC. Slide 2 underwent protein antibody staining as outlined in 2.5.1. During imaging, the flow cell attached to the slide to allow transfer of reagents and fluorophores for cyclic imaging leaked. This leakage as well as deteriorating tissue due to antigen retrieval and cyclical two-day staining required led to variable success of PCF. Approximately 8 of the 41 protein markers tested produced positive staining: They include tumour marker SOX10, MHC class I marker HLA-A, endothelial cell marker CD31, macrophages marker CD68, transcription factor TBET, B cell marker CD20, co-stimulatory molecule CD27 and immune regulatory molecule IDO. Amongst these 8 markers, HLA-A, CD68, CD31 and SOX10 staining were most reliable across multiple samples tested (Figure 5.15) and produced consistent staining on approximately 10 samples (representative images Figure 5.16). Although further testing is required, PCF may not be the ideal platform for post-xenium tissue staining.

5.3.4.4 Haematoxylin and Eosin staining

In order to test the tissue integrity, following the PCF run, slide 2 also underwent H&E staining and imaging. Of the 25 cores that were successfully stained by PCF, 22 cores remained intact to be stained with H&E and imaged (Figure 5.17).

5.4 Discussion

Understanding mechanisms of tumour progression requires a deeper understanding of the TME including individual cell capabilities within tumours. Identifying RNA transcripts in FFPE tumour tissue can provide critical information on the functional state of the cells, helping researchers identify mechanisms of tumour progression and/or control (Yu et al., 2022, Valdes-Mora et al., 2018). This project aimed to understand what cell populations drive immune activation or suppression and disease progression in the TME of melanoma. Initially my

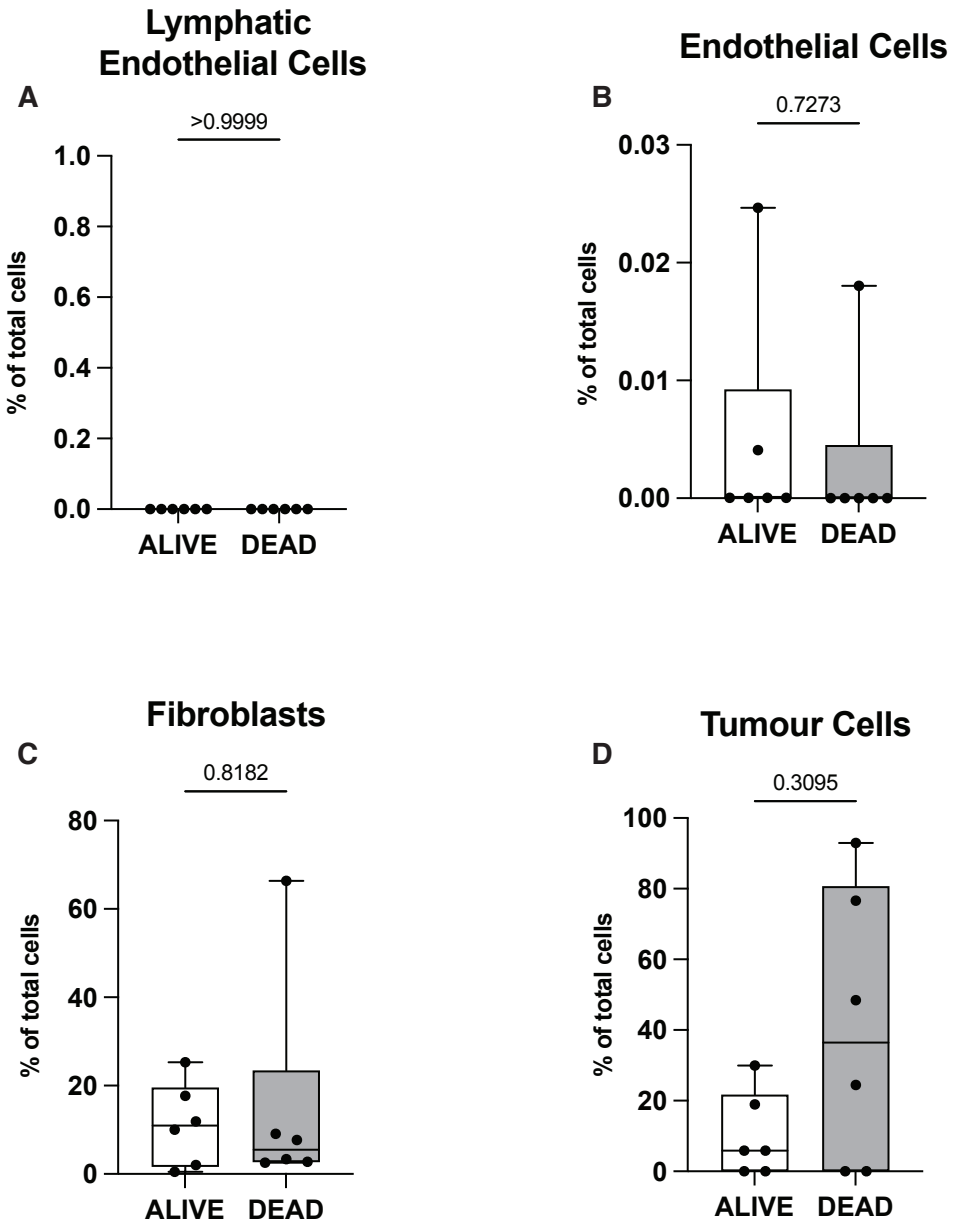

Figure 5.14 No significant differences in proportion of non-immune cells in metastatic melanoma patients alive or dead at follow-up. A smaller patient cohort (11/100) were stained using imaging mass cytometry following transcriptomic (Xenium) staining and imaging. Percentage of **(A)** lymphatic endothelial cells, **(B)** endothelial cells, **(C)** fibroblasts and **(D)** tumour cells as a proportion of total cells in patients alive (n=6) or dead (n=5). Mann-Whitney statistical test performed to determine significance.

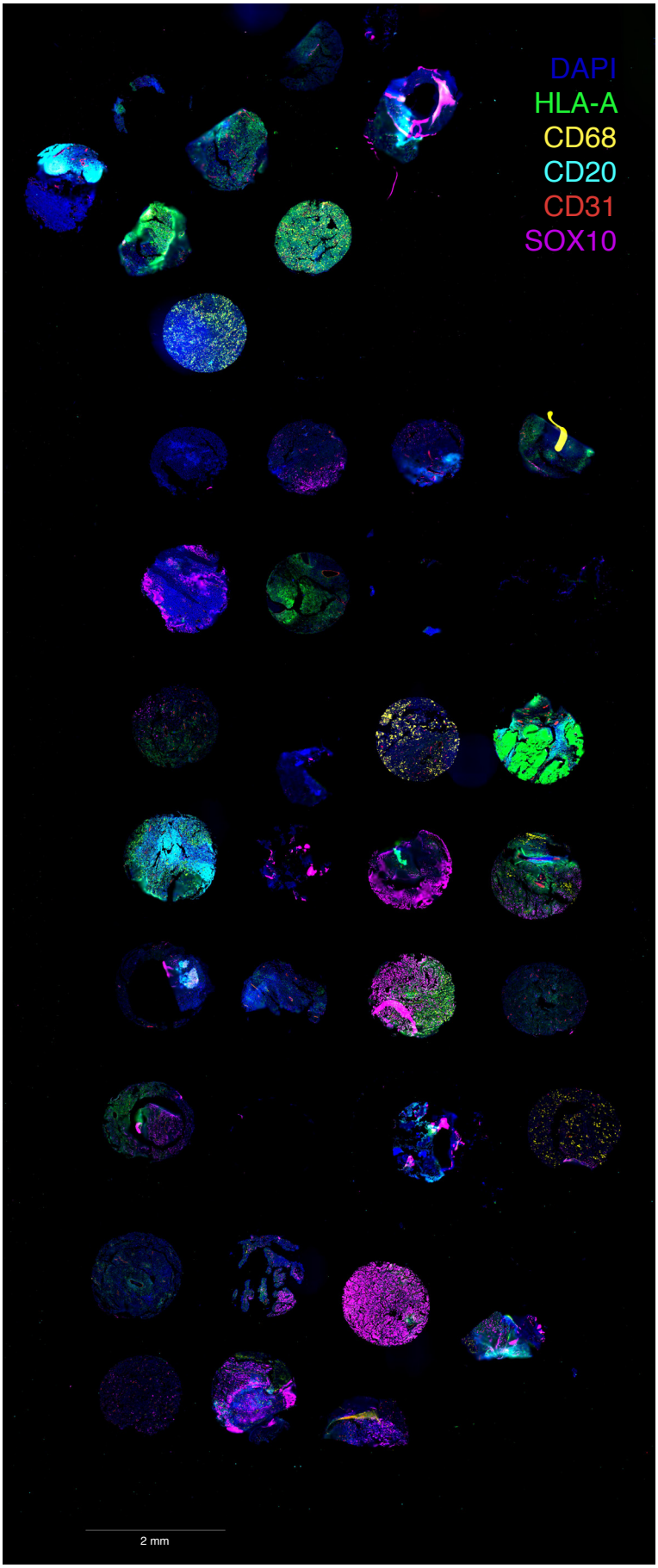

Figure 5.15 Phenocycler Fusion fluorescent image of metastatic melanoma cores after staining and acquisition with Xenium platform. After xenium hybridisation and imaging on Xenium Analyzer, slide 1 of 2 underwent antigen retrieval and PCF staining over two days, before automated cyclic imaging was performed on Phenocycler Fusion Imaging Platform microscope (Akoya Biosciences). Image with six antibody stains overlayed for visualisation: DAPI (blue), HLA-A (green), CD68 (yellow), CD20 (cyan), CD31 (red) and SOX10 (magenta). Scale bar = 2 mm.

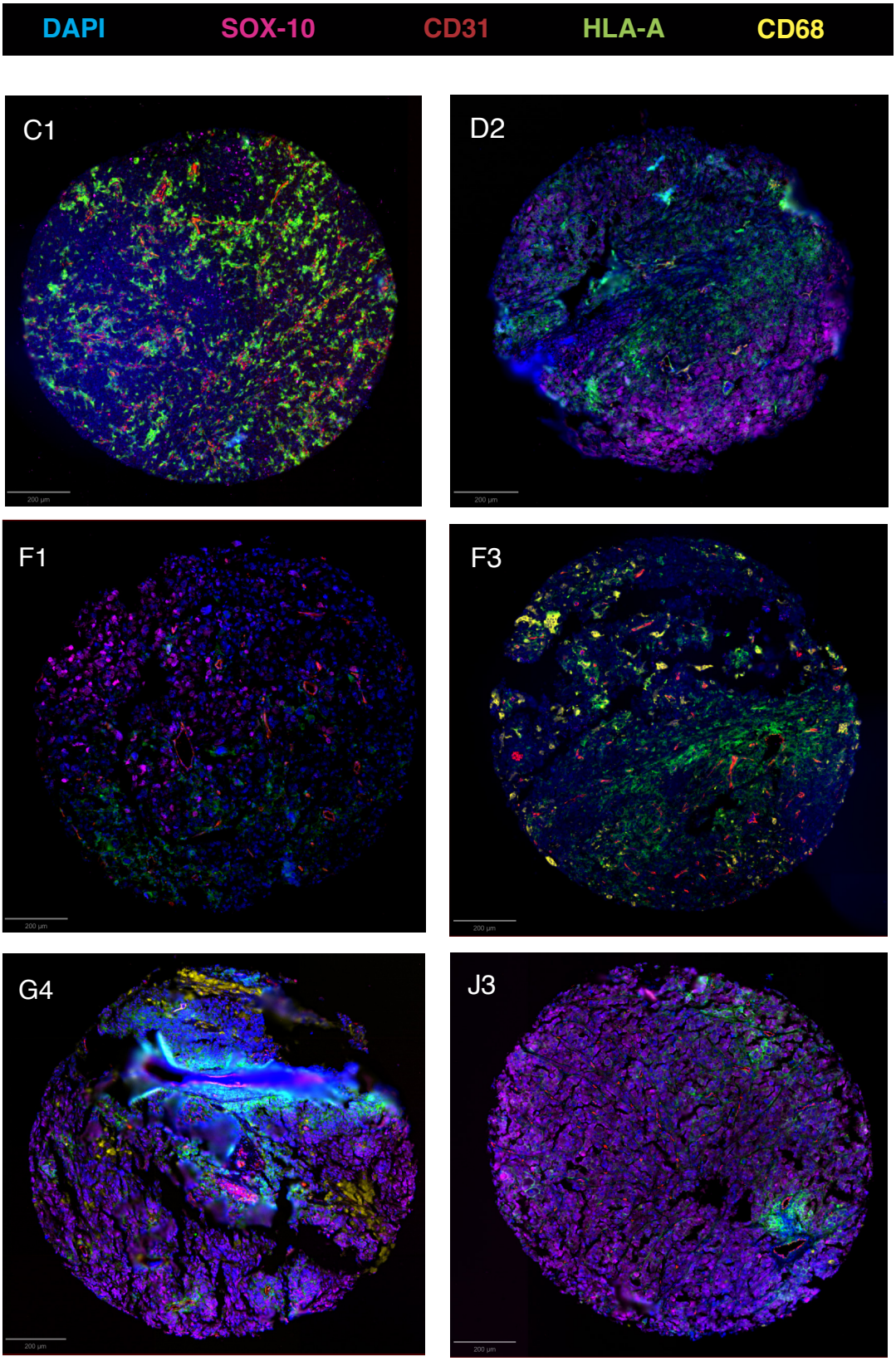

Figure 5.16 Representative images of PCF cores successfully stained after Xenium *in situ* analysis. After xenium hybridisation and imaging on Xenium Analyzer, slide 1 of 2 underwent antigen retrieval and PCF staining over two days, before automated cyclic imaging was performed. Image with six antibody stains overlayed for visualisation: DAPI (blue), HLA-A (green), CD68 (yellow), CD20 (cyan), CD31 (red) and SOX10 (magenta). Sample labels in top left corner correspond to labels in figure [whole Xenium image slide 1]. Scale Bar = 200µM.

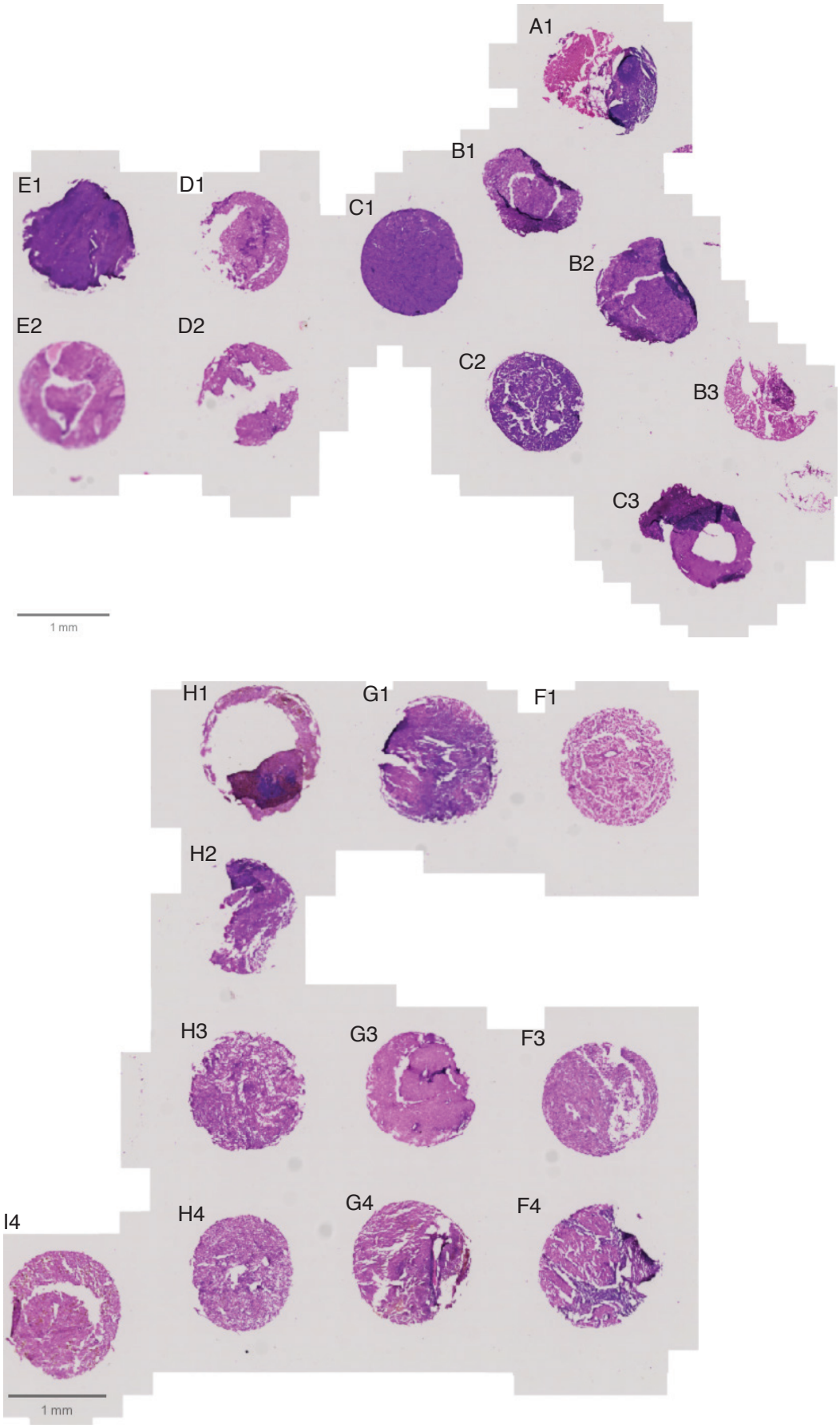

Figure 5.17 H&E staining of samples after mRNA and protein staining. Samples from Xenium Experimental slide #1 (Figure 5.4) after mRNA staining underwent PCF staining and imaging before H&E staining was performed. 22 sample cores were imaged due to tissue loss. Images were taken on Zeiss Axio Scan Z1 at the Australian Centre for Microscopy and Analysis. Scale Bar = 1mm.

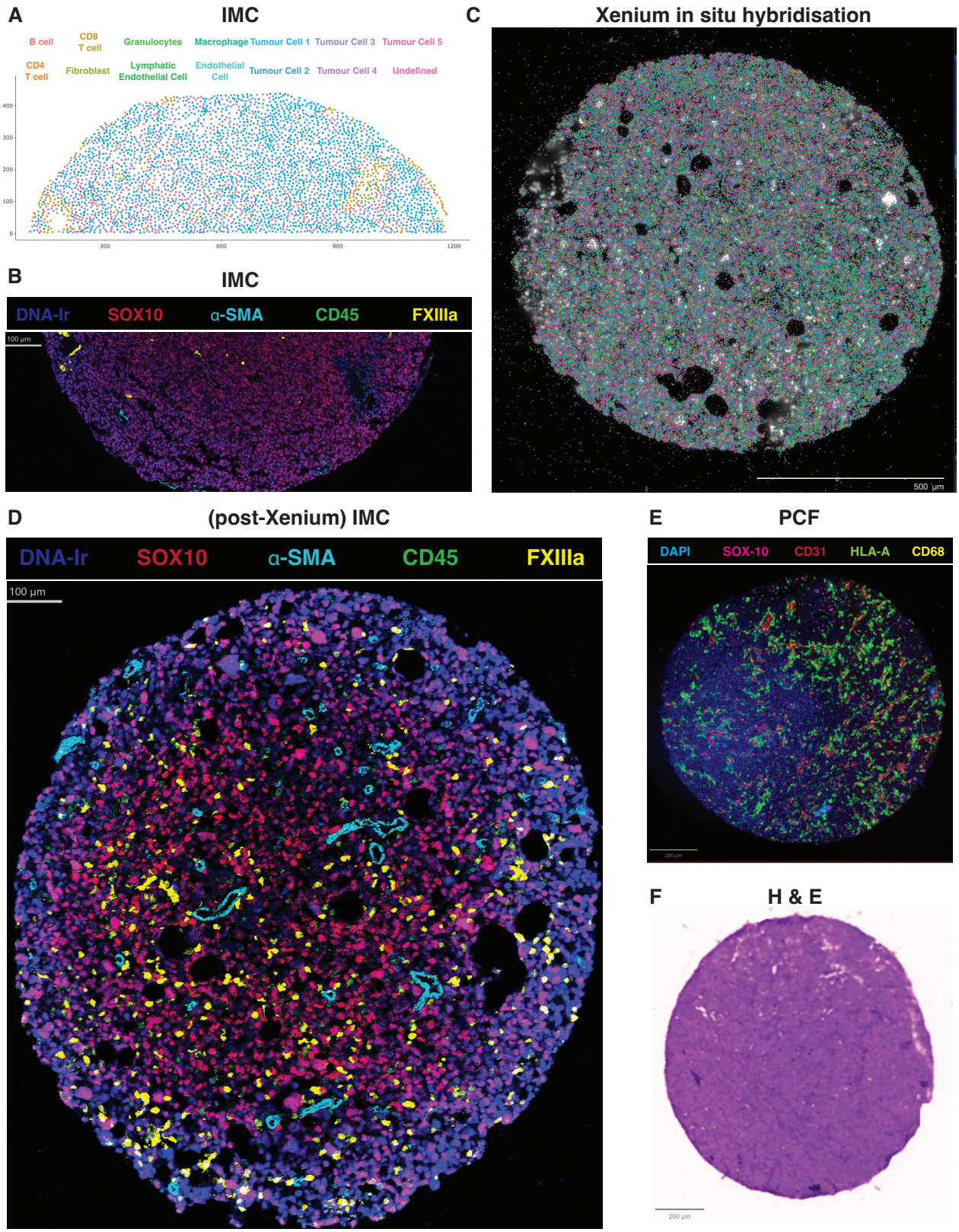

Figure 5.18 IMC, Xenium in situ hybridisation, PCF and H&E staining on one tumour sample. Sample C1 was derived from a male patient treated with adjuvant radiotherapy that relapsed and died by the conclusion of the clinical trial. Serial sections of sample C1 were included across 5 experiments: first section shown in (A) & (B), second section in (C) & (D) and third section in (E) & (F). **(A)** Reconstruction (mirrored) of cell clusters shown on sample C1 as outlined in section 2.4.5. Sample C1 tumour core was partially ablated due to the limits of the mass cytometer (Hyperion). Plot produced using plotly package in R. **(B)** IMC image used for (A) showing DNA-Ir (blue) SOX10 (red) αSMA (cyan) CD45 (green) and FXIIIa (yellow) channels. MCD viewer used to generate images, scale bar = 100 µm. **(C)** Transcripts identified by in situ hybridisation. Xenium Analyzer 2 used to generate images, scale bar = 500 µm. **(D)** IMC performed following in situ hybridisation, channels shown identical to (B). **(E)** PCF and **(F)** H&E staining performed after Xenium in situ hybridisation. Images produced using QuPath, scale bars = 100 µm.

research focused on using a novel methodology optimised as part of this research, RNAscope combined with OPAL mIHC to address this research question. Since performing these experiments, one group has published a method for combining RNAscope and OPAL similar to this study (Millar, 2020). After optimising this novel technique in melanoma tissue, we found the scalability of RNAscope was not able to keep up with the number of RNA targets needed to decipher the functional potential of enough cells in the TME. It was for this reason that we adopted newly available high-parameter spatial transcriptomic platforms to deepen our understanding of the melanoma TME.

We developed protocols for single cell spatial transcriptomics on a selection of the same samples used in chapter 4. These samples were excellent candidates for molecular analysis as the protocol for fixation and storage of FFPE tissues is standardised across pathology labs and hospitals in NSW, Australia. Therefore, these samples provided us an opportunity to establish new protocols using this cutting-edge technology and validate our high-dimensional protein cell map data from these patients. One of the early challenges faced is the requirement by the xenium system that tissue be mounted on a custom slide provided within the kit. This slide has a small target area where tissue must be placed, and if not placed correctly within fiducials, image registration within xenium analyzer will not be performed accurately. As we were using previously prepared clinical trial TMAs, we had limited options to optimise the area of the slide. By collaborating with experienced histopathology researcher Dr Rachael Ireland and consulting available resources, we planned to score the tissue block before cutting to produce two thin sections to be mounted one on each Xenium slide. This initial step was extremely difficult and required a considerable technical skill. The limited area provided on these slides, the requirement to use custom slides and the risks and costs associated need to be weighed when considering performing xenium experiments. Similar technologies such as Visium (10X Genomics) and CosMx (NanoString) permit the use of standard charged slides, allowing researchers more freedom and less risk. We will address these issues in future work by constructing custom TMAs to accommodate for the limited experimental area in this platform, if feasible, and evaluating other transcriptomic methods such as Visum and CosMx.

Due to the novelty of this technology, there is no single accepted analysis pipeline to accurately analyse spatial transcriptomic data, however, by engaging multiple methods, effective analysis pipelines can be constructed (Figure 5.18). The Xenium spatial transcriptomic platform was released in December 2022 and the experiments presented here were performed in early 2024.

While this is a rapidly expanding area of research and many other packages have since been released, at the time analysis was performed there were few (R) packages that incorporated xenium-specific data file format. Our analysis pipeline blended multiple previously used R packages to analyse data produced from xenium (Canete, 2024, Willie, 2024, Hao et al., 2024). Spatial biology and especially spatial transcriptomics are an exciting and rapidly developing research areas. The data produced from these studies are expanding of knowledge of tissue cellular landscapes and as more researchers access this technology, and the data sets produced the quality and accuracy of the available analytic tools will also improve.

This project successfully identified multiple cell clusters that appear to largely mirror the cell clusters identified by *in situ* protein analysis (IMC) in chapter 4. Due to time constraints to fully validate cell segmentation and data extraction, we used the analysis platform provided by 10x Genomics. When we calculated cell proportions and then compared these to see whether the data matched with what we had obtained in chapter 4, we did not see as many differences in the cell clusters identified by transcriptomics between patients grouped by survival or relapse. This may be due to cell cluster identification requires integration of transcriptomic spatial data with proteomic data to produce more accurate and meaningful cell cluster identities. It was for this reason that we aimed to test combining the spatial transcriptomic and protein detection technologies, IMC and PCF methodologies following xenium ISH and analysis, with the aim of registering the stains together to allow for more accurate classification of cells. In this project we were able to obtain analysable data from post-xenium IMC, but not from post-xenium PCF. The lack of analysable data produced from post-xenium PCF was due to two main reasons; firstly, a technical failing of the imaging machine due to leakage in the flow cell, an issue that has since been addressed and secondly, the cyclical nature of PCF staining and imaging results in tissue damage which while tolerated by most ‘naïve’ tissues, results in significant loss of tissue post-xenium ISH and imaging. Since performing these experiments, there have been similar attempts to combine these approaches by other groups (Huynh et al., 2024, Santhosh and Santhosh Sivajothi, 2024). Additionally, since performing these experiments, 10X genomics plan to release kits that contain up to 5000 transcript probes together with up to 30 protein markers, allowing for better cell annotation capabilities (Azevedo, 2024).

We also found that cell segmentation performed by the xenium analyzer is performed without the ability to alter parameters or was not as accurate at cell segmentation as our methods

employed in chapter 4 for our tissue. Again, since performing these experiments, xenium cell segmentation has improved, however as it is all performed within the experiment, and we were unable to re-segment our samples. This was disappointing, as the extremely high cost of this experiment was rationalised as a 'all in one' experiment for the researcher. To address this, we plan to perform our own cell segmentation on both xenium and IMC data, to then analyse with collaborators through packages incorporating multiple spatial cell omics platforms (Ghazanfar et al., 2024, Peters Couto et al., 2023). Performing further analysis will increase the applicability and usefulness of the high-parameter transcriptomic data acquired in this study.

We know that melanoma consists of tumour cells in multiple different transcriptional states (Smalley et al., 2019). Cell cluster #6 was identified as a distinct melanoma tumour cell population and was found to be present in higher proportions in patients that did not relapse and were alive at trial conclusion (Figure 5.9 & 5.10). Interestingly, cluster #6 density did not differ between these patients (Figure 5.9A & 5.10A). Cluster #6 differs from other tumour cell clusters identified by the expression of *CTSK*, *SCNA*, and *MET* (Figure 5.7). Surprisingly, these three genes are largely associated with melanoma tumorigenesis. Upon investigating the role of these genes further and comparing this data with the tumour cell clusters identified in chapter 4, we found some similarities between cluster #6 in this study and tumour cell #1 identified in chapter 4, also associated with better outcomes. As such we considered the possibility that IMC and Xenium identified a similar cluster of cells. *CTSK* encodes a lysosomal cysteine protease cathepsin-K that has been associated with melanoma cell invasion, extracellular matrix degradation and metastasis (Petricevic et al., 2017, Quintanilla-Dieck et al., 2008). As outlined above, *SCNA* is associated with worse outcomes in melanoma. In other cancers, alpha-synuclein has been associated with increased immune infiltration, inhibition of both EMT and tumorigenesis and better patient outcomes (Zhang et al., 2022, Yang et al., 2023, Zhou et al., 2022a). These conflicting accounts may be explained by the degree of alpha-synuclein overexpression. One study performed in human neuroblastoma cells found that a high overexpression of alpha-synuclein stimulation cell proliferation and delayed senescence, while low overexpression caused cell toxicity, oxidative stress and increased senescence (Rodríguez-Losada et al., 2020). As the melanoma tumour cell, cluster #6, was found to be associated with better outcomes in this study, it is possible that SCNA was expressed at a level that led to cell death as in the study above, leading to increased tumour cell death and better patient prognosis. Further studies would be required to investigate this further. The third transcript that differentiates cluster #6 from other tumour cell cells is *MET*. *MET* encodes the MET proto-

oncogene receptor tyrosine kinase, referred to as c-MET or hepatocyte growth factor receptor (HGFR), and its expression in cancer is associated with tumour progression (Zhang et al., 2018, Lee et al., 2011). Interestingly, c-MET expression is strongly correlated with PD-L1 expression in melanoma and lung cancer (Song et al., 2020, Ahn et al., 2019). This provides further evidence of the possible overlap of cell cluster #6 in this study and tumour cell 1 in chapter 4 as tumour cell 1 had high expression of PD-L1 (Figure 4.5). The expression of PD-L1 in tumour cell cluster 1 identified by proteomics and *MET* expression in cluster #6 identified by transcriptomics further supports the possibility that these clusters are comprised of the same cells. To fully elucidate this however, identification of these cells based on both protein and mRNA staining on the same slide would be required.

To progress this work, we will continue to collaborate with bioinformaticians and clinicians on this project to perform improved cell segmentation, quantify spatial interactions between cells, and integrate data produced from IMC for a multimodal analysis approach. We also plan to perform multi-omics experiments on high-TIL regions of patients in this study to compare with the high-tumour data obtained in this study. By profiling immune cell infiltrates in detail and understanding the differences between regions within the tumour, we will add another layer to this detailed profile of the metastatic melanoma TME.

This study has successfully employed novel techniques to identify cell populations associated with relapse and survival in metastatic melanoma. It has also performed successful transcript and protein staining on a single slide allowing acquisition of true multi-omics data. Further analysis and data integration will produce high-quality robust data to understand the functional potential of cells in the metastatic melanoma TME.

6 Discussion

6.1 Introduction

The work presented in this thesis provides a detailed picture of the cellular landscape of the metastatic melanoma TME. It also provides detailed features of the TME associated with better patient outcomes and demonstrates the possibility of a true high-resolution spatial multi-omic experimental approach. The use of multiple different experimental approaches as well as different metastatic melanoma patient cohorts in this study has allowed a robust and detailed understanding of the TME of metastatic melanoma. Here, the experimental and analytical approaches used in this thesis are discussed, as well as the immunopathological and cellular differences we observed across patients.

6.2 Experimental tools in the field of cancer immunology

6.2.1 Flow Cytometry & CyTOF

Suspension cytometry methods, including CyTOF and flow cytometry, allow detailed phenotyping of single cell suspensions, critical in understanding the phenotype of cells present within tumour tissue. In order to obtain accurate data from tumour dissociates, proper handling and timely optimised processing of fresh tumour samples is crucial (Drescher et al., 2021). The process of tissue dissociation can modulate expression of proteins on cells (Lischetti et al., 2023, Guldner et al., 2021, van den Brink et al., 2017) and is a major limitation. We have addressed this by optimising the protocol for tumour dissociation in our tissue and consulting published literature and composition of tissue dissociation kits available (Biotech, 2017, Okolo et al., 2023). Additionally, cytometry panel design requires prior selection of protein targets, limiting the possibility of discovering novel markers or cell subsets (Lischetti et al., 2023). The most significant limitation of cytometry methods remains the absence of spatial context of immune cells owing to samples required to be single cell suspensions. It is for this reason that we combined flow cytometry with spatial experimental approaches in our analysis of tumour tissue in this study. The field of flow cytometry has moved from polychromatic fluorescence detection able to measure up to 30 parameters, to spectral fluorescence which is predicted to detect up to 100 parameters simultaneously in the near future (Robinson et al., 2023).

As with the spatial biology field, a multitude of AI-informed analysis methods are being developed and produced to more accurately and efficiently identify cell populations and visualise flow cytometry data (Robinson et al., 2023). This will assist researchers due to the

considerable time and expertise currently required for analysis of often highly variable data obtained from human samples (Drescher et al., 2021). It is important to note, however, that these methods are only valuable when combined with a strong understanding of immunology and cell biology. Approaches that utilise single-cell suspensions remain critical in tumour immunology as well as biology due to the high-throughput capacity and the ability to sort and collect specific cell populations that can be utilised for functional studies and drug sensitivity testing.

An increasing level of granularity in cancer immunology has enabled us to distinguish rare cell phenotypes associated with outcomes (de Souza et al., 2024). Spatial multiplex imaging platforms such as IMC employ 10-50 protein markers at single cell resolution while preserving tissue architecture. These techniques allow identification of specific cell phenotypes that can help us understand mechanisms within the TME that contribute to tumour progression. As shown in this study, these high-parameter proteomic approaches also allow investigation of interactions between cells, allowing a deeper understanding of mechanisms associated with outcomes (Toki et al., 2019). Samples from clinical trials, such as those used in the studies presented here, are ideal for high-parameter analysis due to the high level of standardisation, detailed annotation of clinical data collected and balanced patient cohorts for factors such as treatment, age and disease stage (de Souza et al., 2024).

6.2.2 Imaging Mass Cytometry

The first reported use of IMC was in breast cancer in a study published 10 years ago (Giesen et al., 2014). Since then, there have been multiple published studies employing IMC to uncover TME characteristics associated with patient outcomes, including work from our group in HNSCC and HCC (Ferguson et al., 2022, Marsh-Wakefield et al., 2024, Hoch et al., 2022). Key disadvantages of IMC are the slower rate at which IMC image data is acquired by laser ablation compared to other imaging techniques (de Souza et al., 2024). Acquisition speed was a particularly challenging and a major disadvantage as this project was conducted during the onset of the COVID pandemic in 2020. This led to sample acquisition being split across multiple sessions. Many studies employing high-plex proteomics have found differences in spatial organisation within tumour tissue with no differences in the quantification of cell populations, demonstrating the importance of not only identifying and quantifying cells but identifying how these cells interact and form specific regions or cellular neighbourhoods within

their environment (Phillips et al., 2021, Sorin et al., 2023). Another study using a separate proteomic analysis method, CODEX (Akoya Biosciences), analysed 51-markers in cutaneous T cell lymphoma patients that responded to PD-1 therapy and compared with patients who did not respond (Phillips et al., 2021). They found no differences in cell densities between responders and non-responders, however, they did see that CD4 T cells were more closely located with tumour cells in PD-1 responders while CD4 T cells were closer to Tregs in non-responders (Phillips et al., 2021). Similarly, in our study, we found that although cell tumour cell cluster 4 and fibroblasts were present in the same proportions across patients, the average distance between these cells was significantly different between patients that relapsed and those that did not (Table 4.4, Figure 4.27A). While further studies are required to fully understand the relevance of this interaction, it is likely that immune regulatory mechanisms are involved.

6.2.3 *In situ* Hybridisation

Detection of individual mRNA molecules in tissue by fluorescent *in situ* hybridisation (FISH) methods was first used in human tissue more than 15 years ago (Itzkovitz et al., 2011, Raj et al., 2008). In 2012, FISH was commercialised by Advanced Cell Diagnostics (ACDBio) with the release of RNAscope (Wang et al., 2012). The availability of FISH as a kit that contained all reagents required for experimental use as well as the claim that RNAscope was more sensitive than other assays due to the Z-stack probe method meant that this was a great option for specific mRNA detection in human FFPE tissues (Wang et al., 2012). Another reason we adopted this technology was the theoretical feasibility of incorporating it with established techniques in our lab (mIHC, IMC). We successfully incorporated RNAscope and OPAL techniques, allowing quantification of cell infiltrates in multiple tumour tissues (Figure 5.1-5.3.). In this way, commercialisation increased the accessibility of *in situ* mRNA hybridisation for our research group. However, the small number of probes that can be detected simultaneously, the reliability of the protocols, reagent performance over time as well as the high cost for individual probes led us to look for better alternatives.

Identifying transcripts in tissue using *in situ* sequencing (ISS) allow the detection of hundreds of mRNA targets simultaneously. However, compared to single molecule FISH methods discussed, ISS methods have low sensitivity. ISS-based methods had issues with specificity of probes identified, stabilisation of padlock probes and tissue damage during technique (Conrad and Altmüller, 2022). The xenium *in situ* hybridisation platform, the first commercially

available ISS instrument released in December 2022, aimed to address these issues to provide improved scalable detection of hundreds of transcripts with subcellular resolution (~30nm) (Conrad and Altmüller, 2022, Azevedo, 2024). The xenium platform currently allows the addition of 100 custom genes to pre-designed panels, as well as fully custom panels of up to 480 genes (Azevedo, 2024). Xenium *in situ* hybridisation has the additional benefit for researchers to be able to re-stain and re-image the tissue section and produce additional data on the same tissue (Rademacher et al., 2024, Azevedo, 2024).

There remains a significant financial barrier to adopting these technologies as not only do the kits cost >$20,000AUD, they require a Xenium Analyzer to acquire data (Conrad and Altmüller, 2022). Despite this, many groups have used the Xenium platform in the 18 months since its release. A recent preprint comparing the performance of spatial transcriptomics platforms capable of single-cell resolution, Xenium, MERSCOPE and CoxMx using a TMA comprised of tumour tissue and normal tissue across multiple sites found Xenium had the shortest and most 'hands off' experimental acquisition of the three, the highest sensitivity, most consistence performance, and was the least sensitive to low quality tissue (Wang et al., 2023b). These findings highlight the importance of tissue and RNA quality in spatial transcriptomic studies, particularly in projects such as ours in which samples were acquired between 2001 and 2007 (Wang et al., 2023b, Conrad and Altmüller, 2022, Henderson et al., 2015). RNA quality is known to be depleted by storage conditions, fixation methods and specimen size (Lin et al., 2024c, von Ahlfen et al., 2007, Zhao et al., 2019). High-quality mRNA can still be found in FFPE tissue stored for decades before stained as long as it is appropriately fixed and stored, as observed in our study and by others (Zhao et al., 2019). Interestingly, one group found xenium detected lowly expressed transcripts compared to other techniques including MERSCOPE, while a different group found MERSCOPE more sensitive than Xenium (Hartman and Satija, 2024, Wang et al., 2023b). The latter study found that although Xenium detected the highest number of transcripts per cell, some of these were determined to be false positive counts (Hartman and Satija, 2024). Overall, projects employing Xenium report strong technical performance. At this stage, data employing these technologies is mostly in preprint form and thus not peer reviewed. As such, it is too early to evaluate fully these technologies.

Early adoption of cutting-edge techniques allows researchers to be at the forefront of exciting technological developments and new biological discoveries. One downside of this is the lack of peer-reviewed studies that evaluate the performance of such technologies to provide

guidance on best practice for experimental acquisition and analysis. Similarly to our study (Chapter 5), one group found Xenium inbuilt cell clustering algorithm performed poorly, but despite this they were able to successfully identify cells from different lineages (Wang et al., 2023b). Multiple other groups have also cited the inaccuracy of xenium cell segmentation in recent pre-prints, favouring the use of alternate cell segmentation took and open-source algorithms to make the best use of this technology (Salas et al., 2023, Cook et al., 2023, Rademacher et al., 2024, Hartman and Satija, 2024, Proietto et al., 2023). Segmentation tools such as *Baysor*, developed specifically to segment spatial transcriptomic data without protein stains, may be more appropriate for performing cell segmentation of this dataset (Petukhov et al., 2022). Current evidence therefore supports xenium as a highly specific and well performing spatial transcriptomic approach but cite inaccuracies in the in-built segmentation software, in line with the results produced in our work. Available literature further supports our plan to perform external cell segmentation on xenium data presented in this thesis, with the aim of producing more accurate data.

6.3 Combining multiple experimental methods

There is an increased need for the integration of multiple datasets in order to construct the most comprehensive overview of the biological environment examined (de Anda-Jáuregui and Hernández-Lemus, 2020). Multi-omics is simply the integration of more than one single cell or spatial approach by both experimental and computational methods. The '-omics' in question include genomics, transcriptomics, proteomics, lipidomic, metabolomics and microbiomics (de Anda-Jáuregui and Hernández-Lemus, 2020). Most incorporations are of proteomic and transcriptomic data in tumour tissue (de Souza et al., 2024). This discussion primarily focuses on transcriptomics and proteomics due to the scope of this study.

Experimental multi-omics is the acquisition of more than one approach on the same tissue. Currently there are few studies that perform multiple omics experiments on the same slide (de Souza et al., 2024). Attempts to perform multi-omics experiments include staining RNA and protein staining of tumour tissue on sequential slides, however subsequent conclusions formed are based on inference (He et al., 2022). Work shown in this thesis establishes successful staining and data acquisition of subcellular transcriptomics (xenium) with proteomics (IMC & PCF), as well as H&E staining. Combined proteomic and transcriptomic kits have very recently become available, with others in development (Azevedo, 2024, Garrido-Trigo et al., 2023). As

our proteomic and transcriptomic profiling detailed in this work is likely to be repeated on a separate TMA, we will need to decide which approach is best, between the cheaper but perhaps more time-consuming choice of further optimisation of methods used in chapter 5 or purchase of commercially available multi-omic kits, such as the thousand xenium panel with protein markers in development that is under development, said to be released this year (Azevedo, 2024).

6.3.1 Practical realities of multi-omic datasets

As spatial experiment data is very large, researchers are required to procure adequate data storage and working memory in order to perform data analysis. This issue was faced in our study, there was a significant delay in accessing the full dataset produced from Xenium due to the core facility not being equipped to transfer data of this size to users. Additionally, the processing power required for unsupervised clustering of spatial transcriptomic (xenium) data was beyond the capabilities of computers available, leading to supervised classification of this data (Figure 5.7, 5.8) Packages such as *SpatialData* have addressed this by employing lazy loading of larger-than-memory data (Marconato et al., 2024). This is one of the many packages available in Bioconductor, a project developed to ensure that the tools required for analysis are able to be accessed by the scientific community (Huber et al., 2015, Gentleman et al., 2004). This clearly demonstrates the high memory and processing power required for analysis of this data that is not accessible for all researchers. Future re-analysis of this data will employ a shared high-processing computer that will allow for unsupervised clustering to be performed.

6.3.2 Projects with many methods require many experts

Projects involving spatial multi-omics of human tissue require a multidisciplinary team to properly evaluate data (Conrad and Altmüller, 2022). The technical expertise of computational methods provided by bioinformaticians, the tissue-specific expertise provided by pathologists and wet-lab researchers as well as guidance on relevant and important clinical questions by specialist clinicians is crucial for the valid and robust use of data science in human biological fields such as immunology (de Anda-Jáuregui and Hernández-Lemus, 2020). The studies presented in chapters 4 and 5 have relied on strong collaboration between our research team (Ruth Allen, Dr Angela Ferguson, A/Prof. Mainthan Palendira) with bioinformaticians (Farhan Ameen and A/Prof. Ellis Patrick) and clinician scientists, Radiation Oncologist (Prof Angela

Hong), Medical Oncologist (Prof. Georgina Long), and anatomical Pathologist (Prof. Richard Scolyer).

Another challenge faced by researchers aiming to integrate transcriptomic and proteomic data is the variable correlation of RNA and protein expression (Lischetti et al., 2023). Work using melanoma biopsies found that multiple targets were detected by RNA but not protein, while other markers were detected by protein staining but not RNA (Lischetti et al., 2023, Raufaste-Cazavieille et al., 2022). This highlights the importance of performing protein and mRNA approaches together to produce data that does not rely on inference. Although the most accurate way to achieve this is to perform RNA and protein stains on the same section as shown in this thesis, performing these stains on sequential sections in the next-best option. Performing image registration and alignment of Xenium data and IMC data from the same samples (chapter 5) will reveal the correlations between mRNA transcripts and protein expression within the cell. This analysis will map the cellular landscape to a level of detail not produced to date. This supports the need for experimental approaches that combine both transcriptomic and proteomic stains in order to more accurately understand individual cell function.

6.3.3 Analysing data efficiently and judiciously

Developments in deep learning (type of machine learning) have also increased in recent years, utilising both high-parameter spatial imaging data and 'simple' image types such as H&E as well as 'prior knowledge' from public datasets or literature to improve clinical diagnosis and prediction power (Zidane et al., 2023, Anderson et al., 2021). Deep learning frameworks such as *NaroNet* have been developed as both research and clinical diagnostic tools. *NaroNet* is a model trained on multiplex images of tumour tissue with clinical information attached to produce a predictive model that can be used on IHC or IMC-stained tumour tissue (Jiménez-Sánchez et al., 2022). Another deep learning approach developed to determine chemotherapy response of breast cancer patients found the model was most predictive of response when images from multiple tumour regions were imported (Taleghamar et al., 2022). This study also supports the importance of representing the heterogeneity of tissue in datasets that are fed into machine learning algorithms. If spatial techniques are to be adapted for clinical use, they need to be simple and reliable enough for pathology labs to perform. Additionally, possible biomarkers would need to be consistently expressed across patients, and machine-learning

analysis of large cohort studies are great tools to identify such biomarkers. The high cost of these experiments remains a significant barrier for clinical use (Lewis et al., 2021).

One of the principle aims in this study as well as tumour immunology in general, is to detect specific molecular pathways, cell populations, interactions or tissue regions associated with patient prognosis, treatment response and survival (Raufaste-Cazavieille et al., 2022). Studies in recent years employing multi-omics to elucidate biomarkers in melanoma have successfully discovered novel predictors of response to immunotherapy and patient outcomes in melanoma and various other cancers (Jin et al., 2023, Leek et al., 2024, He and Wang, 2023, Martin-Hernandez et al., 2023, Demir Karaman and Işık, 2023). Recent work employing spatial proteomics led to the discovery of new treatment strategies for toxic epidermal necrolysis (Nordmann et al., 2024). However, these biomarkers still need to be validated before they can be implemented clinically (Medori et al., 2023, Robert and Gautheret, 2022). Identifying methods to analyse and understand multi-omics datasets, such as those proposed in this study, are essential in moving multi-omics from the bench to the clinic.

6.4 Linking tumour composition with patient outcomes in metastatic melanoma

6.4.1 Investigating the myeloid compartment

It is well understood that CD8 T cells are important for the anti-tumour response. However, less is known about the role of the myeloid compartment in metastatic melanoma. In chapter 3, we profiled the myeloid compartment in metastatic melanoma in detail and quantified 11 populations across 30 patients (Figure 3.2, 3.4 & 3.5). As assessed by CyTOF, we found that two of these myeloid cell populations were found to be elevated in the tumours of responders to anti-PD-1 therapy when compared to non-responders (Figure 3.5). We also saw that macrophages expressed some of the highest proportions of novel immunotherapy target VISTA across the 19 cell populations quantified (Figure 3.3). Our data highlight the role of myeloid cells in response to immunotherapy and adds to our growing understanding of the importance of myeloid cells in the TME. Building on this, our detailed examination of metastatic melanoma through IMC (chapter 4) found that proportions of macrophages were higher in patients that did not relapse, compared to those that did (Table 4.4). We also found that macrophages were located significantly closer to PD-1-expressing endothelial cells in the tumour regions of metastatic melanoma patients that did not survive, suggesting a modulatory role of macrophages in shaping the TME (Figure 4.27). This is in line with current

understanding on the polarising nature of macrophages, both pro- and anti-tumour in the TME (Rannikko and Hollmén, 2024, Yan et al., 2021, Qian and Pollard, 2010, Hume et al., 2023, Biswas and Mantovani, 2010, Zhou et al., 2022b, Mantovani and Sica, 2010). Although we did not see any differences in the proportions of the macrophage cluster identified in our transcriptomic experiment between patients, there may be differences elucidated by spatial analysis of these data. Potentially, this will be elucidated by further spatial analysis we are currently performing on the transcriptomic data shown in chapter 5.

6.4.2 CD4 T cells as important drivers of anti-tumour response

This project has also highlighted the contribution of distinct populations of CD4 T cells to patient response and outcome. Work shown in chapter 3 found that CD4 T cells, not CD8 T cells, comprise the largest proportion of immune cells in metastatic melanoma tumours, with T_H1 cells, the most dominant subset (Figure 3.1). When we looked at novel immunotherapy target VISTA expression across immune cells, we saw that non-T_H1 CD4 subsets (T_H2, T_H17 and $T_H17.1$ cells) also expressed a high proportion of VISTA compared to other cells identified (Figure 3.3). This again supports an important role for CD4 T cells in response to immunotherapy. When we then looked at whether the presence of CD4 T cells is important for anti-tumour response (chapter 4), we saw that not only were CD4 T cells significantly higher in patients that did not relapse and were alive at clinical trial conclusion, a low proportion of CD4 T cells predicted a shorter time to relapse and time to death for patients (Figure 4.9, 4.17, 4.26, 4.27). Although we did report higher proportions and densities of CD8 T cells in patients that did not relapse and survived, we did not see a similar contribution of CD8 T cells to the time to relapse or death as was observed for CD4 T cells. This work therefore highlights the importance of CD4 T cell in anti-tumour responses, as well as the need for multiple analysis strategies to elucidate TME features associated with better patient outcomes.

6.4.3 Approaching tumour heterogeneity

A high degree of tumour cell heterogeneity is observed across many cancers, particularly melanoma, complicating the identification of biomarkers and development of effective treatment strategies (Raufaste-Cazavieille et al., 2022, Cyll et al., 2017, Crucitta et al., 2022, Sztiller-Sikorska et al., 2015, Dagogo-Jack and Shaw, 2018). Our understanding of tumour cells and their underlying phenotypes or capacity for progression is underdeveloped compared to current understanding of immune cell subsets and functional properties (de Souza et al.,

2024, Marusyk et al., 2020). We need to better understand of the relationship between tumour cell heterogeneity and response to treatment as well as outcome if we are to advance treatment strategies that result in a robust, long lasting patient responses (Ng et al., 2022). Due to the spatial context lost by single-cell approaches, as well as the finding that long-term culture of melanoma cells results in the loss of genetic and phenotypic heterogeneity, high-parameter spatially resolved experimental techniques are uniquely suited to investigating tumour cell heterogeneity *in situ* (Gregg, 2021, Proietto et al., 2023). Previously discussed issues of signal-to-noise ratio and different pre-processing and analysis methods used will make the inference of tumour cell populations between different experimental and analysis techniques challenging (Proietto et al., 2023). Again, this can be addressed by employing multimodal analysis tools, standardising approaches to data preprocessing and unsupervised clustering.

In chapter 4 and 5 we identified multiple tumour cell phenotypes in proteomic and transcriptomic datasets using supervised clustering methods (Figures 4.6 & 5.7). Both approaches found the majority of cells in high-tumour regions of the TME were tumour cells. Analysis of IMC data revealed 5 distinct tumour cell clusters, while transcriptomic analysis identified 4 distinct tumour cell clusters. Proteomic experiments revealed that a higher proportion of tumour cell cluster #5 recorded in the metastatic melanoma TME was associated with worse patient outcomes (Figure 4.26 & 4.27). Our analysis also found that tumour cell cluster #4 was significantly closer to, or interacting with, fibroblasts in patients that relapsed, suggesting this tumour cell population may be modulating fibroblasts in order to shape a pro-tumour environment and favour EMT (Figure 4.5). Interestingly, we also report tumour cell cluster (#1), characterised by high checkpoint marker expression, was associated with better patient outcomes (Figure 4.27 & 4.28). Although the proportion of tumour cell #1 in the TME was not different between patients grouped by relapse or survival, having a low proportion of this cell phenotype present in the TME did predict a shorter time to relapse and death (Figure 4.26 & 4.27). These findings further demonstrate the importance of multi-pronged approaches in analysing high-parameter spatial data with well-annotated clinical data. When we performed similar analysis in our spatial transcriptomic (xenium) data, we also saw a unique tumour cell cluster that was significantly higher in patients that were alive and did not relapse at the end point of the clinical trial (Figure 5.9 & 5.10). Our research successfully identified phenotypically distinct tumour cell subsets that were not only present at different proportions, but also have distinct cellular interactions within the TME in patients that had good outcomes (did not relapse and survived) compared to those that relapsed and died by trial conclusion. As

there was limited overlap between the targets (panels) used for proteomics and transcriptomics in this thesis, particularly regarding tumour cell markers, it is difficult to compare tumour cell clusters between experiments. Whether or not these tumour cell clusters have significant overlap will be uncovered with the integration of proteomic and transcriptomic data obtained in chapter 5 which was beyond the scope of this thesis. This work highlights the value of high-parameter spatial analysis in uncovering how TME features relate to tumour progression.

6.5 Comparing cohorts and methods

Interestingly, when we found that the proportions of immune cells were much higher in data acquired by CyTOF and flow cytometry (chapter 3) compared to data produced from IMC and Xenium. This was likely because both experimental technique and tissue regions used were different. Data acquired by CyTOF and flow cytometry (chapter 3) used single cell suspensions of fresh metastatic melanoma tumour biopsies or resections, while IMC, Xenium, post-Xenium IMC, PCF and H&E used resections from high-tumour regions of metastatic melanoma tumours. As such, the suspension studies quantified all cells within tumour samples, of which many were not lymph-node associates. This contrasted with the fixed tissue studies that used high-tumour regions only, defined by a pathologist, in small $1mm^2$ sections. We also saw differences in the proportion of cells detected between IMC and Xenium data as well as of IMC data processed by different cell segmentation methods CellProfiler and *simpleseg* and analysis pipelines (FlowJo manual analysis vs supervised clustering and annotation). These differences between analysis approaches were what assisted us in optimising and adopting the most suitable pipeline for our data. The number of cell clusters identified as well as the cell phenotypes observed did vary between proteomic (IMC, chapter 4) and transcriptomic (xenium, chapter 5) analysis. This is likely due to different analysis methods employed, different cell segmentation methods, lack of image registration, as well as the lack of correlation between protein and transcript expression discussed previously. This difference could also be attributed to fact that transcriptomic analysis used a separate section of the TMA used in Xenium staining due to slide requirements, likely resulting in some different cells being sampled (within 20um).

6.6 Future directions

The next steps in advancing this project are firstly, to perform more accurate cell segmentation of xenium *in situ* data using open-source algorithms developed by our collaborators (Fu et al.,

2024). Once this is performed, analysis including image 'registering' between IMC and xenium will be performed, prior unbiased clustering with our bioinformatics collaborators. Once this is performed, we will be able to embark on the complex task of integrating proteomic and transcriptomic data together with the aim to better understand the biology behind the differences we have reported here. We also plan to perform both spatial proteomics and transcriptomics on a TMA from the same cohort of patients consisting of high-TIL regions from the tumours assessed previously using IMC and xenium (chapters 4 and 5), adding region-specific understanding of the TME in metastatic melanoma.

6.7 Conclusion

This thesis has shown the diversity of both immune and tumour cell phenotypes in metastatic melanoma and linked some of these phenotypes to clinical outcomes (Figure 6.1). In chapter 3, we investigated the TME using suspension cytometry to not only quantify both tumour and immune cells, but to also interrogate established understandings of the myeloid compartment in melanoma (Figure 6.1A and D). We found that myeloid cells are highly heterogenous within tumours and between patients, however we were able to identify both established and novel phenotypes across all samples. Linking these phenotypes to clinical outcomes, we showed that two myeloid population established in this study, Mϕ2 and TIM2 cells, were associated with response to anti-PD-1 immunotherapy (Figure 6.1A). We next employed IMC to profile in detail both the cellular composition of high-tumour regions of metastatic melanoma as well as the interactions between these populations in chapter 4 (Figure 6.1A-E). This study successfully employed a 42-paramter proteomic panel to investigate cellular phenotypes, and also developed and compared novel methodologies for accurately performing experimental high-parameter spatial techniques and analysis. The final study in this thesis built upon this and demonstrated successful transcriptomic and proteomic staining on a single slide, an approach not published at the time the experiment was performed. This chapter also discussed various analytical approaches to analysing multi-omic data, highlighting contemporary issues in this field. As the studies presented in this thesis was the product of a large and diverse team of basic scientists, bioinformaticians and clinicians, this work also provides novel perspectives on the importance of collaborative approaches in the field of spatial biology and immunology. In conclusion, the work presented in this thesis will add to our understanding of mechanisms of melanoma progression, response to therapy and basic tissue and tumour immunology.

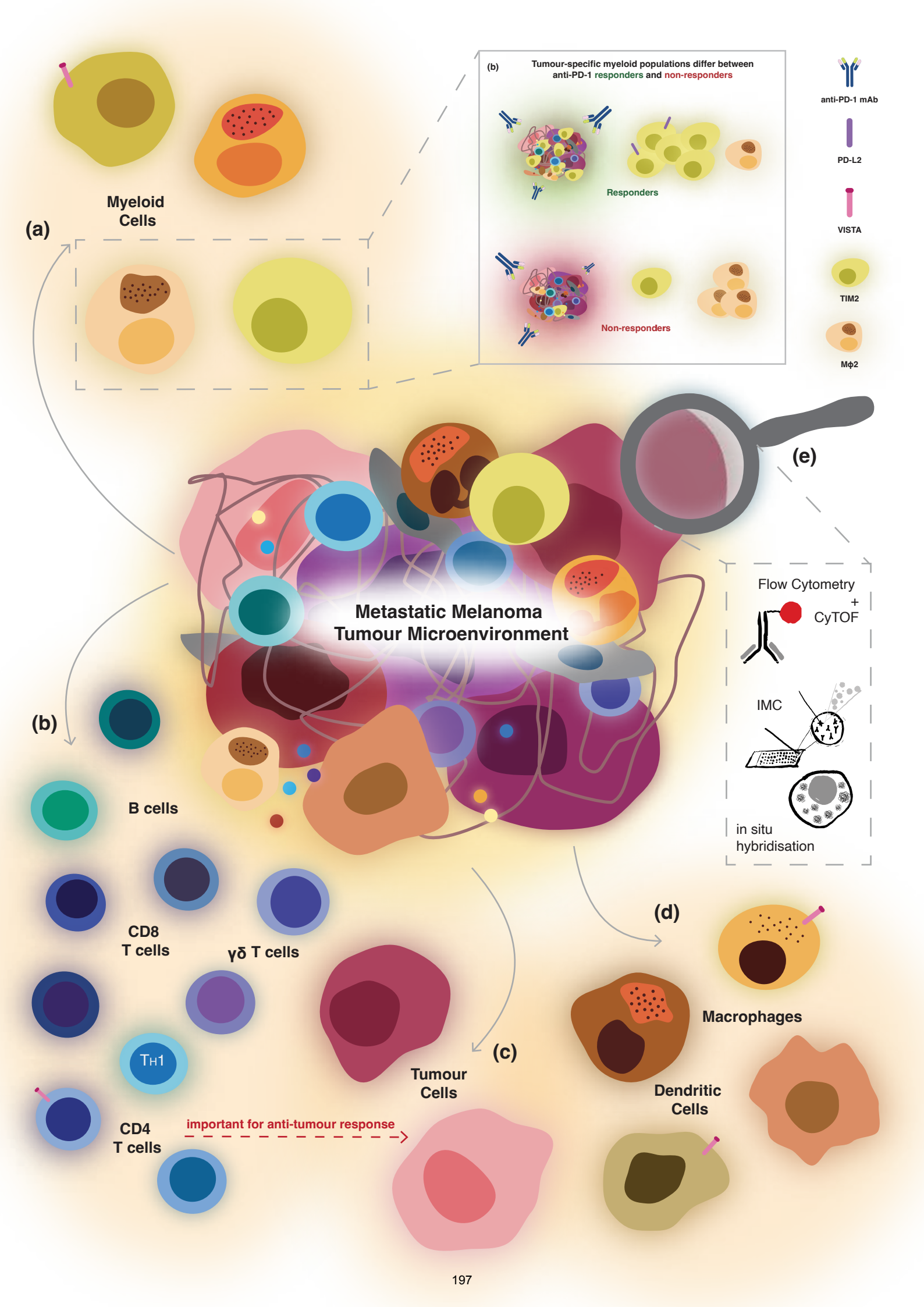
(a)
Myeloid Cells
(b)
Tumour-specific myeloid populations differ between anti-PD-1 responders and non-responders
Responders
Non-responders
anti-PD-1 mAb
PD-L2
VISTA
TIM2
Mϕ2
(e)
Metastatic Melanoma Tumour Microenvironment
Flow Cytometry + CyTOF
IMC
in situ hybridisation
(b)
B cells
CD8 T cells
γδ T cells
TH1
CD4 T cells
important for anti-tumour response
(c)
Tumour Cells
(d)
Macrophages
Dendritic Cells

Figure 6.1 Graphical summary of the findings of this study investigating the cellular composition of metastatic melanoma. (a-d) The immune infiltrate of metastatic melanoma tumours is comprised of tumour cells, lymphocytes, including B and T cells, as well as the diverse innate cell compartment. **(a)** Two tumour-specific myeloid cell phenotypes were found to differ between anti-PD-1 responders and non-responders. TIM2 myeloid cells, characterised by CD1c expression, were present at higher levels in and expressed more PD-L2 compared to the TIM2 cells present in non-responders. Conversely, a tumour-associated macrophage subset characterised by CD13 expression was found to be present at higher levels in patients that did not respond to PD-1 therapy. **(b)** Lymphocytes identified in this work include CD4 T cells, CD8 T cells, gamma delta T cells and B cells. This study highlighted the important anti-tumour role of CD4 T cells by showing the strong correlation of CD4 T cell densities in high tumour regions with better outcomes as well as the number of interactions CD4 T cells had with macrophages in high-tumour regions.**(c)** Proteomic and transcriptomic approaches in chapters 4 and 5 highlight the high level of tumour cell heterogeneity in metastatic melanoma while also being able to identify phenotypically distinct clusters within high-tumour regions. **(d)** Chapter 3 also identifies both established and novel myeloid cell phenotypes in metastaic melanoma, including macrophage and dendritic cell subpopulations. **(e)** The diverse techniques used in this thesis include; flow cytometry and suspension CyTOF, IHC, IMC, and in situ hybridisation. We also show data acquired by PCF, however this was not quantified. Importantly, we establish experimental and analytic methods for combining these approaches.

7 References

2012. Radiation. *IARC Monogr Eval Carcinog Risks Hum,* 100**,** 7-303.

2020a. Method of the Year 2019: Single-cell multimodal omics. *Nature Methods,* 17**,** 1-1.

2020b. Phase 1 Study of CI-8993 Anti-VISTA Antibody in Patients With Advanced Solid Tumor Malignancies.

2020c. Phase I Dose Escalation and Dose Expansion, International, Multicenter Study of W0180 as Single Agent and in Combination With Pembrolizumab (Anti-PD-1) in Adult Participants With Locally Advanced or Metastatic Solid Tumors.

ABBASI, S., SINHA, S., LABIT, E., ROSIN, N. L., YOON, G., RAHMANI, W., JAFFER, A., SHARMA, N., HAGNER, A., SHAH, P., ARORA, R., YOON, J., ISLAM, A., UCHIDA, A., CHANG, C. K., STRATTON, J. A., SCOTT, R. W., ROSSI, F. M. V., UNDERHILL, T. M. & BIERNASKIE, J. 2020. Distinct Regulatory Programs Control the Latent Regenerative Potential of Dermal Fibroblasts during Wound Healing. *Cell Stem Cell,* 27**,** 396-412.e6.

ADAMIK, J., MUNSON, P. V., MAURER, D. M., HARTMANN, F. J., BENDALL, S. C., ARGÜELLO, R. J. & BUTTERFIELD, L. H. 2023. Immuno-metabolic dendritic cell vaccine signatures associate with overall survival in vaccinated melanoma patients. *Nat Commun,* 14**,** 7211.

ADEGOKE, N. A., GIDE, T. N., MAO, Y., QUEK, C., PATRICK, E., CARLINO, M. S., LO, S. N., MENZIES, A. M., PIRES DA SILVA, I., VERGARA, I. A., LONG, G., SCOLYER, R. A. & WILMOTT, J. S. 2023. Classification of the tumor immune microenvironment and associations with outcomes in patients with metastatic melanoma treated with immunotherapies. *J Immunother Cancer,* 11**,** e007144.

AHMADZADEH, H., WEBSTER, M. R., BEHERA, R., JIMENEZ VALENCIA, A. M., WIRTZ, D., WEERARATNA, A. T. & SHENOY, V. B. 2017. Modeling the two-way feedback between contractility and matrix realignment reveals a nonlinear mode of cancer cell invasion. *Proc Natl Acad Sci U S A,* 114**,** E1617-e1626.

AHN, H. K., KIM, S., KWON, D., KOH, J., KIM, Y. A., KIM, K., CHUNG, D. H. & JEON, Y. K. 2019. MET Receptor Tyrosine Kinase Regulates the Expression of Co-Stimulatory and Co-Inhibitory Molecules in Tumor Cells and Contributes to PD-L1-Mediated Suppression of Immune Cell Function. *International Journal of Molecular Sciences,* 20**,** 4287.

ALEXANDROV, T., SAEZ-RODRIGUEZ, J. & SAKA, S. K. 2023. Enablers and challenges of spatial omics, a melting pot of technologies. *Mol Syst Biol,* 19**,** e10571.

ALHUMAID, M., DINAKARAN, D., SMYLIE, M., WALKER, J. & JOSEPH, K. 2023. Can radiation restore immunotherapy response in metastatic melanoma refractory to checkpoint inhibitors: An institutional experience in salvaging immunotherapy resistant disease. *Radiother Oncol,* 185**,** 109712.

AMARIA, R. N., POSTOW, M., BURTON, E. M., TETZLAFF, M. T., ROSS, M. I., TORRES-CABALA, C., GLITZA, I. C., DUAN, F., MILTON, D. R., BUSAM, K., SIMPSON, L., MCQUADE, J. L., WONG, M. K., GERSHENWALD, J. E., LEE, J. E., GOEPFERT, R. P., KEUNG, E. Z., FISHER, S. B., BETOF-WARNER, A., SHOUSHTARI, A. N., CALLAHAN, M., COIT, D., BARTLETT, E. K., BELLO, D., MOMTAZ, P., NICHOLAS, C., GU, A., ZHANG, X., KORIVI, B. R., PATNANA, M., PATEL, S. P., DIAB, A., LUCCI, A., PRIETO, V. G., DAVIES, M. A., ALLISON, J. P., SHARMA, P., WARGO, J. A., ARIYAN, C. & TAWBI, H. A. 2022. Neoadjuvant relatlimab and nivolumab in resectable melanoma. *Nature,* 611**,** 155-160.

AMEEN F, I. S., GHAZANFAR S, PATRICK E 2024. Statial: A package to identify changes in cell state relative to spatial associations. *Bioconductor*.

ANDERSON, P., GADGIL, R., JOHNSON, W. A., SCHWAB, E. & DAVIDSON, J. M. 2021. Reducing variability of breast cancer subtype predictors by grounding deep learning models in prior knowledge. *Comput Biol Med,* 138**,** 104850.

ANDREEFF, M., BECK, J. D., DARZYNKIEWICZ, Z., TRAGANOS, F., GUPTA, S., MELAMED, M. R. & GOOD, R. A. 1978. RNA content in human lymphocyte subpopulations. *Proc Natl Acad Sci U S A,* 75**,** 1938-42.

ANNUNZIATO , F., COSMI , L., SANTARLASCI , V., MAGGI , L., LIOTTA , F., MAZZINGHI , B., PARENTE , E., FILÌ , L., FERRI , S., FROSALI , F., GIUDICI , F., ROMAGNANI , P., PARRONCHI , P., TONELLI , F., MAGGI , E. & ROMAGNANI , S. 2007. Phenotypic and functional features of human Th17 cells. *Journal of Experimental Medicine,* 204**,** 1849-1861.

ARNOLD, M., SINGH, D., LAVERSANNE, M., VIGNAT, J., VACCARELLA, S., MEHEUS, F., CUST, A. E., DE VRIES, E., WHITEMAN, D. C. & BRAY, F. 2022. Global Burden of Cutaneous Melanoma in 2020 and Projections to 2040. *JAMA Dermatol,* 158**,** 495-503.

ASCIERTO, P. A., AGARWALA, S. S., BLANK, C., CARACÒ, C., CARVAJAL, R. D., ERNSTOFF, M. S., FERRONE, S., FOX, B. A., GAJEWSKI, T. F., GARBE, C., GROB, J. J., HAMID, O., KROGSGAARD, M., LO, R. S., LUND, A. W., MADONNA, G., MICHIELIN, O., NEYNS, B., OSMAN, I., PETERS, S., POULIKAKOS, P. I., QUEZADA, S. A., REINFELD, B., ZITVOGEL, L., PUZANOV, I. & THURIN, M. 2022. Perspectives in Melanoma: meeting report from the Melanoma Bridge (December 2nd - 4th, 2021, Italy). *J Transl Med,* 20**,** 391.

ASHHURST, T. M., MARSH-WAKEFIELD, F., PUTRI, G. H., SPITERI, A. G., SHINKO, D., READ, M. N., SMITH, A. L. & KING, N. J. C. 2022. Integration, exploration, and analysis of high-dimensional single-cell cytometry data using Spectre. *Cytometry A,* 101**,** 237-253.

ASPORD, C., LECCIA, M. T., CHARLES, J. & PLUMAS, J. 2013. Plasmacytoid dendritic cells support melanoma progression by promoting Th2 and regulatory immunity through OX40L and ICOSL. *Cancer Immunol Res,* 1**,** 402-15.

ASRIR, A., TARDIVEAU, C., COUDERT, J., LAFFONT, R., BLANCHARD, L., BELLARD, E., VEERMAN, K., BETTINI, S., LAFOURESSE, F., VINA, E., TARROUX, D., ROY, S., GIRAULT, I., MOLINARO, I., MARTINS, F., SCOAZEC, J. Y., ORTEGA, N., ROBERT, C. & GIRARD, J. P. 2022. Tumor-associated high endothelial venules mediate lymphocyte entry into tumors and predict response to PD-1 plus CTLA-4 combination immunotherapy. *Cancer Cell,* 40**,** 318-334.e9.

ATTRILL, G. H., LEE, H., TASKER, A. T., ADEGOKE, N. A., FERGUSON, A. L., DA SILVA, I. P., SAW, R. P. M., THOMPSON, J. F., PALENDIRA, U., LONG, G. V., FERGUSON, P. M., SCOLYER, R. A. & WILMOTT, J. S. 2022a. Detailed spatial immunophenotyping of primary melanomas reveals immune cell subpopulations associated with patient outcome. *Front Immunol,* 13**,** 979993.

ATTRILL, G. H., OWEN, C. N., AHMED, T., VERGARA, I. A., COLEBATCH, A. J., CONWAY, J. W., NAHAR, K. J., THOMPSON, J. F., PIRES DA SILVA, I., CARLINO, M. S., MENZIES, A. M., LO, S., PALENDIRA, U., SCOLYER, R. A., LONG, G. V. & WILMOTT, J. S. 2022b. Higher proportions of CD39+ tumor-resident cytotoxic T cells predict recurrence-free survival in patients with stage III melanoma treated with adjuvant immunotherapy. *J Immunother Cancer,* 10**,** e004771.

AZEVEDO, J. 2024. Optimizing your spatial transcriptomics research with Visium HD and Xenium In Situ. *10x Genomics* [Online]. Available from: https://www.10xgenomics.com/blog/optimizing-your-spatial-transcriptomics-research-with-visium-hd-and-xenium-in-situ [Accessed 09-04-2024 2024].

AZIMI, F., SCOLYER, R. A., RUMCHEVA, P., MONCRIEFF, M., MURALI, R., MCCARTHY, S. W., SAW, R. P. & THOMPSON, J. F. 2012. Tumor-infiltrating lymphocyte grade is an independent predictor of sentinel lymph node status and survival in patients with cutaneous melanoma. *J Clin Oncol,* 30**,** 2678-83.

BALSAMO, M., SCORDAMAGLIA, F., PIETRA, G., MANZINI, C., CANTONI, C., BOITANO, M., QUEIROLO, P., VERMI, W., FACCHETTI, F., MORETTA, A., MORETTA, L., MINGARI, M. C. & VITALE, M. 2009. Melanoma-associated fibroblasts modulate NK cell phenotype and antitumor cytotoxicity. *Proc Natl Acad Sci U S A,* 106**,** 20847-52.

BALSAMO, M., VERMI, W., PARODI, M., PIETRA, G., MANZINI, C., QUEIROLO, P., LONARDI, S., AUGUGLIARO, R., MORETTA, A., FACCHETTI, F., MORETTA, L., MINGARI, M. C. & VITALE, M. 2012. Melanoma cells become resistant to NK-cell-mediated killing when exposed to NK-cell numbers compatible with NK-cell infiltration in the tumor. *Eur J Immunol,* 42**,** 1833-42.

BANKHEAD, P., LOUGHREY, M. B., FERNÁNDEZ, J. A., DOMBROWSKI, Y., MCART, D. G., DUNNE, P. D., MCQUAID, S., GRAY, R. T., MURRAY, L. J., COLEMAN, H. G., JAMES, J. A., SALTO-TELLEZ, M. & HAMILTON, P. W. 2017. QuPath: Open source software for digital pathology image analysis. *Scientific Reports,* 7**,** 16878.

BASDEO, S. A., CLUXTON, D., SULAIMANI, J., MORAN, B., CANAVAN, M., ORR, C., VEALE, D. J., FEARON, U. & FLETCHER, J. M. 2017. Ex-Th17 (Nonclassical Th1) Cells Are Functionally Distinct from Classical Th1 and Th17 Cells and Are Not Constrained by Regulatory T Cells. *The Journal of Immunology,* 198**,** 2249-2259.

BAWDEN, E. G., WAGNER, T., SCHRÖDER, J., EFFERN, M., HINZE, D., NEWLAND, L., ATTRILL, G. H., LEE, A. R., ENGEL, S., FREESTONE, D., DE LIMA MOREIRA, M., GRESSIER, E., MCBAIN, N., BACHEM, A., HAQUE, A., DONG, R., FERGUSON, A. L., EDWARDS, J. J., FERGUSON, P. M., SCOLYER, R. A., WILMOTT, J. S., JEWELL, C. M., BROOKS, A. G., GYORKI, D. E., PALENDIRA, U., BEDOUI, S., WAITHMAN, J., HOCHHEISER, K., HÖLZEL, M. & GEBHARDT, T. 2024. CD4(+) T cell immunity against cutaneous melanoma encompasses multifaceted MHC II-dependent responses. *Sci Immunol,* 9**,** eadi9517.

BELOTE, R. L., LE, D., MAYNARD, A., LANG, U. E., SINCLAIR, A., LOHMAN, B. K., PLANELLS-PALOP, V., BASKIN, L., TWARD, A. D., DARMANIS, S. & JUDSON-TORRES, R. L. 2021. Human melanocyte development and melanoma dedifferentiation at single-cell resolution. *Nat Cell Biol,* 23**,** 1035-1047.

BENGUIGUI, M., COOPER, T. J., KALKAR, P., SCHIF-ZUCK, S., HALABAN, R., BACCHIOCCHI, A., KAMER, I., DEO, A., MANOBLA, B., MENACHEM, R., HAJ-SHOMALY, J., VORONTSOVA, A., RAVIV, Z., BUXBAUM, C., CHRISTOPOULOS, P., BAR, J., LOTEM, M., SZNOL, M., ARIEL, A., SHEN-ORR, S. S. & SHAKED, Y. 2024. Interferon-stimulated neutrophils as a predictor of immunotherapy response. *Cancer Cell,* 42**,** 253-265.e12.

BERESTJUK, I., LECACHEUR, M., CARMINATI, A., DIAZZI, S., ROVERA, C., PROD'HOMME, V., OHANNA, M., POPOVIC, A., MALLAVIALLE, A., LARBRET, F., PISANO, S., AUDEBERT, S., PASSERON, T., GAGGIOLI, C., GIRARD, C. A., DECKERT, M. & TARTARE-DECKERT, S. 2022. Targeting Discoidin Domain Receptors DDR1 and DDR2 overcomes matrix-mediated tumor cell adaptation and tolerance to BRAF-targeted therapy in melanoma. *EMBO Mol Med,* 14**,** e11814.

BERNSTEIN, M. B., KRISHNAN, S., HODGE, J. W. & CHANG, J. Y. 2016. Immunotherapy and stereotactic ablative radiotherapy (ISABR): a curative approach? *Nat Rev Clin Oncol,* 13**,** 516-24.

BETOF WARNER, A., CORRIE, P. G. & HAMID, O. 2023. Tumor-Infiltrating Lymphocyte Therapy in Melanoma: Facts to the Future. *Clin Cancer Res,* 29**,** 1835-1854.

BIOSCIENCE, H. 2021. A Phase 1 Study of HMBD-002-V4C26 (HMBD-002), a Monoclonal Antibody Targeting VISTA, as Monotherapy and Combined With Pembrolizumab, in Patients With Advanced Solid Malignancies. *In:* MERCK, S. & DOHME, L. L. C. (eds.).

BIOTECH, M. 2017. Preservation of cell surface epitopes. *In:* BIOTECH, M. (ed.) *Miltenyi Biotech.* Miltenyi Biotech: Miltenyi Biotech.

BISWAS, S. K. & MANTOVANI, A. 2010. Macrophage plasticity and interaction with lymphocyte subsets: cancer as a paradigm. *Nat Immunol,* 11**,** 889-96.

BLANDO, J., SHARMA, A., HIGA, M. G., ZHAO, H., VENCE, L., YADAV, S. S., KIM, J., SEPULVEDA, A. M., SHARP, M., MAITRA, A., WARGO, J., TETZLAFF, M., BROADDUS, R., KATZ, M. H. G., VARADHACHARY, G. R., OVERMAN, M., WANG, H., YEE, C., BERNATCHEZ, C., IACOBUZIO-DONAHUE, C., BASU, S., ALLISON, J. P. & SHARMA, P. 2019. Comparison of immune infiltrates in melanoma and pancreatic cancer highlights VISTA as a potential target in pancreatic cancer. *Proc Natl Acad Sci U S A,* 116**,** 1692-1697.

BLANK, C. U., LUCAS, M. W., SCOLYER, R. A., VAN DE WIEL, B. A., MENZIES, A. M., LOPEZ-YURDA, M., HOEIJMAKERS, L. L., SAW, R. P. M., LIJNSVELT, J. M., MAHER, N. G., PULLEMAN, S. M., GONZALEZ, M., TORRES ACOSTA, A., VAN HOUDT, W. J., LO, S. N., KUIJPERS, A. M. J., SPILLANE, A., KLOP, W. M. C., PENNINGTON, T. E., ZUUR, C. L., SHANNON, K. F., SEINSTRA, B. A., RAWSON, R. V., HAANEN, J., CH'NG, S., NAIPAL, K. A. T., STRETCH, J., VAN THIENEN, J. V., RTSHILADZE, M. A., WILGENHOF, S., KAPOOR, R., MEERVELD-EGGINK, A., GRIJPINK-ONGERING, L. G., VAN AKKOOI, A. C. J., REIJERS, I. L. M., GYORKI, D. E., GRÜNHAGEN, D. J., SPEETJENS, F. M., VLIEK, S. B., PLACZKE, J., SPAIN, L., STASSEN, R. C., AMINI-ADLE, M., LEBBÉ, C., FARIES, M. B., ROBERT, C., ASCIERTO, P. A., VAN RIJN, R., VAN DEN BERKMORTEL, F., PIERSMA, D., VAN DER WESTHUIZEN, A., VREUGDENHIL, G., AARTS, M. J. B., STEVENSE-DEN BOER, M. A. M., ATKINSON, V., KHATTAK, M., ANDREWS, M. C., VAN DEN EERTWEGH, A. J. M., BOERS-SONDEREN, M. J., HOSPERS, G. A. P., CARLINO, M. S., DE GROOT, J. B., KAPITEIJN, E., SUIJKERBUIJK, K. P. M., RUTKOWSKI, P., SANDHU, S., VAN DER VELDT, A. A. M. & LONG, G. V. 2024. Neoadjuvant Nivolumab and Ipilimumab in Resectable Stage III Melanoma. *N Engl J Med*.

BOSISIO, F. M., WILMOTT, J. S., VOLDERS, N., MERCIER, M., WOUTERS, J., STAS, M., BLOKX, W. A., MASSI, D., THOMPSON, J. F., SCOLYER, R. A., VAN BAREN, N. & VAN DEN OORD, J. J. 2016. Plasma cells in primary melanoma. Prognostic significance and possible role of IgA. *Mod Pathol,* 29**,** 347-58.

BRESSAN, D., BATTISTONI, G. & HANNON, G. J. 2023. The dawn of spatial omics. *Science,* 381**,** eabq4964.

BROUGHTON, T. W. K., ELTANBOULY, M. A., SCHAAFSMA, E., DENG, J., SARDE, A., CROTEAU, W., LI, J., NOWAK, E. C., MABAERA, R., SMITS, N. C., KUTA, A., NOELLE, R. J. & LINES, J. L. 2019. Defining the Signature of VISTA on Myeloid Cell Chemokine Responsiveness. *Front Immunol,* 10**,** 2641.

BURMEISTER, B. H., HENDERSON, M. A., AINSLIE, J., FISHER, R., DI IULIO, J., SMITHERS, B. M., HONG, A., SHANNON, K., SCOLYER, R. A., CARRUTHERS, S., COVENTRY, B. J., BABINGTON, S., DUPRAT, J., HOEKSTRA, H. J. & THOMPSON, J. F. 2012. Adjuvant radiotherapy versus observation alone for patients

at risk of lymph-node field relapse after therapeutic lymphadenectomy for melanoma: a randomised trial. *Lancet Oncol,* 13**,** 589-97.

CABEZA-CABRERIZO, M., CARDOSO, A., MINUTTI, C. M., PEREIRA DA COSTA, M. & REIS E SOUSA, C. 2021. Dendritic Cells Revisited. *Annu Rev Immunol,* 39**,** 131-166.

CABRITA, R., LAUSS, M., SANNA, A., DONIA, M., SKAARUP LARSEN, M., MITRA, S., JOHANSSON, I., PHUNG, B., HARBST, K., VALLON-CHRISTERSSON, J., VAN SCHOIACK, A., LÖVGREN, K., WARREN, S., JIRSTRÖM, K., OLSSON, H., PIETRAS, K., INGVAR, C., ISAKSSON, K., SCHADENDORF, D., SCHMIDT, H., BASTHOLT, L., CARNEIRO, A., WARGO, J. A., SVANE, I. M. & JÖNSSON, G. 2020. Tertiary lymphoid structures improve immunotherapy and survival in melanoma. *Nature,* 577**,** 561-565.

CANETE, N. N., A. PATRICK, E. 2024. simpleSeg: A package to perform simple cell segmentation. *Bioconductor*.

CANETE, N. P., IYENGAR, S. S., ORMEROD, J. T., BAHARLOU, H., HARMAN, A. N. & PATRICK, E. 2022. spicyR: spatial analysis of in situ cytometry data in R. *Bioinformatics,* 38**,** 3099-3105.

CARPENTER, A. E., JONES, T. R., LAMPRECHT, M. R., CLARKE, C., KANG, I. H., FRIMAN, O., GUERTIN, D. A., CHANG, J. H., LINDQUIST, R. A., MOFFAT, J., GOLLAND, P. & SABATINI, D. M. 2006. CellProfiler: image analysis software for identifying and quantifying cell phenotypes. *Genome Biol,* 7**,** R100.

CARTHY, J. M., MEREDITH, A. J., BOROOMAND, S., ABRAHAM, T., LUO, Z., KNIGHT, D. & MCMANUS, B. M. 2015. Versican V1 Overexpression Induces a Myofibroblast-Like Phenotype in Cultured Fibroblasts. *PLoS One,* 10**,** e0133056.

CASROUGE, A., BISIAUX, A., STEPHEN, L., SCHMOLZ, M., MAPES, J., PFISTER, C., POL, S., MALLET, V. & ALBERT, M. L. 2012. Discrimination of agonist and antagonist forms of CXCL10 in biological samples. *Clin Exp Immunol,* 167**,** 137-48.

CHANG, Y. M., BARRETT, J. H., BISHOP, D. T., ARMSTRONG, B. K., BATAILLE, V., BERGMAN, W., BERWICK, M., BRACCI, P. M., ELWOOD, J. M., ERNSTOFF, M. S., GALLAGHER, R. P., GREEN, A. C., GRUIS, N. A., HOLLY, E. A., INGVAR, C., KANETSKY, P. A., KARAGAS, M. R., LEE, T. K., LE MARCHAND, L., MACKIE, R. M., OLSSON, H., ØSTERLIND, A., REBBECK, T. R., SASIENI, P., SISKIND, V., SWERDLOW, A. J., TITUS-ERNSTOFF, L., ZENS, M. S. & NEWTON-BISHOP, J. A. 2009. Sun exposure and melanoma risk at different latitudes: a pooled analysis of 5700 cases and 7216 controls. *Int J Epidemiol,* 38**,** 814-30.

CHAPMAN, P. B., HAUSCHILD, A., ROBERT, C., HAANEN, J. B., ASCIERTO, P., LARKIN, J., DUMMER, R., GARBE, C., TESTORI, A., MAIO, M., HOGG, D., LORIGAN, P., LEBBE, C., JOUARY, T., SCHADENDORF, D., RIBAS, A., O'DAY, S. J., SOSMAN, J. A., KIRKWOOD, J. M., EGGERMONT, A. M., DRENO, B., NOLOP, K., LI, J., NELSON, B., HOU, J., LEE, R. J., FLAHERTY, K. T. & MCARTHUR, G. A. 2011. Improved survival with vemurafenib in melanoma with BRAF V600E mutation. *N Engl J Med,* 364**,** 2507-16.

CHEN, C. & GAO, F. H. 2019. Th17 Cells Paradoxical Roles in Melanoma and Potential Application in Immunotherapy. *Front Immunol,* 10**,** 187.

CHEN, M. L., DE VERE HUNT, I. J., JOHN, E. M., WEINSTOCK, M. A., SWETTER, S. M. & LINOS, E. 2022a. Differences in Thickness-Specific Incidence and Factors Associated With Cutaneous Melanoma in the US From 2010 to 2018. *JAMA Oncol,* 8**,** 755-759.

CHEN, T. Y., YOU, L., HARDILLO, J. A. U. & CHIEN, M. P. 2023a. Spatial Transcriptomic Technologies. *Cells,* 12**,** 2042.

CHEN, W., QIE, C., HU, X., WANG, L., JIANG, J., LIU, W. & LIU, J. 2022b. A small molecule inhibitor of VSIG-8 prevents its binding to VISTA. *Invest New Drugs,* 40**,** 690-699.

CHEN, W. T., LU, A., CRAESSAERTS, K., PAVIE, B., SALA FRIGERIO, C., CORTHOUT, N., QIAN, X., LALÁKOVÁ, J., KÜHNEMUND, M., VOYTYUK, I., WOLFS, L., MANCUSO, R., SALTA, E., BALUSU, S., SNELLINX, A., MUNCK, S., JUREK, A., FERNANDEZ NAVARRO, J., SAIDO, T. C., HUITINGA, I., LUNDEBERG, J., FIERS, M. & DE STROOPER, B. 2020. Spatial Transcriptomics and In Situ Sequencing to Study Alzheimer's Disease. *Cell,* 182**,** 976-991.e19.

CHEN, Z., DOMINELLO, M. M., JOINER, M. C. & BURMEISTER, J. W. 2023b. Proton versus photon radiation therapy: A clinical review. *Front Oncol,* 13**,** 1133909.

CHENG, S., LI, Z., GAO, R., XING, B., GAO, Y., YANG, Y., QIN, S., ZHANG, L., OUYANG, H., DU, P., JIANG, L., ZHANG, B., YANG, Y., WANG, X., REN, X., BEI, J. X., HU, X., BU, Z., JI, J. & ZHANG, Z. 2021. A pan-cancer single-cell transcriptional atlas of tumor infiltrating myeloid cells. *Cell,* 184**,** 792-809.e23.

CHENG, W., NI, P., WU, H., MIAO, X., ZHAO, X. & YAN, D. 2024. Unravelling tumour cell diversity and prognostic signatures in cutaneous melanoma through machine learning analysis. *Journal of Cellular and Molecular Medicine,* 28**,** e18570.

CHICAS-SETT, R., ZAFRA-MARTIN, J., MORALES-ORUE, I., CASTILLA-MARTINEZ, J., BERENGUER-FRANCES, M. A., GONZALEZ-RODRIGUEZ, E., RODRIGUEZ-ABREU, D. & COUÑAGO, F. 2020. Immunoradiotherapy as An Effective Therapeutic Strategy in Lung Cancer: From Palliative Care to Curative Intent. *Cancers (Basel),* 12**,** 2178.

CHOI, J., KIM, Y., YUN, K., WON, C. H., LEE, M. W., CHOI, J., CHANG, S. & LEE, W. 2020. The prognostic significance of VISTA and CD33-positive myeloid cells in cutaneous melanoma and their relationship with PD-1 expression. *Scientific Reports,* 10**,** 14372.

CIPPONI, A., MERCIER, M., SEREMET, T., BAURAIN, J. F., THÉATE, I., VAN DEN OORD, J., STAS, M., BOON, T., COULIE, P. G. & VAN BAREN, N. 2012. Neogenesis of lymphoid structures and antibody responses occur in human melanoma metastases. *Cancer Res,* 72**,** 3997-4007.

COLE, K., PRAVOVEROV, K. & TALMADGE, J. E. 2021. Role of myeloid-derived suppressor cells in metastasis. *Cancer Metastasis Rev,* 40**,** 391-411.

COMITER, C., VAISHNAV, E. D., CIAMPRICOTTI, M., LI, B., YANG, Y., RODIG, S. J., TURNER, M., PFAFF, K. L., JANÉ-VALBUENA, J., SLYPER, M., WALDMAN, J., VIGNEAU, S., WU, J., BLOSSER, T. R., SEGERSTOLPE, Å., ABRAVANEL, D., WAGLE, N., ZHUANG, X., RUDIN, C. M., KLUGHAMMER, J., ROZENBLATT-ROSEN, O., KOBAYASH-KIRSCHVINK, K. J., SHU, J. & REGEV, A. 2023. Inference of single cell profiles from histology stains with the Single-Cell omics from Histology Analysis Framework (SCHAF). *bioRxiv*.

CONRAD, T. & ALTMÜLLER, J. 2022. Single cell- and spatial 'Omics revolutionize physiology. *Acta Physiol (Oxf),* 235**,** e13848.

COOK, D. P., JENSEN, K. B., WISE, K., ROACH, M. J., DEZEM, F. S., RYAN, N. K., ZAMOJSKI, M., VLACHOS, I. S., KNOTT, S. R. V., BUTLER, L. M., WRANA, J. L., BANOVICH, N. E., PLUMMER, J. T. & MARTELOTTO, L. G. 2023. A Comparative Analysis of Imaging-Based Spatial Transcriptomics Platforms. *bioRxiv***,** 2023.12.13.571385.

CORDOVA, A., TOIA, F., LA MENDOLA, C., ORLANDO, V., MERAVIGLIA, S., RINALDI, G., TODARO, M., CICERO, G., ZICHICHI, L., DONNI, P. L., CACCAMO, N., STASSI, G., DIELI, F. & MOSCHELLA, F. 2012. Characterization

of human γδ T lymphocytes infiltrating primary malignant melanomas. *PLoS One,* 7**,** e49878.

CRAMB, S. M., DUNCAN, E. W., AITKEN, J. F., SOYER, H. P., MENGERSEN, K. L. & BAADE, P. D. 2020. Geographical patterns in melanoma incidence across Australia: can thickness differentials reveal the key drivers? *Annals of Cancer Epidemiology,* 4.

CREAGAN, E. T., CUPPS, R. E., IVINS, J. C., PRITCHARD, D. J., SIM, F. H., SOULE, E. H. & O'FALLON, J. R. 1978. Adjuvant radiation therapy for regional nodal metastases from malignant melanoma: a randomized, prospective study. *Cancer,* 42**,** 2206-10.

CRISTINZIANO, L., MODESTINO, L., CAPONE, M., MADONNA, G., MALLARDO, D., GIANNARELLI, D., D'ANGELO, G., FERRARA, A. L., LOFFREDO, S., VARRICCHI, G., VANELLA, V., FESTINO, L., ASCIERTO, P. A. & GALDIERO, M. R. 2022. PD-L1(+) neutrophils as novel biomarkers for stage IV melanoma patients treated with nivolumab. *Front Immunol,* 13**,** 962669.

CROMBIE, I. K. 1979. Variation of melanoma incidence with latitude in North America and Europe. *Br J Cancer,* 40**,** 774-81.

CRUCITTA, S., CUCCHIARA, F., MATHIJSSEN, R., MATEO, J., JAGER, A., JOOSSE, A., PASSARO, A., ATTILI, I., PETRINI, I., VAN SCHAIK, R., DANESI, R. & DEL RE, M. 2022. Treatment-driven tumour heterogeneity and drug resistance: Lessons from solid tumours. *Cancer Treat Rev,* 104**,** 102340.

CUEVAS-DIAZ DURAN, R., WEI, H. & WU, J. 2024. Data normalization for addressing the challenges in the analysis of single-cell transcriptomic datasets. *BMC Genomics,* 25**,** 444.

CURIS, I. 2016. A Phase 1, Open-Label, Dose Escalation and Dose Expansion Trial Evaluating the Safety, Pharmacokinetics, Pharmacodynamics, and Clinical Effects of Orally Administered CA-170 in Patients With Advanced Tumors and Lymphomas.

CYLL, K., ERSVÆR, E., VLATKOVIC, L., PRADHAN, M., KILDAL, W., AVRANDEN KJÆR, M., KLEPPE, A., HVEEM, T. S., CARLSEN, B., GILL, S., LÖFFELER, S., HAUG, E. S., WÆHRE, H., SOORIAKUMARAN, P. & DANIELSEN, H. E. 2017. Tumour heterogeneity poses a significant challenge to cancer biomarker research. *Br J Cancer,* 117**,** 367-375.

DA SILVA, I. P., GALLOIS, A., JIMENEZ-BARANDA, S., KHAN, S., ANDERSON, A. C., KUCHROO, V. K., OSMAN, I. & BHARDWAJ, N. 2014. Reversal of NK-cell exhaustion in advanced melanoma by Tim-3 blockade. *Cancer Immunol Res,* 2**,** 410-22.

DABROSIN, N., JUUL, K. S., GEORGSEN, J. B., ANDRUP, S., SCHMIDT, H., STEINICHE, T., ØLLEGAARD, T. H. & BEHRNDTZ, L. B. 2019. Innate immune cell infiltration in melanoma metastases affects survival and is associated with BRAFV600E mutation status. *Melanoma Research,* 29**,** 30-37.

DAGOGO-JACK, I. & SHAW, A. T. 2018. Tumour heterogeneity and resistance to cancer therapies. *Nat Rev Clin Oncol,* 15**,** 81-94.

DAMEI, I., TRICKOVIC, T., MAMI-CHOUAIB, F. & CORGNAC, S. 2023. Tumor-resident memory T cells as a biomarker of the response to cancer immunotherapy. *Front Immunol,* 14**,** 1205984.

DE ANDA-JÁUREGUI, G. & HERNÁNDEZ-LEMUS, E. 2020. Computational Oncology in the Multi-Omics Era: State of the Art. *Front Oncol,* 10**,** 423.

DE ANDRADE, L. F., LU, Y., LUOMA, A., ITO, Y., PAN, D., PYRDOL, J. W., YOON, C. H., YUAN, G. C. & WUCHERPFENNIG, K. W. 2019. Discovery of specialized NK cell populations infiltrating human melanoma metastases. *JCI Insight,* 4**,** e133103.

DE CICCO, P., ERCOLANO, G. & IANARO, A. 2020. The New Era of Cancer Immunotherapy: Targeting Myeloid-Derived Suppressor Cells to Overcome Immune Evasion. *Front Immunol,* 11**,** 1680.

DE GRUIJL, F. R. 2002. Photocarcinogenesis: UVA vs. UVB radiation. *Skin Pharmacol Appl Skin Physiol,* 15**,** 316-20.

DE JONGE, K., EBERING, A., NASSIRI, S., MABY-EL HAJJAMI, H., OUERTATANI-SAKOUHI, H., BAUMGAERTNER, P. & SPEISER, D. E. 2019. Circulating CD56(bright) NK cells inversely correlate with survival of melanoma patients. *Sci Rep,* 9**,** 4487.

DE LOGU, F., UGOLINI, F., IANNONE, L. F., SIMI, S., MAIO, V., DE GIORGI, V., MARIA DI GIACOMO, A., MIRACCO, C., COSSU, A., PALMIERI, G., MANDALÀ, M. & MASSI, D. 2023. Spatial Proximity and Relative Distribution of Tumor-Infiltrating Lymphocytes and Macrophages Predict Survival in Melanoma. *Lab Invest,* 103**,** 100259.

DE SOUZA, N., ZHAO, S. & BODENMILLER, B. 2024. Multiplex protein imaging in tumour biology. *Nat Rev Cancer,* 24**,** 171-191.

DE WINDE, C. M., GEORGE, S. L., CROSAS-MOLIST, E., HARI-GUPTA, Y., ARP, A. B., BENJAMIN, A. C., MILLWARD, L. J., MAKRIS, S., CARVER, A., IMPERATORE, V., MARTÍNEZ, V. G., SANZ-MORENO, V. & ACTON, S. E. 2021. Podoplanin drives dedifferentiation and amoeboid invasion of melanoma. *iScience,* 24**,** 102976.

DEBACKER, J. M., GONDRY, O., LAHOUTTE, T., KEYAERTS, M. & HUVENNE, W. 2021. The Prognostic Value of CD206 in Solid Malignancies: A Systematic Review and Meta-Analysis. *Cancers (Basel),* 13**,** 3422.

DEHGHANI, T. & PANITCH, A. 2020. Endothelial cells, neutrophils and platelets: getting to the bottom of an inflammatory triangle. *Open Biology,* 10**,** 200161.

DEMIR KARAMAN, E. & IŞIK, Z. 2023. Multi-Omics Data Analysis Identifies Prognostic Biomarkers across Cancers. *Med Sci (Basel),* 11.

DENG, J., LI, J., SARDE, A., LINES, J. L., LEE, Y. C., QIAN, D. C., PECHENICK, D. A., MANIVANH, R., LE MERCIER, I., LOWREY, C. H., VARN, F. S., CHENG, C., LEIB, D. A., NOELLE, R. J. & MABAERA, R. 2019. Hypoxia-Induced VISTA Promotes the Suppressive Function of Myeloid-Derived Suppressor Cells in the Tumor Microenvironment. *Cancer Immunol Res,* 7**,** 1079-1090.

DERAKHSHANI, A., ASADZADEH, Z., BARADARAN, B., SAFARPOUR, H., RAHMANI, S., LEONE, P., ABDOLI SHADBAD, M., HOSSEINKHANI, N., GHASEMIGOL, M., AYROMLOU, H., AHMADI, H., POUYA, S., SHOJAEE, M., TABRIZI, N. J., MIRAKI FERIZ, A., SAFARZADEH, E. & RACANELLI, V. 2022. The expression pattern of VISTA in the PBMCs of relapsing-remitting multiple sclerosis patients: A single-cell RNA sequencing-based study. *Biomed Pharmacother,* 148**,** 112725.

DIAZZI, S., BAERI, A., FASSY, J., LECACHEUR, M., MARIN-BEJAR, O., GIRARD, C. A., LEFEVRE, L., LACOUX, C., IRONDELLE, M., MOUNIER, C., TRUCHI, M., COURALET, M., OHANNA, M., CARMINATI, A., BERESTJUK, I., LARBRET, F., GILOT, D., VASSAUX, G., MARINE, J. C., DECKERT, M., MARI, B. & TARTARE-DECKERT, S. 2022. Blockade of the pro-fibrotic reaction mediated by the miR-143/-145 cluster enhances the responses to targeted therapy in melanoma. *EMBO Mol Med,* 14**,** e15295.

DIETERICH, L. C., IKENBERG, K., CETINTAS, T., KAPAKLIKAYA, K., HUTMACHER, C. & DETMAR, M. 2017. Tumor-Associated Lymphatic Vessels Upregulate PDL1 to Inhibit T-Cell Activation. *Front Immunol,* 8**,** 66.

DRESCHER, H., WEISKIRCHEN, S. & WEISKIRCHEN, R. 2021. Flow Cytometry: A Blessing and a Curse. *Biomedicines,* 9**,** 1613.

DUHEN, T., DUHEN, R., MONTLER, R., MOSES, J., MOUDGIL, T., DE MIRANDA, N. F., GOODALL, C. P., BLAIR, T. C., FOX, B. A., MCDERMOTT, J. E., CHANG, S. C., GRUNKEMEIER, G., LEIDNER, R., BELL, R. B. & WEINBERG, A. D. 2018. Co-expression of CD39 and CD103 identifies tumor-reactive CD8 T cells in human solid tumors. *Nat Commun,* 9**,** 2724.

EDLUNDH-ROSE, E., EGYHÁZI, S., OMHOLT, K., MÅNSSON-BRAHME, E., PLATZ, A., HANSSON, J. & LUNDEBERG, J. 2006. NRAS and BRAF mutations in melanoma tumours in relation to clinical characteristics: a study based on mutation screening by pyrosequencing. *Melanoma Res,* 16**,** 471-8.

EDWARDS, J., TASKER, A., PIRES DA SILVA, I., QUEK, C., BATTEN, M., FERGUSON, A., ALLEN, R., ALLANSON, B., SAW, R. P. M., THOMPSON, J. F., MENZIES, A. M., PALENDIRA, U., WILMOTT, J. S., LONG, G. V. & SCOLYER, R. A. 2019. Prevalence and Cellular Distribution of Novel Immune Checkpoint Targets Across Longitudinal Specimens in Treatment-naïve Melanoma Patients: Implications for Clinical Trials. *Clin Cancer Res,* 25**,** 3247-3258.

EDWARDS, J., WILMOTT, J. S., MADORE, J., GIDE, T. N., QUEK, C., TASKER, A., FERGUSON, A. L., CHEN, J., HEWAVISENTI, R., HERSEY, P., GEBHARDT, T., WENINGER, W., BRITTON, W. J., SAW, R., THOMPSON, J. F., MENZIES, A. M., LONG, G. V., SCOLYER, R. A. & PALENDIRA, U. 2018. CD103+ tumor-resident CD8+ T cells are associated with improved survival in immunotherapy naive melanoma patients and expand significantly during anti-PD1 treatment. *Clin Cancer Res,* 24**,** 3036-3045.

EDY, U., JATMIKO ENDRO, S. & GUNAWAN, S. K. V. K-Means Clustering Optimization Using the Elbow Method and Early Centroid Determination Based on Mean and Median Formula. Proceedings of the 2nd International Seminar on Science and Technology (ISSTEC 2019), 2020/10/11 2020. Atlantis Press, 121-129.

ERDAG, G., SCHAEFER, J. T., SMOLKIN, M. E., DEACON, D. H., SHEA, S. M., DENGEL, L. T., PATTERSON, J. W. & SLINGLUFF, C. L., JR. 2012. Immunotype and immunohistologic characteristics of tumor-infiltrating immune cells are associated with clinical outcome in metastatic melanoma. *Cancer Res,* 72**,** 1070-80.

ERFANIAN, N., HEYDARI, A. A., FERIZ, A. M., IAÑEZ, P., DERAKHSHANI, A., GHASEMIGOL, M., FARAHPOUR, M., RAZAVI, S. M., NASSERI, S., SAFARPOUR, H. & SAHEBKAR, A. 2023. Deep learning applications in single-cell genomics and transcriptomics data analysis. *Biomedicine & Pharmacotherapy,* 165**,** 115077.

FALCON, B. L., STEWART, J., EZELL, S., HANSON, J., WIJSMAN, J., YE, X., WESTIN, E., DONOHO, G., CREDILLE, K. & UHLIK, M. T. 2013. High-content multiplexed tissue imaging and quantification for cancer drug discovery. *Drug Discovery Today,* 18**,** 510-522.

FEDORENKO, I. V., WARGO, J. A., FLAHERTY, K. T., MESSINA, J. L. & SMALLEY, K. S. M. 2015. BRAF Inhibition Generates a Host-Tumor Niche that Mediates Therapeutic Escape. *J Invest Dermatol,* 135**,** 3115-3124.

FEJZA, A., POLANO, M., CAMICIA, L., POLETTO, E., CAROBOLANTE, G., TOFFOLI, G., MONGIAT, M. & ANDREUZZI, E. 2021. The Efficacy of Anti-PD-L1 Treatment in Melanoma Is Associated with the Expression of the ECM Molecule EMILIN2. *Int J Mol Sci,* 22**,** 7511.

FEMINO, A. M., FAY, F. S., FOGARTY, K. & SINGER, R. H. 1998. Visualization of single RNA transcripts in situ. *Science,* 280**,** 585-90.

FENG, R., OERMANN, E. K., SHRIVASTAVA, R., GOLD, A., COLLINS, B. T., KONDZIOLKA, D. & COLLINS, S. P. 2017. Stereotactic Radiosurgery for Melanoma Brain Metastases: A Comprehensive Clinical Case Series. *World Neurosurg,* 100**,** 297-304.

FENG, S., XU, Y., DAI, Z., YIN, H., ZHANG, K. & SHEN, Y. 2022. Integrative Analysis From Multicenter Studies Identifies a WGCNA-Derived Cancer-Associated Fibroblast Signature for Ovarian Cancer. *Front Immunol,* 13**,** 951582.

FERGUSON, A. L., SHARMAN, A. R., ALLEN, R. O., YE, T., LEE, J. H., LOW, T. H., CH'NG, S., PALME, C. E., ASHFORD, B., RANSON, M., CLARK, J. R., PATRICK, E., GUPTA, R. & PALENDIRA, U. 2022. High-Dimensional and Spatial Analysis Reveals Immune Landscape-Dependent Progression in Cutaneous Squamous Cell Carcinoma. *Clin Cancer Res,* 28**,** 4677-4688.

FERNÁNDEZ-CORTÉS, M., DELGADO-BELLIDO, D., BERMÚDEZ-JIMÉNEZ, E., PARAMIO, J. M., O'VALLE, F., VINCKIER, S., CARMELIET, P., GARCIA-DIAZ, A. & OLIVER, F. J. 2023. PARP inhibition promotes endothelial-like traits in melanoma cells and modulates pericyte coverage dynamics during vasculogenic mimicry. *J Pathol,* 259**,** 318-330.

FLAHERTY, K. T., ROBERT, C., HERSEY, P., NATHAN, P., GARBE, C., MILHEM, M., DEMIDOV, L. V., HASSEL, J. C., RUTKOWSKI, P., MOHR, P., DUMMER, R., TREFZER, U., LARKIN, J. M., UTIKAL, J., DRENO, B., NYAKAS, M., MIDDLETON, M. R., BECKER, J. C., CASEY, M., SHERMAN, L. J., WU, F. S., OUELLET, D., MARTIN, A. M., PATEL, K. & SCHADENDORF, D. 2012. Improved survival with MEK inhibition in BRAF-mutated melanoma. *N Engl J Med,* 367**,** 107-14.

FU, X., LIN, Y., LIN, D. M., MECHTERSHEIMER, D., WANG, C., AMEEN, F., GHAZANFAR, S., PATRICK, E., KIM, J. & YANG, J. Y. H. 2024. BIDCell: Biologically-informed self-supervised learning for segmentation of subcellular spatial transcriptomics data. *Nature Communications,* 15**,** 509.

GABR, M. T. & GAMBHIR, S. S. 2020. Discovery and Optimization of Small-Molecule Ligands for V-Domain Ig Suppressor of T-Cell Activation (VISTA). *Journal of the American Chemical Society,* 142**,** 16194-16198.

GAJRA, A., ZALENSKI, A., SANNAREDDY, A., JEUNE-SMITH, Y., KAPINOS, K. & KANSAGRA, A. 2022. Barriers to Chimeric Antigen Receptor T-Cell (CAR-T) Therapies in Clinical Practice. *Pharmaceut Med,* 36**,** 163-171.

GALLUZZI, L., ARYANKALAYIL, M. J., COLEMAN, C. N. & FORMENTI, S. C. 2023. Emerging evidence for adapting radiotherapy to immunotherapy. *Nature Reviews Clinical Oncology,* 20**,** 543-557.

GAO, J., WARD, J. F., PETTAWAY, C. A., SHI, L. Z., SUBUDHI, S. K., VENCE, L. M., ZHAO, H., CHEN, J., CHEN, H., EFSTATHIOU, E., TRONCOSO, P., ALLISON, J. P., LOGOTHETIS, C. J., WISTUBA, II, SEPULVEDA, M. A., SUN, J., WARGO, J., BLANDO, J. & SHARMA, P. 2017a. VISTA is an inhibitory immune checkpoint that is increased after ipilimumab therapy in patients with prostate cancer. *Nat Med,* 23**,** 551-555.

GAO, J., WARD, J. F., PETTAWAY, C. A., SHI, L. Z., SUBUDHI, S. K., VENCE, L. M., ZHAO, H., CHEN, J., CHEN, H., EFSTATHIOU, E., TRONCOSO, P., ALLISON, J. P., LOGOTHETIS, C. J., WISTUBA, II, SEPULVEDA, M. A., SUN, J., WARGO, J., BLANDO, J. & SHARMA, P. 2017b. VISTA is an inhibitory immune checkpoint that is increased after ipilimumab therapy in patients with prostate cancer. *Nat Med,* 23**,** 551-5.

GARRIDO-TRIGO, A., CORRALIZA, A. M., VENY, M., DOTTI, I., MELÓN-ARDANAZ, E., RILL, A., CROWELL, H. L., CORBÍ, Á., GUDIÑO, V., ESTELLER, M., ÁLVAREZ-TEUBEL, I., AGUILAR, D., MASAMUNT, M. C., KILLINGBECK, E., KIM, Y., LEON, M., VISVANATHAN, S., MARCHESE, D., CARATÙ, G., MARTIN-CARDONA, A., ESTEVE, M., ORDÁS, I., PANÉS, J., RICART, E., MEREU, E., HEYN, H. & SALAS, A. 2023. Macrophage and neutrophil heterogeneity at single-cell spatial resolution in human inflammatory bowel disease. *Nature Communications,* 14**,** 4506.

GARUTTI, M., BERGNACH, M., POLESEL, J., PALMERO, L., PIZZICHETTA, M. A. & PUGLISI, F. 2022. BRAF and MEK Inhibitors and Their Toxicities: A Meta-Analysis. *Cancers (Basel),* 15**,** 141.

GEERTSEN, R., ZENKLUSEN, R., KAMARASHEV, J., BURG, G. & DUMMER, R. 1999. Inverse regulation of neuronal cellular adhesion molecule (NCAM) by IFN-γ in melanoma cell cultures established from CNS lesions. *International Journal of Cancer,* 83**,** 135-140.

GENTLEMAN, R. C., CAREY, V. J., BATES, D. M., BOLSTAD, B., DETTLING, M., DUDOIT, S., ELLIS, B., GAUTIER, L., GE, Y., GENTRY, J., HORNIK, K., HOTHORN, T., HUBER, W., IACUS, S., IRIZARRY, R., LEISCH, F., LI, C., MAECHLER, M., ROSSINI, A. J., SAWITZKI, G., SMITH, C., SMYTH, G., TIERNEY, L., YANG, J. Y. & ZHANG, J. 2004. Bioconductor: open software development for computational biology and bioinformatics. *Genome Biol,* 5**,** R80.

GERMAIN, C., GNJATIC, S. & DIEU-NOSJEAN, M. C. 2015. Tertiary Lymphoid Structure-Associated B Cells are Key Players in Anti-Tumor Immunity. *Front Immunol,* 6**,** 67.

GHAZANFAR, S., GUIBENTIF, C. & MARIONI, J. C. 2024. Stabilized mosaic single-cell data integration using unshared features. *Nature Biotechnology,* 42**,** 284-292.

GHILARDI, G., WILLIAMSON, S., PAJARILLO, R., PARUZZO, L., CHEN, L., GRADY, C., DOUCETTE, A., NEMECEK, E., GABRIELLI, G., BARTA, S. K., SVOBODA, J., CHONG, E. A., YELTON, R., NASTA, S. D., LANDSBURG, D. J., UGWUANYI, O., CHEN, A. I., SCHACHTER, L., WHITE, G., BALLARD, H. J., WEBER, E., CURLEY, C., PORTER, D. L., GARFALL, A. L., HWANG, W. T., GUERRA, C. E., MAZIARZ, R. T., SCHUSTER, S. J. & RUELLA, M. 2024. CAR T-Cell Immunotherapy in Minority Patients with Lymphoma. *NEJM Evid,* 3**,** EVIDoa2300213.

GHOUZLANI, A., RAFII, S., KARKOURI, M., LAKHDAR, A. & BADOU, A. 2021. The Promising IgSF11 Immune Checkpoint Is Highly Expressed in Advanced Human Gliomas and Associates to Poor Prognosis. *Frontiers in Oncology,* 10.

GIDE, T. N., PAVER, E. C., YASEEN, Z., MAHER, N., ADEGOKE, N., MENZIES, A. M., PIRES DA SILVA, I., WILMOTT, J. S., LONG, G. V. & SCOLYER, R. A. 2023. Lag-3 expression and clinical outcomes in metastatic melanoma patients treated with combination anti-lag-3 + anti-PD-1-based immunotherapies. *Oncoimmunology,* 12**,** 2261248.

GIESEN, C., WANG, H. A., SCHAPIRO, D., ZIVANOVIC, N., JACOBS, A., HATTENDORF, B., SCHÜFFLER, P. J., GROLIMUND, D., BUHMANN, J. M., BRANDT, S., VARGA, Z., WILD, P. J., GÜNTHER, D. & BODENMILLER, B. 2014. Highly multiplexed imaging of tumor tissues with subcellular resolution by mass cytometry. *Nat Methods,* 11**,** 417-22.

GOLDEN, E. B., CHHABRA, A., CHACHOUA, A., ADAMS, S., DONACH, M., FENTON-KERIMIAN, M., FRIEDMAN, K., PONZO, F., BABB, J. S., GOLDBERG, J., DEMARIA, S. & FORMENTI, S. C. 2015. Local radiotherapy and granulocyte-

macrophage colony-stimulating factor to generate abscopal responses in patients with metastatic solid tumours: a proof-of-principle trial. *Lancet Oncol,* 16**,** 795-803.

GORDON, S. R., MAUTE, R. L., DULKEN, B. W., HUTTER, G., GEORGE, B. M., MCCRACKEN, M. N., GUPTA, R., TSAI, J. M., SINHA, R., COREY, D., RING, A. M., CONNOLLY, A. J. & WEISSMAN, I. L. 2017. PD-1 expression by tumour-associated macrophages inhibits phagocytosis and tumour immunity. *Nature,* 545**,** 495-499.

GRANIER, C., DE GUILLEBON, E., BLANC, C., ROUSSEL, H., BADOUAL, C., COLIN, E., SALDMANN, A., GEY, A., OUDARD, S. & TARTOUR, E. 2017. Mechanisms of action and rationale for the use of checkpoint inhibitors in cancer. *ESMO Open,* 2**,** e000213.

GRASSBERGER, C., HONG, T. S., HATO, T., YEAP, B. Y., WO, J. Y., TRACY, M., BORTFELD, T., WOLFGANG, J. A., EYLER, C. E., GOYAL, L., CLARK, J. W., CRANE, C. H., KOAY, E. J., COBBOLD, M., DELANEY, T. F., JAIN, R. K., ZHU, A. X. & DUDA, D. G. 2018. Differential Association Between Circulating Lymphocyte Populations With Outcome After Radiation Therapy in Subtypes of Liver Cancer. *Int J Radiat Oncol Biol Phys,* 101**,** 1222-1225.

GRAUEL, A. L., NGUYEN, B., RUDDY, D., LASZEWSKI, T., SCHWARTZ, S., CHANG, J., CHEN, J., PIQUET, M., PELLETIER, M., YAN, Z., KIRKPATRICK, N. D., WU, J., DEWECK, A., RIESTER, M., HIMS, M., GEYER, F. C., WAGNER, J., MACISAAC, K., DEEDS, J., DIWANJI, R., JAYARAMAN, P., YU, Y., SIMMONS, Q., WENG, S., RAZA, A., MINIE, B., DOSTALEK, M., CHIKKEGOWDA, P., RUDA, V., IARTCHOUK, O., CHEN, N., THIERRY, R., ZHOU, J., PRUTEANU-MALINICI, I., FABRE, C., ENGELMAN, J. A., DRANOFF, G. & CREMASCO, V. 2020. TGFβ-blockade uncovers stromal plasticity in tumors by revealing the existence of a subset of interferon-licensed fibroblasts. *Nat Commun,* 11**,** 6315.

GREGG, R. K. 2021. Model Systems for the Study of Malignant Melanoma. *Methods Mol Biol,* 2265**,** 1-21.

GRISS, J., BAUER, W., WAGNER, C., SIMON, M., CHEN, M., GRABMEIER-PFISTERSHAMMER, K., MAURER-GRANOFSZKY, M., ROKA, F., PENZ, T., BOCK, C., ZHANG, G., HERLYN, M., GLATZ, K., LÄUBLI, H., MERTZ, K. D., PETZELBAUER, P., WIESNER, T., HARTL, M., PICKL, W. F., SOMASUNDARAM, R., STEINBERGER, P. & WAGNER, S. N. 2019. B cells sustain inflammation and predict response to immune checkpoint blockade in human melanoma. *Nat Commun,* 10**,** 4186.

GROTZ, T. E., JAKUB, J. W., MANSFIELD, A. S., GOLDENSTEIN, R., ENNINGA, E. A., NEVALA, W. K., LEONTOVICH, A. A. & MARKOVIC, S. N. 2015. Evidence of Th2 polarization of the sentinel lymph node (SLN) in melanoma. *Oncoimmunology,* 4**,** e1026504.

GUAN, H., ZHOU, Z., HOU, X., ZHANG, F., ZHAO, J. & HU, K. 2023. Safety and potential increased risk of toxicity of radiotherapy combined immunotherapy strategy. *Asia Pac J Clin Oncol,* 19**,** 35-50.

GUIMARÃES-BASTOS, D., FRONY, A. C., BARJA-FIDALGO, C. & MORAES, J. A. 2022. Melanoma-derived extracellular vesicles skew neutrophils into a pro-tumor phenotype. *J Leukoc Biol,* 111**,** 585-596.

GULDNER, I. H., GOLOMB, S. M., WANG, Q., WANG, E. & ZHANG, S. 2021. Isolation of mouse brain-infiltrating leukocytes for single cell profiling of epitopes and transcriptomes. *STAR Protoc,* 2**,** 100537.

HALIM, L., ROMANO, M., MCGREGOR, R., CORREA, I., PAVLIDIS, P., GRAGEDA, N., HOONG, S. J., YUKSEL, M., JASSEM, W., HANNEN, R. F., ONG, M.,

MCKINNEY, O., HAYEE, B., KARAGIANNIS, S. N., POWELL, N., LECHLER, R. I., NOVA-LAMPERTI, E. & LOMBARDI, G. 2017. An Atlas of Human Regulatory T Helper-like Cells Reveals Features of Th2-like Tregs that Support a Tumorigenic Environment. *Cell Rep,* 20**,** 757-770.

HAO, Y., STUART, T., KOWALSKI, M. H., CHOUDHARY, S., HOFFMAN, P., HARTMAN, A., SRIVASTAVA, A., MOLLA, G., MADAD, S., FERNANDEZ-GRANDA, C. & SATIJA, R. 2024. Dictionary learning for integrative, multimodal and scalable single-cell analysis. *Nature Biotechnology,* 42**,** 293-304.

HARTMAN, A. & SATIJA, R. 2024. Comparative analysis of multiplexed in situ gene expression profiling technologies. bioRxiv.

HASEGAWA, D., HASEGAWA, K., KANEKO, H., YOSHIDA, S., MITARAI, H., ARIMA, M., TOMOKIYO, A., HAMANO, S., SUGII, H., WADA, N., KIYOSHIMA, T. & MAEDA, H. 2020. MEST Regulates the Stemness of Human Periodontal Ligament Stem Cells. *Stem Cells Int,* 2020**,** 9672673.

HATSCHER, L., LEHMANN, C. H. K., PURBOJO, A., ONDERKA, C., LIANG, C., HARTMANN, A., CESNJEVAR, R., BRUNS, H., GROSS, O., NIMMERJAHN, F., IVANOVIĆ-BURMAZOVIĆ, I., KUNZ, M., HEGER, L. & DUDZIAK, D. 2021. Select hyperactivating NLRP3 ligands enhance the T(H)1- and T(H)17-inducing potential of human type 2 conventional dendritic cells. *Sci Signal,* 14**,** eabe1757.

HAUSCHILD, A., GROB, J. J., DEMIDOV, L. V., JOUARY, T., GUTZMER, R., MILLWARD, M., RUTKOWSKI, P., BLANK, C. U., MILLER, W. H., JR., KAEMPGEN, E., MARTÍN-ALGARRA, S., KARASZEWSKA, B., MAUCH, C., CHIARION-SILENI, V., MARTIN, A. M., SWANN, S., HANEY, P., MIRAKHUR, B., GUCKERT, M. E., GOODMAN, V. & CHAPMAN, P. B. 2012. Dabrafenib in BRAF-mutated metastatic melanoma: a multicentre, open-label, phase 3 randomised controlled trial. *Lancet,* 380**,** 358-65.

HAZARIKA, M., CHUK, M. K., THEORET, M. R., MUSHTI, S., HE, K., WEIS, S. L., PUTMAN, A. H., HELMS, W. S., CAO, X., LI, H., ZHAO, H., ZHAO, L., WELCH, J., GRAHAM, L., LIBEG, M., SRIDHARA, R., KEEGAN, P. & PAZDUR, R. 2017. U.S. FDA Approval Summary: Nivolumab for Treatment of Unresectable or Metastatic Melanoma Following Progression on Ipilimumab. *Clin Cancer Res,* 23**,** 3484-3488.

HE, S., BHATT, R., BROWN, C., BROWN, E. A., BUHR, D. L., CHANTRANUVATANA, K., DANAHER, P., DUNAWAY, D., GARRISON, R. G., GEISS, G., GREGORY, M. T., HOANG, M. L., KHAFIZOV, R., KILLINGBECK, E. E., KIM, D., KIM, T. K., KIM, Y., KLOCK, A., KORUKONDA, M., KUTCHMA, A., LEWIS, Z. R., LIANG, Y., NELSON, J. S., ONG, G. T., PERILLO, E. P., PHAN, J. C., PHAN-EVERSON, T., PIAZZA, E., RANE, T., REITZ, Z., RHODES, M., ROSENBLOOM, A., ROSS, D., SATO, H., WARDHANI, A. W., WILLIAMS-WIETZIKOSKI, C. A., WU, L. & BEECHEM, J. M. 2022. High-plex imaging of RNA and proteins at subcellular resolution in fixed tissue by spatial molecular imaging. *Nat Biotechnol,* 40**,** 1794-1806.

HE, Y. & WANG, X. 2023. Identifying biomarkers associated with immunotherapy response in melanoma by multi-omics analysis. *Comput Biol Med,* 167**,** 107591.

HEALTH, A. I. O. & WELFARE 2023. Cancer data in Australia. Canberra: AIHW.

HENDERSON, M. A., BURMEISTER, B. H., AINSLIE, J., FISHER, R., DI IULIO, J., SMITHERS, B. M., HONG, A., SHANNON, K., SCOLYER, R. A., CARRUTHERS, S., COVENTRY, B. J., BABINGTON, S., DUPRAT, J., HOEKSTRA, H. J. & THOMPSON, J. F. 2015. Adjuvant lymph-node field radiotherapy versus observation only in patients with melanoma at high risk of further lymph-node field relapse after lymphadenectomy (ANZMTG 01.02/TROG 02.01): 6-year follow-up of a phase 3, randomised controlled trial. *Lancet Oncol,* 16**,** 1049-1060.

HEUMOS, L., SCHAAR, A. C., LANCE, C., LITINETSKAYA, A., DROST, F., ZAPPIA, L., LÜCKEN, M. D., STROBL, D. C., HENAO, J., CURION, F., ALIEE, H., ANSARI, M., BADIA-I-MOMPEL, P., BÜTTNER, M., DANN, E., DIMITROV, D., DONY, L., FRISHBERG, A., HE, D., HEDIYEH-ZADEH, S., HETZEL, L., IBARRA, I. L., JONES, M. G., LOTFOLLAHI, M., MARTENS, L. D., MÜLLER, C. L., NITZAN, M., OSTNER, J., PALLA, G., PATRO, R., PIRAN, Z., RAMÍREZ-SUÁSTEGUI, C., SAEZ-RODRIGUEZ, J., SARKAR, H., SCHUBERT, B., SIKKEMA, L., SRIVASTAVA, A., TANEVSKI, J., VIRSHUP, I., WEILER, P., SCHILLER, H. B., THEIS, F. J. & SINGLE-CELL BEST PRACTICES, C. 2023. Best practices for single-cell analysis across modalities. *Nature Reviews Genetics,* 24**,** 550-572.

HIRATA, E., GIROTTI, M. R., VIROS, A., HOOPER, S., SPENCER-DENE, B., MATSUDA, M., LARKIN, J., MARAIS, R. & SAHAI, E. 2015. Intravital imaging reveals how BRAF inhibition generates drug-tolerant microenvironments with high integrin β1/FAK signaling. *Cancer Cell,* 27**,** 574-88.

HIRSCHHORN, D., BUDHU, S., KRAEHENBUEHL, L., GIGOUX, M., SCHRÖDER, D., CHOW, A., RICCA, J. M., GASMI, B., DE HENAU, O., MANGARIN, L. M. B., LI, Y., HAMADENE, L., FLAMAR, A. L., CHOI, H., CORTEZ, C. A., LIU, C., HOLLAND, A., SCHAD, S., SCHULZE, I., BETOF WARNER, A., HOLLMANN, T. J., ARORA, A., PANAGEAS, K. S., RIZZUTO, G. A., DUHEN, R., WEINBERG, A. D., SPENCER, C. N., NG, D., HE, X. Y., ALBRENGUES, J., REDMOND, D., EGEBLAD, M., WOLCHOK, J. D. & MERGHOUB, T. 2023. T cell immunotherapies engage neutrophils to eliminate tumor antigen escape variants. *Cell,* 186**,** 1432-1447.e17.

HOCH, T., SCHULZ, D., ELING, N., GÓMEZ, J. M., LEVESQUE, M. P. & BODENMILLER, B. 2022. Multiplexed imaging mass cytometry of the chemokine milieus in melanoma characterizes features of the response to immunotherapy. *Sci Immunol,* 7**,** eabk1692.

HONG, A. 2024. Radiation therapy in the management of melanoma. *In:* ATKINS, M. B. (ed.) *UpToDate.* Wolters Kluwer.

HORNSTEINER, F., VIERTHALER, J., STRANDT, H., RESAG, A., FU, Z., AUSSERHOFER, M., TRIPP, C. H., DIECKMANN, S., KANDUTH, M., FARRAND, K., BREGAR, S., NEMATI, N., HERMANN-KLEITER, N., SERETIS, A., MORLA, S., MULLINS, D., FINOTELLO, F., TRAJANOSKI, Z., WOLLMANN, G., RONCHESE, F., SCHMITZ, M., HERMANS, I. F. & STOITZNER, P. 2024. Tumor-targeted therapy with BRAF-inhibitor recruits activated dendritic cells to promote tumor immunity in melanoma. *J Immunother Cancer,* 12.

HOWELL, N., MIDDLETON, R. J., SIERRO, F., FRASER, B. H., WYATT, N. A., CHACON, A., BAMBERY, K. R., LIVIO, E., DOBIE, C., BEVITT, J. J., DAVIES, J., DOSSETO, A., FRANKLIN, D. R., GARBE, U., GUATELLI, S., HIRAYAMA, R., MATSUFUJI, N., MOHAMMADI, A., MUTIMER, K., RENDINA, L. M., ROSENFELD, A. B. & SAFAVI-NAEINI, M. 2024. Neutron Capture Enhances Dose and Reduces Cancer Cell Viability in and out of Beam During Helium and Carbon Ion Therapy. *International Journal of Radiation Oncology, Biology, Physics,* 120**,** 229-242.

HU, J., LI, X., YANG, L. & LI, H. 2022. Hypoxia, a key factor in the immune microenvironment. *Biomed Pharmacother,* 151**,** 113068.

HUBER, W., CAREY, V. J., GENTLEMAN, R., ANDERS, S., CARLSON, M., CARVALHO, B. S., BRAVO, H. C., DAVIS, S., GATTO, L., GIRKE, T., GOTTARDO, R., HAHNE, F., HANSEN, K. D., IRIZARRY, R. A., LAWRENCE, M., LOVE, M. I., MACDONALD, J., OBENCHAIN, V., OLEŚ, A. K., PAGÈS, H., REYES, A., SHANNON, P., SMYTH, G. K., TENENBAUM, D., WALDRON, L. &

MORGAN, M. 2015. Orchestrating high-throughput genomic analysis with Bioconductor. *Nature Methods,* 12**,** 115-121.

HUME, D. A., MILLARD, S. M. & PETTIT, A. R. 2023. Macrophage heterogeneity in the single-cell era: facts and artifacts. *Blood,* 142**,** 1339-1347.

HUYNH, K., TYC, K., MATUCK, B., EASTER, Q., PRATAPA, A., KUMAR, N., PEREZ, P., KULCHAR, R., PRANZATELLI, T., SOUZA, D., WEAVER, T., QU, X., JUNIOR, L., DOLHNOKOFF, M., KLEINER, D., HEWITT, S., SILVA, L., ROCHA, V., WARNER, B. & LIU, J. 2024. *Spatial Deconvolution of Cell Types and Cell States at Scale Utilizing TACIT,* bioRxiv.

IANNACONE, M. R., YOULDEN, D. R., BAADE, P. D., AITKEN, J. F. & GREEN, A. C. 2015. Melanoma incidence trends and survival in adolescents and young adults in Queensland, Australia. *Int J Cancer,* 136**,** 603-9.

IGLESIA, M. D., PARKER, J. S., HOADLEY, K. A., SERODY, J. S., PEROU, C. M. & VINCENT, B. G. 2016. Genomic Analysis of Immune Cell Infiltrates Across 11 Tumor Types. *J Natl Cancer Inst,* 108**,** djw144.

IRMISCH, A., BONILLA, X., CHEVRIER, S., LEHMANN, K. V., SINGER, F., TOUSSAINT, N. C., ESPOSITO, C., MENA, J., MILANI, E. S., CASANOVA, R., STEKHOVEN, D. J., WEGMANN, R., JACOB, F., SOBOTTKA, B., GOETZE, S., KUIPERS, J., SARABIA DEL CASTILLO, J., PRUMMER, M., TUNCEL, M. A., MENZEL, U., JACOBS, A., ENGLER, S., SIVAPATHAM, S., FREI, A. L., GUT, G., FICEK, J., MIGLINO, N., AEBERSOLD, R., BACAC, M., BEERENWINKEL, N., BEISEL, C., BODENMILLER, B., DUMMER, R., HEINZELMANN-SCHWARZ, V., KOELZER, V. H., MANZ, M. G., MOCH, H., PELKMANS, L., SNIJDER, B., THEOCHARIDES, A. P. A., TOLNAY, M., WICKI, A., WOLLSCHEID, B., RÄTSCH, G. & LEVESQUE, M. P. 2021. The Tumor Profiler Study: integrated, multi-omic, functional tumor profiling for clinical decision support. *Cancer Cell,* 39**,** 288-293.

ITZKOVITZ, S., LYUBIMOVA, A., BLAT, I. C., MAYNARD, M., VAN ES, J., LEES, J., JACKS, T., CLEVERS, H. & VAN OUDENAARDEN, A. 2011. Single-molecule transcript counting of stem-cell markers in the mouse intestine. *Nat Cell Biol,* 14**,** 106-14.

JACKSON, K. C. & PACHTER, L. 2023. A standard for sharing spatial transcriptomics data. *Cell Genom,* 3**,** 100374.

JACQUELOT, N., ROBERTI, M. P., ENOT, D. P., RUSAKIEWICZ, S., SEMERARO, M., JÉGOU, S., FLORES, C., CHEN, L., KWON, B. S., BORG, C., WEIDE, B., AUBIN, F., DALLE, S., KOHRT, H., AYYOUB, M., KROEMER, G., MARABELLE, A., CAVALCANTI, A., EGGERMONT, A. & ZITVOGEL, L. 2016. Immunophenotyping of Stage III Melanoma Reveals Parameters Associated with Patient Prognosis. *J Invest Dermatol,* 136**,** 994-1001.

JANESICK, A., SHELANSKY, R., GOTTSCHO, A. D., WAGNER, F., WILLIAMS, S. R., ROUAULT, M., BELIAKOFF, G., MORRISON, C. A., OLIVEIRA, M. F., SICHERMAN, J. T., KOHLWAY, A., ABOUSOUD, J., DRENNON, T. Y., MOHABBAT, S. H., TAYLOR, S. E. B. & X DEVELOPMENT, T. 2023. High resolution mapping of the tumor microenvironment using integrated single-cell, spatial and in situ analysis. *Nature Communications,* 14**,** 8353.

JANSSEN RESEARCH AND DEVELOPMENT, L. 2016. An Open-label, First-in-Human, Phase 1 Study of the Safety, Pharmacokinetics, and Pharmacodynamics of JNJ-61610588, a Fully Human IgG1 Kappa Anti-VISTA (V-domain Ig Suppressor of T-cell Activation) Monoclonal Antibody, in Subjects With Advanced Cancer. ClinicalTrials.gov.

JAVED, A., SATO, S. & SATO, T. 2016. Autologous melanoma cell vaccine using monocyte-derived dendritic cells (NBS20/eltrapuldencel-T). *Future Oncol,* 12**,** 751-62.

JIMÉNEZ-SÁNCHEZ, D., ARIZ, M., CHANG, H., MATIAS-GUIU, X., DE ANDREA, C. E. & ORTIZ-DE-SOLÓRZANO, C. 2022. NaroNet: Discovery of tumor microenvironment elements from highly multiplexed images. *Med Image Anal,* 78**,** 102384.

JIN, W. J., JAGODINSKY, J. C., VERA, J. M., CLARK, P. A., ZULEGER, C. L., ERBE, A. K., ONG, I. M., LE, T., TETREAULT, K., BERG, T., RAKHMILEVICH, A. L., KIM, K., NEWTON, M. A., ALBERTINI, M. R., SONDEL, P. M. & MORRIS, Z. S. 2023. NK cells propagate T cell immunity following in situ tumor vaccination. *Cell Rep,* 42**,** 113556.

JOHNSTON, R. J., SU, L. J., PINCKNEY, J., CRITTON, D., BOYER, E., KRISHNAKUMAR, A., CORBETT, M., RANKIN, A. L., DIBELLA, R., CAMPBELL, L., MARTIN, G. H., LEMAR, H., CAYTON, T., HUANG, R. Y. C., DENG, X., NAYEEM, A., CHEN, H., ERGEL, B., RIZZO, J. M., YAMNIUK, A. P., DUTTA, S., NGO, J., SHORTS, A. O., RAMAKRISHNAN, R., KOZHICH, A., HOLLOWAY, J., FANG, H., WANG, Y.-K., YANG, Z., THIAM, K., RAKESTRAW, G., RAJPAL, A., SHEPPARD, P., QUIGLEY, M., BAHJAT, K. S. & KORMAN, A. J. 2019. VISTA is an acidic pH-selective ligand for PSGL-1. *Nature,* 574**,** 565-570.

KAKAVAND, H., JACKETT, L. A., MENZIES, A. M., GIDE, T. N., CARLINO, M. S., SAW, R. P. M., THOMPSON, J. F., WILMOTT, J. S., LONG, G. V. & SCOLYER, R. A. 2017. Negative immune checkpoint regulation by VISTA: a mechanism of acquired resistance to anti-PD-1 therapy in metastatic melanoma patients. *Modern Pathology,* 30**,** 1666.

KAMENTSKY, L., JONES, T. R., FRASER, A., BRAY, M. A., LOGAN, D. J., MADDEN, K. L., LJOSA, V., RUEDEN, C., ELICEIRI, K. W. & CARPENTER, A. E. 2011. Improved structure, function and compatibility for CellProfiler: modular high-throughput image analysis software. *Bioinformatics,* 27**,** 1179-80.

KAO, C., OESTREICH, K. J., PALEY, M. A., CRAWFORD, A., ANGELOSANTO, J. M., ALI, M.-A. A., INTLEKOFER, A. M., BOSS, J. M., REINER, S. L., WEINMANN, A. S. & WHERRY, E. J. 2011. Transcription factor T-bet represses expression of the inhibitory receptor PD-1 and sustains virus-specific CD8+ T cell responses during chronic infection. *Nature Immunology,* 12**,** 663-671.

KAOCHAR, S., DONG, J., TORRES, M., RAJAPAKSHE, K., NIKOLOS, F., DAVIS, C. M., EHLI, E. A., COARFA, C., MITSIADES, N. & POULAKI, V. 2018. ICG-001 Exerts Potent Anticancer Activity Against Uveal Melanoma Cells. *Invest Ophthalmol Vis Sci,* 59**,** 132-143.

KARLSSON, M., ZHANG, C., MÉAR, L., ZHONG, W., DIGRE, A., KATONA, B., SJÖSTEDT, E., BUTLER, L., ODEBERG, J., DUSART, P., EDFORS, F., OKSVOLD, P., VON FEILITZEN, K., ZWAHLEN, M., ARIF, M., ALTAY, O., LI, X., OZCAN, M., MARDINOGLU, A., FAGERBERG, L., MULDER, J., LUO, Y., PONTEN, F., UHLÉN, M. & LINDSKOG, C. 2021. A single-cell type transcriptomics map of human tissues. *Sci Adv,* 7**,** eabh2169.

KATOH, K., KANO, Y., AMANO, M., KAIBUCHI, K. & FUJIWARA, K. 2001. Stress fiber organization regulated by MLCK and Rho-kinase in cultured human fibroblasts. *Am J Physiol Cell Physiol,* 280**,** C1669-79.

KAUFFMANN, A., ROSSELLI, F., LAZAR, V., WINNEPENNINCKX, V., MANSUET-LUPO, A., DESSEN, P., VAN DEN OORD, J. J., SPATZ, A. & SARASIN, A. 2008. High expression of DNA repair pathways is associated with metastasis in melanoma patients. *Oncogene,* 27**,** 565-73.

KIBEL, S., KUEHNE, N., RIBEIRO, M. F., MUNIZ, T. P., YE, X. Y., SPREAFICO, A., SAIBIL, S. D., SUN, A., MAK, D. Y., GRAY, D., JONES, B., WONG, P. & BUTLER, M. O. 2023. The Role of Adjuvant Radiotherapy for the Treatment of Resected High-Risk Stage III Cutaneous Melanoma in the Era of Modern Systemic Therapies. *Cancers (Basel),* 15**,** 5867.

KIDO, Y., ANDO, T., IGA, T., EMA, M., KUBOTA, Y. & TAI-NAGARA, I. 2022. Genetic Deletion of Vascular Endothelial Growth Factor Receptor 2 in Endothelial Cells Leads to Immediate Disruption of Tumor Vessels and Aggravation of Hypoxia. *Am J Pathol,* 192**,** 379-388.

KIELLY, M., CARACCIOLO, A., CHACON, A., VOHRADSKY, J., DI VITA, D., HAMATO, A., TASHIMA, H., FRANKLIN, D. R., YAMAYA, T., ROSENFELD, A., CARMINATI, M., FIORINI, C., GUATELLI, S. & SAFAVI-NAEINI, M. 2024. First experimental demonstration of real-time neutron capture discrimination in helium and carbon ion therapy. *Scientific Reports,* 14**,** 2601.

KIM, M. H., KIM, J., HONG, H., LEE, S. H., LEE, J. K., JUNG, E. & KIM, J. 2016. Actin remodeling confers BRAF inhibitor resistance to melanoma cells through YAP/TAZ activation. *Embo j,* 35**,** 462-78.

KIM, Y. J., WON, C. H., LEE, M. W., CHOI, J. H., CHANG, S. E. & LEE, W. J. 2020. Correlation Between Tumor-Associated Macrophage and Immune Checkpoint Molecule Expression and Its Prognostic Significance in Cutaneous Melanoma. *J Clin Med,* 9**,** 2500.

KING, J. W. & NATHAN, P. D. 2014. Role of the MEK inhibitor trametinib in the treatment of metastatic melanoma. *Future Oncol,* 10**,** 1559-70.

KNIGHT, A., KARAPETYAN, L. & KIRKWOOD, J. M. 2023. Immunotherapy in Melanoma: Recent Advances and Future Directions. *Cancers (Basel),* 15**,** 1106.

KOENIG, S. 2011. FDA Approves YERVOY™ (ipilimumab) for the Treatment of Patients with Newly Diagnosed or Previously-Treated Unresectable or Metastatic Melanoma, the Deadliest Form of Skin Cancer. *In:* ELICKER, J. (ed.). Princeton, NJ: Bristol Meyers Squibb.

KOPECKA, J., SALAROGLIO, I. C., PEREZ-RUIZ, E., SARMENTO-RIBEIRO, A. B., SAPONARA, S., DE LAS RIVAS, J. & RIGANTI, C. 2021. Hypoxia as a driver of resistance to immunotherapy. *Drug Resist Updat,* 59**,** 100787.

KRAUSGRUBER, T., REDL, A., BARRECA, D., DOBERER, K., ROMANOVSKAIA, D., DOBNIKAR, L., GUARINI, M., UNTERLUGGAUER, L., KLEISSL, L., ATZMÜLLER, D., MAYERHOFER, C., KOPF, A., SALUZZO, S., LIM, C. X., REXIE, P., WEICHHART, T., BOCK, C. & STARY, G. 2023. Single-cell and spatial transcriptomics reveal aberrant lymphoid developmental programs driving granuloma formation. *Immunity,* 56**,** 289-306.e7.

KRISHNAMURTY, A. T. & TURLEY, S. J. 2020. Lymph node stromal cells: cartographers of the immune system. *Nature Immunology,* 21**,** 369-380.

KRUSE, B., BUZZAI, A. C., SHRIDHAR, N., BRAUN, A. D., GELLERT, S., KNAUTH, K., POZNIAK, J., PETERS, J., DITTMANN, P., MENGONI, M., VAN DER SLUIS, T. C., HÖHN, S., ANTORANZ, A., KRONE, A., FU, Y., YU, D., ESSAND, M., GEFFERS, R., MOUGIAKAKOS, D., KAHLFUS, S., KASHKAR, H., GAFFAL, E., BOSISIO, F. M., BECHTER, O., RAMBOW, F., MARINE, J.-C., KASTENMÜLLER, W., MÜLLER, A. J. & TÜTING, T. 2023. CD4+ T cell-induced inflammatory cell death controls immune-evasive tumours. *Nature,* 618**,** 1033-1040.

KUBURICH, N. A., DEN HOLLANDER, P., PIETZ, J. T. & MANI, S. A. 2022. Vimentin and cytokeratin: Good alone, bad together. *Semin Cancer Biol,* 86**,** 816-826.

KUMASAKA, M. Y., YAJIMA, I., IIDA, M., TAKAHASHI, H., INOUE, Y., FUKUSHIMA, S., IHN, H., TAKEDA, K., NAITO, Y., YOSHIKAWA, T. & KATO, M. 2015. Correlated expression levels of endothelin receptor B and Plexin C1 in melanoma. *Am J Cancer Res,* 5**,** 1117-23.

KÜNZLI, K., FAVRE, B., CHOFFLON, M. & BORRADORI, L. 2016. One gene but different proteins and diseases: the complexity of dystonin and bullous pemphigoid antigen 1. *Experimental Dermatology,* 25**,** 10-16.

LABANI, S., ASTHANA, S., RATHORE, K. & SARDANA, K. 2021. Incidence of melanoma and nonmelanoma skin cancers in Indian and the global regions. *J Cancer Res Ther,* 17**,** 906-911.

LANDSBERG, J., KOHLMEYER, J., RENN, M., BALD, T., ROGAVA, M., CRON, M., FATHO, M., LENNERZ, V., WÖLFEL, T., HÖLZEL, M. & TÜTING, T. 2012. Melanomas resist T-cell therapy through inflammation-induced reversible dedifferentiation. *Nature,* 490**,** 412-6.

LAURINDO, M. F., THIES, F. G., PEREZ, E. C., NOVAES E BRITO, R. R., MARIANO, M. & POPI, A. F. 2013. B16 melanoma cells increase B-1 cell survival, IL-10 production and radioresistance in vitro. *Immunobiology,* 218**,** 609-19.

LAZARUS, J., AKISKA, Y., PERUSINA LANFRANCA, M., DELROSARIO, L., SUN, L., LONG, D., SHI, J., CRAWFORD, H., DI MAGLIANO, M. P., ZOU, W. & FRANKEL, T. 2019. Optimization, Design and Avoiding Pitfalls in Manual Multiplex Fluorescent Immunohistochemistry. *J Vis Exp*.

LAZOVICH, D., VOGEL, R. I., BERWICK, M., WEINSTOCK, M. A., ANDERSON, K. E. & WARSHAW, E. M. 2010. Indoor tanning and risk of melanoma: a case-control study in a highly exposed population. *Cancer Epidemiol Biomarkers Prev,* 19**,** 1557-68.

LEAL ROJAS, I. M., MOK, W. H., PEARSON, F. E., MINODA, Y., KENNA, T. J., BARNARD, R. T. & RADFORD, K. J. 2017. Human Blood CD1c(+) Dendritic Cells Promote Th1 and Th17 Effector Function in Memory CD4(+) T Cells. *Front Immunol,* 8**,** 971.

LEAMAN-ALCIBAR, O., LÓPEZ-CAMPOS, F., ALLER, J., CALÍN-LORCA, A., ZATARAIN-NICOLÁS, E., BANDE, M. F. & NAVARRO-MARTIN, A. 2022. Toxicity When Combining Immunotherapy and Radiotherapy. *In:* REZAEI, N. (ed.) *Handbook of Cancer and Immunology.* Cham: Springer International Publishing.

LEE, H., FERGUSON, A. L., QUEK, C., VERGARA, I. A., PIRES DASILVA, I., ALLEN, R., GIDE, T. N., CONWAY, J. W., KOUFARIOTIS, L. T., HAYWARD, N. K., WADDELL, N., CARLINO, M. S., MENZIES, A. M., SAW, R. P. M., SHKLOVSKAYA, E., RIZOS, H., LO, S., SCOLYER, R. A., LONG, G. V., PALENDIRA, U. & WILMOTT, J. S. 2023. Intratumoral CD16+ Macrophages Are Associated with Clinical Outcomes of Patients with Metastatic Melanoma Treated with Combination Anti-PD-1 and Anti-CTLA-4 Therapy. *Clin Cancer Res,* 29**,** 2513-2524.

LEE, S., AMICI, S., TAVORI, H., ZENG, W. M., FREELAND, S., FAZIO, S. & NOTTERPEK, L. 2014. PMP22 is critical for actin-mediated cellular functions and for establishing lipid rafts. *J Neurosci,* 34**,** 16140-52.

LEE, Y. J., KIM, D. H., LEE, S. H., KIM, D. W., NAM, H. S. & CHO, M. K. 2011. Expression of the c-Met Proteins in Malignant Skin Cancers. *Ann Dermatol,* 23**,** 33-8.

LEEK, L. V. M., NOTOHARDJO, J. C. L., DE JOODE, K., VELKER, E. L., HAANEN, J., SUIJKERBUIJK, K. P. M., AARTS, M. J. B., DE GROOT, J. W. B., KAPITEIJN, E., VAN DEN BERKMORTEL, F., WESTGEEST, H. M., DE GRUIJL, T. D., RETEL, V. P., CUPPEN, E., VAN DER VELDT, A. A. M., LABOTS, M., VOEST, E. E., VAN DE HAAR, J. & VAN DEN EERTWEGH, A. J. M. 2024. Multi-omic analysis

identifies hypoalbuminemia as independent biomarker of poor outcome upon PD-1 blockade in metastatic melanoma. *Sci Rep,* 14**,** 11244.

LEHMANN, J., CADUFF, N., KRZYWIŃSKA, E., STIERLI, S., SALAS-BASTOS, A., LOOS, B., LEVESQUE, M. P., DUMMER, R., STOCKMANN, C., MÜNZ, C., DIENER, J. & SOMMER, L. 2023. Escape from NK cell tumor surveillance by NGFR-induced lipid remodeling in melanoma. *Sci Adv,* 9**,** eadc8825.

LEICK, K. M., RODRIGUEZ, A. B., MELSSEN, M. M., BENAMAR, M., LINDSAY, R. S., EKI, R., DU, K. P., PARLAK, M., ABBAS, T., ENGELHARD, V. H. & SLINGLUFF, C. L., JR. 2019. The Barrier Molecules Junction Plakoglobin, Filaggrin, and Dystonin Play Roles in Melanoma Growth and Angiogenesis. *Ann Surg,* 270**,** 712-722.

LEPPER, A., BITSCH, R., ÖZBAY KURT, F. G., ARKHYPOV, I., LASSER, S., UTIKAL, J. & UMANSKY, V. 2023. Melanoma patients with immune-related adverse events after immune checkpoint inhibitors are characterized by a distinct immunological phenotype of circulating T cells and M-MDSCs. *Oncoimmunology,* 12**,** 2247303.

LEVSKY, J. M., SHENOY, S. M., PEZO, R. C. & SINGER, R. H. 2002. Single-cell gene expression profiling. *Science,* 297**,** 836-40.

LEWIS, S. M., ASSELIN-LABAT, M.-L., NGUYEN, Q., BERTHELET, J., TAN, X., WIMMER, V. C., MERINO, D., ROGERS, K. L. & NAIK, S. H. 2021. Spatial omics and multiplexed imaging to explore cancer biology. *Nature Methods,* 18**,** 997-1012.

LI, A. & YANG, D.-H. 2020. Application of Immunohistochemistry in Basic and Clinical Studies. *In:* VANCUROVA, I. & ZHU, Y. (eds.) *Immune Mediators in Cancer: Methods and Protocols.* New York, NY: Springer US.

LI, G., YANG, Q., ZHU, Y., WANG, H. R., CHEN, X., ZHANG, X. & LU, B. 2013. T-Bet and Eomes Regulate the Balance between the Effector/Central Memory T Cells versus Memory Stem Like T Cells. *PLoS One,* 8**,** e67401.

LI, H., VAN DER LEUN, A. M., YOFE, I., LUBLING, Y., GELBARD-SOLODKIN, D., VAN AKKOOI, A. C. J., VAN DEN BRABER, M., ROZEMAN, E. A., HAANEN, J., BLANK, C. U., HORLINGS, H. M., DAVID, E., BARAN, Y., BERCOVICH, A., LIFSHITZ, A., SCHUMACHER, T. N., TANAY, A. & AMIT, I. 2019. Dysfunctional CD8 T Cells Form a Proliferative, Dynamically Regulated Compartment within Human Melanoma. *Cell,* 176**,** 775-789.e18.

LI, J., LI, J., PENG, Y., DU, Y., YANG, Z. & QI, X. 2023a. Dendritic cell derived exosomes loaded neoantigens for personalized cancer immunotherapies. *J Control Release,* 353**,** 423-433.

LI, J., LIU, J., MAO, X., TANG, Q. & LU, H. 2014. IL-7 receptor blockade inhibits IL-17-producing γδ cells and suppresses melanoma development. *Inflammation,* 37**,** 1444-52.

LI, K., SUN, L., WANG, Y., CEN, Y., ZHAO, J., LIAO, Q., WU, W., SUN, J. & ZHOU, M. 2023b. Single-cell characterization of macrophages in uveal melanoma uncovers transcriptionally heterogeneous subsets conferring poor prognosis and aggressive behavior. *Experimental & Molecular Medicine,* 55**,** 2433-2444.

LI, N., YANG, S., REN, Y., TAI, R., LIU, H., WANG, Y., LI, J., WANG, F., XING, J., ZHANG, Y., ZHU, X., XU, S., HOU, X. & WANG, G. 2023c. Chemotherapy induces immune checkpoint VISTA expression in tumor cells via HIF-2alpha. *Biochem Pharmacol,* 210**,** 115492.

LI, S., CHEN, K., YANG, M., HLAING, S. S., CHEN, M., GU, P., MENG, Y. & YANG, H. 2022. Radiotherapy improves the outcomes of immunotherapy with Sintilimab in non-small-cell lung cancer: A real-world analysis. *Front Immunol,* 13**,** 991431.

LI, S., WANG, G., REN, Y., LIU, X., WANG, Y., LI, J., LIU, H., YANG, J., XING, J., ZHANG, Y., HE, C., XU, S., HOU, X. & LI, N. 2024. Expression and function of VISTA on myeloid cells. *Biochemical Pharmacology,* 222**,** 116100.

LI, T. T., JIANG, J. W., QIE, C. X., XUAN, C. X., HU, X. L., LIU, W. M., CHEN, W. T. & LIU, J. 2021. Identification of active small-molecule modulators targeting the novel immune checkpoint VISTA. *BMC Immunol,* 22**,** 55.

LI, X., KARRAS, P., TORRES, R., RAMBOW, F., VAN DEN OORD, J., MARINE, J. C. & KOS, L. 2020. Disseminated Melanoma Cells Transdifferentiate into Endothelial Cells in Intravascular Niches at Metastatic Sites. *Cell Rep,* 31**,** 107765.

LIN, S., DAI, Y., HAN, C., HAN, T., ZHAO, L., WU, R., LIU, J., ZHANG, B., HUANG, N., LIU, Y., LAI, S., SHI, J., WANG, Y., LOU, M., XIE, J., CHENG, Y., TANG, H., YAO, H., FANG, H., ZHANG, Y., WU, X., SHEN, L., YE, Y., XUE, L. & WU, Z. B. 2024a. Single-cell transcriptomics reveal distinct immune-infiltrating phenotypes and macrophage-tumor interaction axes among different lineages of pituitary neuroendocrine tumors. *Genome Med,* 16**,** 60.

LIN, Y., CHOUKRANI, G., DUBBEL, L., ROCKSTEIN, L., FREILE, J. A., QI, Y., WIERSMA, V., ZHANG, H., KOCH, K. W., AMMATUNA, E., SCHURINGA, J. J., VAN MEERTEN, T., HULS, G. & BREMER, E. 2024b. VISTA drives macrophages towards a pro-tumoral phenotype that promotes cancer cell phagocytosis yet down-regulates T cell responses. *Exp Hematol Oncol,* 13**,** 35.

LIN, Y., DONG, Z. H., YE, T. Y., YANG, J. M., XIE, M., LUO, J. C., GAO, J. & GUO, A. Y. 2024c. Optimization of FFPE preparation and identification of gene attributes associated with RNA degradation. *NAR Genom Bioinform,* 6**,** lqae008.

LINDERMAN, G. C., RACHH, M., HOSKINS, J. G., STEINERBERGER, S. & KLUGER, Y. 2019. Fast interpolation-based t-SNE for improved visualization of single-cell RNA-seq data. *Nat Methods,* 16**,** 243-245.

LISCHETTI, U., TASTANOVA, A., SINGER, F., GROB, L., CARRARA, M., CHENG, P. F., MARTÍNEZ GÓMEZ, J. M., SELLA, F., HAUNERDINGER, V., BEISEL, C. & LEVESQUE, M. P. 2023. Dynamic thresholding and tissue dissociation optimization for CITE-seq identifies differential surface protein abundance in metastatic melanoma. *Commun Biol,* 6**,** 830.

LIU, C. & MAK, M. 2022. Fibroblast-mediated uncaging of cancer cells and dynamic evolution of the physical microenvironment. *Scientific Reports,* 12**,** 791.

LIU, C. L., PAN, H. W., TORNG, P. L., FAN, M. H. & MAO, T. L. 2019a. SRPX and HMCN1 regulate cancer-associated fibroblasts to promote the invasiveness of ovarian carcinoma. *Oncol Rep,* 42**,** 2706-2715.

LIU, D., SCHILLING, B., LIU, D., SUCKER, A., LIVINGSTONE, E., JERBY-ARNON, L., ZIMMER, L., GUTZMER, R., SATZGER, I., LOQUAI, C., GRABBE, S., VOKES, N., MARGOLIS, C. A., CONWAY, J., HE, M. X., ELMARAKEBY, H., DIETLEIN, F., MIAO, D., TRACY, A., GOGAS, H., GOLDINGER, S. M., UTIKAL, J., BLANK, C. U., RAUSCHENBERG, R., VON BUBNOFF, D., KRACKHARDT, A., WEIDE, B., HAFERKAMP, S., KIECKER, F., IZAR, B., GARRAWAY, L., REGEV, A., FLAHERTY, K., PASCHEN, A., VAN ALLEN, E. M. & SCHADENDORF, D. 2019b. Integrative molecular and clinical modeling of clinical outcomes to PD1 blockade in patients with metastatic melanoma. *Nat Med,* 25**,** 1916-1927.

LIU, J., LIN, W. P., XIAO, Y., YANG, Q. C., BUSHABU FIDELE, N., YU, H. J. & SUN, Z. J. 2023. VISTA blockade alleviates immunosuppression of MDSCs in oral squamous cell carcinoma. *Int Immunopharmacol,* 125**,** 111128.

LIU, L., STOKES, J. V., TAN, W. & PRUETT, S. B. 2022a. An optimized flow cytometry panel for classifying macrophage polarization. *J Immunol Methods,* 511**,** 113378.

LIU, M., BERTOLAZZI, G., SRIDHAR, S., LEE, R. X., JAYNES, P., MULDER, K., SYN, N., HOPPE, M. M., FAN, S., PENG, Y., THNG, J., CHUA, R., JAYALAKSHMI, BATUMALAI, Y., DE MEL, S., POON, L., CHAN, E. H. L., LEE, J., HUE, S. S.-S.,

CHANG, S.-T., CHUANG, S.-S., CHANDY, K. G., YE, X., PAN-HAMMARSTRÖM, Q., GINHOUX, F., CHEE, Y. L., NG, S.-B., TRIPODO, C. & JEYASEKHARAN, A. D. 2024. Spatially-resolved transcriptomics reveal macrophage heterogeneity and prognostic significance in diffuse large B-cell lymphoma. *Nature Communications,* 15**,** 2113.

LIU, T., ZHOU, L., YANG, K., IWASAWA, K., KADEKARO, A. L., TAKEBE, T., ANDL, T. & ZHANG, Y. 2019c. The β-catenin/YAP signaling axis is a key regulator of melanoma-associated fibroblasts. *Signal Transduct Target Ther,* 4**,** 63.

LIU, X., WANG, Y., BAUER, A. T., KIRSCHFINK, M., DING, P., GEBHARDT, C., BORSIG, L., TÜTING, T., RENNÉ, T., HÄFFNER, K., HU, W., SCHNEIDER, S. W. & GORZELANNY, C. 2022b. Neutrophils activated by membrane attack complexes increase the permeability of melanoma blood vessels. *Proc Natl Acad Sci U S A,* 119**,** e2122716119.

LIU, Z., YU, Z., CHEN, D., VERMA, V., YUAN, C., WANG, M., WANG, F., FAN, Q., WANG, X., LI, Y., MA, Y., WU, M. & YU, J. 2022c. Pivotal roles of tumor-draining lymph nodes in the abscopal effects from combined immunotherapy and radiotherapy. *Cancer Commun (Lond),* 42**,** 971-986.

LOMAX, A. J., MCGUIRE, H. M., MCNEIL, C., CHOI, C. J., HERSEY, P., KARIKIOS, D., SHANNON, K., VAN HAL, S., CARR, U., CROTTY, A., GUPTA, S. K., HOLLINGSWORTH, J., KIM, H., FAZEKAS DE ST GROTH, B. & MCGILL, N. 2017. Immunotherapy-induced sarcoidosis in patients with melanoma treated with PD-1 checkpoint inhibitors: Case series and immunophenotypic analysis. *Int J Rheum Dis,* 20**,** 1277-1285.

LONG, G. V., MENZIES, A. M. & SCOLYER, R. A. 2023a. Neoadjuvant Checkpoint Immunotherapy and Melanoma: The Time Is Now. *J Clin Oncol,* 41**,** 3236-3248.

LONG, G. V., SWETTER, S. M., MENZIES, A. M., GERSHENWALD, J. E. & SCOLYER, R. A. 2023b. Cutaneous melanoma. *Lancet,* 402**,** 485-502.

LONG, L., ZHANG, L., YANG, Y., ZHOU, Y. & CHEN, H. 2022. Different clinical significance of novel B7 family checkpoints VISTA and HHLA2 in human lung adenocarcinoma. *Immunotherapy,* 14**,** 419-431.

LUNDBERG, S. M. & LEE, S.-I. 2017. A unified approach to interpreting model predictions. *Proceedings of the 31st International Conference on Neural Information Processing Systems.* Long Beach, California, USA: Curran Associates Inc.

MA, M. W., MEDICHERLA, R. C., QIAN, M., VEGA-SAENZ DE MIERA, E., FRIEDMAN, E. B., BERMAN, R. S., SHAPIRO, R. L., PAVLICK, A. C., OTT, P. A., BHARDWAJ, N., SHAO, Y., OSMAN, I. & DARVISHIAN, F. 2012. Immune response in melanoma: an in-depth analysis of the primary tumor and corresponding sentinel lymph node. *Mod Pathol,* 25**,** 1000-10.

MA, Q. & XU, D. 2022. Deep learning shapes single-cell data analysis. *Nature Reviews Molecular Cell Biology,* 23**,** 303-304.

MA, S., QIN, L., WANG, X., WANG, W., LI, J., WANG, H., LI, H., CAI, X., YANG, Y. & QU, M. 2022. The Expression of VISTA on CD4+ T Cells Associate with Poor Prognosis and Immune Status in Non-small Cell Lung Cancer Patients. *Bosn J Basic Med Sci,* 22**,** 707-715.

MAHER, N. G., VERGARA, I. A., LONG, G. V. & SCOLYER, R. A. 2024. Prognostic and predictive biomarkers in melanoma. *Pathology,* 56**,** 259-273.

MALLARDO, D., FORDELLONE, M., WHITE, A., OTTAVIANO, M., SPARANO, F., BAILEY, M., FACCHINI, A. B., ONG, S., MAIOLINO, P., CARACÒ, C., CHURCH, S., CAVALCANTI, E., WARREN, S., BUDILLON, A., CESANO, A., SIMEONE, E., CHIODINI, P. & ASCIERTO, P. A. 2023. CD39 and LDHA affects the prognostic role

of NLR in metastatic melanoma patients treated with immunotherapy. *J Transl Med,* 21**,** 610.

MANTOVANI, A. & MARCHESI, F. 2022. A topology perspective on macrophages in melanoma metastasis. *Cell Rep Med,* 3**,** 100643.

MANTOVANI, A., MARCHESI, F., JAILLON, S., GARLANDA, C. & ALLAVENA, P. 2021. Tumor-associated myeloid cells: diversity and therapeutic targeting. *Cell Mol Immunol,* 18**,** 566-578.

MANTOVANI, A. & SICA, A. 2010. Macrophages, innate immunity and cancer: balance, tolerance, and diversity. *Current Opinion in Immunology,* 22**,** 231-237.

MARCONATO, L., PALLA, G., YAMAUCHI, K. A., VIRSHUP, I., HEIDARI, E., TREIS, T., VIERDAG, W.-M., TOTH, M., STOCKHAUS, S., SHRESTHA, R. B., ROMBAUT, B., POLLARIS, L., LEHNER, L., VÖHRINGER, H., KATS, I., SAEYS, Y., SAKA, S. K., HUBER, W., GERSTUNG, M., MOORE, J., THEIS, F. J. & STEGLE, O. 2024. SpatialData: an open and universal data framework for spatial omics. *Nature Methods*.

MARINE, J. C. & LOZANO, G. 2010. Mdm2-mediated ubiquitylation: p53 and beyond. *Cell Death & Differentiation,* 17**,** 93-102.

MARSH-WAKEFIELD, F., SANTHAKUMAR, C., FERGUSON, A. L., ASHHURST, T. M., SHIN, J.-S., GUAN, F. H. X., SHIELDS, N. J., PLATT, B. J., PUTRI, G. H., GUPTA, R., CRAWFORD, M., PULITANO, C., SANDROUSSI, C., LAURENCE, J. M., LIU, K., MCCAUGHAN, G. W. & PALENDIRA, U. 2024. Spatial mapping of the hepatocellular carcinoma landscape identifies unique intratumoural perivascular-immune neighbourhoods. *medRxiv***,** 2023.09.15.23295451.

MARTIN, A. S., MOLLOY, M., UGOLKOV, A., VON ROEMELING, R. W., NOELLE, R. J., LEWIS, L. D., JOHNSON, M., RADVANYI, L. & MARTELL, R. E. 2023. VISTA expression and patient selection for immune-based anticancer therapy. *Front Immunol,* 14**,** 1086102.

MARTIN-HERNANDEZ, R., ESPESO-GIL, S., DOMINGO, C., LATORRE, P., HERVAS, S., HERNANDEZ MORA, J. R. & KOTELNIKOVA, E. 2023. Machine learning combining multi-omics data and network algorithms identifies adrenocortical carcinoma prognostic biomarkers. *Front Mol Biosci,* 10**,** 1258902.

MARTIN-OROZCO, N., MURANSKI, P., CHUNG, Y., YANG, X. O., YAMAZAKI, T., LU, S., HWU, P., RESTIFO, N. P., OVERWIJK, W. W. & DONG, C. 2009. T helper 17 cells promote cytotoxic T cell activation in tumor immunity. *Immunity,* 31**,** 787-98.

MARTINEK, J., LIN, J., KIM, K. I., WANG, V. G., WU, T. C., CHIORAZZI, M., BORUCHOV, H., GULATI, A., SEENIRAJ, S., SUN, L., MARCHES, F., ROBSON, P., RONGVAUX, A., FLAVELL, R. A., GEORGE, J., CHUANG, J. H., BANCHEREAU, J. & PALUCKA, K. 2022. Transcriptional profiling of macrophages in situ in metastatic melanoma reveals localization-dependent phenotypes and function. *Cell Rep Med,* 3**,** 100621.

MARUSYK, A., JANISZEWSKA, M. & POLYAK, K. 2020. Intratumor Heterogeneity: The Rosetta Stone of Therapy Resistance. *Cancer Cell,* 37**,** 471-484.

MARX, V. 2021. Method of the Year: spatially resolved transcriptomics. *Nature Methods,* 18**,** 9-14.

MARX, V. 2022. How single-cell multi-omics builds relationships. *Nature Methods,* 19**,** 142-146.

MASSI, D., RULLI, E., COSSA, M., VALERI, B., RODOLFO, M., MERELLI, B., DE LOGU, F., NASSINI, R., DEL VECCHIO, M., DI GUARDO, L., DE PENNI, R., GUIDA, M., SILENI, V. C., DI GIACOMO, A. M., TUCCI, M., OCCELLI, M., PORTELLI, F., VALLACCHI, V., CONSOLI, F., QUAGLINO, P., QUEIROLO, P.,

BARONI, G., CARNEVALE-SCHIANCA, F., CATTANEO, L., MINISINI, A., PALMIERI, G., RIVOLTINI, L. & MANDALÀ, M. 2019. The density and spatial tissue distribution of CD8(+) and CD163(+) immune cells predict response and outcome in melanoma patients receiving MAPK inhibitors. *J Immunother Cancer,* 7**,** 308.

MATHES, S., LINDWEDEL, K. S., NILSEN, L. T., KAISER, I., PFAHLBERG, A. B. & GEFELLER, O. 2023. Global Tanning Bed Advertising: A Comparison of Legal Regulations on Three Continents. *Cancers (Basel),* 15**,** 4362.

MATLUNG, H. L., BABES, L., ZHAO, X. W., VAN HOUDT, M., TREFFERS, L. W., VAN REES, D. J., FRANKE, K., SCHORNAGEL, K., VERKUIJLEN, P., JANSSEN, H., HALONEN, P., LIEFTINK, C., BEIJERSBERGEN, R. L., LEUSEN, J. H. W., BOELENS, J. J., KUHNLE, I., VAN DER WERFF TEN BOSCH, J., SEEGER, K., RUTELLA, S., PAGLIARA, D., MATOZAKI, T., SUZUKI, E., MENKE-VAN DER HOUVEN VAN OORDT, C. W., VAN BRUGGEN, R., ROOS, D., VAN LIER, R. A. W., KUIJPERS, T. W., KUBES, P. & VAN DEN BERG, T. K. 2018. Neutrophils Kill Antibody-Opsonized Cancer Cells by Trogoptosis. *Cell Rep,* 23**,** 3946-3959.e6.

MATSUO, Y. & KAMITANI, T. 2010. Parkinson's disease-related protein, alpha-synuclein, in malignant melanoma. *PLoS One,* 5**,** e10481.

MATTES, J., HULETT, M., XIE, W., HOGAN, S., ROTHENBERG, M. E., FOSTER, P. & PARISH, C. 2003. Immunotherapy of cytotoxic T cell-resistant tumors by T helper 2 cells: an eotaxin and STAT6-dependent process. *J Exp Med,* 197**,** 387-93.

MAZURKIEWICZ, J., SIMICZYJEW, A., DRATKIEWICZ, E., PIETRASZEK-GREMPLEWICZ, K., MAJKOWSKI, M., KOT, M., ZIĘTEK, M., MATKOWSKI, R. & NOWAK, D. 2022. Melanoma cells with diverse invasive potential differentially induce the activation of normal human fibroblasts. *Cell Commun Signal,* 20**,** 63.

MCARTHUR, G. A., CHAPMAN, P. B., ROBERT, C., LARKIN, J., HAANEN, J. B., DUMMER, R., RIBAS, A., HOGG, D., HAMID, O., ASCIERTO, P. A., GARBE, C., TESTORI, A., MAIO, M., LORIGAN, P., LEBBÉ, C., JOUARY, T., SCHADENDORF, D., O'DAY, S. J., KIRKWOOD, J. M., EGGERMONT, A. M., DRÉNO, B., SOSMAN, J. A., FLAHERTY, K. T., YIN, M., CARO, I., CHENG, S., TRUNZER, K. & HAUSCHILD, A. 2014. Safety and efficacy of vemurafenib in BRAF(V600E) and BRAF(V600K) mutation-positive melanoma (BRIM-3): extended follow-up of a phase 3, randomised, open-label study. *Lancet Oncol,* 15**,** 323-32.

MCCARTER, M., CLARKE, J., RICHTER, D. & WILSON, C. 2005. Melanoma skews dendritic cells to facilitate a T helper 2 profile. *Surgery,* 138**,** 321-8.

MEDORI, M. C., DONATO, K., DHULI, K., MALTESE, P. E., TANZI, B., TEZZELE, S., MARESO, C., MIERTUS, J., GENERALI, D., DONOFRIO, C. A., COMINETTI, M., FIORAVANTI, A., RICCIO, L., BECCARI, T., CECCARINI, M. R., GISONDI, P., BELLINATO, F., STUPPIA, L., GATTA, V., CECCHIN, S., MARCEDDU, G. & BERTELLI, M. 2023. Omics sciences and precision medicine in melanoma. *Clin Ter,* 174**,** 29-36.

MELERO, I., GOMEZ-ROCA, C., FERRE, P., FERRE, P., CHETAILLE, E., PETAIN, A., THUILLIEZ, C., VANDENBERGHE, I., CRUZALEGUI, F., BOUDRIBILA, A., PAVLYUK, M. & MARABELLE, A. 2020. 315 W0180 novel anti-VISTA antibody: Rationale for target patient population and first-in-human trial design in monotherapy and in combination with anti-PD1 antibody. *Journal for ImmunoTherapy of Cancer,* 8**,** A193.

MILLAR, M. 2020. Mixed Multiplex Staining: Automated RNAscope™ and OPAL™ for Multiple Targets. *Methods Mol Biol,* 2148**,** 277-298.

MILLER, B. C., SEN, D. R., AL ABOSY, R., BI, K., VIRKUD, Y. V., LAFLEUR, M. W., YATES, K. B., LAKO, A., FELT, K., NAIK, G. S., MANOS, M., GJINI, E., KUCHROO, J. R., ISHIZUKA, J. J., COLLIER, J. L., GRIFFIN, G. K., MALERI, S., COMSTOCK, D. E., WEISS, S. A., BROWN, F. D., PANDA, A., ZIMMER, M. D., MANGUSO, R. T., HODI, F. S., RODIG, S. J., SHARPE, A. H. & HAINING, W. N. 2019. Subsets of exhausted CD8(+) T cells differentially mediate tumor control and respond to checkpoint blockade. *Nat Immunol,* 20**,** 326-336.

MOGENSEN, M. & JEMEC, G. B. 2010. The potential carcinogenic risk of tanning beds: clinical guidelines and patient safety advice. *Cancer Manag Res,* 2**,** 277-82.

MOLDOVEANU, D., RAMSAY, L., LAJOIE, M., ANDERSON-TROCME, L., LINGRAND, M., BERRY, D., PERUS, L. J. M., WEI, Y., MORAES, C., ALKALLAS, R., RAJKUMAR, S., ZUO, D., DANKNER, M., XU, E. H., BERTOS, N. R., NAJAFABADI, H. S., GRAVEL, S., COSTANTINO, S., RICHER, M. J., LUND, A. W., DEL RINCON, S. V., SPATZ, A., MILLER, W. H., JR., JAMAL, R., LAPOINTE, R., MES-MASSON, A. M., TURCOTTE, S., PETRECCA, K., DUMITRA, S., MEGUERDITCHIAN, A. N., RICHARDSON, K., TREMBLAY, F., WANG, B., CHERGUI, M., GUIOT, M. C., WATTERS, K., STAGG, J., QUAIL, D. F., MIHALCIOIU, C., METERISSIAN, S. & WATSON, I. R. 2022. Spatially mapping the immune landscape of melanoma using imaging mass cytometry. *Sci Immunol,* 7**,** eabi5072.

MOLE, R. H. 1953. Whole body irradiation; radiobiology or medicine? *Br J Radiol,* 26**,** 234-41.

MOLLOY, M. 2016. *IDENTIFICATION OF VSG8 AS THE PUTATIVE VISTA RECEPTOR (V-R) AND USE*

THEREOF TO PRODUCE VISTA/VSG8 AGONSTS AND ANTAGONSTS. US patent application US20160159927A1.

MOSES, L. & PACHTER, L. 2022. Museum of spatial transcriptomics. *Nat Methods,* 19**,** 534-546.

MOSTBÖCK, S., WU, H. H., FENN, T., RIEGLER, B., STRAHLHOFER, S., HUANG, Y., HANSEN, G., KROE-BARRETT, R., TIRAPU, I. & VOGT, A. B. 2022. Distinct immune stimulatory effects of anti-human VISTA antibodies are determined by Fc-receptor interaction. *Front Immunol,* 13**,** 862757.

MULATI, K., HAMANISHI, J., MATSUMURA, N., CHAMOTO, K., MISE, N., ABIKO, K., BABA, T., YAMAGUCHI, K., HORIKAWA, N., MURAKAMI, R., TAKI, M., BUDIMAN, K., ZENG, X., HOSOE, Y., AZUMA, M., KONISHI, I. & MANDAI, M. 2019. VISTA expressed in tumour cells regulates T cell function. *Br J Cancer,* 120**,** 115-127.

MULDER, K., PATEL, A. A., KONG, W. T., PIOT, C., HALITZKI, E., DUNSMORE, G., KHALILNEZHAD, S., IRAC, S. E., DUBUISSON, A., CHEVRIER, M., ZHANG, X. M., TAM, J. K. C., LIM, T. K. H., WONG, R. M. M., PAI, R., KHALIL, A. I. S., CHOW, P. K. H., WU, S. Z., AL-ERYANI, G., RODEN, D., SWARBRICK, A., CHAN, J. K. Y., ALBANI, S., DEROSA, L., ZITVOGEL, L., SHARMA, A., CHEN, J., SILVIN, A., BERTOLETTI, A., BLÉRIOT, C., DUTERTRE, C. A. & GINHOUX, F. 2021. Cross-tissue single-cell landscape of human monocytes and macrophages in health and disease. *Immunity,* 54**,** 1883-1900.e5.

MULHOLLAND, E. & LEEDHAM, S. 2024. Redefining clinical practice through spatial profiling: a revolution in tissue analysis. *The Annals of The Royal College of Surgeons of England,* 106**,** 305-312.

NAHAR, K. J., MARSH-WAKEFIELD, F., RAWSON, R. V., GIDE, T. N., FERGUSON, A. L., ALLEN, R., QUEK, C., DA SILVA, I. P., TATTERSAL, S., KIELY, C. J.,

SANDANAYAKE, N., CARLINO, M. S., MCCAUGHAN, G., WILMOTT, J. S., SCOLYER, R. A., LONG, G. V., MENZIES, A. M. & PALENDIRA, U. 2022. Distinct pretreatment innate immune landscape and posttreatment T cell responses underlie immunotherapy-induced colitis. *JCI Insight,* 7**,** e157839.

NANDAKUMAR, S., VIJAYAN, B., KISHORE, A. & THEKKUVEETTIL, A. 2017. Autophagy enhancement is rendered ineffective in presence of α-synuclein in melanoma cells. *J Cell Commun Signal,* 11**,** 381-394.

NETWORK, C. G. A. 2015. Genomic Classification of Cutaneous Melanoma. *Cell,* 161**,** 1681-96.

NEVALA, W. K., VACHON, C. M., LEONTOVICH, A. A., SCOTT, C. G., THOMPSON, M. A. & MARKOVIC, S. N. 2009. Evidence of systemic Th2-driven chronic inflammation in patients with metastatic melanoma. *Clin Cancer Res,* 15**,** 1931-9.

NG, M. F., SIMMONS, J. L. & BOYLE, G. M. 2022. Heterogeneity in Melanoma. *Cancers (Basel),* 14**,** 3030.

NGUYEN, T., THOMAS, W., ZHANG, X. D., GRAY, C. & HERSEY, P. 2000. Immunologically-mediated tumour cell apoptosis: the role of TRAIL in T cell and cytokine-mediated responses to melanoma. *Forum (Genova),* 10**,** 243-52.

NIEDERBERGER, E., MÖLLER, M., MUNGO, E., HASS, M., WILKEN-SCHMITZ, A., MANDERSCHEID, C., MÖSER, C. V. & GEISSLINGER, G. 2023. Distinct molecular mechanisms contribute to the reduction of melanoma growth and tumor pain after systemic and local depletion of alpha-Synuclein in mice. *Faseb j,* 37**,** e23287.

NOELLE, R. J., LINES, J. L., LEWIS, L. D., MARTELL, R. E., GUILLAUDEUX, T., LEE, S. W., MAHONEY, K. M., VESELY, M. D., BOYD-KIRKUP, J., NAMBIAR, D. K. & SCOTT, A. M. 2023. Clinical and research updates on the VISTA immune checkpoint: immuno-oncology themes and highlights. *Front Oncol,* 13**,** 1225081.

NORDMANN, T. M., ANDERTON, H., HASEGAWA, A., SCHWEIZER, L., ZHANG, P., STADLER, P. C., SINHA, A., METOUSIS, A., ROSENBERGER, F. A., ZWIEBEL, M., SATOH, T. K., ANZENGRUBER, F., STRAUSS, M. T., TANZER, M. C., SAITO, Y., GONG, T., THIELERT, M., KIMURA, H., SILKE, N., RODRIGUEZ, E. H., RESTIVO, G., NGUYEN, H. H., GROSS, A., FELDMEYER, L., JOERG, L., LEVESQUE, M. P., MURRAY, P. J., INGEN-HOUSZ-ORO, S., MUND, A., ABE, R., SILKE, J., JI, C., FRENCH, L. E. & MANN, M. 2024. Spatial proteomics identifies JAKi as treatment for a lethal skin disease. *Nature*.

NORMAN, K. E., MOORE, K. L., MCEVER, R. P. & LEY, K. 1995. Leukocyte Rolling In Vivo Is Mediated by P-Selectin Glycoprotein Ligand-1. *Blood,* 86**,** 4417-4421.

OKOLO, O., YU, V., FLASHNER, S., MARTIN, C., NAKAGAWA, H., LIN, D. T., PURAM, S. V. & PARIKH, A. S. 2023. Protocol for tumor dissociation and fluorescence-activated cell sorting of human head and neck cancers. *STAR Protoc,* 4**,** 102294.

OLIVEIRA, G., STROMHAUG, K., CIERI, N., IORGULESCU, J. B., KLAEGER, S., WOLFF, J. O., RACHIMI, S., CHEA, V., KRAUSE, K., FREEMAN, S. S., ZHANG, W., LI, S., BRAUN, D. A., NEUBERG, D., CARR, S. A., LIVAK, K. J., FREDERICK, D. T., FRITSCH, E. F., WIND-ROTOLO, M., HACOHEN, N., SADE-FELDMAN, M., YOON, C. H., KESKIN, D. B., OTT, P. A., RODIG, S. J., BOLAND, G. M. & WU, C. J. 2022. Landscape of helper and regulatory antitumour CD4(+) T cells in melanoma. *Nature,* 605**,** 532-538.

OLIVEIRA, G., STROMHAUG, K., KLAEGER, S., KULA, T., FREDERICK, D. T., LE, P. M., FORMAN, J., HUANG, T., LI, S., ZHANG, W., XU, Q., CIERI, N., CLAUSER, K. R., SHUKLA, S. A., NEUBERG, D., JUSTESEN, S., MACBEATH, G., CARR, S. A., FRITSCH, E. F., HACOHEN, N., SADE-FELDMAN, M., LIVAK, K. J., BOLAND, G. M., OTT, P. A., KESKIN, D. B. & WU, C. J. 2021. Phenotype,

specificity and avidity of antitumour CD8(+) T cells in melanoma. *Nature,* 596**,** 119-125.

OLLIVIER, L., ORIONE, C., BORE, P., MISERY, L., LEGOUPIL, D., LECLERE, J. C., COSTE, A., GIRAULT, G., SICARD-CRAS, I., KACPEREK, C., LUCIA, F., STEFAN, D., THILLAYS, F., RIO, E., LESUEUR, P., BERTHOU, C., HEYMANN, D., CHAMPIAT, S., SUPIOT, S., VAUGIER, L. & KAO, W. 2022. Abscopal Response in Metastatic Melanoma: Real-World Data of a Retrospective, Multicenter Study. *Cancers (Basel),* 14**,** 4213.

ONKEN, M. D., EHLERS, J. P., WORLEY, L. A., MAKITA, J., YOKOTA, Y. & HARBOUR, J. W. 2006. Functional gene expression analysis uncovers phenotypic switch in aggressive uveal melanomas. *Cancer Res,* 66**,** 4602-9.

PAN, Y., YANG, W., TANG, B., WANG, X., ZHANG, Q., LI, W. & LI, L. 2023. The protective and pathogenic role of Th17 cell plasticity and function in the tumor microenvironment. *Front Immunol,* 14**,** 1192303.

PARK, B. C., NARAYANAN, S., GAVRALDIS, A., YE, F., FAN, R., SULLIVAN, R. J., BOLAND, G., REYNOLDS, K. L., BALKO, J. M., CARLINO, M. S., LONG, G. V., ZUBIRI, L., MENZIES, A. M. & JOHNSON, D. B. 2023. Rare immune-related adverse events in patients with melanoma: incidence, spectrum, and clinical presentations. *Oncoimmunology,* 12**,** 2188719.

PARK, S. L., BUZZAI, A., RAUTELA, J., HOR, J. L., HOCHHEISER, K., EFFERN, M., MCBAIN, N., WAGNER, T., EDWARDS, J., MCCONVILLE, R., WILMOTT, J. S., SCOLYER, R. A., TÜTING, T., PALENDIRA, U., GYORKI, D., MUELLER, S. N., HUNTINGTON, N. D., BEDOUI, S., HÖLZEL, M., MACKAY, L. K., WAITHMAN, J. & GEBHARDT, T. 2019. Tissue-resident memory CD8(+) T cells promote melanoma-immune equilibrium in skin. *Nature,* 565**,** 366-371.

PARODI, M., PEDRAZZI, M., CANTONI, C., AVERNA, M., PATRONE, M., CAVALETTO, M., SPERTINO, S., PENDE, D., BALSAMO, M., PIETRA, G., SIVORI, S., CARLOMAGNO, S., MINGARI, M. C., MORETTA, L., SPARATORE, B. & VITALE, M. 2015. Natural Killer (NK)/melanoma cell interaction induces NK-mediated release of chemotactic High Mobility Group Box-1 (HMGB1) capable of amplifying NK cell recruitment. *Oncoimmunology,* 4**,** e1052353.

PATEL, S. P., OTHUS, M., CHEN, Y., WRIGHT, G. P., JR., YOST, K. J., HYNGSTROM, J. R., HU-LIESKOVAN, S., LAO, C. D., FECHER, L. A., TRUONG, T. G., EISENSTEIN, J. L., CHANDRA, S., SOSMAN, J. A., KENDRA, K. L., WU, R. C., DEVOE, C. E., DEUTSCH, G. B., HEGDE, A., KHALIL, M., MANGLA, A., REESE, A. M., ROSS, M. I., POKLEPOVIC, A. S., PHAN, G. Q., ONITILO, A. A., YASAR, D. G., POWERS, B. C., DOOLITTLE, G. C., IN, G. K., KOKOT, N., GIBNEY, G. T., ATKINS, M. B., SHAHEEN, M., WARNEKE, J. A., IKEGUCHI, A., NAJERA, J. E., CHMIELOWSKI, B., CROMPTON, J. G., FLOYD, J. D., HSUEH, E., MARGOLIN, K. A., CHOW, W. A., GROSSMANN, K. F., DIETRICH, E., PRIETO, V. G., LOWE, M. C., BUCHBINDER, E. I., KIRKWOOD, J. M., KORDE, L., MOON, J., SHARON, E., SONDAK, V. K. & RIBAS, A. 2023. Neoadjuvant-Adjuvant or Adjuvant-Only Pembrolizumab in Advanced Melanoma. *N Engl J Med,* 388**,** 813-823.

PATRINELY, J. R., JR., JOHNSON, R., LAWLESS, A. R., BHAVE, P., SAWYERS, A., DIMITROVA, M., YEOH, H. L., PALMERI, M., YE, F., FAN, R., DAVIS, E. J., RAPISUWON, S., LONG, G. V., HAYDON, A., OSMAN, I., MEHNERT, J. M., CARLINO, M. S., SULLIVAN, R. J., MENZIES, A. M. & JOHNSON, D. B. 2021. Chronic Immune-Related Adverse Events Following Adjuvant Anti-PD-1 Therapy for High-risk Resected Melanoma. *JAMA Oncol,* 7**,** 744-748.

PAULIN, D., LILIENBAUM, A., KARDJIAN, S., AGBULUT, O. & LI, Z. 2022. Vimentin: Regulation and pathogenesis. *Biochimie,* 197**,** 96-112.

PETERS COUTO, B. Z., ROBERTSON, N., PATRICK, E. & GHAZANFAR, S. 2023. MoleculeExperiment enables consistent infrastructure for molecule-resolved spatial omics data in bioconductor. *Bioinformatics,* 39**,** btad550.

PETRICEVIC, S. J., PAVLOVIC, A., CAPKUN, V., BECIC, K. & DURDOV, M. G. 2017. Cathepsin K expression in melanoma is associated with metastases. *Histol Histopathol,* 32**,** 711-716.

PETUKHOV, V., XU, R. J., SOLDATOV, R. A., CADINU, P., KHODOSEVICH, K., MOFFITT, J. R. & KHARCHENKO, P. V. 2022. Cell segmentation in imaging-based spatial transcriptomics. *Nature Biotechnology,* 40**,** 345-354.

PHILLIPS, D., MATUSIAK, M., GUTIERREZ, B. R., BHATE, S. S., BARLOW, G. L., JIANG, S., DEMETER, J., SMYTHE, K. S., PIERCE, R. H., FLING, S. P., RAMCHURREN, N., CHEEVER, M. A., GOLTSEV, Y., WEST, R. B., KHODADOUST, M. S., KIM, Y. H., SCHÜRCH, C. M. & NOLAN, G. P. 2021. Immune cell topography predicts response to PD-1 blockade in cutaneous T cell lymphoma. *Nat Commun,* 12**,** 6726.

PIMENTEL, M. A. 2020. Comment on "racial limitations of fitzpatrick skin type". *Cutis,* 105**,** 319-320.

PINTO-PAZ, M. E., COTRINA-CONCHA, J. M. & BENITES-ZAPATA, V. A. 2021. Mortality in cutaneous malignant melanoma and its association with Neutrophil-to-Lymphocyte ratio. *Cancer Treatment and Research Communications,* 29**,** 100464.

PONCETTE, L., BLUHM, J. & BLANKENSTEIN, T. 2022. The role of CD4 T cells in rejection of solid tumors. *Curr Opin Immunol,* 74**,** 18-24.

POPOVIC, A. & TARTARE-DECKERT, S. 2022. Role of extracellular matrix architecture and signaling in melanoma therapeutic resistance. *Front Oncol,* 12**,** 924553.

POSTOW, M. A., CALLAHAN, M. K., BARKER, C. A., YAMADA, Y., YUAN, J., KITANO, S., MU, Z., RASALAN, T., ADAMOW, M., RITTER, E., SEDRAK, C., JUNGBLUTH, A. A., CHUA, R., YANG, A. S., ROMAN, R. A., ROSNER, S., BENSON, B., ALLISON, J. P., LESOKHIN, A. M., GNJATIC, S. & WOLCHOK, J. D. 2012. Immunologic correlates of the abscopal effect in a patient with melanoma. *N Engl J Med,* 366**,** 925-31.

POZNIAK, J., PEDRI, D., LANDELOOS, E., VAN HERCK, Y., ANTORANZ, A., VANWYNSBERGHE, L., NOWOSAD, A., RODA, N., MAKHZAMI, S., BERVOETS, G., MACIEL, L. F., PULIDO-VICUÑA, C. A., POLLARIS, L., SEURINCK, R., ZHAO, F., FLEM-KARLSEN, K., DAMSKY, W., CHEN, L., KARAGIANNI, D., CINQUE, S., KINT, S., VANDEREYKEN, K., ROMBAUT, B., VOET, T., VERNAILLEN, F., ANNAERT, W., LAMBRECHTS, D., BOECXSTAENS, V., SAEYS, Y., VAN DEN OORD, J., BOSISIO, F., KARRAS, P., SHAIN, A. H., BOSENBERG, M., LEUCCI, E., PASCHEN, A., RAMBOW, F., BECHTER, O. & MARINE, J. C. 2024. A TCF4-dependent gene regulatory network confers resistance to immunotherapy in melanoma. *Cell,* 187**,** 166-183.e25.

PROIETTO, M., CRIPPA, M., DAMIANI, C., PASQUALE, V., SACCO, E., VANONI, M. & GILARDI, M. 2023. Tumor heterogeneity: preclinical models, emerging technologies, and future applications. *Front Oncol,* 13**,** 1164535.

QENDRO, V., LUNDGREN, D. H., REZAUL, K., MAHONY, F., FERRELL, N., BI, A., LATIFI, A., CHOWDHURY, D., GYGI, S., HAAS, W., WILSON, L., MURPHY, M. & HAN, D. K. 2014. Large-scale proteomic characterization of melanoma expressed proteins reveals nestin and vimentin as biomarkers that can potentially distinguish melanoma subtypes. *J Proteome Res,* 13**,** 5031-40.

QIAN, B. Z. & POLLARD, J. W. 2010. Macrophage diversity enhances tumor progression and metastasis. *Cell,* 141**,** 39-51.

QUINTANILLA-DIECK, M. J., CODRIANSKY, K., KEADY, M., BHAWAN, J. & RÜNGER, T. M. 2008. Cathepsin K in melanoma invasion. *J Invest Dermatol,* 128**,** 2281-8.

RADEMACHER, A., HUSEYNOV, A., BORTOLOMEAZZI, M., WILLE, S. J., SCHUMACHER, S., SANT, P., KEITEL, D., OKONECHNIKOV, K., GHASEMI, D. R., PAJTLER, K. W., MALLM, J.-P. & RIPPE, K. 2024. Comparison of spatial transcriptomics technologies using tumor cryosections. *bioRxiv***,** 2024.04.03.586404.

RAHIMI, N., REZAZADEH, K., MAHONEY, J. E., HARTSOUGH, E. & MEYER, R. D. 2012. Identification of IGPR-1 as a novel adhesion molecule involved in angiogenesis. *Mol Biol Cell,* 23**,** 1646-56.

RAHNEA-NITA, R. A., REBEGEA, L. F., TOMA, R. V., MOCANU, H., SOARE, I., MIHAILOV, R., NECHIFOR, A., GULICIUC, M., CONSTANTIN, G. B. & RAHNEA-NITA, G. 2024. Immunotherapy Combined with Radiation in Malignant Melanoma without BRAF Mutations Brain Metastases-Favorable Response after Immunotherapy Continued beyond Progression. *J Pers Med,* 14**,** 86.

RAJ, A., VAN DEN BOGAARD, P., RIFKIN, S. A., VAN OUDENAARDEN, A. & TYAGI, S. 2008. Imaging individual mRNA molecules using multiple singly labeled probes. *Nat Methods,* 5**,** 877-9.

RAJABI, P., KARIMIAN, P. & HEIDARPOUR, M. 2012. The relationship between MDM2 expression and tumor thickness and invasion in primary cutaneous malignant melanoma. *J Res Med Sci,* 17**,** 452-5.

RANNIKKO, J. H. & HOLLMÉN, M. 2024. Clinical landscape of macrophage-reprogramming cancer immunotherapies. *Br J Cancer,* 131**,** 627-640.

RASKIN, L., FULLEN, D. R., GIORDANO, T. J., THOMAS, D. G., FROHM, M. L., CHA, K. B., AHN, J., MUKHERJEE, B., JOHNSON, T. M. & GRUBER, S. B. 2013. Transcriptome profiling identifies HMGA2 as a biomarker of melanoma progression and prognosis. *J Invest Dermatol,* 133**,** 2585-2592.

RATNAYAKE, G., REINWALD, S., EDWARDS, J., WONG, N., YU, D., WARD, R., SMITH, R., HAYDON, A., AU, P. M., VAN ZELM, M. C. & SENTHI, S. 2022. Blood T-cell profiling in metastatic melanoma patients as a marker for response to immune checkpoint inhibitors combined with radiotherapy. *Radiother Oncol,* 173**,** 299-305.

RAUFASTE-CAZAVIEILLE, V., SANTIAGO, R. & DROIT, A. 2022. Multi-omics analysis: Paving the path toward achieving precision medicine in cancer treatment and immuno-oncology. *Front Mol Biosci,* 9**,** 962743.

RAZAVI, A., KESHAVARZ-FATHI, M., PAWELEK, J. & REZAEI, N. 2021. Chimeric antigen receptor T-cell therapy for melanoma. *Expert Rev Clin Immunol,* 17**,** 209-223.

REIJERS, I. L. M., MENZIES, A. M., VAN AKKOOI, A. C. J., VERSLUIS, J. M., VAN DEN HEUVEL, N. M. J., SAW, R. P. M., PENNINGTON, T. E., KAPITEIJN, E., VAN DER VELDT, A. A. M., SUIJKERBUIJK, K. P. M., HOSPERS, G. A. P., ROZEMAN, E. A., KLOP, W. M. C., VAN HOUDT, W. J., SIKORSKA, K., VAN DER HAGE, J. A., GRÜNHAGEN, D. J., WOUTERS, M. W., WITKAMP, A. J., ZUUR, C. L., LIJNSVELT, J. M., TORRES ACOSTA, A., GRIJPINK-ONGERING, L. G., GONZALEZ, M., JÓŹWIAK, K., BIERMAN, C., SHANNON, K. F., CH'NG, S., COLEBATCH, A. J., SPILLANE, A. J., HAANEN, J., RAWSON, R. V., VAN DE WIEL, B. A., VAN DE POLL-FRANSE, L. V., SCOLYER, R. A., BOEKHOUT, A. H., LONG, G. V. & BLANK, C. U. 2022. Personalized response-directed surgery and adjuvant therapy after neoadjuvant ipilimumab and nivolumab in high-risk stage III melanoma: the PRADO trial. *Nat Med,* 28**,** 1178-1188.

REMM, F., FRANZ, W. M. & BRENNER, C. 2016. Gliptins and their target dipeptidyl peptidase 4: implications for the treatment of vascular disease. *Eur Heart J Cardiovasc Pharmacother,* 2**,** 185-93.

ROBERT, C. & GAUTHERET, D. 2022. Multi-omics prediction in melanoma immunotherapy: A new brick in the wall. *Cancer Cell,* 40**,** 14-16.

ROBINSON, J. P., OSTAFE, R., IYENGAR, S. N., RAJWA, B. & FISCHER, R. 2023. Flow Cytometry: The Next Revolution. *Cells,* 12**,** 1875.

RODGERS, C. B., MUSTARD, C. J., MCLEAN, R. T., HUTCHISON, S. & PRITCHARD, A. L. 2022. A B-cell or a key player? The different roles of B-cells and antibodies in melanoma. *Pigment Cell Melanoma Res,* 35**,** 303-319.

RODRIGUEZ-ACEVEDO, A. J., GREEN, A. C., SINCLAIR, C., VAN DEVENTER, E. & GORDON, L. G. 2020. Indoor tanning prevalence after the International Agency for Research on Cancer statement on carcinogenicity of artificial tanning devices: systematic review and meta-analysis. *Br J Dermatol,* 182**,** 849-859.

RODRÍGUEZ-LOSADA, N., DE LA ROSA, J., LARRIVA, M., WENDELBO, R., AGUIRRE, J. A., CASTRESANA, J. S. & BALLAZ, S. J. 2020. Overexpression of alpha-synuclein promotes both cell proliferation and cell toxicity in human SH-SY5Y neuroblastoma cells. *J Adv Res,* 23**,** 37-45.

ROGERS, S. J., PURIC, E., EBERLE, B., DATTA, N. R. & BODIS, S. B. 2019. Radiotherapy for Melanoma: More than DNA Damage. *Dermatol Res Pract,* 2019**,** 9435389.

ROMANO, V., BELVISO, I., VENUTA, A., RUOCCO, M. R., MASONE, S., ALIOTTA, F., FIUME, G., MONTAGNANI, S., AVAGLIANO, A. & ARCUCCI, A. 2021. Influence of Tumor Microenvironment and Fibroblast Population Plasticity on Melanoma Growth, Therapy Resistance and Immunoescape. *Int J Mol Sci,* 22**,** 5283.

ROSENBAUM, S. R., KNECHT, M., MOLLAEE, M., ZHONG, Z., ERKES, D. A., MCCUE, P. A., CHERVONEVA, I., BERGER, A. C., LO, J. A., FISHER, D. E., GERSHENWALD, J. E., DAVIES, M. A., PURWIN, T. J. & APLIN, A. E. 2020. FOXD3 Regulates VISTA Expression in Melanoma. *Cell Rep,* 30**,** 510-524.e6.

ROUSSEL, M., FERRELL, P. B., JR., GREENPLATE, A. R., LHOMME, F., LE GALLOU, S., DIGGINS, K. E., JOHNSON, D. B. & IRISH, J. M. 2017. Mass cytometry deep phenotyping of human mononuclear phagocytes and myeloid-derived suppressor cells from human blood and bone marrow. *J Leukoc Biol,* 102**,** 437-447.

ROVIRA, J., RENNER, P., SABET-BAKTACH, M., EGGENHOFER, E., KOEHL, G. E., LANTOW, M., LANG, S. A., SCHLITT, H. J., CAMPISTOL, J. M., GEISSLER, E. K. & KROEMER, A. 2016. Cyclosporine A Inhibits the T-bet-Dependent Antitumor Response of CD8(+) T Cells. *Am J Transplant,* 16**,** 1139-47.

RUGGIERI, A. N., YARCHOAN, M., GOYAL, S., LIU, Y., SHARON, E., CHEN, H. X., OLSON, B. M., PAULOS, C. M., EL-RAYES, B. F., MAITHEL, S. K., AZAD, N. S. & LESINSKI, G. B. 2022. Combined MEK/PD-L1 Inhibition Alters Peripheral Cytokines and Lymphocyte Populations Correlating with Improved Clinical Outcomes in Advanced Biliary Tract Cancer. *Clin Cancer Res,* 28**,** 4336-4345.

SAGINALA, K., BARSOUK, A., ALURU, J. S., RAWLA, P. & BARSOUK, A. 2021. Epidemiology of Melanoma. *Med Sci (Basel),* 9**,** 63.

SAIAG, P., MOLINIER, R., ROGER, A., BORU, B., OTMEZGUINE, Y., OTZ, J., VALERY, C. A., BLOM, A., LONGVERT, C., BEAUCHET, A. & FUNCK-BRENTANO, E. 2022. Efficacy of Large Use of Combined Hypofractionated Radiotherapy in a Cohort of Anti-PD-1 Monotherapy-Treated Melanoma Patients. *Cancers (Basel),* 14**,** 4069.

SAITO, Y., KOMORI, S., KOTANI, T., MURATA, Y. & MATOZAKI, T. 2022. The Role of Type-2 Conventional Dendritic Cells in the Regulation of Tumor Immunity. *Cancers (Basel),* 14**,** 1976.

SALAS, S. M., CZARNEWSKI, P., KUEMMERLE, L. B., HELGADOTTIR, S., MATSSON-LANGSETH, C., TISMEYER, S., AVENEL, C., REHMAN, H., TIKLOVA, K., ANDERSSON, A., CHATZINIKOLAOU, M., THEIS, F. J., LUECKEN, M. D., WÄHLBY, C., ISHAQUE, N. & NILSSON, M. 2023. Optimizing Xenium In Situ data utility by quality assessment and best practice analysis workflows. *bioRxiv***,** 2023.02.13.528102.

SALERNO, E. P., BEDOGNETTI, D., MAULDIN, I. S., DEACON, D. H., SHEA, S. M., PINCZEWSKI, J., OBEID, J. M., COUKOS, G., WANG, E., GAJEWSKI, T. F., MARINCOLA, F. M. & SLINGLUFF, C. L., JR. 2016. Human melanomas and ovarian cancers overexpressing mechanical barrier molecule genes lack immune signatures and have increased patient mortality risk. *Oncoimmunology,* 5**,** e1240857.

SANDRI, S., HEBEDA, C. B., BROERING, M. F., DE PAULA SILVA, M., MOREDO, L. F., DE BARROS, E. S. M. J., SAPATA MOLINA, A., LOPES PINTO, C. A., DUPRAT NETO, J. P., REUTELINGSPERGER, C. P., GIL, C. D. & FARSKY, S. H. P. 2023. Role of Annexin A1 Secreted by Neutrophils in Melanoma Metastasis. *Cells,* 12**,** 425.

SANTHOSH, S. & SANTHOSH SIVAJOTHI, E. S. S. B. W. F. F. E. T. C. 2024. FFPE Tissue Processing for Multimodal Imaging Assays (Phenocycler-Fusion + H&E) following Xenium In Situ Gene Expression. *protocols.io*.

SCHEDEL, F., MAYER-HAIN, S., PAPPELBAUM, K. I., METZE, D., STOCK, M., GOERGE, T., LOSER, K., SUNDERKÖTTER, C., LUGER, T. A. & WEISHAUPT, C. 2020. Evidence and impact of neutrophil extracellular traps in malignant melanoma. *Pigment Cell Melanoma Res,* 33**,** 63-73.

SCHOENFELD, J. D., MAHADEVAN, A., FLOYD, S. R., DYER, M. A., CATALANO, P. J., ALEXANDER, B. M., MCDERMOTT, D. F. & KAPLAN, I. D. 2015. Ipilmumab and cranial radiation in metastatic melanoma patients: a case series and review. *J Immunother Cancer,* 3**,** 50.

SCHONFELD, S. J., TUCKER, M. A., ENGELS, E. A., DORES, G. M., SAMPSON, J. N., SHIELS, M. S., CHANOCK, S. J. & MORTON, L. M. 2022. Immune-Related Adverse Events After Immune Checkpoint Inhibitors for Melanoma Among Older Adults. *JAMA Netw Open,* 5**,** e223461.

SCHWARTZ, L. H., LITIÈRE, S., DE VRIES, E., FORD, R., GWYTHER, S., MANDREKAR, S., SHANKAR, L., BOGAERTS, J., CHEN, A., DANCEY, J., HAYES, W., HODI, F. S., HOEKSTRA, O. S., HUANG, E. P., LIN, N., LIU, Y., THERASSE, P., WOLCHOK, J. D. & SEYMOUR, L. 2016. RECIST 1.1-Update and clarification: From the RECIST committee. *Eur J Cancer,* 62**,** 132-7.

SCHWARZE, J. K., TIJTGAT, J., AWADA, G., CRAS, L., VASATURO, A., BAGNALL, C., FORSYTH, R., DUFAIT, I., TUYAERTS, S., VAN RIET, I. & NEYNS, B. 2022. Intratumoral administration of CD1c (BDCA-1)(+) and CD141 (BDCA-3)(+) myeloid dendritic cells in combination with talimogene laherparepvec in immune checkpoint blockade refractory advanced melanoma patients: a phase I clinical trial. *J Immunother Cancer,* 10**,** e005141.

SEE, P., DUTERTRE, C. A., CHEN, J., GÜNTHER, P., MCGOVERN, N., IRAC, S. E., GUNAWAN, M., BEYER, M., HÄNDLER, K., DUAN, K., SUMATOH, H. R. B., RUFFIN, N., JOUVE, M., GEA-MALLORQUÍ, E., HENNEKAM, R. C. M., LIM, T., YIP, C. C., WEN, M., MALLERET, B., LOW, I., SHADAN, N. B., FEN, C. F. S., TAY, A., LUM, J., ZOLEZZI, F., LARBI, A., POIDINGER, M., CHAN, J. K. Y., CHEN, Q., RÉNIA, L., HANIFFA, M., BENAROCH, P., SCHLITZER, A., SCHULTZE, J. L., NEWELL, E. W. & GINHOUX, F. 2017. Mapping the human DC

lineage through the integration of high-dimensional techniques. *Science,* 356**,** eaag3009.

SEYMOUR, L., BOGAERTS, J., PERRONE, A., FORD, R., SCHWARTZ, L. H., MANDREKAR, S., LIN, N. U., LITIÈRE, S., DANCEY, J., CHEN, A., HODI, F. S., THERASSE, P., HOEKSTRA, O. S., SHANKAR, L. K., WOLCHOK, J. D., BALLINGER, M., CARAMELLA, C. & DE VRIES, E. G. E. 2017. iRECIST: guidelines for response criteria for use in trials testing immunotherapeutics. *Lancet Oncol,* 18**,** e143-e152.

SHAHBAZ, S., DUNSMORE, G., KOLEVA, P., XU, L., HOUSTON, S. & ELAHI, S. 2020. Galectin-9 and VISTA Expression Define Terminally Exhausted T Cells in HIV-1 Infection. *J Immunol,* 204**,** 2474-2491.

SHAHBAZ, S., XU, L., SLIGL, W., OSMAN, M., BOZORGMEHR, N., MASHHOURI, S., REDMOND, D., PEREZ ROSERO, E., WALKER, J. & ELAHI, S. 2021. The Quality of SARS-CoV-2-Specific T Cell Functions Differs in Patients with Mild/Moderate versus Severe Disease, and T Cells Expressing Coinhibitory Receptors Are Highly Activated. *J Immunol,* 207**,** 1099-1111.

SHARABI, A. B., NIRSCHL, C. J., KOCHEL, C. M., NIRSCHL, T. R., FRANCICA, B. J., VELARDE, E., DEWEESE, T. L. & DRAKE, C. G. 2015. Stereotactic Radiation Therapy Augments Antigen-Specific PD-1-Mediated Antitumor Immune Responses via Cross-Presentation of Tumor Antigen. *Cancer Immunol Res,* 3**,** 345-55.

SHEKARI, N., SHANEHBANDI, D., KAZEMI, T., ZARREDAR, H., BARADARAN, B. & JALALI, S. A. 2023. VISTA and its ligands: the next generation of promising therapeutic targets in immunotherapy. *Cancer Cell Int,* 23**,** 265.

SHEKOOHI, S., RAJASEKARAN, S., PATEL, D., YANG, S., LIU, W., HUANG, S., YU, X. & WITT, S. N. 2021. Knocking out alpha-synuclein in melanoma cells dysregulates cellular iron metabolism and suppresses tumor growth. *Sci Rep,* 11**,** 5267.

SHI, L. Z., WANG, R., HUANG, G., VOGEL, P., NEALE, G., GREEN, D. R. & CHI, H. 2011. HIF1alpha-dependent glycolytic pathway orchestrates a metabolic checkpoint for the differentiation of TH17 and Treg cells. *J Exp Med,* 208**,** 1367-76.

SIEVERT, C. 2020. Interactive web-based data visualization with R, plotly, and shiny. Boca Ranton, Florida: CRC Press.

SINGH, Y., TRAUTWEIN, C., ROMANI, J., SALKER, M. S., NECKEL, P. H., FRACCAROLI, I., ABEDITASHI, M., WOERNER, N., ADMARD, J., DHARIWAL, A., DUEHOLM, M. K. D., SCHÄFER, K.-H., LANG, F., OTZEN, D. E., LASHUEL, H. A., RIESS, O. & CASADEI, N. 2023. Overexpression of human alpha-Synuclein leads to dysregulated microbiome/metabolites with ageing in a rat model of Parkinson disease. *Molecular Neurodegeneration,* 18**,** 44.

SMALLEY, I., KIM, E., LI, J., SPENCE, P., WYATT, C. J., EROGLU, Z., SONDAK, V. K., MESSINA, J. L., BABACAN, N. A., MARIA-ENGLER, S. S., DE ARMAS, L., WILLIAMS, S. L., GATENBY, R. A., CHEN, Y. A., ANDERSON, A. R. A. & SMALLEY, K. S. M. 2019. Leveraging transcriptional dynamics to improve BRAF inhibitor responses in melanoma. *EBioMedicine,* 48**,** 178-190.

SMITH, S. L., DAMATO, B. E., SCHOLES, A. G., NUNN, J., FIELD, J. K. & HEIGHWAY, J. 2002. Decreased endothelin receptor B expression in large primary uveal melanomas is associated with early clinical metastasis and short survival. *Br J Cancer,* 87**,** 1308-13.

SONG, K. Y., DESAR, S., PENGO, T., SHANLEY, R. & GIUBELLINO, A. 2020. Correlation of MET and PD-L1 Expression in Malignant Melanoma. *Cancers (Basel),* 12**,** 1847.

SORIN, M., REZANEJAD, M., KARIMI, E., FISET, B., DESHARNAIS, L., PERUS, L. J. M., MILETTE, S., YU, M. W., MARITAN, S. M., DORÉ, S., PICHETTE, É.,

ENLOW, W., GAGNÉ, A., WEI, Y., ORAIN, M., MANEM, V. S. K., RAYES, R., SIEGEL, P. M., CAMILLERI-BROËT, S., FISET, P. O., DESMEULES, P., SPICER, J. D., QUAIL, D. F., JOUBERT, P. & WALSH, L. A. 2023. Single-cell spatial landscapes of the lung tumour immune microenvironment. *Nature,* 614**,** 548-554.

SPAAS, M., SUNDAHL, N., KRUSE, V., ROTTEY, S., DE MAESENEER, D., DUPREZ, F., LIEVENS, Y., SURMONT, V., BROCHEZ, L., REYNDERS, D., DANCKAERT, W., GOETGHEBEUR, E., VAN DEN BEGIN, R., VAN GESTEL, D., RENARD, V., DIRIX, P. & OST, P. 2023. Checkpoint Inhibitors in Combination With Stereotactic Body Radiotherapy in Patients With Advanced Solid Tumors: The CHEERS Phase 2 Randomized Clinical Trial. *JAMA Oncol,* 9**,** 1205-1213.

SPARKS, A., DAYAL, S., DAS, J., ROBERTSON, P., MENENDEZ, S. & SAVILLE, M. K. 2014. The degradation of p53 and its major E3 ligase Mdm2 is differentially dependent on the proteasomal ubiquitin receptor S5a. *Oncogene,* 33**,** 4685-96.

SPEISER, D. E., CHIJIOKE, O., SCHAEUBLE, K. & MÜNZ, C. 2023. CD4+ T cells in cancer. *Nature Cancer,* 4**,** 317-329.

SPERANDIO, M., SMITH, M. L., FORLOW, S. B., OLSON, T. S., XIA, L., MCEVER, R. P. & LEY, K. 2003. P-selectin glycoprotein ligand-1 mediates L-selectin-dependent leukocyte rolling in venules. *J Exp Med,* 197**,** 1355-63.

STACK, E. C., WANG, C., ROMAN, K. A. & HOYT, C. C. 2014. Multiplexed immunohistochemistry, imaging, and quantitation: a review, with an assessment of Tyramide signal amplification, multispectral imaging and multiplex analysis. *Methods,* 70**,** 46-58.

STEINERT, E. M., SCHENKEL, J. M., FRASER, K. A., BEURA, L. K., MANLOVE, L. S., IGYÁRTÓ, B. Z., SOUTHERN, P. J. & MASOPUST, D. 2015. Quantifying Memory CD8 T Cells Reveals Regionalization of Immunosurveillance. *Cell,* 161**,** 737-49.

STEPPERT, C., KRUGMANN, J. & STERLACCI, W. 2020. Simultaneous endocrine expression and loss of melanoma markers in malignant melanoma metastases, a retrospective analysis. *Pathol Oncol Res,* 26**,** 1777-1779.

STIRLING, D. R., SWAIN-BOWDEN, M. J., LUCAS, A. M., CARPENTER, A. E., CIMINI, B. A. & GOODMAN, A. 2021. CellProfiler 4: improvements in speed, utility and usability. *BMC Bioinformatics,* 22**,** 433.

SUNDAHL, N., SEREMET, T., VAN DORPE, J., NEYNS, B., FERDINANDE, L., MEIRESON, A., BROCHEZ, L., KRUSE, V. & OST, P. 2019. Phase 2 Trial of Nivolumab Combined With Stereotactic Body Radiation Therapy in Patients With Metastatic or Locally Advanced Inoperable Melanoma. *Int J Radiat Oncol Biol Phys,* 104**,** 828-835.

SWITZER, B., PUZANOV, I., SKITZKI, J. J., HAMAD, L. & ERNSTOFF, M. S. 2022. Managing Metastatic Melanoma in 2022: A Clinical Review. *JCO Oncol Pract,* 18**,** 335-351.

SZTILLER-SIKORSKA, M., HARTMAN, M. L., TALAR, B., JAKUBOWSKA, J., ZALESNA, I. & CZYZ, M. 2015. Phenotypic diversity of patient-derived melanoma populations in stem cell medium. *Laboratory Investigation,* 95**,** 672-683.

TAGUCHI, K., ONOE, T., YOSHIDA, T., YAMASHITA, Y., TANAKA, Y. & OHDAN, H. 2020. Tumor Endothelial Cell–Mediated Antigen-Specific T-cell Suppression via the PD-1/PD-L1 Pathway. *Molecular Cancer Research,* 18**,** 1427-1440.

TALEGHAMAR, H., JALALIFAR, S. A., CZARNOTA, G. J. & SADEGHI-NAINI, A. 2022. Deep learning of quantitative ultrasound multi-parametric images at pre-treatment to predict breast cancer response to chemotherapy. *Sci Rep,* 12**,** 2244.

TAN, L. Y., COCKSHELL, M. P., MOORE, E., MYO MIN, K. K., ORTIZ, M., JOHAN, M. Z., EBERT, B., RUSZKIEWICZ, A., BROWN, M. P., EBERT, L. M. & BONDER, C.

S. 2022. Vasculogenic mimicry structures in melanoma support the recruitment of monocytes. *Oncoimmunology,* 11**,** 2043673.

TAN, W. C. C., NERURKAR, S. N., CAI, H. Y., NG, H. H. M., WU, D., WEE, Y. T. F., LIM, J. C. T., YEONG, J. & LIM, T. K. H. 2020. Overview of multiplex immunohistochemistry/immunofluorescence techniques in the era of cancer immunotherapy. *Cancer Commun (Lond),* 40**,** 135-153.

TANG, C., WELSH, J. W., DE GROOT, P., MASSARELLI, E., CHANG, J. Y., HESS, K. R., BASU, S., CURRAN, M. A., CABANILLAS, M. E., SUBBIAH, V., FU, S., TSIMBERIDOU, A. M., KARP, D., GOMEZ, D. R., DIAB, A., KOMAKI, R., HEYMACH, J. V., SHARMA, P., NAING, A. & HONG, D. S. 2017. Ipilimumab with Stereotactic Ablative Radiation Therapy: Phase I Results and Immunologic Correlates from Peripheral T Cells. *Clin Cancer Res,* 23**,** 1388-1396.

TAUBE, J. M., AKTURK, G., ANGELO, M., ENGLE, E. L., GNJATIC, S., GREENBAUM, S., GREENWALD, N. F., HEDVAT, C. V., HOLLMANN, T. J., JUCO, J., PARRA, E. R., REBELATTO, M. C., RIMM, D. L., RODRIGUEZ-CANALES, J., SCHALPER, K. A., STACK, E. C., FERREIRA, C. S., KORSKI, K., LAKO, A., RODIG, S. J., SCHENCK, E., STEELE, K. E., SURACE, M. J., TETZLAFF, M. T., VON LOGA, K., WISTUBA, I. I. & BIFULCO, C. B. 2020. The Society for Immunotherapy of Cancer statement on best practices for multiplex immunohistochemistry (IHC) and immunofluorescence (IF) staining and validation. *Journal for ImmunoTherapy of Cancer,* 8**,** e000155.

TAUTZ, D. & PFEIFLE, C. 1989. A non-radioactive in situ hybridization method for the localization of specific RNAs in Drosophila embryos reveals translational control of the segmentation gene hunchback. *Chromosoma,* 98**,** 81-5.

TAWBI, H. A., FORSYTH, P. A., HODI, F. S., ALGAZI, A. P., HAMID, O., LAO, C. D., MOSCHOS, S. J., ATKINS, M. B., LEWIS, K., POSTOW, M. A., THOMAS, R. P., GLASPY, J., JANG, S., KHUSHALANI, N. I., PAVLICK, A. C., ERNSTOFF, M. S., REARDON, D. A., KUDCHADKAR, R., TARHINI, A., CHUNG, C., RITCHINGS, C., DURANI, P., ASKELSON, M., PUZANOV, I. & MARGOLIN, K. A. 2021. Long-term outcomes of patients with active melanoma brain metastases treated with combination nivolumab plus ipilimumab (CheckMate 204): final results of an open-label, multicentre, phase 2 study. *Lancet Oncol,* 22**,** 1692-1704.

TAYLOR, J., GANDHI, A., GRAY, E. & ZAENKER, P. 2022. Checkpoint inhibitor immune-related adverse events: A focused review on autoantibodies and B cells as biomarkers, advancements and future possibilities. *Front Immunol,* 13**,** 991433.

THAKKAR, D., PALIWAL, S., DHARMADHIKARI, B., GUAN, S., LIU, L., KAR, S., TULSIAN, N. K., GRUBER, J. J., DIMASCIO, L., PASZKIEWICZ, K. H., INGRAM, P. J. & J, D. B.-K. 2022. Rationally targeted anti-VISTA antibody that blockades the C-C' loop region can reverse VISTA immune suppression and remodel the immune microenvironment to potently inhibit tumor growth in an Fc independent manner. *J Immunother Cancer,* 10**,** e003382.

TIAN, Y., KONG, L., LI, Y., LIAO, Z., CAI, X., DENG, S., YANG, X., ZHANG, B., WANG, Y., ZHANG, Z., WU, B., WEN, L., HUANG, F., HU, Y., WAN, C., LIAO, Y., SUN, Y. & YANG, K. 2023. Dipeptidyl peptidase 4 inhibition sensitizes radiotherapy by promoting T cell infiltration. *Oncoimmunology,* 12**,** 2268257.

TINOCO, R., CARRETTE, F., BARRAZA, M. L., OTERO, D. C., MAGAÑA, J., BOSENBERG, M. W., SWAIN, S. L. & BRADLEY, L. M. 2016. PSGL-1 Is an Immune Checkpoint Regulator that Promotes T Cell Exhaustion. *Immunity,* 44**,** 1190-203.

TOIA, F., DI STEFANO, A. B., MERAVIGLIA, S., LO PRESTI, E., PIRRELLO, R., RINALDI, G., FULFARO, F., DIELI, F. & CORDOVA, A. 2019. Γδ T Cell-Based Immunotherapy in Melanoma: State of the Art. *J Oncol,* 2019**,** 9014607.

TOKI, M. I., MERRITT, C. R., WONG, P. F., SMITHY, J. W., KLUGER, H. M., SYRIGOS, K. N., ONG, G. T., WARREN, S. E., BEECHEM, J. M. & RIMM, D. L. 2019. High-Plex Predictive Marker Discovery for Melanoma Immunotherapy-Treated Patients Using Digital Spatial Profiling. *Clin Cancer Res,* 25**,** 5503-5512.

TOUSSI, A., MANS, N., WELBORN, J. & KIURU, M. 2020. Germline mutations predisposing to melanoma. *J Cutan Pathol,* 47**,** 606-616.

ULLRICH, S. E. & BYRNE, S. N. 2012. The immunologic revolution: photoimmunology. *J Invest Dermatol,* 132**,** 896-905.

VALDES-MORA, F., HANDLER, K., LAW, A. M. K., SALOMON, R., OAKES, S. R., ORMANDY, C. J. & GALLEGO-ORTEGA, D. 2018. Single-Cell Transcriptomics in Cancer Immunobiology: The Future of Precision Oncology. *Front Immunol,* 9**,** 2582.

VAN DEN BRINK, S. C., SAGE, F., VÉRTESY, Á., SPANJAARD, B., PETERSON-MADURO, J., BARON, C. S., ROBIN, C. & VAN OUDENAARDEN, A. 2017. Single-cell sequencing reveals dissociation-induced gene expression in tissue subpopulations. *Nature Methods,* 14**,** 935-936.

VAN RAVENSWAAY CLAASEN, H. H., KLUIN, P. M. & FLEUREN, G. J. 1992. Tumor infiltrating cells in human cancer. On the possible role of CD16+ macrophages in antitumor cytotoxicity. *Lab Invest,* 67**,** 166-74.

VEATCH, J. R., LEE, S. M., SHASHA, C., SINGHI, N., SZETO, J. L., MOSHIRI, A. S., KIM, T. S., SMYTHE, K., KONG, P., FITZGIBBON, M., JESERNIG, B., BHATIA, S., TYKODI, S. S., HALL, E. T., BYRD, D. R., THOMPSON, J. A., PILLARISETTY, V. G., DUHEN, T., MCGARRY HOUGHTON, A., NEWELL, E., GOTTARDO, R. & RIDDELL, S. R. 2022. Neoantigen-specific CD4(+) T cells in human melanoma have diverse differentiation states and correlate with CD8(+) T cell, macrophage, and B cell function. *Cancer Cell,* 40**,** 393-409.e9.

VEENSTRA, J., DIMITRION, P., YAO, Y., ZHOU, L., OZOG, D. & MI, Q. S. 2021. Research Techniques Made Simple: Use of Imaging Mass Cytometry for Dermatological Research and Clinical Applications. *J Invest Dermatol,* 141**,** 705-712.e1.

VERHOEVEN, J., JACOBS, K. A., RIZZOLLO, F., LODI, F., HUA, Y., POŹNIAK, J., NARAYANAN SRINIVASAN, A., HOUBAERT, D., SHANKAR, G., MORE, S., SCHAAF, M. B., DUBROJA LAKIC, N., GANNE, M., LAMOTE, J., VAN WEYENBERGH, J., BOON, L., BECHTER, O., BOSISIO, F., UCHIYAMA, Y., BERTRAND, M. J., MARINE, J. C., LAMBRECHTS, D., BERGERS, G., AGRAWAL, M. & AGOSTINIS, P. 2023. Tumor endothelial cell autophagy is a key vascular-immune checkpoint in melanoma. *EMBO Mol Med,* 15**,** e18028.

VERMA, V., CUSHMAN, T. R., TANG, C. & WELSH, J. W. 2018. Toxicity of radiation and immunotherapy combinations. *Adv Radiat Oncol,* 3**,** 506-511.

VESELY, M. D., KIDACKI, M., GAULE, P., GUPTA, S., CHAN, N. N. N., HAN, X., YEUNG, J. T. & CHEN, L. 2024. Immune Inhibitory Molecule PD-1 Homolog (VISTA) Colocalizes with CD11b Myeloid Cells in Melanoma and Is Associated with Poor Outcomes. *J Invest Dermatol,* 144**,** 106-115.e4.

VILLANI, A. C., SATIJA, R., REYNOLDS, G., SARKIZOVA, S., SHEKHAR, K., FLETCHER, J., GRIESBECK, M., BUTLER, A., ZHENG, S., LAZO, S., JARDINE, L., DIXON, D., STEPHENSON, E., NILSSON, E., GRUNDBERG, I., MCDONALD, D., FILBY, A., LI, W., DE JAGER, P. L., ROZENBLATT-ROSEN, O., LANE, A. A., HANIFFA, M., REGEV, A. & HACOHEN, N. 2017. Single-cell RNA-seq reveals new

types of human blood dendritic cells, monocytes, and progenitors. *Science,* 356**,** eaah4573.

VILLASEÑOR-CARDOSO, M. I., FRAUSTO-DEL-RÍO, D. A. & ORTEGA, E. 2013. Aminopeptidase N (CD13) is involved in phagocytic processes in human dendritic cells and macrophages. *Biomed Res Int,* 2013**,** 562984.

VIRATHAM PULSAWATDI, A., CRAIG, S. G., BINGHAM, V., MCCOMBE, K., HUMPHRIES, M. P., SENEVIRATHNE, S., RICHMAN, S. D., QUIRKE, P., CAMPO, L., DOMINGO, E., MAUGHAN, T. S., JAMES, J. A. & SALTO-TELLEZ, M. 2020. A robust multiplex immunofluorescence and digital pathology workflow for the characterisation of the tumour immune microenvironment. *Mol Oncol,* 14**,** 2384-2402.

VITALI, F., COLUCCI, R., DI PAOLA, M., PINDO, M., DE FILIPPO, C., MORETTI, S. & CAVALIERI, D. 2022. Early melanoma invasivity correlates with gut fungal and bacterial profiles. *Br J Dermatol,* 186**,** 106-116.

VON AHLFEN, S., MISSEL, A., BENDRAT, K. & SCHLUMPBERGER, M. 2007. Determinants of RNA quality from FFPE samples. *PLoS One,* 2**,** e1261.

WANG, B., OU, Z., ZHONG, W., HUANG, L., LIAO, W., SHENG, Y., GUO, Z., CHEN, J., YANG, W., CHEN, K., HUANG, X., YANG, T., LIN, T. & HUANG, J. 2023a. Effective Antitumor Immunity Can Be Triggered by Targeting VISTA in Combination with a TLR3-Specific Adjuvant. *Cancer Immunol Res,* 11**,** 1656-1670.

WANG, F., FLANAGAN, J., SU, N., WANG, L. C., BUI, S., NIELSON, A., WU, X., VO, H. T., MA, X. J. & LUO, Y. 2012. RNAscope: a novel in situ RNA analysis platform for formalin-fixed, paraffin-embedded tissues. *J Mol Diagn,* 14**,** 22-9.

WANG, H., HUANG, R., NELSON, J., GAO, C., TRAN, M., YEATON, A., FELT, K., PFAFF, K. L., BOWMAN, T., RODIG, S. J., WEI, K., GOODS, B. A. & FARHI, S. L. 2023b. Systematic benchmarking of imaging spatial transcriptomics platforms in FFPE tissues. *bioRxiv*.

WANG, J., RIEDER, S. A., WU, J., HAYES, S., HALPIN, R. A., DE LOS REYES, M., SHRESTHA, Y., KOLBECK, R. & RAJA, R. 2019. Evaluation of ultra-low input RNA sequencing for the study of human T cell transcriptome. *Scientific Reports,* 9**,** 8445.

WANG, L., GUO, W., GUO, Z., YU, J., TAN, J., SIMONS, D. L., HU, K., LIU, X., ZHOU, Q., ZHENG, Y., COLT, E. A., YIM, J., WAISMAN, J. & LEE, P. P. 2024. PD-L1-expressing tumor-associated macrophages are immunostimulatory and associate with good clinical outcome in human breast cancer. *Cell Rep Med,* 5**,** 101420.

WANG, L., WANG, S., ZHANG, J., PENG, J., CHENG, B., LI, H. & HU, Q. 2023c. Radiotherapy upregulated immune checkpoints contribute to the development of second primary OSCC. *Oral Dis,* 30**,** 2188-2201.

WARE, O. R., DAWSON, J. E., SHINOHARA, M. M. & TAYLOR, S. C. 2020. Racial limitations of fitzpatrick skin type. *Cutis,* 105**,** 77-80.

WEBER, R., FLEMING, V., HU, X., NAGIBIN, V., GROTH, C., ALTEVOGT, P., UTIKAL, J. & UMANSKY, V. 2018. Myeloid-Derived Suppressor Cells Hinder the Anti-Cancer Activity of Immune Checkpoint Inhibitors. *Front Immunol,* 9**,** 1310.

WEIDE, L. M., SCHEDEL, F. & WEISHAUPT, C. 2023. Neutrophil Extracellular Traps Correlate with Tumor Necrosis and Size in Human Malignant Melanoma Metastases. *Biology (Basel),* 12**,** 822.

WENNERBERG, E., LHUILLIER, C., VANPOUILLE-BOX, C., PILONES, K. A., GARCÍA-MARTÍNEZ, E., RUDQVIST, N. P., FORMENTI, S. C. & DEMARIA, S. 2017. Barriers to Radiation-Induced In Situ Tumor Vaccination. *Front Immunol,* 8**,** 229.

WENTHE, J., ERIKSSON, E., HELLSTRÖM, A. C., MORENO, R., ULLENHAG, G., ALEMANY, R., LÖVGREN, T. & LOSKOG, A. 2023. Immunostimulatory gene

therapy targeting CD40, 4-1BB and IL-2R activates DCs and stimulates antigen-specific T-cell and NK-cell responses in melanoma models. *J Transl Med,* 21**,** 506.

WERTHMÖLLER, N., FREY, B., RÜCKERT, M., LOTTER, M., FIETKAU, R. & GAIPL, U. S. 2016. Combination of ionising radiation with hyperthermia increases the immunogenic potential of B16-F10 melanoma cells in vitro and in vivo. *Int J Hyperthermia,* 32**,** 23-30.

WILLIAMS, C. G., LEE, H. J., ASATSUMA, T., VENTO-TORMO, R. & HAQUE, A. 2022. An introduction to spatial transcriptomics for biomedical research. *Genome Medicine,* 14**,** 68.

WILLIE, E. 2024. A Correlation Based Multiview Self Organising Maps Clustering for IMC Datasets. *Bioconductor*.

WILLSMORE, Z. N., HARRIS, R. J., CRESCIOLI, S., HUSSEIN, K., KAKKASSERY, H., THAPA, D., CHEUNG, A., CHAUHAN, J., BAX, H. J., CHENOWETH, A., LADDACH, R., OSBORN, G., MCCRAW, A., HOFFMANN, R. M., NAKAMURA, M., GEH, J. L., MACKENZIE-ROSS, A., HEALY, C., TSOKA, S., SPICER, J. F., PAPA, S., BARBER, L., LACY, K. E. & KARAGIANNIS, S. N. 2020. B Cells in Patients With Melanoma: Implications for Treatment With Checkpoint Inhibitor Antibodies. *Front Immunol,* 11**,** 622442.

WISTUBA-HAMPRECHT, K., MARTENS, A., HAEHNEL, K., GEUKES FOPPEN, M., YUAN, J., POSTOW, M. A., WONG, P., ROMANO, E., KHAMMARI, A., DRENO, B., CAPONE, M., ASCIERTO, P. A., DEMUTH, I., STEINHAGEN-THIESSEN, E., LARBI, A., SCHILLING, B., SCHADENDORF, D., WOLCHOK, J. D., BLANK, C. U., PAWELEC, G., GARBE, C. & WEIDE, B. 2016. Proportions of blood-borne Vδ1+ and Vδ2+ T-cells are associated with overall survival of melanoma patients treated with ipilimumab. *Eur J Cancer,* 64**,** 116-26.

WOLCHOK, J. D., CHIARION-SILENI, V., GONZALEZ, R., GROB, J. J., RUTKOWSKI, P., LAO, C. D., COWEY, C. L., SCHADENDORF, D., WAGSTAFF, J., DUMMER, R., FERRUCCI, P. F., SMYLIE, M., BUTLER, M. O., HILL, A., MÁRQUEZ-RODAS, I., HAANEN, J., GUIDOBONI, M., MAIO, M., SCHÖFFSKI, P., CARLINO, M. S., LEBBÉ, C., MCARTHUR, G., ASCIERTO, P. A., DANIELS, G. A., LONG, G. V., BAS, T., RITCHINGS, C., LARKIN, J. & HODI, F. S. 2022. Long-Term Outcomes With Nivolumab Plus Ipilimumab or Nivolumab Alone Versus Ipilimumab in Patients With Advanced Melanoma. *J Clin Oncol,* 40**,** 127-137.

WOLCHOK, J. D., CHIARION-SILENI, V., GONZALEZ, R., RUTKOWSKI, P., GROB, J. J., COWEY, C. L., LAO, C. D., WAGSTAFF, J., SCHADENDORF, D., FERRUCCI, P. F., SMYLIE, M., DUMMER, R., HILL, A., HOGG, D., HAANEN, J., CARLINO, M. S., BECHTER, O., MAIO, M., MARQUEZ-RODAS, I., GUIDOBONI, M., MCARTHUR, G., LEBBÉ, C., ASCIERTO, P. A., LONG, G. V., CEBON, J., SOSMAN, J., POSTOW, M. A., CALLAHAN, M. K., WALKER, D., ROLLIN, L., BHORE, R., HODI, F. S. & LARKIN, J. 2017. Overall Survival with Combined Nivolumab and Ipilimumab in Advanced Melanoma. *N Engl J Med,* 377**,** 1345-1356.

WOLFE, A. R., CHABLANI, P., SIEDOW, M. R., MILLER, E. D., WALSTON, S., KENDRA, K. L., WUTHRICK, E. & WILLIAMS, T. M. 2021. BRAF mutation correlates with worse local-regional control following radiation therapy in patients with stage III melanoma. *Radiat Oncol,* 16**,** 181.

WU, D., HACKING, S., VITKOVSKI, T. & NASIM, M. 2021. Superpixel image segmentation of VISTA expression in colorectal cancer and its relationship to the tumoral microenvironment. *Sci Rep,* 11**,** 17426.

WU, Z., LEI, K., LI, H., HE, J. & SHI, E. 2022. Transcriptome-based network analysis related to M2-like tumor-associated macrophage infiltration identified VARS1 as a potential target for improving melanoma immunotherapy efficacy. *J Transl Med,* 20**,** 489.

XIAO, L., WANG, Q. & PENG, H. 2023. Tumor-associated macrophages: new insights on their metabolic regulation and their influence in cancer immunotherapy. *Front Immunol,* 14**,** 1157291.

XIAOYAN QIAN, D. L., HSIN WEN CHANG, DANIEL GYLLBORG, KATRÍN HALLDÓRSDÓTTIR, ACE SANTIAGO, KRISTEN PHAM, JAMES PERNA, JOSH GU, IVAR KARAM, HAYATO IKOMA, PATRICK RÖLLI, PAUL RYVKIN, NEIL WEISENFELD, VERONICA GONZALEZ MUÑOZ 2024. Improved multimodal morphology-based cell segmentation for Xenium. Advances in Genome Biology and Technology Conference 2024.

XIE, L., FANG, J., YU, J., ZHANG, W., HE, Z., YE, L. & WANG, H. 2023. The role of CD4(+) T cells in tumor and chronic viral immune responses. *MedComm (2020),* 4**,** e390.

XIE, X., CHEN, C., CHEN, W., JIANG, J., WANG, L., LI, T., SUN, H. & LIU, J. 2021. Structural Basis of VSIG3: The Ligand for VISTA. *Frontiers in Immunology,* 12.

XU, X., PETERSEN, S., RODRIGUEZ, C. & YI, G. 2021. VISTA facilitates phagocytic clearance of HIV infected CEM-SS T cells. *Heliyon,* 7**,** e07496.

YAMAGUCHI, H. & SAKAI, R. 2015. Direct Interaction between Carcinoma Cells and Cancer Associated Fibroblasts for the Regulation of Cancer Invasion. *Cancers (Basel),* 7**,** 2054-62.

YAMAZAKI, T., KIRCHMAIR, A., SATO, A., BUQUÉ, A., RYBSTEIN, M., PETRONI, G., BLOY, N., FINOTELLO, F., STAFFORD, L., NAVARRO MANZANO, E., AYALA DE LA PEÑA, F., GARCÍA-MARTÍNEZ, E., FORMENTI, S. C., TRAJANOSKI, Z. & GALLUZZI, L. 2020. Mitochondrial DNA drives abscopal responses to radiation that are inhibited by autophagy. *Nat Immunol,* 21**,** 1160-1171.

YAN, K., WANG, Y., LU, Y. & YAN, Z. 2021. Coexpressed Genes That Promote the Infiltration of M2 Macrophages in Melanoma Can Evaluate the Prognosis and Immunotherapy Outcome. *J Immunol Res,* 2021**,** 6664791.

YAN, M., GU, Y., SUN, H. & GE, Q. 2023. Neutrophil extracellular traps in tumor progression and immunotherapy. *Front Immunol,* 14**,** 1135086.

YANG, H.-M., CHENG, Y.-Z., HOU, T.-Z., FAN, J.-K., GU, L., ZHANG, J.-N. & ZHANG, H. 2023. Upregulation of Parkinson's disease-associated protein alpha-synuclein suppresses tumorigenesis via interaction with mGluR5 and gamma-synuclein in liver cancer. *Archives of Biochemistry and Biophysics,* 744**,** 109698.

YAZDANI, M., JAAFARI, M. R., VERDI, J., ALANI, B., NOUREDDINI, M. & BADIEE, A. 2020. Ex vivo-generated dendritic cell-based vaccines in melanoma: the role of nanoparticulate delivery systems. *Immunotherapy,* 12**,** 333-349.

YEAP, W. H., WONG, K. L., SHIMASAKI, N., TEO, E. C., QUEK, J. K., YONG, H. X., DIONG, C. P., BERTOLETTI, A., LINN, Y. C. & WONG, S. C. 2016. CD16 is indispensable for antibody-dependent cellular cytotoxicity by human monocytes. *Sci Rep,* 6**,** 34310.

YILMAZ, M. T., ELMALI, A. & YAZICI, G. 2019. Abscopal Effect, From Myth to Reality: From Radiation Oncologists' Perspective. *Cureus,* 11**,** e3860.

YOON, K. W., BYUN, S., KWON, E., HWANG, S. Y., CHU, K., HIRAKI, M., JO, S. H., WEINS, A., HAKROUSH, S., CEBULLA, A., SYKES, D. B., GREKA, A., MUNDEL, P., FISHER, D. E., MANDINOVA, A. & LEE, S. W. 2015. Control of signaling-mediated clearance of apoptotic cells by the tumor suppressor p53. *Science,* 349**,** 1261669.

YOUSEF, S., JOY, C., VELAIUTHAM, S., MACLEAN, F. M., HARRAWAY, J., GILL, A. J. & VARGAS, A. C. 2022. Dedifferentiated melanoma with MDM2 gene amplification mimicking dedifferentiated liposarcoma. *Pathology,* 54**,** 371-374.

YU, J., ZHUANG, A., GU, X., HUA, Y., YANG, L., GE, S., RUAN, J., CHAI, P., JIA, R. & FAN, X. 2023. Nuclear PD-L1 promotes EGR1-mediated angiogenesis and accelerates tumorigenesis. *Cell Discovery,* 9**,** 33.

YU, Q., JIANG, M. & WU, L. 2022. Spatial transcriptomics technology in cancer research. *Front Oncol,* 12**,** 1019111.

YUAN, J., LI, X. & YU, S. 2024. Global, Regional, and National Incidence Trend Analysis of Malignant Skin Melanoma Between 1990 and 2019, and Projections Until 2034. *Cancer Control,* 31**,** 10732748241227340.

YUAN, L., TATINENI, J., MAHONEY, K. M. & FREEMAN, G. J. 2021. VISTA: A Mediator of Quiescence and a Promising Target in Cancer Immunotherapy. *Trends Immunol,* 42**,** 209-227.

ZAPAŁA, Ł., KUNC, M., SHARMA, S., PĘKSA, R., POPĘDA, M., BIERNAT, W. & RADZISZEWSKI, P. 2022. Immune checkpoint receptor VISTA on immune cells is associated with expression of T-cell exhaustion marker TOX and worse prognosis in renal cell carcinoma with venous tumor thrombus. *J Cancer Res Clin Oncol,* 149**,** 4131-4139.

ZAPALSKA-SOZONIUK, M., CHROBAK, L., KOWALCZYK, K. & KANKOFER, M. 2019. Is it useful to use several "omics" for obtaining valuable results? *Mol Biol Rep,* 46**,** 3597-3606.

ZENNADI, R., ABDEL-WAHAB, Z., SEIGLER, H. F. & DARROW, T. L. 2001. Generation of melanoma-specific, cytotoxic CD4(+) T helper 2 cells: requirement of both HLA-DR15 and Fas antigens on melanomas for their lysis by Th2 cells. *Cell Immunol,* 210**,** 96-105.

ZHAN, H., MA, J. Y. & JIAN, Q. C. 2018. Prognostic significance of pretreatment neutrophil-to-lymphocyte ratio in melanoma patients: A meta-analysis. *Clin Chim Acta,* 484**,** 136-140.

ZHANG, H., WANG, Y., QU, M., LI, W., WU, D., CATA, J. P. & MIAO, C. 2023. Neutrophil, neutrophil extracellular traps and endothelial cell dysfunction in sepsis. *Clinical and Translational Medicine,* 13**,** e1170.

ZHANG, T., YU, H., NI, C., ZHANG, T., LIU, L., LV, Q., ZHANG, Z., WANG, Z., WU, D., WU, P., CHEN, G., WANG, L., WEI, Q., HUANG, J. & WANG, X. 2017. Hypofractionated stereotactic radiation therapy activates the peripheral immune response in operable stage I non-small-cell lung cancer. *Sci Rep,* 7**,** 4866.

ZHANG, X., WU, Z. & MA, K. 2022. SNCA correlates with immune infiltration and serves as a prognostic biomarker in lung adenocarcinoma. *BMC Cancer,* 22**,** 406.

ZHANG, Y., XIA, M., JIN, K., WANG, S., WEI, H., FAN, C., WU, Y., LI, X., LI, X., LI, G., ZENG, Z. & XIONG, W. 2018. Function of the c-Met receptor tyrosine kinase in carcinogenesis and associated therapeutic opportunities. *Molecular Cancer,* 17**,** 45.

ZHAO, H. 2022. Design and Implementation of an Improved K-Means Clustering Algorithm. *Mobile Information Systems,* 2022**,** 6041484.

ZHAO, Q., WANG, Q., WANG, T., XU, J., LI, T., LIU, Q., YAO, Q. & WANG, P. 2021. Pattern Recognition Receptors (PRRs) in Macrophages Possess Prognosis and Immunotherapy Potential for Melanoma. *Front Immunol,* 12**,** 765615.

ZHAO, Y., MEHTA, M., WALTON, A., TALSANIA, K., LEVIN, Y., SHETTY, J., GILLANDERS, E. M., TRAN, B. & CARRICK, D. M. 2019. Robustness of RNA sequencing on older formalin-fixed paraffin-embedded tissue from high-grade ovarian serous adenocarcinomas. *PLoS One,* 14**,** e0216050.

ZHAO, Z., DING, Y., TRAN, L. J., CHAI, G. & LIN, L. 2023. Innovative breakthroughs facilitated by single-cell multi-omics: manipulating natural killer cell functionality correlates with a novel subcategory of melanoma cells. *Front Immunol,* 14**,** 1196892.

ZHOU, L. X., ZHENG, H., TIAN, Y., LUO, K. F., MA, S. J., WU, Z. W., TANG, P., JIANG, J. & WANG, M. H. 2022a. SNCA inhibits epithelial-mesenchymal transition and correlates to favorable prognosis of breast cancer. *Carcinogenesis,* 43**,** 1071-1082.

ZHOU, Q., FANG, T., WEI, S., CHAI, S., YANG, H., TAO, M. & CAO, Y. 2022b. Macrophages in melanoma: A double-edged sword and targeted therapy strategies (Review). *Exp Ther Med,* 24**,** 640.

ZHOU, Q., WU, X., WANG, X., YU, Z., PAN, T., LI, Z., CHANG, X., JIN, Z., LI, J., ZHU, Z., LIU, B. & SU, L. 2020. The reciprocal interaction between tumor cells and activated fibroblasts mediated by TNF-α/IL-33/ST2L signaling promotes gastric cancer metastasis. *Oncogene,* 39**,** 1414-1428.

ZIANI, L., SAFTA-SAADOUN, T. B., GOURBEIX, J., CAVALCANTI, A., ROBERT, C., FAVRE, G., CHOUAIB, S. & THIERY, J. 2017. Melanoma-associated fibroblasts decrease tumor cell susceptibility to NK cell-mediated killing through matrix-metalloproteinases secretion. *Oncotarget,* 8**,** 19780-19794.

ZIDANE, M., MAKKY, A., BRUHNS, M., ROCHWARGER, A., BABAEI, S., CLAASSEN, M. & SCHÜRCH, C. M. 2023. A review on deep learning applications in highly multiplexed tissue imaging data analysis. *Front Bioinform,* 3**,** 1159381.

ZIMMERMANNOVA, O., FERREIRA, A. G., ASCIC, E., VELASCO SANTIAGO, M., KUROCHKIN, I., HANSEN, M., MET, Ö., CAIADO, I., SHAPIRO, I. E., MICHAUX, J., HUMBERT, M., SOTO-CABRERA, D., BENONISSON, H., SILVÉRIO-ALVES, R., GOMEZ-JIMENEZ, D., BERNARDO, C., BAUDEN, M., ANDERSSON, R., HÖGLUND, M., MIHARADA, K., NAKAMURA, Y., HUGUES, S., GREIFF, L., LINDSTEDT, M., ROSA, F. F., PIRES, C. F., BASSANI-STERNBERG, M., SVANE, I. M. & PEREIRA, C. F. 2023. Restoring tumor immunogenicity with dendritic cell reprogramming. *Sci Immunol,* 8**,** eadd4817.

ZOCCHI, M. R., MARIA, V. & ALESSANDRO, P. 1993. Involvement of CD56/N-CAM Molecule in the Adhesion of Human Solid Tumor Cell Lines to Endothelial Cells. *Experimental Cell Research,* 204**,** 130-135.

ZONG, L., MO, S., SUN, Z., LU, Z., YU, S., CHEN, J. & XIANG, Y. 2022. Analysis of the immune checkpoint V-domain Ig-containing suppressor of T-cell activation (VISTA) in endometrial cancer. *Mod Pathol,* 35**,** 266-273.

ZONG, L., MO, S., YU, S., ZHOU, Y., ZHANG, M., CHEN, J. & XIANG, Y. 2020. Expression of the immune checkpoint VISTA in breast cancer. *Cancer Immunol Immunother,* 69**,** 1437-1446.

ZUO, B., LI, T., LIU, X., WANG, S., CHENG, J., LIU, X., CUI, W., SHI, H. & LING, C. 2023. Dipeptidyl peptidase 4 inhibitor reduces tumor-associated macrophages and enhances anti-PD-L1-mediated tumor suppression in non-small cell lung cancer. *Clinical and Translational Oncology,* 25**,** 3188-3202.

Presentations During Candidature

2023 **Chris O'Brien Lifehouse Research Symposium** (Sydney) *Poster*
Spatial Signatures of Immune Cells in the Tumour Microenvironment predicts outcomes in Stage III Melanoma"

International Cancer Immunotherapy Conference (Milan, Italy) *Poster*
Poster "Spatial Signatures of Immune Cells in the Tumour Microenvironment predicts outcomes in Stage III Melanoma".

BACR Conference "Tumour Microenvironment and 3D Modelling" (Nottingham, UK) *Poster*
"Spatial Signatures of Immune Cells in the Tumour Microenvironment predicts outcomes in Stage III Melanoma".

Melanoma Institute of Australia MTRG Showcase (Sydney) *Oral Presentation*
"Using Imaging Mass Cytometry to map the immune landscape of melanoma to predict clinical outcomes".

Australasian Melanoma Conference (Brisbane) *Oral Presentation*
"Immune Mapping of Radio-responsive tumours using Imaging Mass Cytometry"

2022 **Australian Society of Immunology** (Melbourne) *Poster*
"Immune Mapping of radio-responsive tumours using Imaging Mass Cytometry"

Melanoma Institute of Australia MTRG Showcase (Sydney) *Oral Presentation* "Using Imaging Mass Cytometry to map the immune landscape of melanoma to predict clinical outcomes".

2021 **Sydney Catalyst Research Showcase** (Sydney) *Oral Presentation*
"High-dimensional and spatial analysis reveals progression dependent immune landscape in cutaneous squamous cell carcinoma of the head and neck".

2020 **Sydney Cancer Network CRN PG and ECR Symposium** (Online) *Oral Presentation*
"VISTA in the Tumour Microenvironment of Metastatic Melanoma"

Awards and Grants Received During Candidature

Awards	**Chris O'Brien Lifehouse Research Symposium Poster Prize** for Clinical Impact Category *2023*
	Best Rapid-Fire Presentation for oral presentation at Sydney Catalyst Postgraduate & Early Career Researcher Symposium *2020*
Grants	**Cancer Institute NSW Travel Grant** to cover international conference costs for CICON *2023*
	Charles Perkins Centre Early to Mid-Career Researcher Professional Development Grant *2023*
	Student Conference Grant from Sydney Cancer Partners *2022*
	Student Bursary from the Australian Society of Immunology to cover registration and flights for ASI National Meeting *2022*
Scholarships	**Research Training Program Stipend Scholarship** from Australian Government Department of Education *2020 – 2024*
	Melanoma Institute of Australia Postgraduate Research Top-Up Scholarship *2020 – 2024*